# Laser powder bed fusion of Inconel 939: from parameter optimization to microstructural design

by

Ignacio Rodríguez Barber

A dissertation submitted in partial fulfillment of the requirements for the degree of Doctor of Philosophy in

Materials Science and Engineering

Universidad Carlos III de Madrid

Advisor:

Dr. María Teresa Pérez Prado

Tutor:

Prof. Mónica Campos Gómez

September 2025

A mi madre, al meu pare,

# ACKNOWLEDGEMENTS

This research has been supported by the Spanish Ministry of Science, Innovation and Universities, under project PID2019-111285RB-I00. I am also grateful for the FPI fellowship awarded by the same ministry, Ref. PRE2020-094256, which has funded this work throughout these years.

When I started this long adventure, I did not know what to expect. I could have never imagined it would be what it has been: an incredible journey. This has been possible thanks to all the people I have had the immense luck to share it with. I will take the freedom to thank those I feel most obliged to in my own words.

First, I have to thank Dr. Teresa Pérez Prado, the best supervisor I could have asked for. Gracias por darme esta oportunidad, por haber sido una gran guía y un enorme apoyo. Gracias por enseñarme tanto, a nivel académico y a nivel humano. A lo largo de una tesis hay muchos altibajos, pero tú eres una constante, siempre con una buena cara y con palabras de ánimo y de aliento. Qué inmensa suerte haber podido trabajar contigo.

Gracias también a mis tutores académicos. Al Prof. Srdjan Milenkovic, aunque nuestros caminos se separaran, y a la Prof. Mónica Campos, por acogernos sin reparos.

I also have to thank Prof. Zack Cordero and his team at MIT for giving me the opportunity of being part of your team, even if just for a short while. Thank you for challenging me to grow, for your teaching and guidance. Isha, Roger, Chris, Tim, Spencer, Harsh, thank you for welcoming me with open arms, forever grateful. Great places are made by great people, and you all are the greatest.

A toda la gente de ITP Aero, gracias por ayudarme a dar mis primeros pasos, cuando era un absoluto novato. En especial, gracias a Ana Fernández e Iñaki Madariaga, por hacerme ver las cosas desde distintas perspectivas. Ha sido un placer trabajar con vosotros.

Gracias a los que hacéis posible que todo salga adelante en IMDEA Materiales. A Amalia, gracias por tu paciencia, y por tantas horas compartidas aislados, puliendo, o cortando. Espero haberme portado bien. A Manu, por las muchas horas entre SEMs y TEMs, dentro y fuera de IMDEA. A Teri, ¡qué gran fichaje!. Gracias por estar siempre dispuesta a arrimar el hombro. Gracias a Vanesa, José Luís, Miguel, Javi, Mónica (aunque me matarais, sigo estando agradecido). Sois los que mantenéis esto en pie. Gracias Cris por alegrarnos todas las mañanas, aunque no seas del equipo bueno. Gracias Cyril, Pilar, Paco, Gema, Juana, Carlos, sois los héroes silenciosos.

Sergi, a tu no se si donar-te les gràcies o maleïr-te. Tan tranquil com estava i vas haver de portar-me a Madrid. No cal que et digui quant t'admiro, gràcies per ser una inspiració.

To all the members of the best research group there will ever be, thank you. Gracias Clara por ser mi primera maestra y por aguantarme. To Dongfeng, for your honesty. To Xueze, for always being willing to help. To Shruti, for your kindness. To Souvik, for sharing your immense knowledge. To Henry, for your energy, the best (though a bit late) addition to the team! Saumya, thank you for your bad jokes and your doodles, and for being the most thoughtful

person. Marcos, gracias por aguantar mis divagaciones sobre láseres y melt pools, me has hecho crecer y aprender. Lo mereces todo y más.

I want to express my heartfelt gratitude to every person I've shared my time with at IMDEA. If I were to name them all, this thesis would be longer than the Bible, so I won't, but thank you for making these some of the greatest years of my life. Coming to work was always easy with you.

Eugenia, mi Mariu, gracias por alegrarme con un "mi viiiida", por ser una gran amiga, una tremenda científica, una inmejorable compañera. Cillian, mi broder, thank you for making our Mondays a bit more fun, for all the laughs, for making our lives better. Ignacio José, siempre fue un placer trabajar contigo, y nunca fue tan fácil aguantar una chapa. Gracias por ser el Nacho bueno. Carmen, gracias por tu autenticidad, y por recordarnos cuál es nuestro sitio. No cambies. Ángela, gracias por cuidarnos a todos, de corazón. Davide, gracias por dejarnos ver la gran persona que eres, y que no todo en la vida son lunes. Jose, gracias por romper el cascarón y unirte a esta familia. Lola, gracias por ser un ejemplo en todo, eres enorme. Maral, thank you for your smiles and your high-fives, and sorry for all the times I snapped my fingers. Carlos, desde la admiración más profunda, gracias por compartir la lectura y tu sabiduría conmigo. Yuyao, thank you for making the second floor a more cheerful place. Óscar, gracias por hacer más llevaderas tantas horas de laboratorio, desde el primer día hasta el último. Alberto, Pedro, Jesús, María, gracias por enseñarme que este oficio también puede ser divertido. A toda la gente de la segunda planta: Mónica, Jorge, Valerio, Raúl, Adrián, Thomas, gracias estar ahí. Nabil, Rafa, María, Isa, Ángela, Franck, David y tantxs más, al final no eráis tan malos. A todos y todas, gracias por las horas compartidas, los cafés, comidas, carnavales, fiestas. Hacéis de este un sitio maravilloso.

Gracias también a toda la gente con la que he compartido y que me ha ayudado durante estos años fuera de IMDEA. Júlia, gràcies per fer de Madrid una casa per mi. Marta, gracias por ser otra hermana. Lara y Juanma, gracias por ser los mejores vecinos y amigos. Almu, gracias por compartir tu mundo con nosotros, ¡qué bueno que viniste!

Laura, llegaste un poco tarde. Supongo que le chiocciole vanno lente, ma arrivano, e quello è l'importante. Gracias por acompañarme en este último tramo, por ayudarme, por ilusionarme.

Delabat, has hecho que Madrid sea casi tan buena como Barcelona. Gracias por hacer que la vida sea más divertida, aquí, en Luleå, en Cetina, y allí donde nos quiera llevar la vida.

Jorge, gracias por alegrarnos cada momento en esta santa casa, por ser tan bueno (demasiado, si me preguntas), por dejarme ser tu padre. Tu mera presencia lo mejora todo, gracias.

Guille, no sé por dónde empezar. Gracias por compartirlo todo conmigo. Creo que ya desde tu primer café en IMDEA supe que ibas a ser importante, pero nunca podría haber imaginado cuánto. Si te tengo que agradecer todo lo que has hecho, esto no termina. Gracias.

Por último, gracias a toda mi familia, por haberme animado siempre, en todas mis aventuras, por apoyarme sin reparos. Mamá, pare, Elena, Blanca, gracias. Nada de esto sería posible sin vosotros.

## PUBLISHED AND SUBMITTED CONTENT

1. **"Laser powder bed fusion of the Ni superalloy Inconel 939 using pulsed wave emission"**
   **I. Rodríguez-Barber**, A.M. Fernández-Blanco, I. Unanue-Arruti, I. Madariaga-Rodríguez, S. Milenkovic, M. T. Pérez-Prado.
   Published in *Materials Science and Engineering A*, vol. 870 (2023), 144864.
   https://doi.org/10.1016/j.msea.2023.144864
   This article is partially included in Chapter 4.
   The material from this source included in this thesis is not singled out with typographic means and references.
   Role: methodology, investigation, analysis, writing.

2. **"Precontouring as a tool to improve the laser powder bed fusion printability of Inconel 939 thin walls"**
   **I. Rodríguez-Barber**, A.M. Fernández-Blanco, I. Unanue-Arruti, I. Madariaga-Rodríguez, S. Milenkovic, M. T. Pérez-Prado.
   Published in *Advanced Engineering Materials 2401929* (2024) 1-8.
   https://doi.org/10.1002/adem.202401929
   This article is partially included in Chapter 5.
   The material from this source included in this thesis is not singled out with typographic means and references.
   Role: methodology, investigation, analysis, writing.
3. **"On the role of the melt pool overlap in texture selection of a PBF-LB/M Ni-based superalloy"**
   **I. Rodríguez-Barber**, M.T. Pérez-Prado.
   Submitted to *Additive Manufacturing*.
   This article is partially included in Chapter 7.
   The material from this source included in this thesis is not singled out with typographic means and references.
   Role: methodology, investigation, analysis, writing.

4. **"Understanding the effect of pre-sintering scanning strategy on the relative density of Zr-modified Al7075 processed by laser powder bed fusion"**
   N. Nothomb, **I. Rodríguez-Barber**, M. T. Pérez-Prado, N. Jimenez Mena, G. Pyka, A. Simar.
   Published in *Additive Manufacturing Letters 11* (2024) 100253.
   https://doi.org/10.1016/j.addlet.2024.100253
   This article is not included in the thesis.
   Role: experimental work, analysis.

5. **"Understanding the effect of a tailored heat treatment on Zr-modified Al7075 processed by laser powder bed fusion"**
   N. Nothomb, **I. Rodríguez-Barber**, M. Avettand-Fénoël, M.T. Pérez-Prado, M. Marinova, A. Simar.
   Submitted to *Materials and Design*.
   This article is not included in the thesis.
   Role: experimental work, analysis.

## ARTICLES IN PREPARATION

**"On the influence of the initial microstructure on the thermal treatment of PBF-LB/M"**

**I. Rodríguez-Barber**, T. Voisin, M. Naeem, L. Romero-Reséndiz, A.M. Fernández-Blanco, I. Madariaga-Rodríguez, M.T. Pérez-Prado.
This article is partially included in Chapter 6.
The material from this source included in this thesis is not singled out with typographic means and references.
Role: methodology, investigation, analysis, writing.

# OTHER RESEARCH MERITS

## ORAL PRESENTATIONS AT NATIONAL AND INTERNATIONAL CONFERENCES

1. **"Laser powder bed fusion of Inconel 939"**
   **I. Rodríguez-Barber**, A.M. Fernández-Blanco, I. Unanue-Arruti, I. Madariaga-Rodríguez, S. Milenkovic, M. T. Pérez-Prado.
   18th European Mechanics of Materials Conference (EMMC18).
   University of Oxford Oxford, UK, April 4th-6th 2022.

2. **"Additive Manufacturing of high-temperature superalloys for sustainable air transportation"**
   **I. Rodríguez-Barber**, A.M. Fernández-Blanco, I. Unanue-Arruti, I. Madariaga-Rodríguez, S. Milenkovic, M. T. Pérez-Prado.
   National Conference of Materials 2022 (CNMAT2022).
   Universidad de Castilla-La Mancha, Ciudad Real, Spain, June 27th-July 1st 2022.

3. **"Thermal treatment study of L-PBFed IN939"**
   **I. Rodríguez-Barber**, A.M. Fernández-Blanco, I. Unanue-Arruti, I. Madariaga-Rodríguez, S. Milenkovic, M. T. Pérez-Prado.
   Alloys for Additive Manufacturing Symposium 2022 (AAMS22).
   Universität der Bundeswehr, Munich, Germany, September 11th-14th 2022.

4. **"Microstructural tuning of L-PBFed IN939 through laser scanning parameter modification"**
   **I. Rodríguez-Barber**, S. Milenkovic, M. T. Pérez-Prado.
   Alloys for Additive Manufacturing Symposium 2023 (AAMS23).
   Universidad Carlos III de Madrid, Madrid, Spain, September 27th-29th 2023.

5. **"Pre-contour scans as a new design tool for PBF-LB/M thin-wall structures"**
   **I. Rodríguez-Barber**, A. D. Boccardo, S. Milenkovic, M. T. Pérez-Prado.
   19th European Mechanics of Materials Conference (EMMC19).
   Universidad Politécnica de Madrid, Madrid, Spain, May 29th–31st 2024.

6. **"An analytical approach to scanning parameter selection: adapting normalized enthalpy to complex geometries for microstructural design"**
   **I. Rodríguez-Barber**, S. Milenkovic, M. T. Pérez-Prado.
   Alloys for Additive Manufacturing Symposium 2024 (AAMS24).
   École Polytechnique, Palaiseau, Paris, France, September 4th-6th 2024.

# ABSTRACT

Powder bed fusion of Ni-based superalloys has seen rapid development and improvements over recent years, both at academic and industrial levels. The high-temperature strength and oxidation resistance of Ni-based superalloys, together with the design flexibility inherent to additive manufacturing, enable the production of optimized components for gas and aircraft turbines. There are, however, certain challenges related to the fabrication and post-processing of γ'-strengthened alloys by PBF-LB/M.

This thesis investigates PBF-LB/M fabrication of IN939, focusing on understanding the interplay between processing and post-processing parameters, microstructure, and the resulting properties of printed parts using a wide range of experimental techniques. An appropriate processability window for IN939 using a pulsed wave laser is identified, yielding defect-free parts (>99.5 % relative density) with minimal crack formation. The influence of the energy input on microstructural features such as grain morphology and crystallographic texture is examined. The fabrication of thin-walled IN939 parts is also investigated. The incorporation of a pre-contour scan before hatch scanning effectively enhances thermal diffusivity at a subsurface level, leading to reduced melt pool depth and mitigating keyhole porosity, particularly for walls thinner than 1 mm.

The influence of the as-built microstructure on the recrystallization kinetics is also explored. The presence of MC carbides in the as-built state retards the onset of recrystallization via Smith-Zener pinning. Additionally, as-built samples with a smaller initial grain size, coupled with a weaker crystallographic texture, recrystallize at lower temperatures. A modified solution treatment consisting of 8 h at 1200ºC is proposed to induce recrystallization of PBF-LB/M irrespective of the initial microstructure.

Mechanical testing from room temperature to 950ºC is performed for samples following the standard and modified thermal treatments. The latter hinders diffusion-related deformation mechanisms, and thus results in superior yield and ultimate tensile strengths along the full temperature range.

Finally, the possibility of locally tailoring the microstructure in-situ via scanning parameter modifications is tested. The horizontal melt pool overlap is identified as a useful variable to control and predict the degree of epitaxial growth, and therefore the final microstructure.

# RESUMEN

La fusión en lecho de polvo por láser (PBF-LB/M por sus siglas en inglés) de superaleaciones base níquel ha experimentado un rápido desarrollo y mejoras en los últimos años, tanto a nivel académico como industrial. Las buenas propiedades mecánicas y resistencia a la oxidación a altas temperaturas de estas aleaciones, combinadas con la flexibilidad de diseño propia de la fabricación aditiva, permiten la producción de componentes más eficientes para turbinas en los sectores energético y aeronáuticos. Sin embargo, existen ciertos desafíos asociados a la fabricación mediante PBF-LB/M de aleaciones endurecidas por precipitación.

Esta tesis investiga el procesamiento de IN939 mediante PBF-LB/M con el objetivo de comprender la interacción entre los parámetros de fabricación y posprocesado, la microestructura resultante y las propiedades finales de las piezas impresas, utilizando una amplia gama de técnicas experimentales. Dos conjuntos de parámetros de escaneado distintos son identificados cómo óptimos para procesar IN939. Con ambos se pueden obtener piezas libres de defectos (densidades relativas por encima del 99.5%) y con mínimo agrietamiento. Este estudio también pone de manifiesto una influencia clara de la energía aportada en la microestructura, tanto a nivel de tamaño y morfología de los granos como de la textura cristalográfica.

Asimismo, se analiza la fabricación de piezas delgadas de IN939, mostrando cómo la incorporación de un primer escaneo de contorno mejora la difusividad térmica en zonas cercanas a la superficie de las muestras, reduciendo la formación de porosidad tipo *keyhole*, en especial en espesores inferiores a 1 mm.

El efecto de la microestructura de partida en la cinética de recristalización también ha sido investigado. La presencia de carburos retrasa el inicio de la recristalización debido al anclaje (*pinning*) de Smith-Zener. Un tamaño de grano inicial más fino, combinado con una textura cristalográfica más débil, acelera la recristalización al proporcionar más puntos favorables a la nucleación y crecimiento de grano. Se propone un tratamiento térmico de solución modificado consistente en 8 h a 1200 °C para inducir la recristalización en piezas fabricadas por PBF-LB/M, independientemente de la microestructura de partida**.**

Muestras tratadas térmicamente siguiendo tanto el tratamiento estándar como el tratamiento modificado son ensayadas mecánicamente a distintas temperaturas (de

temperatura ambiente hasta 950ºC). El tratamiento modificado induce el crecimiento de granos, que a su vez reduce la influencia de mecanismos de deformación relacionados con la difusión, aumentando el límite elástico y la tensión de rotura en todo el rango de temperaturas.

Finalmente, se estudia la posibilidad de modificar localmente la microestructura mediante ajustes en los parámetros de escaneado in-situ, usando el solapamiento horizontal de los cordones de fusión (*melt pool*) como una variable para controlar y predecir el grado de crecimiento epitaxial, y por tanto, la microestructura final.

# Table of contents

## LIST OF FIGURES

# LIST OF TABLES

# LIST OF ABREVIATIONS AND SYMBOLS

| | |
|---|---|
| AB | As-built |
| AM | Additive manufacturing |
| ANOVA | Analysis of variance |
| AR | Aspect ratio |
| ASTM | American society for testing and materials |
| BCT | Body-centered tetragonal |
| BD | Build direction |
| BF | Bright field |
| BJT | Binder jetting |
| BSE | Backscattered electrons |
| CAD | Computer-aided design |
| CBS | Concentric backscattered |
| CET | Columnar to equiaxed transition |
| CW | Continuous wave |
| DED | Directed energy deposition |
| DoE | Design of experiments |
| EA | Electric arc |
| EB | Electron beam |
| EBSD | Electron backscatter diffraction |
| EDS/EDX | Energy-dispersive X-ray spectroscopy |
| ETD | Everhart-Thornley detector |
| FCC | Face-centered cubic |
| FEG | Field emission gun |
| FIB | Focused ion beam |
| GB | Grain boundary |
| GBS | Grain boundary sliding |
| GND | Geometrically necessary dislocations |
| HAADF | High angle annular dark field |
| HAGB | High angle grain boundary |
| HAZ | Heat affected zone |

| | |
|---|---|
| HIP | Hot isostatic pressing |
| HT | Heat-treated |
| ICME | Integrated computational materials engineering |
| ICP-MS | Inductively coupled plasma mass spectroscopy |
| ICP-OES | Inductively coupled plasma optical emission spectroscopy |
| IPF | Inverse pole figure |
| KAM | Kernel average misorientation |
| LAGB | Low angle grain boundary |
| LB | Laser beam |
| LI | Line intercept |
| LIR | Line intercept ratio |
| LOF | Lack of fusion |
| MUD | Multiples of uniform distribution |
| ODF | Orientation distribution function |
| ODS | Oxide dispersion strengthened |
| OM | Optical microscopy |
| OPS | Oxide polishing suspension |
| PBF | Powder bed fusion |
| PBF-LB/M | Powder bed fusion – laser beam/metals |
| PF | Pole figure |
| PSD | Particle size distribution |
| PW | Pulsed wave |
| RBV | Reduced build volume |
| RT | Room temperature |
| RX | Recrystallized/recrystallization |
| SAC | Strain age cracking |
| SAD | Selected area diffraction |
| SD | Scanning direction |
| SE | Secondary electron |
| SEM | Scanning electron microscopy |
| STEM | Scanning transmission electron microscopy |

| | |
|---|---|
| TB | Twin boundary |
| TCP | Topologically close-packed |
| TEM | Transmission electron microscopy |
| TWIP | Twinning induced plasticity |
| UTS | Ultimate tensile strength |
| YAG | Yttrium aluminum garnet |
| YLF | Yttrium lithium fluoride |
| YS | Yield strength |

| | |
|---|---|
| A | Laser absorptivity |
| $\alpha$ | Thermal diffusivity |
| b | Burgers vector |
| $C_p$ | Specific heat capacity |
| d | Melt pool depth |
| $\varepsilon$ | Strain |
| E | Young’s Modulus |
| $\dot{\varepsilon}$ | Strain rate |
| $E_l$ | Linear energy density |
| $e_t$ | Exposure time |
| $E_v$ | Volumetric energy density |
| $E_v^*$ | Dimensionless volumetric energy density |
| $F_v$ | Volume fraction (of secondary particles) |
| G | Thermal gradient / Shear modulus[*] |
| $\gamma_b$ | Grain boundary energy |
| $\gamma_m$ | Energy of a high angle grain boundary |
| H | Enthalpy |
| $h_d$ | Hatch distance |
| $h_d^*$ | Dimensionless hatch distance |
| $h_s$ | Enthalpy of melting |
| $I_{max}$ | Maximum intensity (of an inverse pole figure) |
| $\kappa$ | Thermal conductivity |
| l | Scan track length |
| $LI_l$ | Longitudinal line intercept |
| $LI_t$ | Transverse line intercept |
| $L_m$ | Latent heat of melting |
| m | Strain rate sensitivity |
| $O_h$ | Horizontal melt pool overlap |
| P | Laser power |

---

[*] Specified in the corresponding chapter

| | |
|---|---|
| $P_c$ | Retarding pressure from grain boundary curvature |
| $P_d$ | Driving pressure for recrystallization |
| $p_d$ | Point distance |
| $P_{SZ}$ | Smith-Zener pinning pressure |
| $\theta$ | Misorientation angle |
| $\theta_m$ | Critical misorientaion angle (15º) |
| $q$ | Absorbed laser power |
| $q^*$ | Dimensionless beam power |
| $\rho$ | Density |
| $\rho_a$ | Apparent density |
| $\rho_t$ | Tap density |
| $R$ | Solidification rate / Radius of a newly nucleated grain[*] |
| $r$ | Radial distance |
| $\sigma$ | Stress |
| $\sigma_y$ | Yield stress |
| $t$ | Layer thickness |
| $t^*$ | Dimensionless layer thickness |
| $T$ | Temperature |
| $\dot{T}$ | Cooling rate |
| $T_m$ | Melting temperature |
| $T_{preheat}$ | Powder bed preheat temperature |
| $T_s$ | Solidus temperature |
| $T_0$ | Starting temperature |
| $t_d$ | Time delay |
| $t_r$ | Rescan time |
| $v$ | Scanning speed |
| $v^*$ | Dimensionless scanning speed |
| $V_f$ | Volume fraction (of texture components) |

---

[*] Specified in the corresponding chapter

| | |
|---|---|
| $V_{f<001>//BD}$ | Volume fraction of a <001> component in a direction parallel to the BD |
| w | Melt pool width |
| $\omega$ | Laser beam radius |

# 1. INTRODUCTION

## 1.1. Project frame

This work started as a collaboration between IMDEA Materials Institute and ITP Aero, one of the world-leading aircraft component manufacturers [1], with the ultimate goal of developing a viable methodology to produce parts for next-generation aircrafts. ITP Aero has made a strong commitment to additive manufacturing as a solution to meet the challenges of the future of aviation, becoming the first aeroengine manufacturer to obtain certification for an AM structural component from the European Union Aviation Safety Agency (EASA), a key milestone [2]. The technology of choice, laser powder bed fusion (PBF-LB/M, from Powder Bed Fusion – Laser Beam/Metals), offers numerous advantages, including a reduced buy-to-fly ratio and the ability to produce optimized components with lower mass and improved performance [3,4].

Ni-based superalloys are exceptional materials with outstanding high-temperature properties, which makes them ideal for gas turbine or aircraft components [5]. The synergy between PBF-LB/M capabilities and the properties of Ni-based superalloys is crucial to advancing toward a more efficient and environmentally sustainable aviation industry. Amongst the many available alloys we selected Inconel 939 (IN939) for its excellent oxidation resistance and high strength at elevated temperatures, making it an ideal candidate for both energy and aeronautical applications.

As this thesis was preparing for takeoff, the literature on PBF-LB/M of IN939 was scarce, and strong efforts were needed to better understand the process at many different levels, from the laser-material interactions during fabrication, to the mechanical behavior of manufactured parts at high temperatures. This overarching aim defines the main objective of this thesis: to understand the link between processing, microstructure, and properties in PBF-LB/M of IN939.

## 1.2.Outline

The following chapters constitute the structure of this thesis. Chapter 2 provides a literature review, starting with a brief introduction to the different additive manufacturing techniques. We then focus on PBF-LB/M, the technique employed in this study, playing close attention to the main processing parameters and to how these affect the outcome of the printing process, in particular the defects and microstructure of PBF-LB/M parts. This is followed by an introduction to Ni-based superalloys, their principal alloying elements, and the specific challenges associated to processing these materials using PBF-LB/M. A more detailed review of the current state of the art regarding PBF-LB/M of IN939 concludes the chapter.

Chapter 3 describes the materials and the main experimental techniques used throughout this work in detail.

The core results are presented in the next four chapters. Chapter 4 details the optimization of the printing process for bulk parts, including the study of the influence of processing parameters on defect formation and microstructural features. Chapter 5 addresses improvements in the processability of thin sections. Chapter 6 explores the thermal treatment of PBF-LB/M parts, focusing on the solution treatment and on the influence of the as-built (AB) microstructure on the recrystallization kinetics. Finally, Chapter 7 investigates the potential for locally tailoring microstructures in a simple and direct way by modifying scanning parameters.

All of these results are then summarized in Chapter 8, where the main outcomes are highlighted, followed by suggestions for future research directions in Chapter 9.

# 2. LITERATURE REVIEW

## 2.1. Additive manufacturing

### *2.1.1. Overview*

Additive manufacturing (AM), also known as 3D printing, can be defined as “the process of joining materials to make parts from 3D model data, usually layer upon layer, as opposed to subtractive manufacturing and formative manufacturing methodologies” [6]. In general, for most layer-based AM processes, the first step is to design the geometry to be produced with the help of a CAD software. This 3D shape can be defined by its surface using a series of triangles and their normal vectors (.STL files). These files are then sliced in different layers (with a fixed layer thickness), determining the 2D cross-sections corresponding to each layer.

First developed as a rapid prototyping technique, it quickly evolved to become a group of manufacturing techniques for complex functional parts. Following some early inventions starting in the 1960s, stereolithography was the first AM technique to be commercialized in 1987 [7]. This was followed by rapid development of other techniques and systems, leading to the current state of AM as a consolidated industry, with roughly 22 billion $US in revenue in 2024 (Figure 2-1) [8].

Additive manufacturing (AM) processes are commonly categorized into seven main types, based on factors such as the feedstock material, energy source, and deposition or consolidation mechanisms [6]. These categories are: binder jetting, directed energy deposition, material extrusion, material jetting, powder bed fusion, sheet lamination, and vat photopolymerization.

Perhaps the biggest advantage of AM processes, compared to subtractive o formative manufacturing technologies, is the freedom and flexibility of design. This enables the production of geometrically complex parts that would otherwise be unachievable, increases the utilization of feedstock materials—since the manufactured parts are typically near-net-shape—and allows for the easy and rapid fabrication of fully customized components. However, several drawbacks still limit the broader adoption of AM technologies in certain fields, including the high cost of printed parts, limitations in fabrication speed, and relatively small build volumes [9,10]. The aforementioned AM processes, along with their respective advantages and limitations, are generally applicable across all types of feedstock materials. Currently, a wide variety of additively manufactured products and components can be found in various sectors, from the aerospace and automotive industries to the biomedical field.

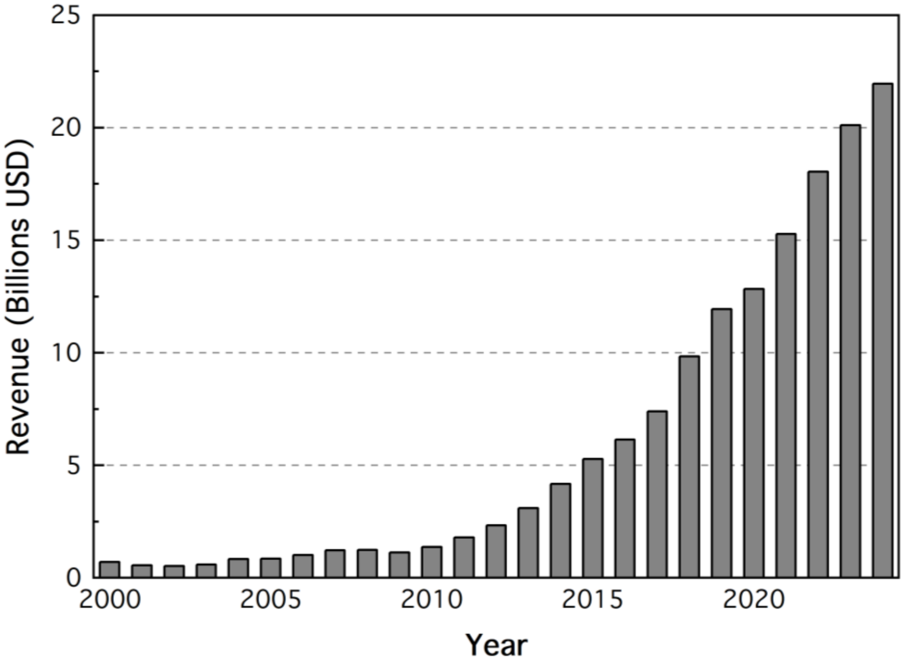

Figure 2-1: Revenue of the additive manufacturing market per year, from 2000 to 2024. Adapted from [8].

### *2.1.2. Metal additive manufacturing*

Since this thesis focuses on a metallic material, the most relevant additive manufacturing technologies for metals [11] are outlined below:

- *Powder bed fusion (PBF)*, using either a laser or an electron beam (LB and EB, respectively). A melt-based technique, where the energy source is focused towards a metal powder layer spread on top of a substrate, and the desired sections are selectively melted. This is the most widely used metal AM process [9,12].
- *Directed energy deposition (DED)*, another melt-based process. Apart from laser and electron beams (LB, EB), it can also use electric arcs (EA) as energy inputs. The feedstock material, which can be either powder or wire, is delivered into the melt pool simultaneous to the energy input [9,12].
- *Binder jetting (BJT)* is the third most popular metal AM technique. A binder is deposited onto the powder bed and subsequently heated to form the green parts, which are then post processed to achieve the final sintered parts. Since it does not

rely on melting of the feedstock material, it is the least energy-intensive of the three [13].

Each process has its advantages and limitations, and the final application and requirements will determine the best suited option. Some of the main characteristics of each of the main processes listed above are summarized in Table 2-1.

Table 2-1: Main characteristics of key metal AM technologies. According to the 52900 ASTM standard, the nomenclature of a specific process starts with the acronym of the technique, followed by the energy source (preceded by a dash -), and finally by the type of material (preceded by a slash /) [6]. The build rates were left as comparative given the high variability in reported values in the literature [9,12,13].

| | **PBF-LB/M** | **PBF-EB/M** | **DED-LB/M** | **BJT/M** |
|---|---|---|---|---|
| **Build size** | 500 x 400 x 500 mm$^3$ | 500 x 300 x 300 mm$^3$ | In the meter scale | 2200 x 1200 x 600 mm$^3$ |
| **Build rate** | Low | Moderate | High | Very high |
| **Dimensional accuracy** | 0.04-0.1 mm | 0.2-0.5 mm | 0.3-1 mm | 0.2-0.5 mm |
| **Surface roughness (Ra)** | 10-20 μm | 20-50 μm | 20-100 μm | 20-50 μm |
| **Post-processing** | Thermal treatments (including HIP). Surface quality improvement only in selected cases. | Thermal treatments. Surface quality improvement. | Machining to improve surface quality. | Sintering, machining to improve surface quality. |
| **Advantages** | High precision; excellent mechanical properties; fine feature resolution. | Medium resolution; heated powder bed helps reduce residual stresses; processing of refractory alloys. | High deposition rates; suitable for large components and repairs. | Cost-effective; high throughput; minimal support structures. |

## 2.2. Laser powder bed fusion

Laser powder bed fusion (PBF-LB/M) is the AM process that has been used in this thesis. In the following, this process is reviewed in detail.

In PBF-LB/M, the feedstock material is in the form of powder. The powder is spread on a substrate using a recoater, and the 2D cross-sections corresponding to that layer are then melted using a high-power laser beam. This laser beam is focused and directed towards the intended locations using an optical unit composed by a series of lenses and mirrors. After a layer has been melted, the substrate is lowered by a predefined layer thickness, and a new thin layer of powder is spread and melted by the laser beam. This process is repeated, layer-upon-layer, until the final 3D part is fabricated. Once the printing is finished, the unmelted powder is collected (it can be reused following a sieving step), and the parts are removed from the substrate – typically by electro-discharge machining or other machining methods-, and post-processed if necessary. Figure 2-2 illustrates the basic functioning of a PBF-LB/M setup similar to the one used in this thesis.

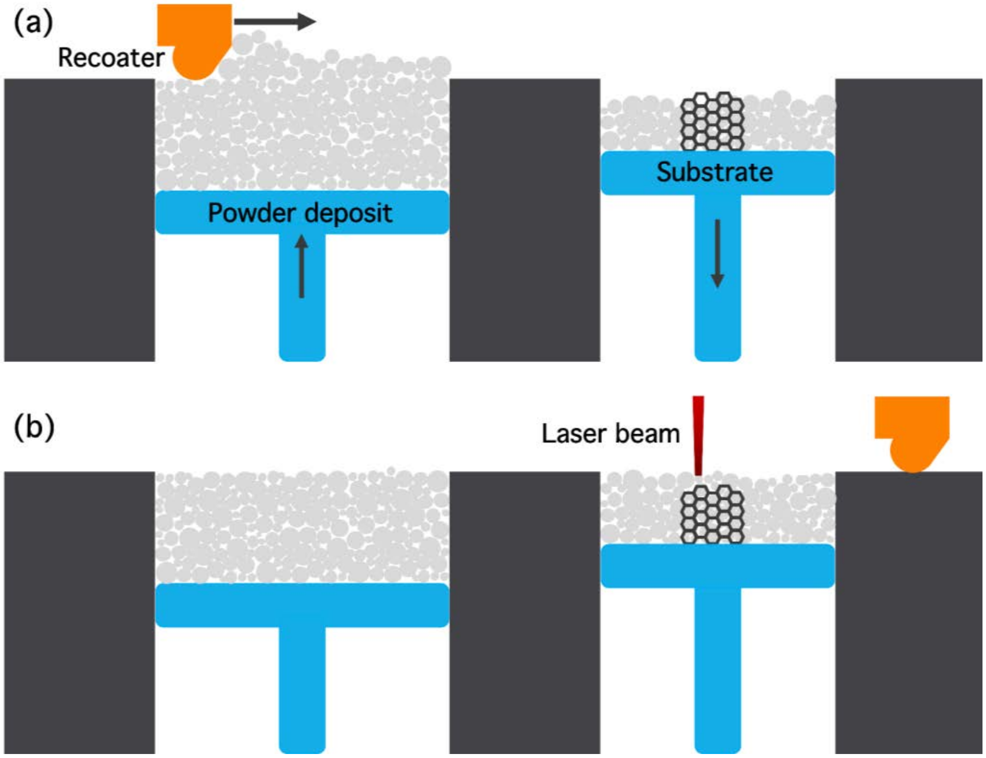

Figure 2-2: Schematical representation of a PBF-LB/M setup (a) during the powder deposition step, and (b) during the scanning process.

### *2.2.1. Melting process: the melt pool as a building block*

When the laser beam interacts with the powder bed, it is reflected in multiple directions, in influencing the overall energy absorption. Factors such as the particle size distribution, the nature of the powder, the surface quality, or the compaction of the powder bed all affect the fraction of laser energy effectively used for melting [14]. Shortly after exposure to the laser beam, the temperature of the powder bed rises above the melting point and can even reach vaporization temperatures. When the feedstock powder is melted, together with the substrate or with a fraction of previously solidified scan tracks and layers, a melt pool is generated [15].

Under stable low- and medium-energy conditions -referred to as conduction-mode melting- the melt pools tend to exhibit a semicircular shape (Figure 2-3a,b). In this regime, the heat transfer between the melt pool and its surrounding media occurs primarily through thermal conduction, mainly towards the substrate. Additionally, convection within the liquid metal arises due to Marangoni flow inside the melt pool [16]. Nevertheless, conduction to the surrounding solid metal remains the dominant heat transfer mechanism [15,17,18].

As the energy input increases and significant evaporation takes place, a cavity may be formed in the melt pool due to recoil pressure overcoming the surface tension of the liquid metal. The laser penetrates and reflects within this cavity, increasing its absorptivity (A), and causing the melt pool to deepen, thereby losing the semicircular shape characteristic of conduction-mode melting (Figure 2-3a,c) [15,19]. This melting mode is known as the keyhole regime. In this regime, conduction to the surrounding media is no longer the dominant heat transfer mechanism; instead, radiation and convection become increasingly important, with the latter being the main form of heat transfer. Under carefully controlled conditions, stable keyholes can form, allowing deep laser penetration and melting of larger volumes compared to conduction-mode melting - an effect exploited in welding to enhance productivity. However, the inherent (albeit small) stochasticity of standard PBF-LB/M processes makes it highly challenging to achieve stable keyholes. In most cases, the keyhole becomes unstable, i.e. the walls of the cavity collapse, entrapping part of the metal vapor, increasing the ejection of droplets from the melt pool (spatter particles), and triggering a series of uncontrollable physical phenomena [15,20,21]. Melt pools in this unstable keyhole regime are irregular in shape and often contain spherical pores caused by the entrapped vapor.

Controlling the melt pool shape and size is of paramount importance to achieve high-quality prints, as these factors influence defect formation and determine the microstructure of as-built parts. In general, scanning parameters that promote melting in the so-called transition mode (conduction mode, but as close to the keyhole regime as possible) are preferred, for the melt pools are larger yet stable, enhancing productivity without compromising print quality [17,21].

In this thesis, PBF-LB/M parts are considered as a three-dimensional stacking of melt pools, with the melt pool regarded as the fundamental building block. Therefore, the following discussions of processing parameters, energy input, and microstructural features will primarily focus on the melt pool length scale.

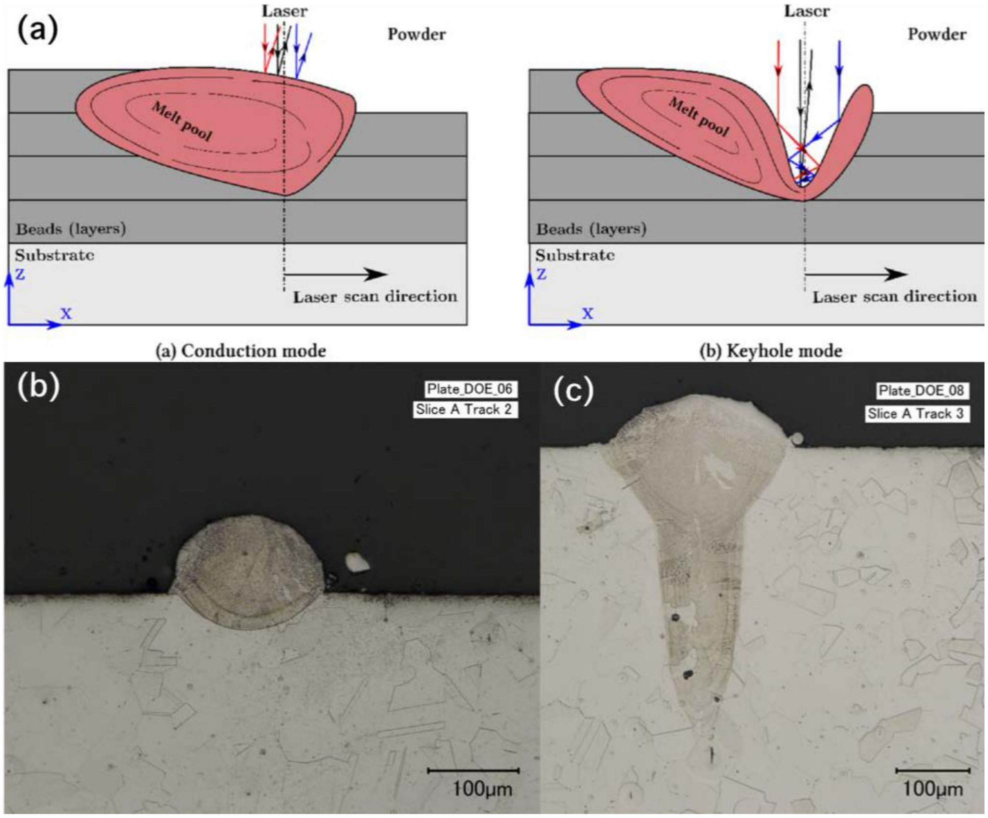

Figure 2-3: (a) Melt pool formation in conduction and keyhole modes. In keyhole mode, the reflections of the trapped laser beam are shown using blue and red arrows [22]. (b) Semicircular melt pool typical of conduction-mode melting, and (c) deep, V-shaped melt pool typical of keyhole-mode melting (adapted from [21]).

### *2.2.2. Critical processing parameters*

PBF-LB/M is a fast and complex process influenced by numerous factors. Including both process- and material-related aspects, more than 130 different parameters can affect the outcome of the print [23]. Attempting to describe and characterize them all would be a colossal task, exceeding the scope of this work. Therefore, in the following, we briefly describe the influence of the most critical parameters, specifically those referenced throughout this thesis.

#### *2.2.2.1. Laser beam*

The energy source used to heat and melt the powder feedstock is the laser beam, its main characteristic features being its nature, its diameter, its distribution, and its emission mode. Most PBF systems use Nd:YAG, Nd:YLF, or Yb fiber lasers, characterized by a wavelength of 1050-1070 nm [24]. Using an appropriate wavelength for a given alloy is crucial, for the absorptivity of each material is wavelength-dependent [14]. For instance, Cu-based alloys tend to have very limited absorptivity levels for infrared lasers operating at 1050-1070 nm, hindering their processability, and the use of green laser working at wavelengths of 515-532 nm is a potential solution [25]. Fortunately, Ni-based alloys show good laser absorptivity at the larger wavelengths typical of Yb fiber or Nd:YAG/YLF lasers [24].

The laser spot size, controlled by the optical system of the PBF-LB setup, determines both the minimum feature size and the power density. Adjusting the laser beam focal point (i.e. focusing the laser a few mm above or below the powder bed surface) modifies both the relative power density and the laser spot size [26]. A smaller the spot size enables more precise and controlled printing but reduces productivity.

Most PBF-LB/M systems employ lasers with a Gaussian power distribution. However, other beam profiles like top-hat or doughnut/ring can also be used in PBF. It is generally accepted that a Gaussian laser power profile results in deeper melt pools, steeper temperature gradients, and a higher geometrical accuracy. In contrast, top-hat or ring power profiles can be leveraged to increase productivity or to tailor the solidification microstructure of the printed parts [27–30].

The use of lasers with either continuous wave (CW) or pulsed wave (PW) emission also influences the outcome of the printing process. As their names imply, CW lasers deliver constant power over a set period, while PW lasers emit power in short, intense pulses ranging from femto- to microseconds. A PW laser is characterized by its peak energy, the pulse duration, and the time interval between pulses. In PBF-LB/M PW lasers result in higher cooling rates, rounder and narrower melt pools, and smaller heat affected zones (HAZ) compared to CW lasers. Thus, PW lasers offer advantages such as improved dimensional accuracy and reduced solute diffusion, whereas CW lasers typically enable faster build rates [31–34].

In this work, we have used a PW Yb fiber laser with a Gaussian power profile, and with a spot size of ~70 μm at the focal point.

### *2.2.2.2. Scanning parameters*

Four of the main scanning parameters that the user can modify are: laser power (*P*), scanning speed (*v*), hatch distance ($h_d$), and layer thickness (*t*) (Figure 2-4). Their combination will determine the size and shape of the melt pools, which in turn will define the as-built (AB) microstructure.

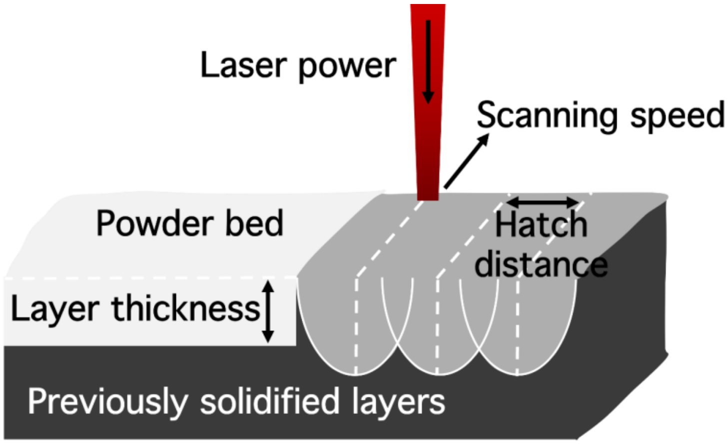

Figure 2-4: Representation of the melting of a layer, showing the main process parameters, adapted from [35].

Most PBF-LB/M systems use laser beams with power ranges from 30 to 1000 W [10]. The laser power is directly proportional to the energy input during the process, and thus has a direct effect on the volume of melted material. The laser beam diameter will determine the power density, and the powder feedstock absorptivity will influence the fraction of power that is effectively used and that which is reflected [25].

The scanning speed, as the name suggests, is the velocity at which the laser moves across the substrate. In PBF-LB/M the scanning speed can range from the tens to thousands of $m \cdot s^{-1}$ [9]. The scanning speed also has a direct impact on the energy input (see Section 2.2.3). Additionally, the scanning speed has strong implications on the solidification microstructure, for it is proportional to the solidification rate in PBF-LB/M [36]. In a PW system, the scanning speed is calculated as $v = p_d/(e_t + t_d)$, where $p_d$ is the point distance (i.e. the distance between consecutive points on which the laser is directed), $e_t$ is the exposure time, and $t_d$ is the time delay between laser exposures.

The hatch spacing or hatch distance ($h_d$) is defined as the distance between adjacent scanning tracks. Usually in the 50-150 μm range, the hatch distance must be adjusted in a manner such that full melting is achieved. The larger the $h_d$, the more productive the fabrication process becomes; however, this also reduces the remelt fraction and increases the risk of lack-of-fusion defects [37].

After processing each layer, the substrate is lowered by a defined distance known as the layer thickness (*t*). This value must be selected based on factors such as the particle size distribution and the maximum laser power of the PBF-LB/M system [38] Typical values of *t* range from 20-100 μm and are directly linked to process productivity as the build rate increases linearly with *t* [39]. However, while a larger layer thickness improves productivity, it can also lead to increased surface roughness, particularly on inclined surfaces [40,41]. An important consideration regarding layer thickness is the distinction between the nominal *t* (i.e., the distance by which the substrate is lowered), and the actual or effective powder layer thickness. Regardless of how compacted the powder is during deposition, it is always less dense than the fused metal. As a result, the deposited powder layer is always thicker than the nominal *t*, sometimes by as much as a factor of five [41,42].

The effect of each of the aforementioned scanning parameters on the melt pool size and morphology is complex and often difficult to isolate. For instance, it is commonly accepted that a higher P results in deeper melt pools, while a slower v tends to produce wider ones [21,43]. However, this is a simplified view that holds true only when all other scanning parameters remain constant, an uncommon scenario in practice. Therefore, it is particularly useful to define variables that capture the combined effects of multiple parameters, as discussed in section 0.

#### *2.2.2.3. Scanning strategies*

Another crucial aspect in the printing process is the scanning strategy, the path followed by the laser during the processing of a layer. It significantly influences the thermal history, the residual stress distribution, the AB microstructure, or the dimensional accuracy [40,44].

The simplest scanning strategy is the meander or raster scanning strategy (Figure 2-5), in which the laser moves back and forth in a zig-zag pattern across the entire part. The minimization of jumps between points makes it the most productive strategy. However, for large parts, it can lead to excessive heat accumulation and elevated thermal stresses [45]. The stripes scanning strategy is also widely used in the PBF-LB/M field. Similar to the meander approach, it divides the cross-section into stripes of fixed width (Figure 2-5). This segmentation helps reduce heat accumulation commonly observed in the meander scanning strategy and promotes a more uniform thermal distribution [46]. The island or chessboard scanning strategy divides the cross-section into squares (or islands), which are melted using alternating scan rotations in a pattern resembling a chessboard (Figure 2-5). While this strategy is believed to reduce residual stresses, heat buildup at the island borders can compromise dimensional accuracy [47,48].

An important aspect of the scanning strategy, regardless of the scan path selected, is the interlayer rotation. The latter is employed to reduce the accumulation of residual stresses and to minimize microstructural anisotropy. The most used interlayer rotation angle in the industry is 67º, as it avoids the periodic repetition of features due to not being a divisor of 360º, and it helps suppress the formation of strongly textured columnar grains. Scan rotations of 45 or 90º are also frequently used; however, since they are divisors of 360º, they may result in the development of repetitive microstructural patterns [49,50].

Other aspects of the scanning strategy that can also strongly affect the print quality are the border or contour scans. One or more outer scans can be added before or after the hatch (also referred to as infill or bulk) scanning. These contour scans have a strong impact on surface roughness, residual stress distribution, and mechanical properties. They are particularly important for complex, near-net-shape parts where post-processing is difficult or impractical [51–53].

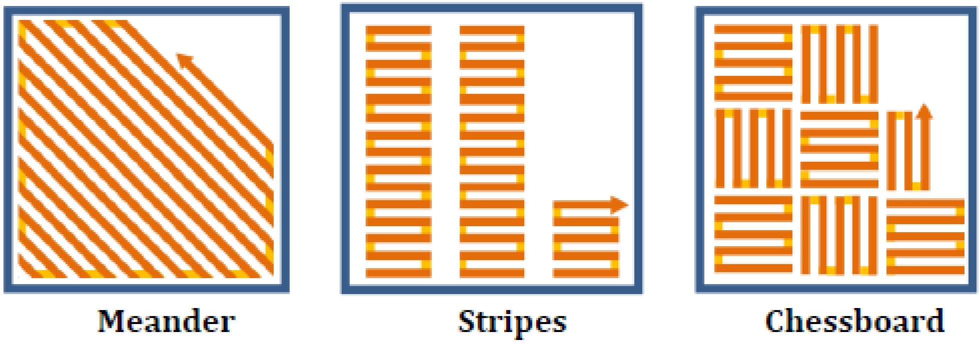

Figure 2-5: Schematical representation of meander, stripes, and chessboard scanning strategies.

### *2.2.3. Quantification of the energy input in PBF-LB/M*

Given the large number of parameters (both scanning- and material-related) that influence the outcome of the printing process, it is of clear interest to develop simplified variables that describe the energy levels applied during fabrication.

In the PBF community, the most commonly used of these variables are the linear and volumetric energy densities. Linear energy density is defined as [54]:

$$E_l = \frac{P}{v} \tag{2.1}$$

By incorporating the effects of layer thickness ($t$) and hatch distance ($h_d$), the linear energy density ($E_l$) is extended to define the volumetric energy density (VED, or $E_v$), which provides a more comprehensive measure of the energy input per unit volume during fabrication [55]:

$$E_v = \frac{P}{v h_d t} \tag{2.2}$$

The volumetric energy density encompasses four key laser scanning parameters into a single, simplified expression. For a given setup and material, it generally provides a useful approximation of three distinct energy input regimes: insufficient (mostly linked to the appearance of lack-of-fusion defects), optimum, and excessive energy (related to keyhole porosity). When working with a fixed setup, layer thickness, and powder feedstock, *Ev* serves as a practical and straightforward tool to identify a processing window that yields fully dense parts. However, it does not account for the laser beam radius or material-specific properties, which limits its usefulness for cross-comparisons. Moreover, different combinations of scanning parameters can yield similar values of $E_v$, and a wide range of so-called "optimal $E_v$" values can be found for the same alloy [56,57].

One way to overcome the limitations of $E_v$ is to normalize certain variables. This is a common approach in the welding community that was later adapted to PBF-LB/M, in a rather straight-forward modification due to the similarities between both processes. A first example of normalized variables for energy input evaluation during laser processing comes from the work of Ion et al. [58], who defined a dimensionless beam power $q^*$ and a dimensionless beam traverse rate $v^*$ (i.e. dimensionless scanning speed):

$$q^* = \frac{AP}{\omega \kappa (T_m - T_0)} \tag{2.3}$$

$$v^* = \frac{v\omega}{\alpha} \tag{2.4}$$

where A is the laser absorptivity, $\omega$ is the laser beam radius, $\kappa$ is the thermal conductivity, $T_m$ and $T_0$ are the melting and starting temperatures, and $\alpha$ is the thermal diffusivity. Using these dimensionless variables, the authors define three different laser processing regimes: heating, melting, and vaporization.

Based on this approach, and adding the dimensionless $h_d$ ($h_d^*$) and dimensionless $t$ ($t^*$) - $h_d^* = h_d/\omega$ and $t^* = 2t/\omega$ -, Thomas et al. [59] defined the dimensionless or normalized $E_v$ ($E_v^*$, termed $E_0^*$ in their publication) for additive layer manufacturing:

$$E_v^* = \frac{q^*}{v^* t^* h_d^*} = \frac{AP}{2vth_d\rho C_p(T_m - T_0)} \quad (2.5),$$

where ρ is the density of the material, and $C_p$ is the specific heat capacity. This modification of the volumetric energy density is obtained considering the minimum necessary energy input per unit volume to melt the material. Since it includes some material-related properties, $E_v^*$ allows for comparison between different alloys.

Also stemming from the welding community, the normalized enthalpy is a different (albeit quite similar) approach to dimensionless energy input quantification. In this case, the applied energy in the form of enthalpy (ΔH) is normalized by the enthalpy of melting of the alloy ($h_s$):

$$\frac{\Delta H}{h_s} = \frac{AP}{\rho(C_p(T_m - T_0) + L_m)\sqrt{\pi\omega^3 v\alpha}} \quad (2.6),$$

with $L_m$ the latent heat of melting. Hann et al. [60] showed that this normalized enthalpy can be directly related to the dimensionless melt pool depth (normalized by the laser beam radius) in laser welding, following an alloy-agnostic correlation. This approach has been successfully applied to PBF-LB/M, with some interesting outcomes [21,61,62]. First, the correlation between normalized enthalpy and melt pool depth also applies in PBF-LB/M, and it is again independent of alloy composition. Second, King et al. [21] demonstrated that there is a specific range of normalized enthalpy values in which the transition between conduction and keyhole melting mode takes place ($\frac{\Delta H}{h_s} = 30 \pm 4$). Third, Ghasemi-Tabasi et al. [61] introduced a simple *material translation rule*, based on which it is possible to determine the optimum scanning parameter combinations for a given alloy knowing only the powder bed laser absorptivity and some (approximated) material properties.

Both $E_v^*$ and $\Delta H/h_s$ consider the thermal properties of the alloy at room temperature (RT), and they allow to obtain good first approximations to the energy input when working with new alloys. However, while $\Delta H/h_s$ has the clear advantage of directly correlating the energy input with melt pool dimensions, it fails to account for the $h_d$, one of the key scanning parameters, which is contemplated in $E_v^*$.

### *2.2.4. Microstructure and defects in PBF-LB/M*

The mechanical, chemical, and functional properties of a PBF-LB/M part are heavily influenced by the metal microstructure, which is multi-scale in nature. Thus the influence of microstructure can only be fully understood by considering the coupling of phenomena taking place at atomic- (solute trapping, segregation), meso- (grain size, texture, grain boundaries, porosity, cracking) and macro-levels (thermal stresses, warping, etc). In this section we will describe the microstructure features and defects that are most relevant to the research reported in this thesis.

#### *2.2.4.1. Solidification and crystal growth*

Solidification during PBF-LB/M takes place out-of-equilibrium due to a combination of steep thermal gradients ($G$), high cooling rates ($\dot{T}$), and fast growth rates ($R$). The resulting microstructures are very distinct from other solidification microstructures, e.g. those observed in casting [63].

The solidification conditions may vary in different locations of the printed parts, and even inside a single melt pool. Depending on the temperature gradient and on the growth rate, the morphology of the solidified structure can be classified as planar, cellular, columnar dendritic, and equiaxed dendritic (Figure 2-6) [64]. With temperature gradients in the order of $10^6$-$10^7$ K·m$^{-1}$, and growth rates in the same order of magnitude as the scanning speeds (m·s$^{-1}$), most alloys undergo columnar dendritic growth during solidification [50]. Following laser exposure and melting of the powder layer (together with a fraction of the previously solidified layers and scan tracks), the first grains will nucleate at the melt pool boundary and they will grow in a columnar dendritic fashion towards the melt pool center. In the absence of inoculants, nucleation inside the melt pool is rare, and epitaxial growth of grains from previous layers is favored. Many efforts have been made to induce the columnar to equiaxed transition (CET) in order to avoid anisotropy. There are examples of successful control of the CET in PBF-EB/M or in DED for a number of different alloys, favored by smaller temperature gradients and slower growth rates [9,50,65,66]. However, in PBF-LB/M, the CET rarely happens [67]. One common strategy to avoid columnar growth in PBF-LB/M is the addition of inoculants to the powder feedstock, either as micro/nanoparticles or as alloying elements. Increasing the number of nucleation sites promotes growth competition, thereby hindering the epitaxial growth of columnar grains [50].

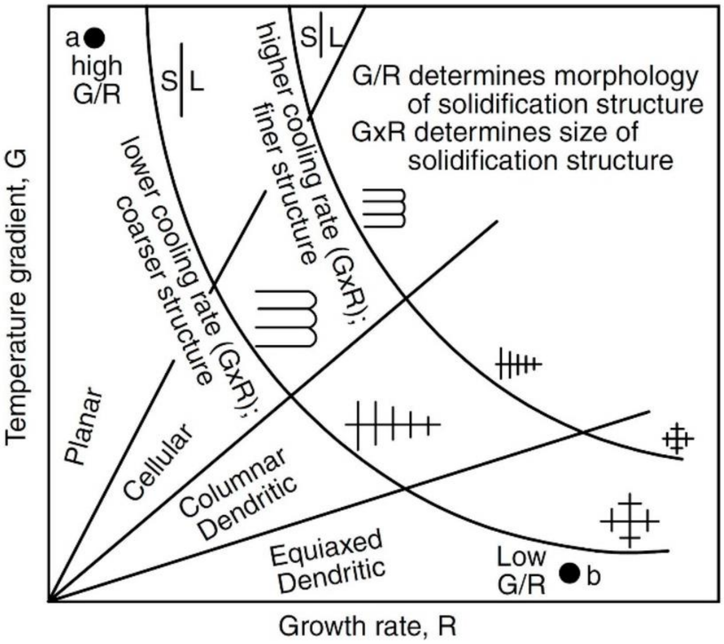

Figure 2-6: Solidification microstructure as a function of temperature gradient (*G*) and growth rate (*R*) [12].

The direction of heat dissipation will greatly affect grain growth and crystallographic texture. Growth of grains with their preferred crystal growth direction best aligned with the temperature gradient will be favored during growth competition and thus PBF-LB/M processes usually result in the development of distinct textures [64]. At the melt pool level, such thermal gradients are usually normal to the melt pool boundary and, thus, the melt pool morphology will have a direct effect in the crystallographic texture of the AB parts [68]. For example, in FCC alloys, in which <001> is the preferred growth direction, wide and shallow melt pools favor the growth of grains with <001> parallel to the BD (<001>//BD); in turn, narrow and deep melt pools promote the growth of grains with <001> directions perpendicular to the BD (Figure 2-7) [69]. The crystallographic texture of a PBF-LB/M part then depends on the scanning parameters, since these affect melt pool shape, but also on the scanning strategy. In the absence of scan rotation, and for semicircular melt pools, AB parts tend to exhibit a <011> fiber texture, where <011> directions align preferentially with the build direction (BD) (<011>//BD), although regions with columnar grains oriented with <001> directions parallel to BD (<001>//BD) are also present in the vicinity of the melt pool centerlines. When a rotation is applied between layers (typically 90 or 67º), the intensity of the <011>//BD component decreases, and in turn the <001>//BD texture becomes dominant

[70–72]. Thus, the microstructure of most PBF-LB/M cubic alloys is formed by columnar grains with a strong <001>//BD texture [50].

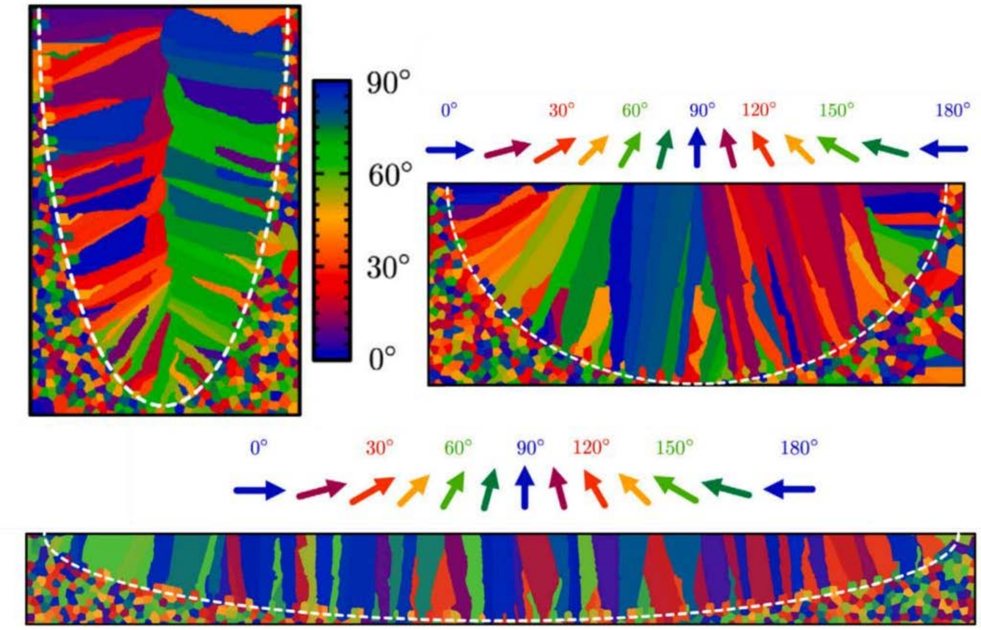

Figure 2-7: Grain growth directions in differently shaped melt pools. Adapted from [68].

### 2.2.4.2. Defects

The defects present in PBF-LB/M components can also highly affect the properties of the AB parts. The most common defects include lack of fusion (LOF) voids, porosity, cracking, balling, delamination due to thermal strains, or composition heterogeneities due to evaporation of certain elements [12,50]. The first three are the most relevant to this PhD research.

Lack of fusion voids are characterized by an irregular shape and sharp edges (Figure 2-8a), which can be particularly detrimental for the fatigue life of PBF-LB/M components [12,73]. These defects appear when the overlap and bonding between adjacent scan tracks or between consecutive layers is insufficient. This occurs when the melt pool dimensions are not sufficient to achieve full melting with a given set of scanning parameters. To ensure LOF defects do not appear in the final parts, the melt pools must be deeper than the layer thickness and wider than the hatch distance. Tang et al. [37] proposed a geometrical criterion for full melting and thus for the prevention of LOF defects:

$$\left(\frac{h_d}{w}\right)^2 + \left(\frac{t}{d}\right)^2 \leq 1 \qquad (2.7).$$

Another common type of defect is gas porosity, which can result from the release of entrapped gas present in the powder feedstock, the dissolution of shielding gas into the liquid metal, or, most commonly, from keyhole collapse [12]. In PBF-LB/M, keyholes often exhibit instabilities, and when they collapse, part of the vapor responsible for forming the keyhole may become trapped within the melt pool. If this vapor is not released before the melt pool solidifies, it leads to the formation of spherical pores that remain in the final part (Figure 2-8b) [74].

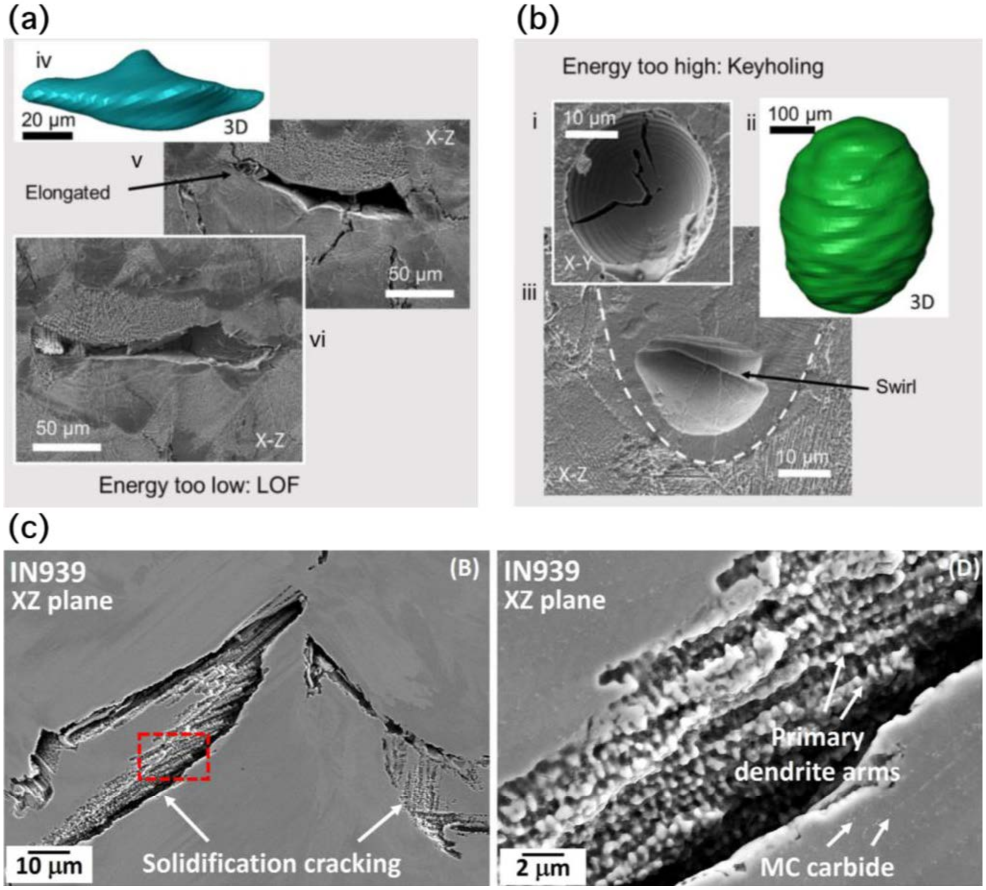

Figure 2-8: Examples of (a) lack of fusion voids, (b) keyhole porosity in IN713C samples (adapted from [75]). (c) Examples of solidification cracking in IN939 [76].

Certain alloys, such as some Al alloys, Ni-based superalloys, and austenitic steels, are susceptible to cracking during the printing process. Cracking can occur at various stages of fabrication, and it is typically associated to segregation or to the precipitation of secondary phases. The two main types of cracking in PBF-LB/M are solidification cracking and liquation cracking [50]. Solidification cracking, also known as hot tearing, occurs when the remaining liquid trapped between solidifying grains is torn apart due to thermal strain and the limited ductility of the mushy zone (Figure 2-8c). Melting and solidification of an alloy occurs over a specific temperature interval known as the solidification or freezing range $\Delta T$ [76]. The wider this range, the more prone the alloy is to solidification cracking. Liquation cracking is similar in nature but occurs in the heat affected zones (HAZ) where the local solidus temperature may be depressed due to elemental segregation [77]. During fabrication, the solidified parts undergo a series of thermomechanical cycles (thermal expansion and contraction). If the resulting thermal strains are sufficiently high, they can trigger liquation cracking [78,79]. Some strategies to reduce or prevent cracking during PBF-LB/M include microstructure refinement [78,80,81] or alloy modification to narrow the freezing range and reduce segregation [76,82,83].

## 2.3. Ni-based superalloys

### *2.3.1. Overview*

Superalloys are defined as alloys with outstanding mechanical properties and oxidation resistance up to temperatures close to their melting point [5]. Their primary applications lie in turbine components for the aerospace and energy industries, where high-temperature strength and oxidation resistance are critical. First developed in the 1940s, Ni-based superalloys typically contain 10 or more alloying elements, each contributing specific properties [5]. The most common alloying elements found in Ni-based superalloys are listed in Table 2-2. Over the years, significant advances have been made in the development of superalloys, ranging from the incorporation of rare-earth elements to the fabrication of single-crystal components with improved creep resistance.

Table 2-2: List of the principal alloying elements in Ni-based superalloys and their main contributions [5,84].

| **Element** | **Main role** |
|---|---|
| Co | γ’ stabilizer. Solid solution strengthener. |
| Cr | Corrosion and oxidation resistance. Carbide former. |
| Fe | Solid solution strengthener. |
| Al | γ’ former. |
| Ti | γ’ and carbide former. |
| W | Carbide former. |
| Ta | Carbide former. Solid solution strengthening. |
| Nb | Carbide and γ’’ former. |
| Zr | Thought to be a carbide stabilizer, its role is not completely understood. |
| C | Carbide former. Grain boundary strengthening. |
| B | Boride former. Grain boundary strengthening. |

Ni has a face-cetered-cubic (FCC) crystal structure (γ), and polycrystalline Ni-based superalloys are generally classified into two main categories, with self-explanatory names. *Solution-strengthened superalloys* consist of a saturated matrix in which alloying elements are present in solid solution; the strengthening arises from this saturation. *Precipitation-strengthened superalloys* on the other hand, derive their mechanical strength from a variety of precipitates -both intra- and intergranular- that provide resistance across a wide temperature range [5,73,84]. Some of the most common precipitates found in this class of superalloys include [5]:

- γ′ ($Ni_3(Al,Ti)$): This phase has an $L1_2$ crystal structure and forms as a coherent precipitate within the matrix. It provides high strength and excellent creep resistance at medium to elevated temperatures.
- γ″ ($Ni_3Nb$): With a body centered tetragonal (BCT) structure and lattice parameters similar to γ’, this phase contributes to mechanical strength at low to medium temperatures. However, it can transform into the δ phase, a lenticular, incoherent precipitate which can embrittle the material.
- $M_xC_y$ carbides: Most precipitation-strengthened Ni-based superalloys contain small amounts of carbon to promote carbide formation. MC carbides usually precipitate

during solidification, while $M_{23}C_6$ carbides tend to form at the grain boundaries during post-processing heat treatments. These carbides play a critical role in enhancing high-temperature creep resistance.

- Topologically close-packed (TCP) phases: These precipitates are generally considered detrimental to the mechanical properties of Ni-based superalloys due to their embrittling effect (like the aforementioned δ phase). With complex crystal structures, the most common TCP phases are δ, Laves, σ, or η.

A schematic representation of the different precipitates in a polycrystalline Ni-based superalloy can be found in Figure 2-9.

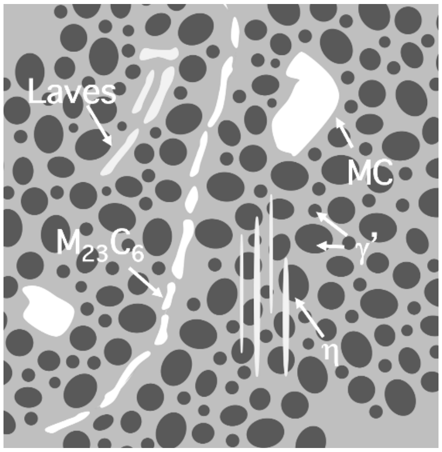

Figure 2-9: Schematic illustrating the microstructure of a Ni-based superalloy, showing some of the main precipitates. MC carbides are shown inside the grains, while $M_{23}C_6$ are present at the grain boundary.

### *2.3.2. PBF-LB/M of Ni-based superalloys*

Since the advent of metal AM, Ni-based superalloys have been at the forefront of its development. They represent the third most extensively studied class of alloys, following steels and titanium alloys. Numerous studies on the AM of Ni-based superalloys are documented in several comprehensive review articles, which highlight both the major advancements and the remaining challenges in the field [84–87].

While additively manufactured Ni-based parts have already been implemented in certain applications, one major concern remains: their weldability. Many Ni-based superalloys are susceptible to cracking, making them poorly weldable. In addition to their sensitivity to solidification cracking, primarily due to a ductility dip at temperatures between 0.5 and 0.9 $T_s$ , the solidus temperature [50], some alloys also experience strain-age cracking (SAC). This latter form of cracking is directly related to γ' precipitation. The combination of thermal stresses and the localized stress arising from the small lattice misfit between the γ matrix and γ’ precipitates can be sufficient to trigger cracking in γ’-strengthened Ni-based superalloys [77,88]. While a wide range of alloying elements can influence solidification and liquation cracking, SAC is primarily associated with the Al and Ti contents (the main γ’-forming elements) [76,77,86,88]. An estimation of the weldability of Ni-based superalloys as a function of their Cr, Co, Al, and Ti content is given in Figure 2-10. It is no surprise that the Ni-based alloys for which there is a larger body of literature are the ones classified as *Weldable* in Figure 2-10 (IN718, IN625, and Hastelloy X [89]).

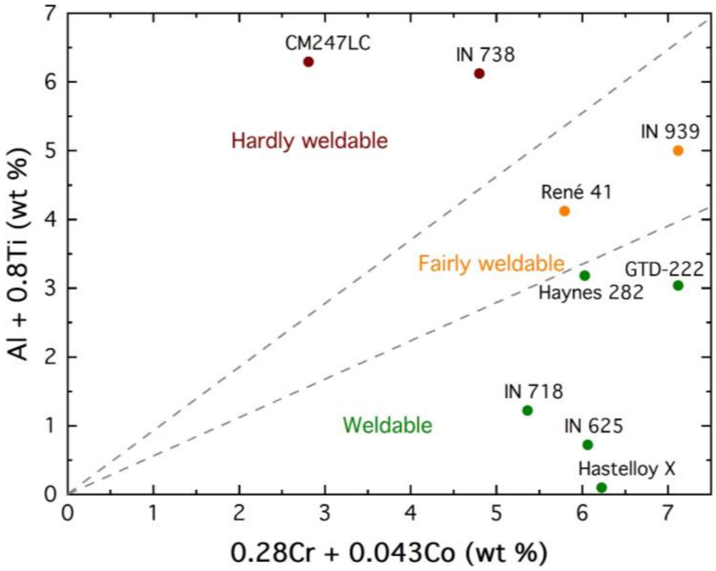

Figure 2-10: Weldability of different Ni-based superalloys as a function of their Cr, Co, Al, and Ti wt.%. Adapted from [86].

Hard-to-weld alloys such as CM247LC or IN939 were originally developed for investment casting or forging. Two main approaches have been pursued to mitigate their cracking during PBF-LB/M processing: advanced scanning strategies and modifications to elemental composition. In the latter case, advances in integrated computational materials engineering (ICME) have enabled the design of new Ni-based superalloys specially tailored for AM. While this represents a promising and significant advancement, the limited availability of feedstock powders and the cumbersome validation processes required in certain industries hinder widespread adoption. As a result, the use of legacy alloys remains highly relevant.

#### *2.3.2.1. Microstructure of PBF-LB/M Ni-based superalloys*

The microstructure of AB parts depends largely on the feedstock composition and on the processing parameters. However, there are some typical features common to most PBF-LB/M-processed Ni-based superalloys, shown in Figure 2-11. In general, the combination of a fast solidification rate and high temperature gradients results in the formation of a dendritic γ matrix. Dendrites grow into columnar grains with a strong <001> texture parallel to the BD (a commonly observed texture in FCC alloys), favored by epitaxial growth in the layer-by-layer process. Another common feature is the cellular structure at the sub-grain level, which forms as a result of rapid solidification. A certain degree of segregation can be expected at the cell and grain boundaries (mainly involving Nb, Mo, Al, Ta, and C), which might contribute to solidification or liquation cracking, as previously discussed. In some cases, precipitates like γ' or certain carbides can be found in the AB state. These precipitates may form during solidification or afterward, due to the thermomechanical cycles experienced by the solidified layers during fabrication. Regardless of the presence of precipitates in the AB state, most PBF-LB/M parts undergo some form of thermal treatment to improve their properties [50].

While the control of solidification mode in PBF-LB/M is extremely difficult (as opposed to DED or PBF-EB/M, where solidification rates and thermal gradients can be lower), there are some strategies to modify the strongly textured columnar microstructure described above. First, the crystallographic texture can be controlled by adjusting the scanning strategy or the scanning parameters. To disrupt the columnar grain structure, inoculants can be introduced, as seen in oxide dispersion strengthened (ODS) alloys, which promote the formation of new grains after melting and thus inhibit epitaxial growth. Other strategies to interrupt columnar growth include applying external disturbances or modifying the alloy composition.

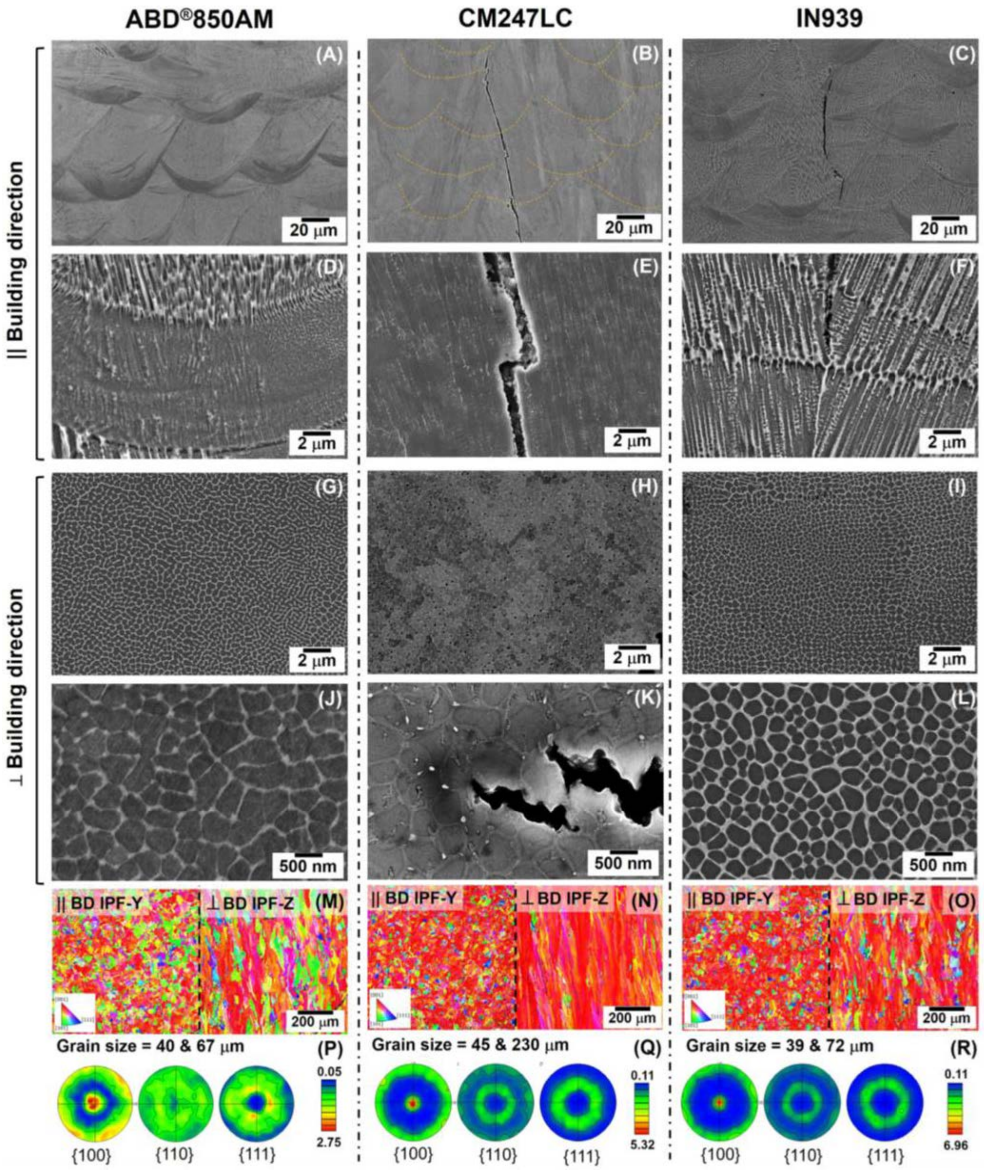

Figure 2-11: Typical PBF-LB/M microstructures of three different Ni-based superalloys, showing the melt pool morphology, the cell-like structures, and the columnar grains with strong <001>//BD textures [76].

## 2.4.IN939

### *2.4.1. Overview*

Inconel 939 (IN939) is the Ni-based superalloy selected for this study. With outstanding oxidation resistance and mechanical behavior at temperatures up to the vicinity of 900ºC, it is an excellent option for gas turbine vanes or for the hot section of aircraft turbines. Originally developed by the International Nickel Company, its intended service temperature is ~850ºC.

IN939 is a precipitation-strengthened superalloy, with high contents of Cr and Co, it also contains a relatively high fraction of Al and Ti (Table 2-3). γ' is the main strengthening precipitate, and MC and $M_{23}C_6$ provide additional creep resistance at high temperatures. The corrosion and oxidation resistance of IN939 is mostly attributed to the formation of a $Cr_2O_3$ protective outer layer. The role of all the different elements can be found in Table 2-2.

Table 2-3: Nominal composition of IN939 [90,91].

| Element | Ni | Cr | Co | Al | Ti | W | Ta | Nb | C | Zr | B |
|---|---|---|---|---|---|---|---|---|---|---|---|
| wt. % | Bal. | 22 | 19 | 2 | 3.5 | 2 | 1.4 | 1 | <0.15 | <0.1 | <0.05 |

The standard thermal treatment schedule for cast or wrought IN939 is composed of a solution treatment at 1160ºC for 4 h. followed by a two-step ageing treatment (1000ºC/6 h., and 800ºC/4 h.). This leads to a bimodal distribution of γ' precipitates, and to the precipitation of fine $M_{23}C_6$ carbides at the grain boundaries. Table 2-4 shows typical values of yield strength, ultimate tensile strength, and elongation for cast IN939 at room temperature (RT), 750ºC, and 850ºC.

Table 2-4: Mechanical properties of IN939 at RT, 750ºC and 850ºC. The values have been obtained from [91–93].

| | **RT** | **750ºC** | **850ºC** |
|---|---|---|---|
| **Yield strength (MPa)** | 800 | 650 | 400 |
| **Ultimate tensile strength (MPa)** | 1050 | 900 | 600 |
| **Elongation (%)** | 5 | 7 | 15 |

### *2.4.2. PBF-LB/M of IN939*

Although IN939 is relatively difficult to weld, recent years have seen growing efforts to process it using PBF-LB/M. At the outset of this doctoral thesis, only a handful of studies had reported somewhat successful processing of IN939 via PBF-LB/M, primarily focused on identifying an acceptable processability window [94–98]. The body of work has since grown considerably, extending beyond advances in processability [49,99], to include the fabrication of thin sections [100,101], investigations into post-processing strategies [102–105], and even studies on the effects of minor compositional variations [106,107].

Most of the studies on PBF-LB/M of IN939 report fully dense samples with as-built microstructures consisting of columnar grains oriented with a <001> direction parallel to the

BD, in line with typical microstructures of melt-based AM Ni-based superalloys. These columnar grains contain intragranular cell structures, also commonly found in PBF-LB/M. Arguably, the only ambiguous aspect of the as-built microstructure in PBF-LB/M IN939 concerns the presence and distribution of precipitates. While some studies claim that only some small (Ti,Nb)C or (Ti,Nb,Ta)C carbides are present in the AB state [95,105,108–113], others suggest that minor fractions of γ' [96], or even of the deleterious η phase [102], can also be found.

Fardan et al. [100] studied the effect of part thickness and build angle on the AB crystallographic texture and on the mechanical properties, showing an increase in texture intensity with decreasing thickness, which the authors attribute to the directionality of heat dissipation. Doğu et al. [49] examined the impact of scanning strategy on microstructure and defect formation, showing that that a 67° interlayer rotation reduced the intensity of the <001> fiber texture, while also decreasing the residual stresses and solidification cracking. As an alternative scanning approach, Hu et al. [110] demonstrated that remelting could effectively alleviate cracking. Additionally, Zeng et al. [106] and Ding et al. [107] assessed the impact of Si additions on the weldability of IN939, yielding promising results.

A relatively wide range of post-processing thermal treatments has been explored for PBF-LB/M IN939 parts, with some contradicting results, especially regarding the initial solution step. In the first published study on PBF-LB/M or IN939, Kanagarajah et al. [94] applied a 1160ºC/4 h. solution treatment, which led to near complete recrystallization. Using the same treatment, Šulák et al. [105] reported only partial recrystallization, while Kuběna et al. [114] observed no clear indications of recrystallization. Notably, in both of these latter studies, the non-recrystallized PBF-LB/M samples outperformed their cast counterparts at both room and elevated temperatures, raising the question of whether solution treatment is necessary for PBF-LB/M IN939. Shaikh et al. [102] performed a study to tackle this question, concluding that, if direct aging is performed, small η precipitates in the AB microstructure can grow, embrittling the material. To mitigate this, they proposed a solution treatment of 1190ºC/4 h, which has also been adopted by Fardan et al. [100], Nahmany et al. [115], and Kumar et al. [113], all of whom reported no evidence of recrystallization. Doğu et al. [103] conducted a parametric study of the influence of solution treatment temperature on microstructural evolution, finding some early signs of recrystallization for 1160ºC/4 h., and nearly complete recrystallization only after a 1240ªC/4 h. treatment. The diversity of thermal treatments tested, along with the inconclusive results, leaves several open questions regarding optimal post-processing strategies for IN939.

Concerning the mechanical properties of PBF-LB IN939, several studies have reported results both in both the as-built and in heat treated conditions, with overall very promising results. In tensile testing, Kanagarajah et al. [94] reported higher yield strengths in both the as-built and the heat treated conditions compared to cast IN939 at room temperature. Similarly, Šulák et al. [105] observed superior yield and ultimate tensile strengths in the heat treated condition from room temperature up to 800ºC. Piwowarski et al. [116] investigated the effect of the solution treatment temperature on tensile performance at room temperature and 700ºC, finding optimal results following a 1210ºC/8 h treatment. Banoth et al. [108], Sedlak et al. [117], and Kumar et al. [113] studied the creep properties of PBF-LB/M. Although tailored thermal treatments, including hot isostatic pressing, led to some improvements, additively manufactured parts still exhibit inferior creep resistance compared to their cast counterparts.

## 2.5. Motivation and research objectives

In view of the current state of the art on PBF-LB/M processing of IN939, a clear need has emerged for a deeper understanding of the interplay between processing and post-processing parameters, microstructure, and the resulting properties of printed parts. Addressing this knowledge gap constitutes the main overarching objective of this thesis. To pursue this aim, the broader goal has been divided into three main focus areas:

1. Finding the PBF-LB/M processability window for the IN939 alloy using a pulsed laser source, both for bulk samples and for thin sections.
2. Understanding the PBF-LB/M processing-microstructure-mechanical properties relationship within the processability window.
3. Examining the influence of solution post-processing heat treatments on microstructure development and mechanical behavior.
4. Defining an approach for local microstructural design and control during PBF/M-LB of complex geometry parts.

# 3. MATERIALS AND METHODS

## 3.1. Feedstock powder

The feedstock material utilized throughout this thesis was gas-atomized IN939 powder, provided by Eckart TLS GmbH. Its chemical composition (Table 3-1) was measured using inductively coupled plasma mass spectroscopy (ICP-MS) and optical emission spectroscopy (ICP-OES), as well as by infrared absorption of combustion gases. The measured composition falls within the limits of the standard nominal composition of IN939 [118].

Table 3-1: Chemical composition of the IN939 feedstock powder.

| Element | Ni | Cr | Co | Al | Ti | W | Ta | Nb | C | Zr | B |
|---|---|---|---|---|---|---|---|---|---|---|---|
| wt. % | Bal. | 21.90 | 19.30 | 1.72 | 2.40 | 2.00 | 1.38 | 0.99 | 0.14 | 0.03 | 0.04 |

The quality of the feedstock powder is of utmost importance to ensure a good outcome of the printed parts. Aside from the chemical composition, we have characterized the morphology, the internal porosity, the particle size distribution, the flow rate, and the apparent and tap densities.

The morphology of the powder particles was characterized by scanning electron microscopy (SEM) (Fig.Figure *3-1*a, b), with a small quantity of powder particles deposited on carbon tape. The powder shows good sphericity, with a limited amount of satellites and elongated particles. The internal porosity was measured by image analysis of optical micrographs of polished powder particles, embedded in resin (Fig. Figure *3-1*c). The powder has an average relative density above 99.7 %, with only a few, localized pores in selected particles.

The particle size distribution (PSD) was measured using a Malvern Mastersizer 2000 laser interferometer (Figure 3-1d). Powder particles are somewhat small, with $d_{10} = 11$ μm, $d_{50} = 24$ μm, and $d_{90} = 43$ μm, but within acceptable values for PBF-LB/M (< 63 μm).

The flow rate of the powder was evaluated using a Hall flowmeter funnel according to standard ASTM B213. The flow rate is defined as the time it takes a certain mass of powder (50.0 g) to flow through the orifice of a standard funnel. In the event that the powder fails to start flowing, a small tap on the funnel rim is allowed, but no other manipulation of the powder is permitted. We conducted three attempts at measuring the flow rate, all unsuccessful, as no powder flowed through the funnel. The PSD, skewed towards fine sizes, may hinder the flowability of the powder. However, the powder did show good spreading behavior in the chamber during recoating, and was thus deemed appropriate for fabrication.

The apparent ($\rho_a$) and tap ($\rho_t$) densities were measured following standards ASTM B417 and B527, respectively. The apparent density is calculated by filling a glass cylinder with a fixed mass of powder, carefully leveling the surface with a spatula, and measuring the volume occupied by the powder, which is used to calculate apparent density ($\rho_a = m/V$). For tap density, once the glass cylinder is filled and the surface leveled, the container is tapped - either mechanically or by hand- striking the base of the cylinder on a hard rubber surface until no further decrease in volume is observed. The final volume, as indicated by the graduated cylinder, is then used to calculate tap density as $\rho_t = m/V$. Both measurements were performed three times. In our case, the apparent and tap densities amounted to 4.62 and to 5.75 g·cm$^{-3}$, respectively.

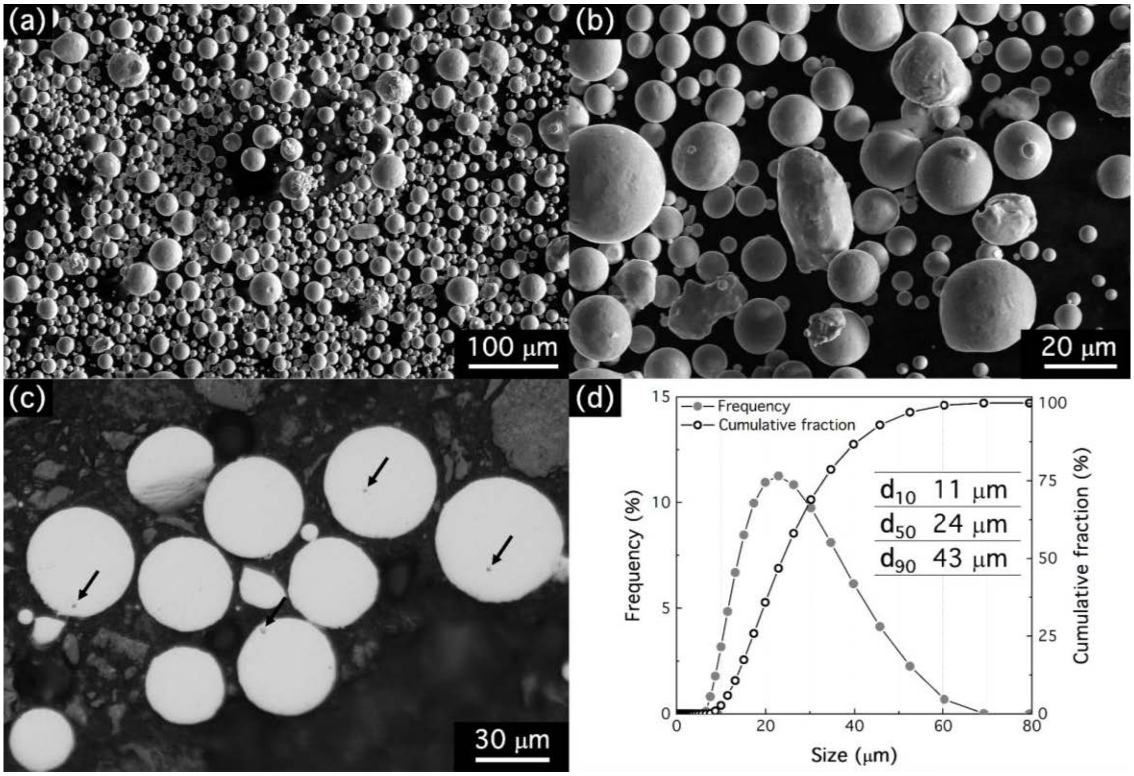

Figure 3-1: Feedstock powder characterization: (a) and (b) SEM micrographs illustrating the quasi-spherical morpholigy; (c) optical micrographs of polished cross-sections of powder particles to evaluate internal porosity; (d) particle size distribution (PSD), including the cumulative fraction.

## 3.2.Sample fabrication

### *3.2.1. PBF-LB/M*

The samples presented in this study were manufactured using a Renishaw AM 400 laser melting system (Figure 3-2a). This system is equipped with a pulsed wave 400 W Yb-fiber laser, with a beam diameter of 70 µm. The Renishaw AM 400 has a build volume of 250 x 250 x 300 mm$^3$. However, in this project we used a reduced build volume (RBV) setup to minimize the use of powder, with a maximum build volume of 78 x 78 x 55 mm$^3$ (Figure 3-2b). The RBV is specially designed for research environments, and for cases in which there is a limited availability of feedstock powder.

The printing is conducted under Ar atmosphere, with a constant flux inside the chamber, with the recirculation frequency set at 50 Hz. The content of $O_2$ inside the chamber was kept below 500 ppm during fabrication (the printing process does not start above the threshold $O_2$ content, which then gradually decreases as the fabrication advances).

A standard meander scanning strategy with a 67º layer rotation was employed in all samples, except for the parallelepipeds from which tensile testing samples were machined (Section 4.3.3). The layer thickness was fixed at 60 µm, a relatively large value, selected for productivity purposes. The remaining scanning parameters are specified in the corresponding sections.

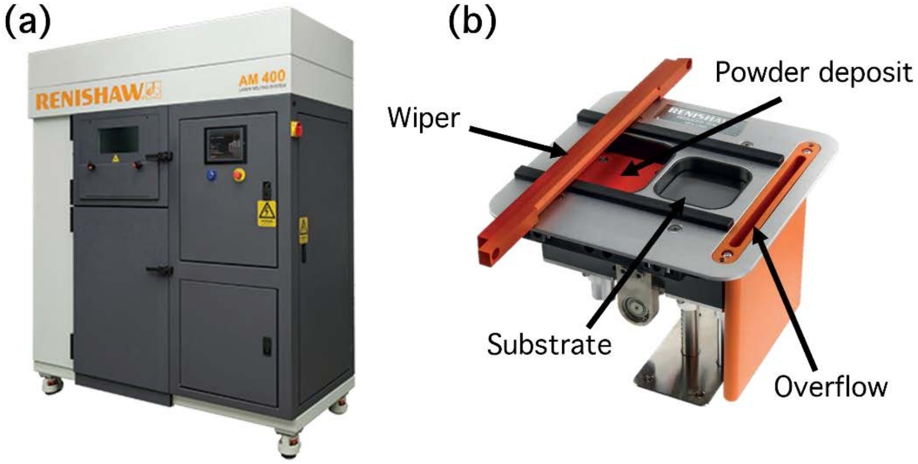

Figure 3-2: (a) Renishaw AM400 laser melting system, and (b) reduced build volume (RBV), the setup used to produce the samples presented in this thesis.

### *3.2.2. Thermal treatments*

In order to achieve the required mechanical properties, IN939 parts usually undergo a thermal treatment, consisting of a solution step followed by different aging steps [91]. Any thermal treatment is composed of a heating ramp, a dwell time, and a cooling ramp. These will impact the microstructure at multiple levels, e.g. the degree of homogeneity, the grain size, or the nature of the precipitates, and thus must be well controlled. In this thesis two different furnaces were used to perform the thermal treatments presented.

A Naberthem 3000 tube furnace was used for the treatments presented in section 6. With a maximum service temperature of 3000ºC, the treatments can be performed in vacuum conditions or under inert atmospheres. The heating rate is limited to 4.5 ºC·min$^{-1}$, and the cooling rate to 2.5 ºC·min$^{-1}$. The temperature can be recorded using a S-type thermocouple. This setup allows for very good control of the temperatures, and of the heating and cooling ramps. Additionally, the possibility of working under vacuum or inert atmosphere helps prevent high-temperature oxidation during the treatment.

A Carbolite CWF 1300 chamber furnace (Carbolite Gero Ltd.) was employed for the thermal treatments reported in Section 6.3.3. The maximum working temperature is 1300ºC, with heating rates up to 30ºC·min$^{-1}$, and it is equipped with N- and K-type thermocouples. The treatments are performed in air, and after treatment the parts can be either cooled in the furnace, air cooled, or quenched. Compared to the Naberthem tube furnace, this chamber furnace has the clear advantage of allowing different cooling rates, crucial to obtain the desired precipitation.

## **3.3. Characterization**

### *3.3.1. Defect quantification*

A key indicator used to assess the quality of the printed parts is the density. After fabrication, the samples were removed from the stainless steel substrates using either electro-discharge machining or a precision cutting machine (Struers Secotom 20). Once separated from the substrate, different cross-sections were cut, both parallel and perpendicular to the build direction (BD). The exposed sample surfaces were first ground using progressively finer SiC grinding papers, and they were then polished using diamond suspensions down to a 1 μm particle size. Once polished, optical micrographs (OM) of the different cross-sections were obtained using an Olympus BX51 light emission microscope. Micrographs of the full cross-sections were acquired at a 50X magnification to get an estimate of the relative density. Higher magnification micrographs (100X and 200X) were then taken of selected regions of each sample to better characterize porosity and cracking. All micrographs were analyzed using the Fiji software [119]. The images were segmented into pores, cracks, and defect-free regions using the Weka segmentation plug-in [120]. Relative density values (i.e., compared to bulk IN939) were calculated by determining the fraction of the total area free of defects such as pores or cracks. Crack density was expressed as the total crack length per unit area (mm/mm$^2$).

### *3.3.2. Microstructure*

The microstructure of both as-built (AB) and heat-treated (HT) samples was characterized using a wide range of techniques, and at different scales.

#### *3.3.2.1. Optical microscopy*

The first characterization step is conducted using optical microscopy (OM). Samples prepared following the metallographic procedures described in section 3.3.1, were subsequently electrochemically etched by immersion in a 10% oxalic acid solution, during approximately 8-10 s, and with an applied voltage of 5.5 V. The etched surface reveals the melt pool boundaries, as well as the dendritic microstructure of the AB samples. The melt pool dimensions can be measured form the optical micrographs using the Fiji software. The shape and size of the melt pools can provide a large amount of information about the quality of the print, the effective energy input, or the melting mode.

#### *3.3.2.2. Scanning electron microscopy (SEM)*

Scanning electron microscopy, as its name implies, is a technique that produces images by scanning the surface of a sample using a focused electron beam. The beam is emitted from an electron gun, then condensed and directed towards the sample surface using a series of coils and electromagnetic lenses. When the electron beam impacts the surface, it interacts with the sample, generating an interaction volume. This interaction causes the emission of various electrons and electromagnetic radiation, which can be collected by specific detectors. In this study, we mostly used secondary electrons (SE), backscattered electrons (BSE), and X-rays. Secondary electrons are ejected from the conduction or valence bands of the atoms from the specimen after interaction with the emitted electrons. Because SE have low energies, they provide detailed information about the surface topography. An Everhart-Thornley detector (ETD) is used to obtain images from the SE signal. Backscattered electrons, on the other hand, are high-energy electrons reflected elastically (or backscattered) from the specimen. They provide compositional contrast, offering information about the chemical composition of the sample. Although the ETD can also capture the BSE signal, our SEM is also equipped with a concentric backscattered (CBS) detector specifically for this purpose. Additionally, BSEs are used in electron backscatter diffraction (EBSD) to analyze the crystal structure of the samples, which will be described in Section 3.3.2.3. Finally, X-rays emitted due to electron–specimen interactions enable the analysis of local chemical composition through energy-dispersive X-ray spectroscopy (EDS or EDX). Each element presents a unique X-ray emission spectrum which provides qualitative and quantitative information of the elemental composition at a surface level. In the body of this thesis, only results obtained with TEM-EDS are reported.

In this study, we used two different field emission gun (FEG) SEMs, a Helios NanoLab 600i and an Apreo 2S LoVac, from ThermoFisher Scientific. Both are equipped with ETD and CBS detectors. as well as with EDS detectors (Ultim Max and Symmetry S2, respectively, both from Oxford Instruments).

The sample preparation for SEM characterization consisted of the same grinding and polishing steps described in section 3.3.1, followed by a final chemical polishing step using a 0.04 μm colloidal silica oxide polishing suspension (OPS).

#### *3.3.2.3.Electron backscatter diffraction (EBSD)*

One of the main characterization techniques utilized in this thesis is electron backscatter diffraction (EBSD). A powerful tool, it provides local information about the crystal structure and about the spatial distribution of orientations. The EBSD detector is equipped with a phosphorescent screen that captures the diffraction patterns formed by backscattered electrons, known as Kikuchi patterns. From the width and position of the pattern lines, it is possible to determine the crystal system and the crystallographic orientation. With EBSD data we can obtain information regarding grain size, grain boundary distribution, intragranular rotations, or dislocation density.

The sample preparation procedure for EBSD data acquisition was the same as for other SEM characterization techniques. Samples were placed on a sample holder with a 70º tilt to increase the yield of BSE, thereby improving the signal quality. The acceleration voltage for EBSD mapping was set at 20 kV, with a beam current of either 3.2 or 6.4 nA, depending on the sample, and the working distance was fixed between 13 and 14 mm. The step size was adjusted to the map type and size, and will be specified in the corresponding sections.

All the maps shown in this manuscript were acquired using the Apreo 2S LoVac SEM equipped with a Symmetry S2 EBSD detector from Oxford Instruments. EBSD data processing and analysis was performed using both the HKL Channel5 software (Oxford Instruments) and the MTEX toolbox (5.10.2 version) [121] in MatLab, to obtain different maps and distributions. Inverse pole figure (IPF) maps illustrating the crystallographic directions parallel and perpendicular to the BD were obtained. Grain boundary maps were acquired considering high angle grain boundaries (HAGB) have a minimum misorientation angle of 15º, and low angle grain boundaries (LAGB) have misorientation angles between 2 and 15º. Grain sizes were estimated using the line intercepts (LI), in the directions both parallel (longitudinal LI) and perpendicular (transverse LI) to the BD. The direct pole figures (PF) were plotted using a de la Vallée Poussin kernel, a band width of 10º, and a cluster size of 5º. Texture analysis and quantification was done using both the multiples of uniform distribution (MUD) from the PFs, and calculating the volume fractions ($V_f$) of different texture components. These $V_f$ were calculated by integrating the orientation distribution function (ODF), allowing for a spread of 15º from the corresponding pole. Geometrically necessary dislocation (GND) maps and distributions were also calculated. GNDs give an idea of the local misorientations -calculated from the kernel average misorientations (KAM)-, assuming that those local misorientations are accommodated in the form of dislocations [122].

### 3.3.2.4. *Transmission electron microscopy (TEM) and energy dispersive X-ray spectroscopy (EDS)*

The characterization of the microstructure at smaller scales was conducted using transmission electron microscopy (TEM). In this technique, the electron beam is transmitted through a thin specimen (usually below 100 nm in thickness), allowing the detection of features down to atomic resolution. In this thesis, we employed a Talos F200X scanning TEM

(ThermoFisher Scientific), working at an accelerating voltage of 200 kV. Imaging was performed in bright field (BF) mode and in STEM mode, using a high-angle annular dark field (HAADF) detector. Selected area diffraction (SAD) was also carried out in order to identify the crystal phases present in the samples. Additionally, the TEM was equipped with a Super-X EDS detector (ThermoFisher Scientific), which was used to perform elemental mapping.

For TEM characterization, samples are first thinned by grinding into 0.1 mm thick foils, from which 3 mm discs are punched. These discs are then electropolished using a Struers TenuPol 5 double jet electropolisher, using an electrolyte consisting of 10 % perchloric acid, 30 % butanol, and 60 % ethanol, at -22ºC, and operating at 30 V.

### *3.3.3. Mechanical properties*

IN939 is required to exhibit good mechanical properties across a wide temperature range. In this study, the mechanical performance of the printed samples was evaluated through uniaxial tensile testing. During these tests, the samples are subjected to a tensile load until failure. By recording the applied force and the elongation of the gauge section, strain ($\varepsilon$) and stress ($\sigma$) values can be calculated. From the stress-strain curves key mechanical properties such as the yield strength ($\sigma_y$), the ultimate tensile strength (UTS), the Young's modulus (E), the maximum elongation, or the strain-hardening behavior can be determined. This study focuses primarily on the yield and ultimate tensile strengths, and on the maximum elongation.

Tensile tests were performed at 23 ± 3 °C in accordance with ASTM E8-21, and at 700 ± 3 °C, 800 ± 3 °C, and 950 ± 3 °C following the ASTM E21-20 standard. The tests were conducted using an MTS 370.10 universal testing machine equipped with an MTS 653 high-temperature furnace. An initial strain rate of 0.005 $\text{min}^{-1}$ was applied up to 1% strain, followed by an increased rate of 0.05 $\text{min}^{-1}$ until failure.

Cylindrical tensile specimens with the dimensions specified in Figure 3-3 were machined from PBF-LB/M parallelepipeds (55 x 12 x 50 $\text{mm}^3$). These parts were printed using a stripes scanning strategy, with a stripe overlap of 0.02 mm, and a stripe width of 5 mm. Additional scanning parameters are detailed in the corresponding sections.

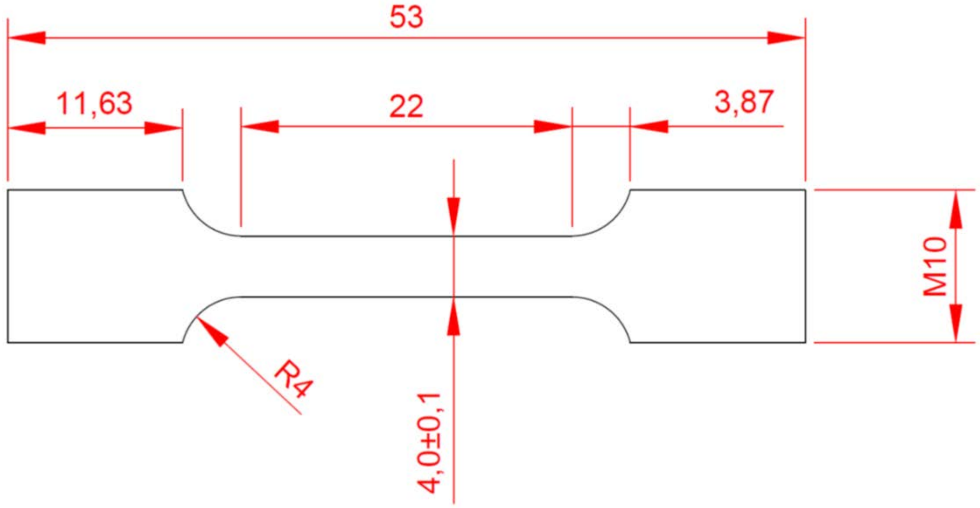

Figure 3-3: tensile specimen geometry and dimensions.

# 4. PULSED WAVE PBF-LB/M PROCESS OPTIMIZATION

## 4.1. Background

PBF-LB/M processing of Ni-based superalloys has been extensively investigated, with several reviews summarizing the main findings and key aspects [84–87]. As established in Section 2.3.2. PBF-LB/M of Ni-based superalloys, most of these studies focus on weldable alloys such as Inconel 718, Inconel 625, or Hastelloy X, with crack-prone alloys posing a significant challenge in terms of their PBF-LB/M processability.

Inconel 939 is one of these crack-prone alloys. Despite being hard to weld, successful processing of IN939 through PBF-LB/M has been achieved. The main characteristics and advances have been highlighted in Section 2.4.2. PBF-LB/M of IN939At the outset of this work, the literature on the topic was rather scarce, and focused mostly on attempts to find a suitable processing window [94–98]. In addition, the available studies utilized a continuous wave (CW) laser source, and the PBF-LB/M processability window for IN939 using a pulsed wave laser emission (PW) remained unexplored.

This chapter presents the first experimental study conducted for this thesis, where the main objective is, first, to find optimum PBF-LB/M processing conditions for IN939 that result in a minimum defect density using a PW laser. Second, we aim to establish a relationship between the PBF-LB/M processing parameters, the microstructure, and the mechanical behavior of the manufactured parts over a large temperature range. The results obtained have been discussed in light of the literature existing at the time the study was performed.

## 4.2.Methods

The laser power (P), the hatch distance ($h_d$) and the scanning speed (v) were optimized using a full factorial design of experiments (DoE) approach and a bidirectional (or meander) scanning strategy, with a 67º rotation between layers. Half cubes with dimensions 3 x 7 x 7 $mm^3$ were printed with a total of 27 parameter sets resulting from combining three P values, three $h_d$ values, and three v values, as shown in Table 4-1. The corresponding volumetric energy densities ($E_v$) ranged from 33 to 114 $J \cdot mm^{-3}$.

Table 4-1: List of the 27 parameter sets that were utilized for PBF-LB/M optimization of the IN939 alloy. The two resulting “optimized” processing conditions are highlighted in bold letters.

| **Power (W)** | **Hatch distance (µm)** | **v (mm·s$^{-1}$)** | **E$_v$ (J·mm$^{-3}$)** | **Relative density (%)** | **Crack density (x10$^{-2}$ mm·mm$^{-2}$)** |
|---|---|---|---|---|---|
| 250 | 50 | 875 | 95 | 99.25 | 7.59 |
| **250** | **50** | **1167** | **71** | **99.81** | **0.27** |
| 250 | 50 | 1400 | 60 | 99.40 | 1.46 |
| 250 | 70 | 875 | 68 | 98.97 | 18.17 |
| **250** | **70** | **1167** | **51** | **99.54** | **0.25** |
| 250 | 70 | 1400 | 43 | 98.99 | 0.49 |
| 250 | 90 | 875 | 53 | 98.16 | 22.36 |
| 250 | 90 | 1167 | 40 | 98.51 | 5.79 |
| 250 | 90 | 1400 | 33 | 95.44 | 54.68 |
| 275 | 50 | 875 | 105 | 98.38 | 8.08 |
| 275 | 50 | 1167 | 79 | 99.59 | 3.73 |
| 275 | 50 | 1400 | 65 | 99.37 | 0.54 |
| 275 | 70 | 875 | 75 | 98.52 | 22.68 |
| 275 | 70 | 1167 | 56 | 99.21 | 2.06 |
| 275 | 70 | 1400 | 47 | 98.89 | 0.46 |
| 275 | 90 | 875 | 58 | 98.13 | 17.48 |
| 275 | 90 | 1167 | 44 | 97.26 | 3.01 |
| 275 | 90 | 1400 | 36 | 93.61 | 45.05 |
| 300 | 50 | 875 | 114 | 99.09 | 1.97 |
| 300 | 50 | 1167 | 86 | 98.75 | 2.40 |
| 300 | 50 | 1400 | 71 | 98.90 | 1.12 |
| 300 | 70 | 875 | 82 | 98.94 | 5.63 |
| 300 | 70 | 1167 | 61 | 98.29 | 2.70 |
| 300 | 70 | 1400 | 51 | 96.95 | 4.25 |
| 300 | 90 | 875 | 63 | 98.02 | 14.59 |
| 300 | 90 | 1167 | 48 | 97.79 | 2.87 |
| 300 | 90 | 1400 | 40 | 96.98 | 22.29 |

The determination of the optimum processability window was carried out by minimization of the relative density and the crack density. These magnitudes were measured by optical microscopy (OM) on cross sections parallel to the building direction (BD) that were prepared following standard metallography protocols as described in 3.3.1. The values of the relative density and of the crack density were, furthermore, used as input for an analysis of variance (ANOVA) in order to determine the isolated and coupled influence of individual scanning parameters on defect formation.

The microstructure of the samples was further characterized by scanning electron microscopy (SEM), and by electron backscattered diffraction (EBSD). The EBSD maps presented in this section were acquired using a 1 μm step size, an accelerating voltage of 20 kV, and a beam current between 2.7 and 3.2 nA. Additionally, the microstructure was examined at higher magnification by transmission electron microscopy (TEM). For this study, TEM lamellae were obtained by the trenching-and-lift-out method using a focused ion beam (FIB) on a FEI Helios NanoLab 600i FEGSEM operating at 30 kV.

The mechanical behavior of the PW-PBF-LB/M processed IN939 alloy was characterized in tension along a direction perpendicular to BD at a wide range of temperatures including 23±3ºC (room temperature, RT), 700ºC±3ºC, 800ºC±3ºC and 950ºC±3ºC, following the standards described in 3.3.3. The cylindrical tensile samples with 22 mm gauge length and 4 mm diameter (Figure 3-3) were machined out of PBF-LB/M processed 55 x 12 x 50 $mm^3$ blanks. The latter were manufactured using the optimum PW-PBF-LB/M processing conditions (P, $h_d$, v) found in the first part of the current study. However, a stripe scanning strategy had to be utilized instead of the previously used meander strategy in order to overcome the warping associated to the larger cross-section of the blanks (as compared to the half cubes).

Before testing, the tensile samples were heat treated in a Nabertherm 3000 vacuum furnace following the standard treatment schedule for cast IN939 [91], consisting of a solution step at 1160ºC for 4 h, and two aging steps at 1000ºC for 6 h and at 800ºC for 4 h, respectively. The heating and cooling rates were ~4.5 and ~2.5ºC$\cdot$$min^{-1}$, respectively. Due to the impossibility of opening the furnace in between the different heat treatment steps, this cooling rate value was slower than that associated to quenching or fast air cooling and, thus, to what is considered desirable to achieve an optimum precipitate distribution in Ni-based superalloys, an aspect to be accounted for in the mechanical properties assessment. The mechanical behavior of the IN939 PBF-LB/M samples was compared to that of the cast material.

## 4.3. Results

### *4.3.1. PW PBF-LB/M process optimization*

Figure 4-1 illustrates the variation of the relative density and of the crack density (in mm**.**mm$^{-2}$) as a function of the $E_v$ for the 27 PBF-LB/M parameter combinations that were investigated in the current study, together with micrographs showing optimum, excessive, and insufficient energy inputs (Figure 4-1a,b,c). The actual values of these two magnitudes corresponding to each set of processing parameters are summarized in Table 4-1. Figure 4-1 also includes representative optical micrographs illustrating the defects present in samples processed using low, medium and high $E_v$ levels. Overall, it can be seen that the density of the printed parts increases with the $E_v$ until a maximum densification level (99.8%) is reached between 50 and 70 J·mm$^{-3}$. Further increases in $E_v$ lead to a steady decrease in the density of the printed samples. The low densities obtained in samples manufactured using $E_v$ values below 45 J·mm$^{-3}$ point towards an insufficient energy input leading to lack of fusion defects, deficient layer bonding, and other instabilities. Indeed, as shown in micrograph (c) of Figure 4-1, lack of fusion defects, with their characteristic irregular morphology, are profusely present in the sample printed using an $E_v$ value of 33 J·mm$^{-3}$. In the $E_v$ range comprised between 45 and 65 J·mm$^{-3}$, the dependency between $E_v$ and the formation of defects becomes complex, and similar energy inputs can give rise to very different values of relative density. For example, while a relatively low density of 96.95 % is obtained for an $E_v$ value of 51 J·mm$^{-3}$, but with the same energy input we also reach a relative density value of 99.54 %. Micrograph (a) in Figure 4-1 illustrates the maximum densification achieved in the current study (99.81 %), which corresponds to a sample processed with an $E_v$ value of 71 J·mm$^{-3}$. PBF-LB/M processing with $E_v$ values higher than 75 J·mm$^{-3}$ leads to the development of keyhole porosity due to an excessive thermal input, as evidenced in micrograph (b) of Figure 4-1. Although using the $E_v$ as a control variable is useful as a first approximation, for it contains all the scanning parameters, the isolated influence of P, v, and $h_d$ cannot be inferred from this type of analysis. In the following, the individual effect of these parameters is analyzed separately.

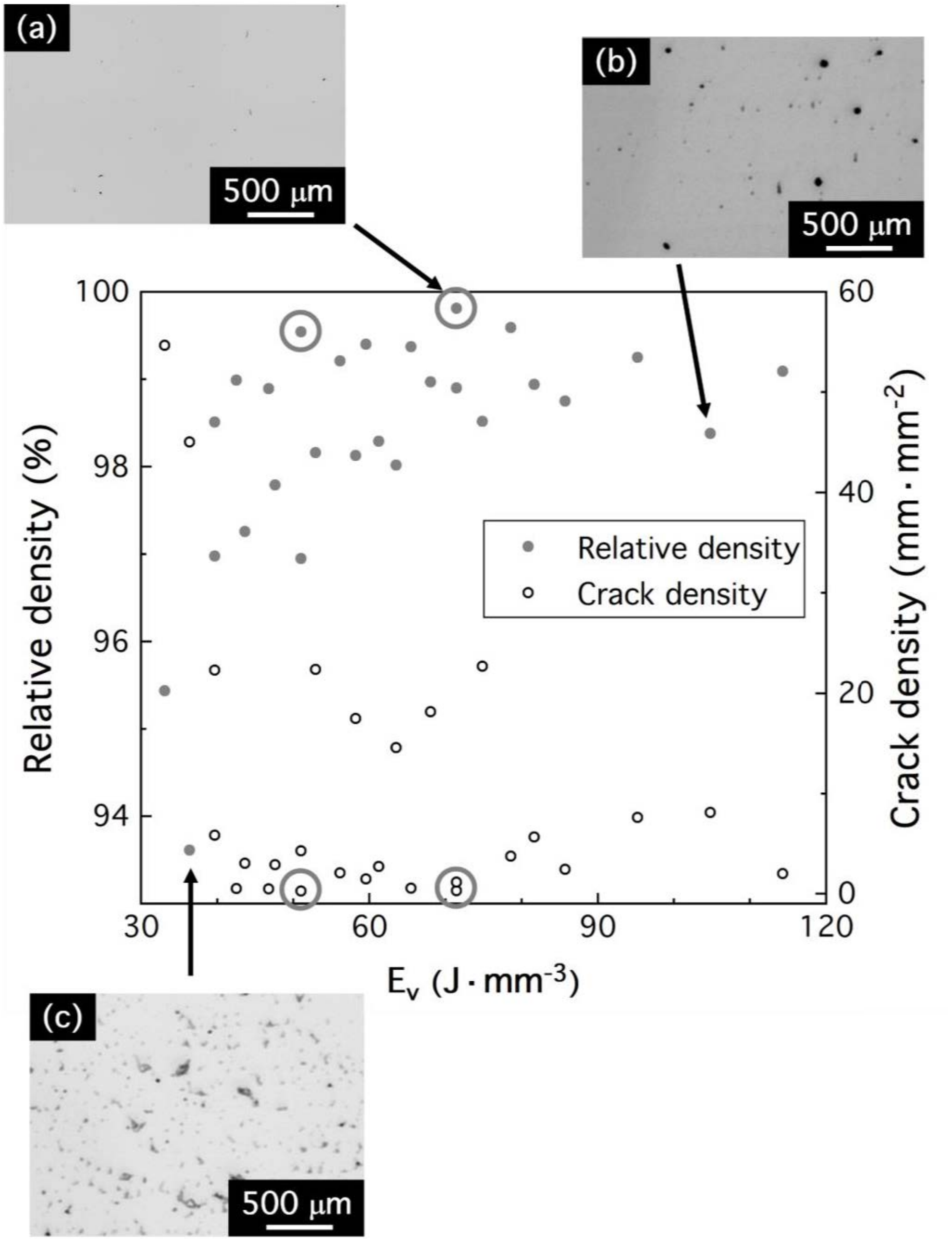

Figure 4-1: Relative density (% - full symbols), and crack density (mm·mm$^{-2}$ - empty symbols) as a function of $E_v$ for the 27 different PBF-LB/M scanning parameter combinations. Optical micrographs of samples with (a) medium $E_v$ and low density of defects, (b) high $E_v$ and keyhole porosity, and (c) low $E_v$ and lack-of-fusion porosity.

First, a single-parameter ANOVA analysis was performed in order to determine the statistical significance of the influence of P, $h_d$, v, and on the relative density and on the crack density. The corresponding F and p-values are summarized in Table 4-2. According to this analysis, for a reference statistical significance ($\alpha$) of 0.05, only $h_d$ can be considered to have a statistically significant and isolated effect on the relative density (p-value=0.0009) and the crack density (p-value=0.0078), while the values of the scanning speed and of the laser power included in this study cannot be considered to be statistically distinguishable. The box charts shown in Figure 4-2a and Figure *4-2*b depict the relative density and the crack density as a function of P, $h_d$, and v for the 27 combinations of PBF-LB/M parameters investigated. It can be seen that $h_d$ = 90 μm consistently yields the worst results both in terms of relative density and of crack density, while an intermediate speed value of v = 1.167 $m \cdot s^{-1}$ provides the best densification conditions, with the lowest crack density. The relation between P and the defectology is not as straightforward as in the case of the two other scanning parameters. On the one hand, the highest relative density values are obtained with the smallest laser power (P = 250 W); on the other hand, the highest laser power (P = 300 W) yields the lowest crack density, while a large variability is associated to P = 250 and 275 W. These results highlight the complexity of isolating the influence of individual PBF-LB/M processing parameters.

Table 4-2: F and p-values obtained from a single-factor ANOVA. The critical F value for a system with 2 and 24 degrees of freedom between and within groups respectively is 3.403 when $\alpha$=0.05.

| | **Relative density** | | **Crack density** | |
|---|---|---|---|---|
| | **F** | **p-value** | **F** | **p-value** |
| **Hatch distance** | 9.601 | 0.0009 | 5.985 | 0.0078 |
| **Scanning speed** | 2.021 | 0.1544 | 2.233 | 0.1290 |
| **Laser power** | 0.442 | 0.6481 | 0.466 | 0.6333 |

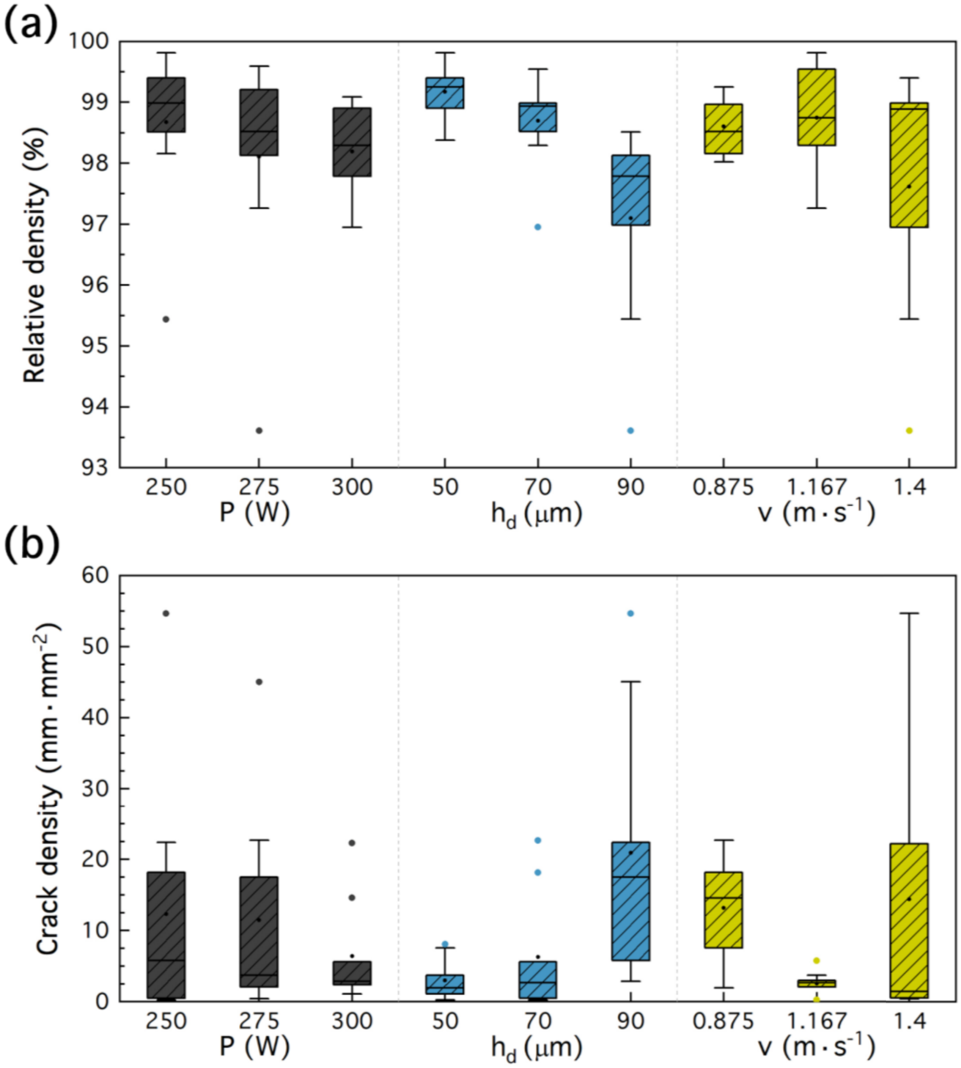

Figure 4-2: Box charts showing the effect of laser power, hatch distance, and scanning speed on (a) the relative density and (b) the crack density of PBF-LB/M-processed IN939 samples.

The previous analysis allows us nevertheless to define optimum PBF-LB/M conditions for the IN939 alloy. In particular, from the 27 sets of processing parameters examined, two were selected. Both sets share the same laser power (P = 250 W), which rendered the highest relative density (Figure 4-2a), and the same scan velocity (v = 1.167 m·s$^{-1}$), which provided, simultaneously, the best values of densification and the lowest cracking densities (Figure 4-2a and 4-2b). Additionally, one set includes $h_d$ = 70 μm ($E_v$ = 51 J·mm$^{-3}$) and the second set includes $h_d$ = 50 μm ($E_v$ = 71 J·mm$^{-3}$), as these two hatch distance values yielded similar, and equally good, results. From here on, these two sets of scanning parameters will be referred to as *$h_d$70* and *$h_d$50*. The relative densities and the crack densities corresponding to these two parameter sets are highlighted in Figure 4-1 using circles. They amount, respectively, to 99.81 and 99.54% and to $2.7\cdot10^{-3}$ and $2.5\cdot10^{-3}$ mm·mm$^{-2}$. Figure 4-3 includes two optical micrographs illustrating the high densification level resulting from PBF-LB/M processing of the IN939 alloy using the two optimized conditions (Figure 4-3a,c), as well as two optical micrographs showing the corresponding melt pool geometry (Figure 4-3b,d). The stability of the process under the two selected optimized processing conditions is consistent with the homogeneous nature of the melt pools.

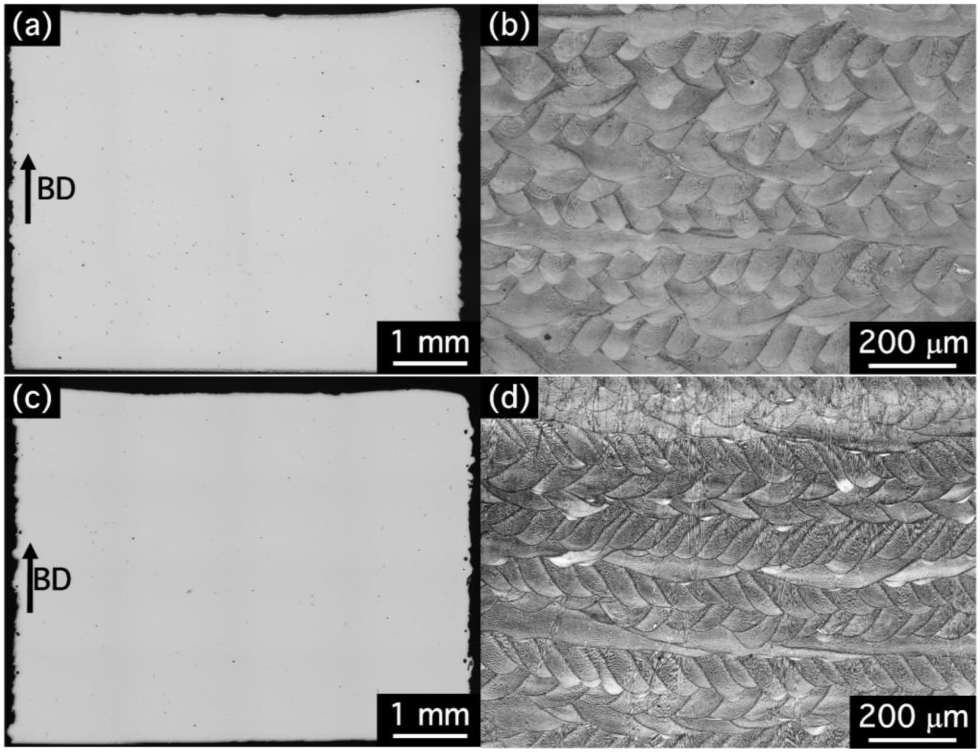

Figure 4-3: Optical micrographs illustrating (a, b) the reduced levels of defects present in the samples processed using optimized PBF-LB/M bulk conditions, and (c, d) the melt pool geometry resulting from the two optimized processing conditions. The BD is parallel to the vertical direction. The printing conditions are (a, b) $P = 250$ W, $v = 1167$ mm·s$^{-1}$, $h_d = 70$ µm ($E_v = 51$ J·mm$^{-3}$); (c, d) $P = 250$ W, $v = 1167$ mm·s$^{-1}$, $h_d = 50$ µm ($E_v = 71$ J·mm$^{-3}$).

### *4.3.2. Microstructure of PBF-LB/M IN939 specimens processed using optimum processing parameters*

Figure 4-4 illustrates the microstructure of the two PBF-LB/M IN939 specimens processed using the two sets of optimum processing conditions. In particular, EBSD inverse pole (IPF) maps in the BD as well as {100}, {110}, and {111} direct pole figures are included for each sample. It can be seen that the microstructure of the $h_d70$ sample, processed using the lower $E_v$ (Figure 4-4a) is a polycrystal with a weak texture and irregularly shaped grains.

An increase in the $E_v$ to 71 $J\cdot mm^{-3}$ (Figure 4-4b, $h_d50$) leads to a more columnar microstructure, to an overall increase of the grain size, and to the formation of a stronger <100> fiber texture, where the fiber axis is parallel to the BD. In the EBSD maps, black lines represent high angle boundaries, with misorientations higher than 15°, while white lines represent low angle boundaries, with misorientations lower than 15°. As is commonly found in PBF-LB/M processed materials, an intragranular array of low angle boundaries is present in both samples. This cell structure was further investigated by SEM and TEM. Figure 4-5 contains several SEM images acquired on etched surfaces of two PBF-LB/M IN939 specimens processed using the two sets of optimum processing conditions, $h_d50$ and $h_d70$. The white contrast reveals the presence of segregated species at cell boundaries and allows for an estimation of the cell sizes, which amounted to 675 ± 168 nm and 658 ± 163 nm for the $h_d70$ and the $h_d50$ samples, respectively. The cell structures being very similar in the two investigated samples could be indicative of comparable solidification rates regardless of the processing conditions [123,124].

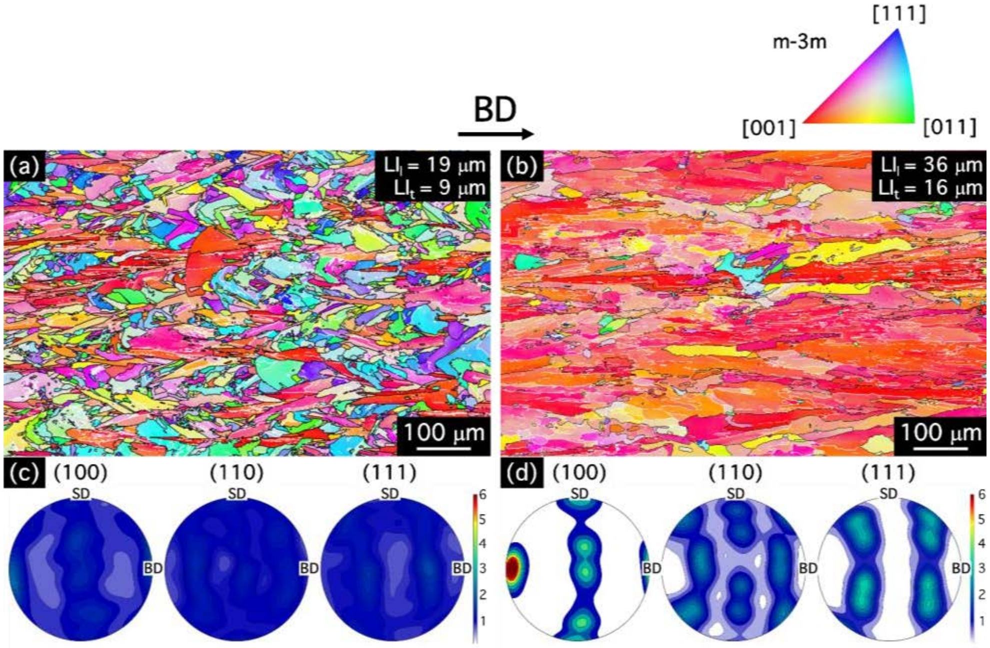

Figure 4-4: EBSD IPF maps in the BD and {100}, {110}, and {111} direct pole figures corresponding to the PBF-LB/M IN939 samples printed using the two optimum sets of scanning parameters. In the EBSD maps, black lines represent high angle boundaries, with misorientations higher than 15°, while white lines represent low angle boundaries, with misorientations lower than 15°. Scanning parameter conditions: (a) $h_d70$, (b) $h_d50$. The average linear intercepts along the BD ($LI_l$) and along a direction perpendicular to BD ($LI_t$) are also included.

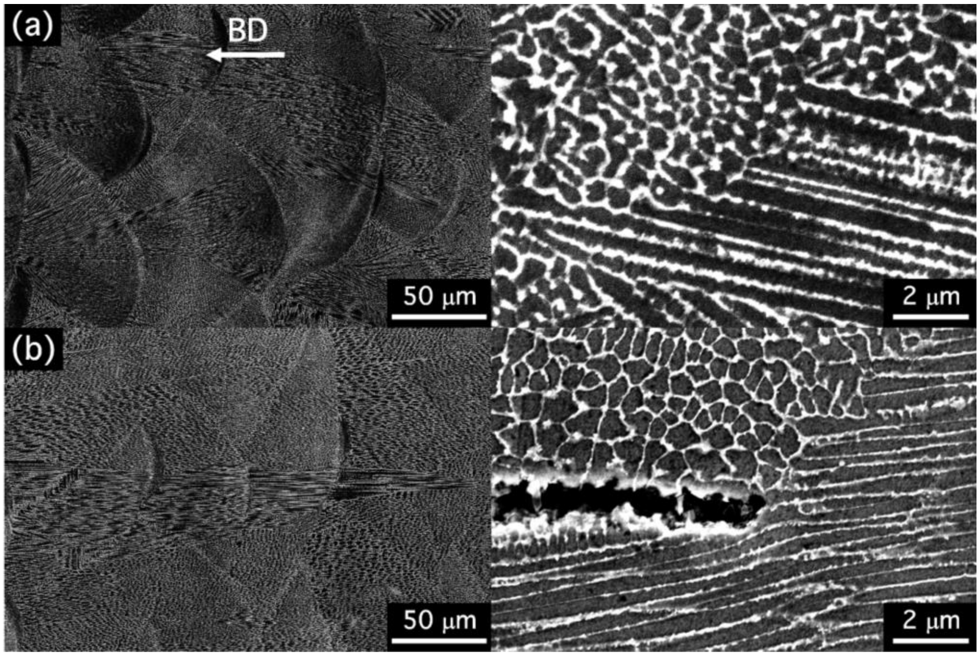

Figure 4-5 SEM micrographs illustrating the intragranular cell structure in the PW LPBF IN939 samples printed using the two optimum sets of scanning parameters: (a) $h_d70$, (b) $h_d50$.

In order to examine the cell structure in more detail, and to evaluate the nature of the atomic segregations at cell walls, a TEM lamella was extracted from the specimen processed with 71 J·mm$^{-3}$ ($h_d50$). Figure 4-6a and 4-6b provide images of the cells at different magnifications, acquired along a <100> zone axis. The average cell size measured from the TEM images is 723 ± 206 nm. Figure 4-6c reveals the presence of dislocations at cell interiors, as is commonly observed in PBF-LB/M samples. EDX mapping was carried out at different locations in order to investigate the nature of the segregations at cell boundary walls. Figure 4-7, which consists of a representative high angle annular dark field (HAADF) image and the corresponding elemental maps, proves that cell walls are populated with Ti and Nb atomic segregations, as well as with some $(Ti,Nb)_xC_y$ carbides. No indications of either γ’ or η particles were noticeable in any of the analyzed regions.

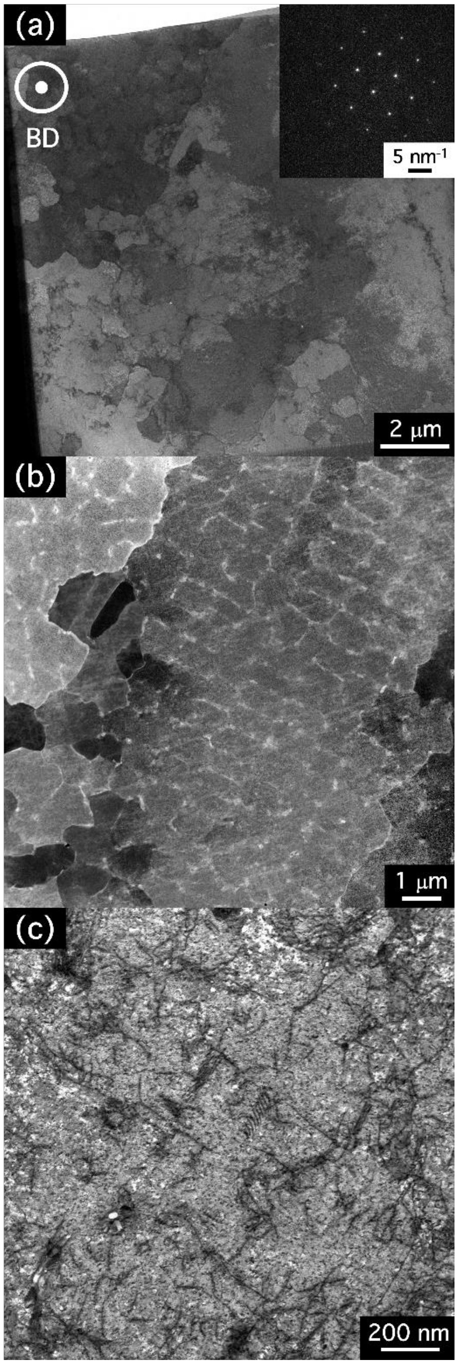

Figure 4-6: TEM micrographs depicting the microstructure of the sample processed using the optimized parameter set *$h_d$50*. (a) STEM image of the entire TEM lamella, illustrating the cell structure; (b) HAADF image at higher magnification of the cell structure, where the lighter gray color corresponds to segregated species; (c) a high magnification view of the presence of dislocations at cell interiors. Imaging was performed along a <001> zone axis.

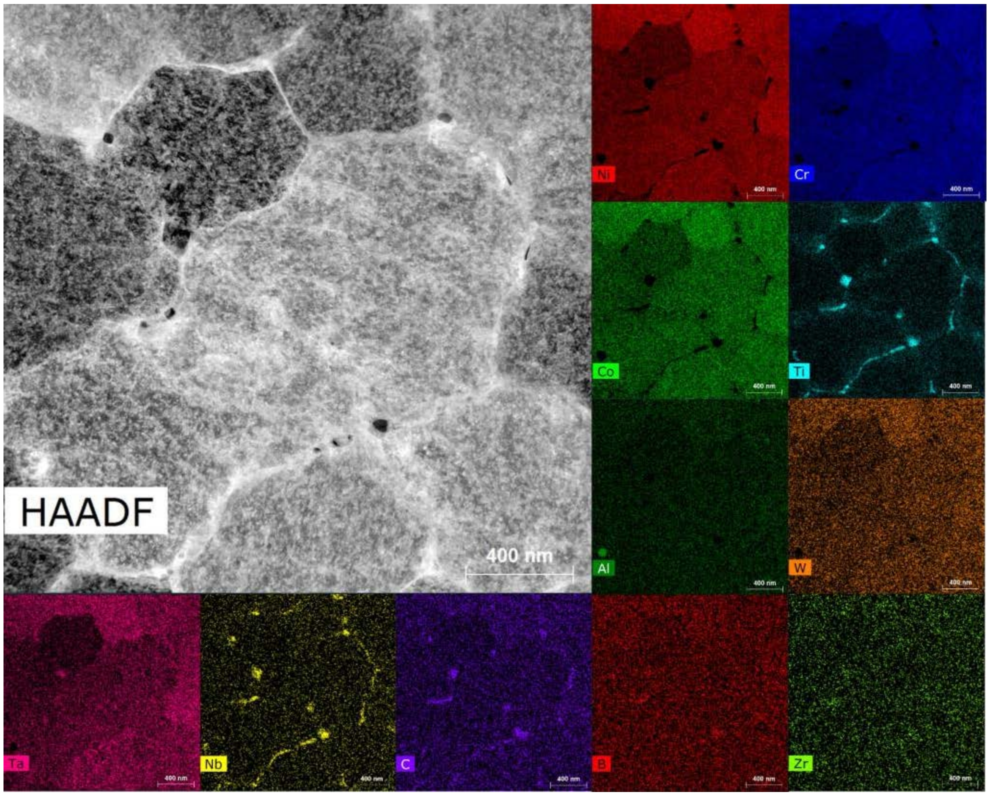

Figure 4-7: EDX mapping of a representative region of the cell structure of the sample processed using the optimized parameter set $h_d50$. HAADF image and the corresponding elemental maps.

### *4.3.3. Mechanical behavior of PBF-LB/M IN939*

Figure 4-8 illustrates the microstructure of the (undeformed) grips of the tensile specimens, which were printed using the two optimized sets of PBF-LB/M processing parameters but using a *stripes* scanning strategy, and that were subsequently heat treated using standard heat treatment conditions. EBSD IPF maps in the BD, as well as {100}, {110}, and {111} direct pole figures are included for each sample. Comparison of Figure 4-8 with Figure 4-4 reveals that changing the scanning strategy from meander (cube specimens printed for process parameter optimization) to stripes (tensile specimens) does not alter significantly the resulting microstructure. Indeed, the microstructure of the $h_d70$ tensile sample (Figure 4-8a) is also a polycrystal with a weak texture and irregularly shaped grains. Increasing the $E_v$ (Figure 4-8b, $h_d50$) leads, again, to a more columnar microstructure, to an overall increase of the grain size, and to the formation of a stronger <100> fiber texture, where the fiber axis is parallel to the BD. However, both the grain size and the maximum texture intensity increase moderately when the strategy is changed from meander to stripes. In particular, the average line intercept in a direction parallel to the BD increases from 13 (meander) to 22 (stripes) μm and from 36 (meander) to 41 (stripes) μm in the $h_d70$ and $h_d50$ samples, respectively. The maximum texture intensity increases from 2.5 to 3.9 in the $h_d70$ sample and from 10.6 to 14.9 in the $h_d50$ sample.

A homogeneous distribution of γ′ particles precipitate during aging in the specimens with the two microstructures under study. As a representative example, the precipitate distribution corresponding to the grip section of $h_d70$ tensile specimens, both polished and etched using the previously described procedure, is shown at different magnifications in the SEM micrographs of Figure 4-9. A bimodal distribution of γ’ precipitates is observed, where the larger particles have an irregular, flower-like morphology, and sizes ranging from about 500 nm to ~2 μm (with a few particles exceeding 4 μm), whilst smaller (or secondary) γ’ particles exhibit a rounder shape with sizes smaller than 100 nm (Figure 4-9b,c). Figure 4-9a, additionally, reveals the presence of carbides (white contrast), which are located preferentially at grain boundaries.

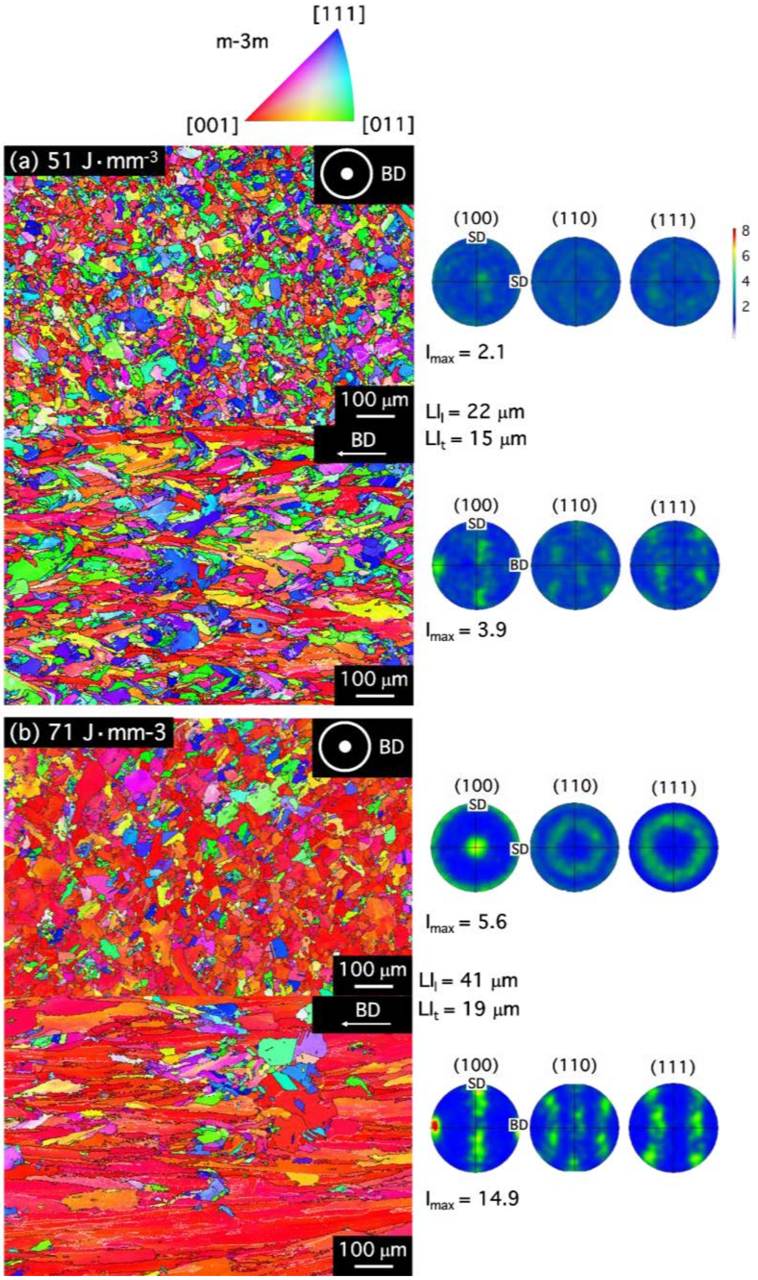

Figure 4-8: EBSD IPF maps in the BD and the corresponding {100}, {110}, and {111} direct pole figures corresponding to the PBF-LB/M IN939 samples printed using the two optimum sets of scanning parameters: (a) *$h_d$70*, (b) *$h_d$50*. For each sample, maps along cross sections perpendicular and parallel to BD are presented. In the EBSD maps, black lines represent high angle boundaries, with misorientations higher than 15°, while white lines represent low angle boundaries, with misorientations lower than 15°. The average linear intercepts along the BD ($LI_l$) and along a direction perpendicular to BD ($LI_t$) are also included.

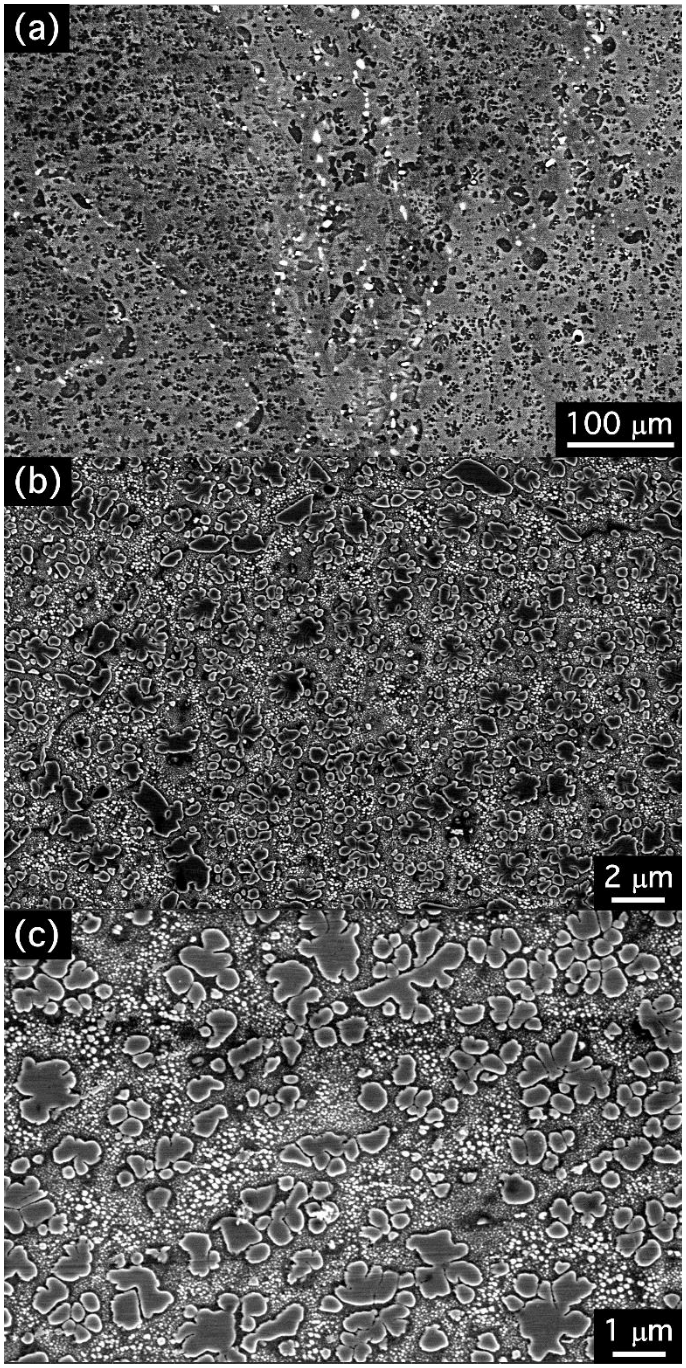

Figure 4-9: SEM micrographs of the grips of the heat-treated PBF-LB/M IN939 tensile specimens at (a) lower magnification showing some γ' precipitates as well as the presence of carbide particles in white contrast (back-scattered electron signal of a polished sample), and (b,c) higher magnification micrographs of electrochemically etched samples, illustrating the bimodal distribution of γ' in more detail .

Figure 4-10 compares the tensile properties of the PBF-LB/M IN939 alloy of the present study (empty symbols) and those of the same alloy processed by conventional casting (full symbols) [91–93] at a wide range of temperatures including 23 ± 3ºC (room temperature, RT), 700ºC± 3ºC, 800ºC± 3ºC and 950ºC ± 3ºC. In both cases, the tensile specimens were heat treated using the standard heat treatment following processing [91]. Since the specimens manufactured using the two optimized PBF-LB/M processing conditions rendered similar mechanical properties, the data points in Figure 4-10 were obtained from tests carried out in both types of samples. The microstructure of the cast alloy, as is well known [91,92,125], consists of randomly oriented large grains with an average grain size close to 1 mm. MC and $M_{23}C_6$ carbides commonly precipitate along grain boundaries, and a bimodal dispersion of γ′ precipitates is present, with average sizes of ~150 nm and ~50 nm for primary and secondary γ', respectively. It can be seen in Figure 4-10 that, at RT and 700ºC, the additively manufactured IN939 outperforms the cast material in terms of yield strength by 11% and 17%, respectively. As expected, temperature leads to softening in both the PBF-LB/M and the cast alloys. However, the PBF-LB/M material softens significantly already at 700ºC, reaching values that are comparable to those of cast specimens, whereas cast samples show good mechanical stability up to 800ºC. The yield strength values of the additively manufactured alloy at 800ºC and 950ºC, respectively, are 30 % and 34 % lower than those of the cast material. The ductility of the PBF-LB/M IN939 is comparable to that of the cast alloy over the entire temperature range investigated.

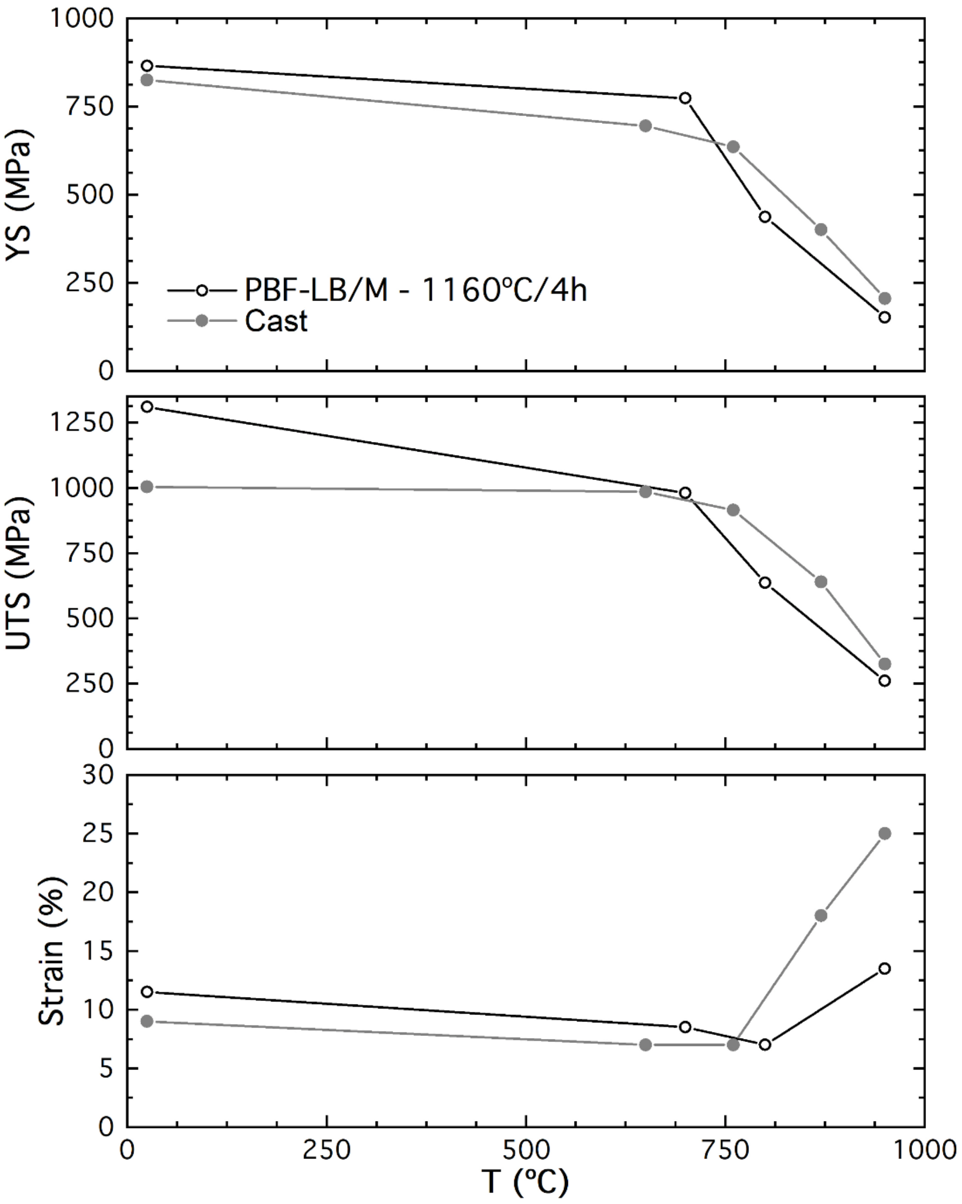

Figure 4-10: Comparison of the mechanical properties of IN939 in two conditions: after a standard heat treatment following PBF-LB/M using optimized processing parameters (this study, empty symbols) and after a standard heat treatment following casting ([91–93], full symbols).

Fracture surfaces were found to be similar in the tensile specimens processed using the two optimized PBF-LB/M conditions. Figure 4-11 illustrates representative images of the fracture surfaces corresponding to the $h_d70$ specimen at temperatures ranging from RT to 800ºC. In all cases the typical features of a ductile fracture, with large areas populated by dimples and some river markings, are apparent. Occasionally flatter areas, associated to local cleavage, can also be detected (Figure 4-11c). In addition, some pores containing carbide particles can also be observed (Figure 4-11d). Overall, as expected given the relatively large strain values obtained (~10-15 %), the fracture surfaces are consistent with a ductile fracture.

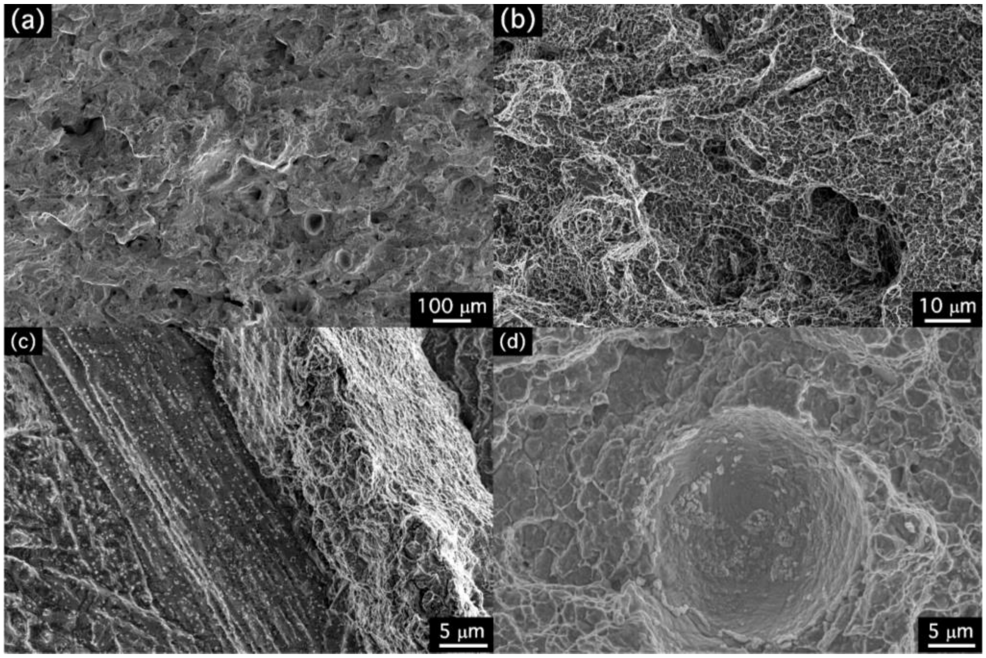

Figure 4-11: Representative secondary electron SEM images of fracture surfaces corresponding to the $h_d70$ specimen at (a,b) RT, (c) 700ºC, and (d) 800ºC.

## 4.4. Discussion

### *4.4.1. Pulsed wave vs. continuous wave laser processing of IN939*

Pulsed wave laser emission offers several advantages with respect to continuous laser emission in PBF-LB/M, including a higher flexibility to tune the heat accumulation by adjusting the point distance and the time exposure, besides the laser power, as well as higher cooling rates [31,126–128]. Melt pools in PW processing are known to exhibit a heartbeat-like (contraction-expansion) motion, rounder shape, and shorter lengths [31,129,130]. Moreover, PW processing is associated with an oscillating temperature profile, and a larger tilt (~15° more) of the solidification front with respect to the building direction [33]. CW lasers are, thus, reportedly preferred to build fully dense, large parts, while PW lasers are considered more suitable to manufacture thin sections that require higher dimensional accuracy, such as those present in lattice structures [31,126–128,131]. Additionally, PW PBF-LB/M has been reported to reduce solute diffusion due to the faster solidification rates and to smaller heat affected zones (HAZ) as compared to CW PBF-LB/M. This, in turn, often leads to reduced precipitate fractions [34]. The type of laser emission naturally also influences the size and orientation of grains in polycrystalline additively manufactured parts. Earlier works carried out on alloys such as Inconel 718 [33,34], AlSi10Mg [129], and Ti-6Al-4V (wt.%) [130] report, in particular, the presence of finer and more isotropic, i.e., more randomly oriented, microstructures in components processed using PW.

The few earlier works on PBF-LB/M of IN939 that had been published to date had been carried out using CW laser radiation [94–96,98,100,102,106,108], with the only exception of [76], in which IN939 is not the main focus and is used merely for comparison with other alloys. Some of these studies report the precipitation of $\eta$ or $\gamma'$ phases in the as-built microstructures. The absence of these phases in the PW PBF-LB/M IN939 alloy of the present study is consistent with the faster cooling rates associated to PW laser emission. Also, earlier works carried out with CW laser emission describe the preferential development of columnar structures with <001> directions parallel to BD. Our study reveals that the use of a pulsed laser allows for a significantly greater flexibility in microstructural design in dense IN939 samples. As described above, processing using the two sets of optimized scanning parameters ($h_d70$ and $h_d50$, Figure 4-4), a comparatively large texture variation can already be obtained. In particular, the lower $E_v$ value (51 $J{\cdot}mm^{-3}$) gives rise to a weak texture, with a maximum intensity close to 2, while increasing the $E_v$ (71 $J{\cdot}mm^{-3}$) leads to a clearly defined <001> fiber texture, with a maximum intensity higher than 10.

Indeed, the texture of PW PBF-LB/M IN939 might be widely tuned by altering the $E_v$. Figure 4-12 illustrates, by means of EBSD IPF maps in the BD, as well as by the corresponding {100}, {110}, and {111} direct pole figures, the microstructure and the microtexture of several PW PBF-LB/M IN939 samples as a function of the $E_v$, for $E_v$ values ranging from 33 to 114 $J{\cdot}mm^{-3}$. In the EBSD maps, black lines denote grain boundaries with misorientations larger than 15° and white lines denote grain boundaries with misorientations smaller than 15°. The linear intercepts measured along directions parallel ($LI_l$) and perpendicular to BD ($LI_t$) are also included. It can be seen that, with increasing $E_v$, the microstructure evolves from a randomly oriented aggregate of irregularly shaped grains ($E_v < 51$ $J{\cdot}mm^{-3}$) to a columnar grain structure with a well-defined <001> fiber texture, in which the fiber axis is parallel to BD (51 $J{\cdot}mm^{-3} < E_v < 82$ $J.mm^{-3}$). Further increases of the $E_v$ lead to the development of a strong single component texture, in which the BD is also parallel to a <001> direction. A similar texture evolution with increasing $E_v$ (i.e., from a random to a single component texture) was reported recently for a PBF-LB/M processed Ti-6%Al-4%V (wt.%) alloy in [132] and for cubic polycrystalline alloys processed by PBF-LB/M, including Ni-based superalloys, Ti alloys, Al alloys, 316L steel and its nanocomposites in [133].

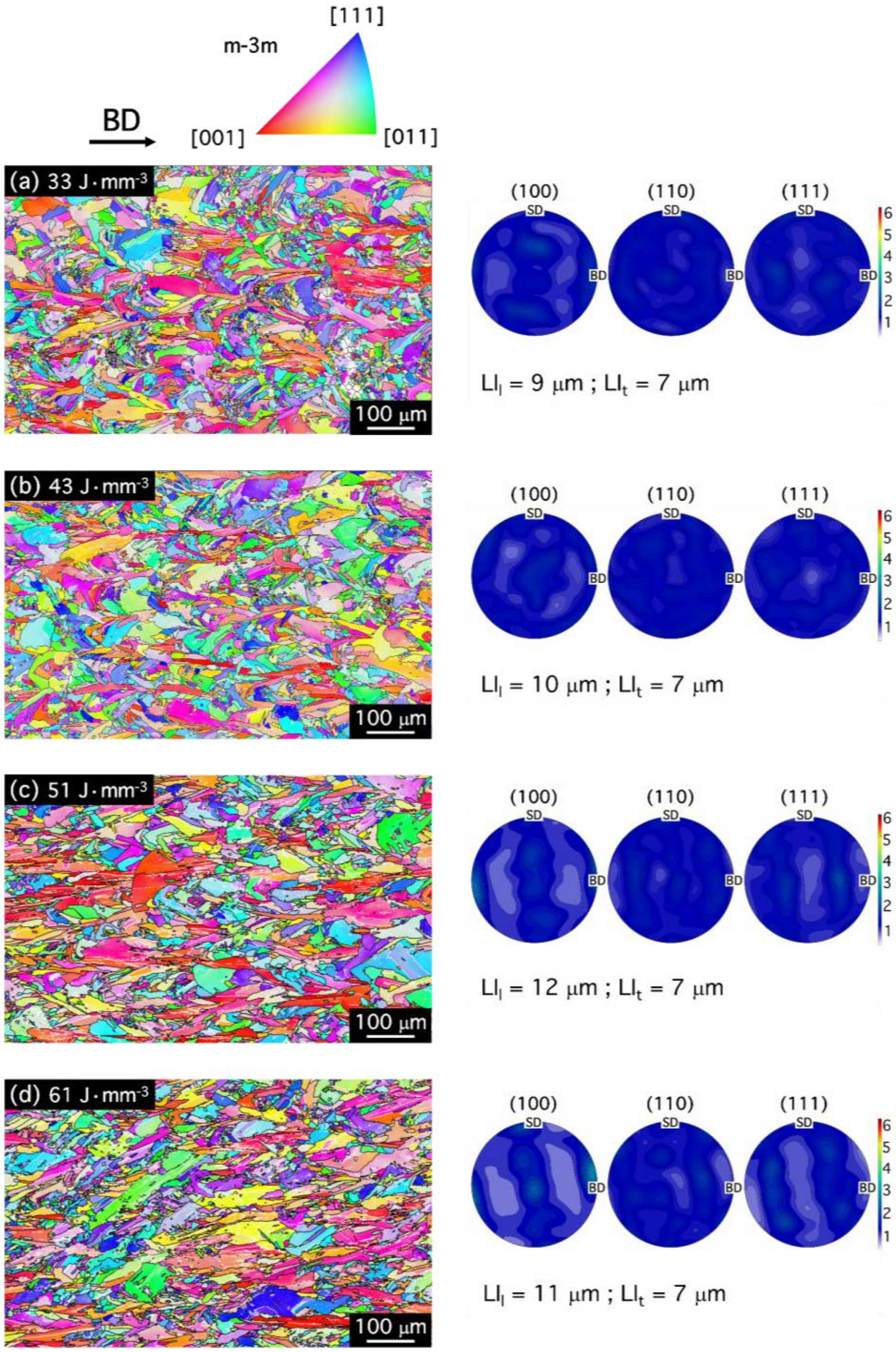

(caption below the next figure)

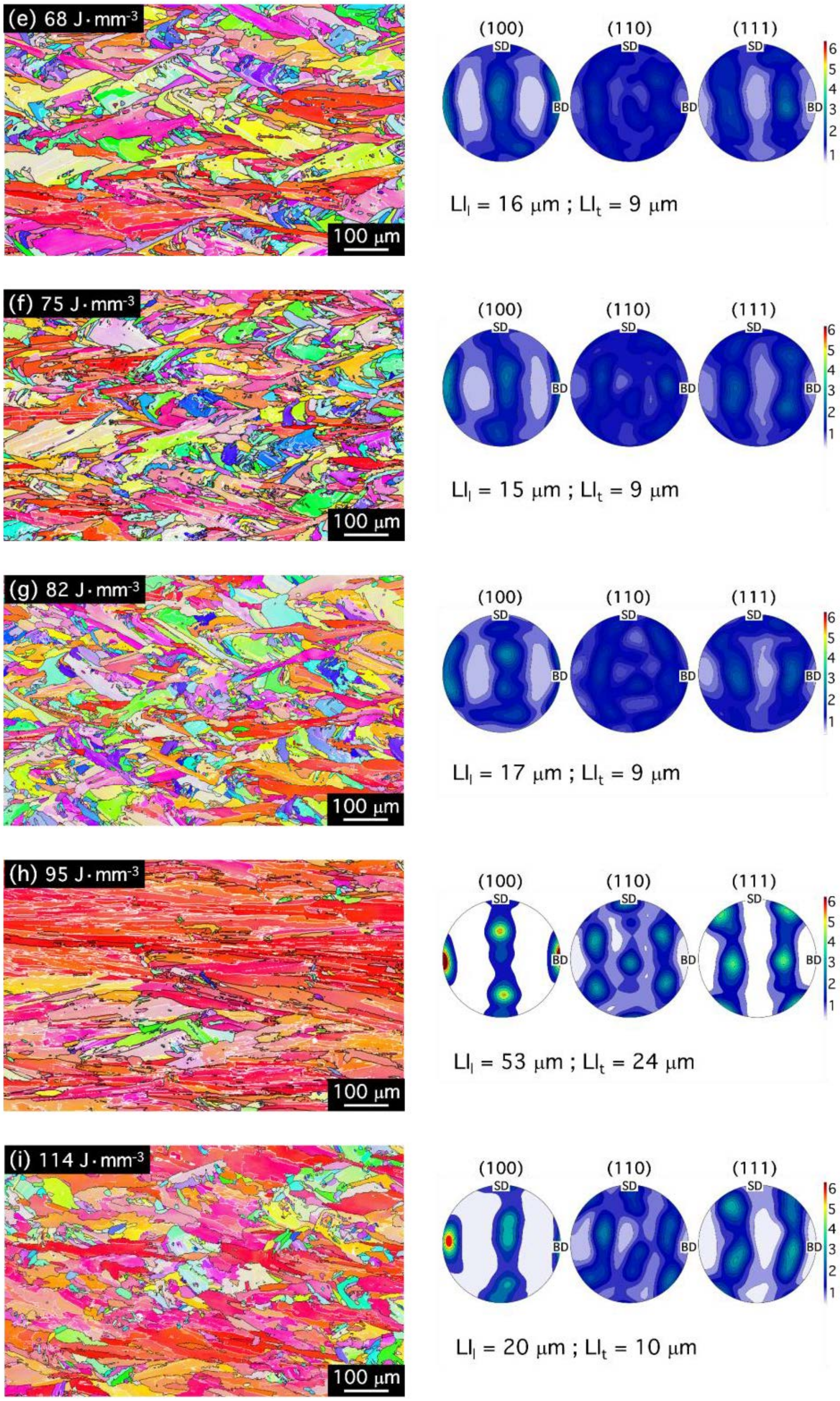

Figure 4-12: Evolution of the texture of PW PBF-LB/M IN939 with $E_v$ values ranging from 33 to 114 J·mm$^{-3}$. For each sample the following representations are included: an inverse pole figure (IPF) map in the BD, which is parallel to the horizontal direction, and the {001}, {110}, and {111} direct pole figures. In the EBSD maps, black lines denote grain boundaries with misorientations larger than 15° and white lines denote grain boundaries with misorientations smaller than 15°. The average line intercept values are also reported for the directions parallel and perpendicular to the building direction ($LI_l$ and $LI_t$ respectively).

### *4.4.2. Mechanical behavior*

Our results show, on the one hand, that the PBF-LB/M IN939 alloy, heat treated using standard conditions, exhibits an enhanced mechanical behavior at T≤ 700°C with respect to cast specimens post-processed with a similar heat treatment. This may be attributed to the finer microstructure of the additively manufactured samples, which thus allow for a stronger Hall-Petch effect [134], which offsets the deleterious effects of a less efficient $\gamma'$ phase distribution. Indeed, the grain size in the PBF-LB/M samples is close to two orders of magnitude smaller than that present in cast specimens [91–93].

On the other hand, at T> 700°C pronounced softening takes place in the PBF-LB/M samples, rendering an inferior mechanical behavior with respect to cast specimens. In order to better understand the origin of the softening observed in the additively manufactured IN939 at T> 700°C, we calculate the strain rate sensitivity ($m$) corresponding to tests carried out in both PBF-LB/M (present study) and cast samples [135] at all the temperatures investigated and under the same strain rate ($\dot{\varepsilon}$) conditions. The value of $m$ is given by the following equation [136]:

$$m = \left(\frac{\partial \ln \sigma}{\partial \ln \dot{\varepsilon}}\right)_{T,\varepsilon} \tag{4.1}$$

where σ is the flow stress at the corresponding strain rate. Figure 4-13 shows the evolution of $m$ as a function of temperature. It can be seen that, in the cast material, $m$ is smaller than 0.1 at all the temperatures investigated. The sensitivity of the additively manufactured material is always higher than that of the cast material and the difference between both values increases with temperature, being particularly pronounced at T> 700°C. The rapid increase in $m_{\text{PBF-LB/M}}$ at high temperatures indicates that diffusion-controlled phenomena play a larger role in the additively manufactured IN939 specimens than in the cast ones [136], thus promoting the observed softening. In particular, grain boundary sliding (GBS) or the sliding of grains assisted by diffusion along their interfaces [137] is likely more pronounced in the PBF-LB/M samples, as the grain boundary area is significantly larger due to the presence of smaller grains. Also, as described earlier, the presence of a coarser precipitate distribution might facilitate the (diffusion-assisted) climb of dislocations over obstacles [136]. Our study, thus, suggests that the high temperature mechanical behavior of the PBF-LB/M IN939 alloy could be greatly improved via the optimization of post-processing heat treatments aimed at both increasing the grain size and at improving the hardening potential of the γ′ precipitate distribution.

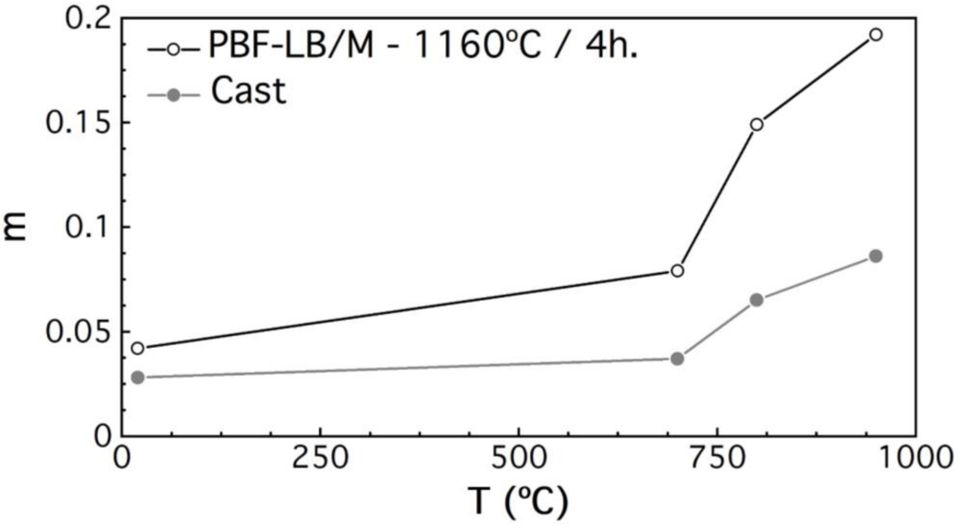

Figure 4-13: Variation of the strain rate sensitivity (m) with temperature for PBF-LB/M and cast IN939.

## 4.5. Conclusions

The aim of this work is to determine the laser powder bed fusion processability window of the fairly weldable IN939 using pulsed laser emission for the first time. The following conclusions have been drawn from this study:

1. An optimum PW PBF-LB/M processing window was found for the production of IN939 samples with densities exceeding 99.5%. In particular, among the specific parameter sets explored in the current study, two were selected as "optimized" conditions, namely $P = 250$ W, $v = 1.167$ m·s$^{-1}$, $h_d = 70$ μm, $E_v = 51$ J·mm$^{-3}$, and $P = 250$ W, $v = 1.167$ m·s$^{-1}$, $h_d = 50$ μm, $E_v = 71$ J·mm$^{-3}$.
2. A relatively large microstructure variation was detected in as-built samples processed within the optimum processability window, allowing for a relatively large degree of flexibility in microstructural design. In particular, processing conditions corresponding to lower $E_v$ values give rise to weakly textured polycrystals, with irregularly shaped grains, while processing conditions corresponding to higher $E_v$ values yield columnar structures with strong <001> fiber textures. This variation is larger than that reported in earlier studies carried out using continuous laser emission.

3. As-built IN939 microstructures contain carbide particles but no γ′ or η phases were detected. The absence of these phases, which were reportedly present in some earlier studies carried out using continuous laser emission, is attributed to the faster cooling rates associated to pulsed laser emission.
4. The room temperature mechanical behavior of PBF-LB/M IN939 samples following a standard heat treatment was found to be stronger than that of cast specimens at T≤ 700°C. This is attributed to a strong Hall-Petch strengthening effect in the additively manufactured samples, whose grain size is close to two orders of magnitude smaller than that of cast specimens. This effect offsets the deleterious effects of a less efficient γ′ phase distribution.
5. The high temperature mechanical behavior of PBF-LB/M IN939 samples following a standard heat treatment was found to be weaker than that of cast specimens at T> 700°C. The strong softening observed within that temperature range is attributed to the higher activation of diffusion-controlled mechanisms including grain boundary sliding, stimulated by the presence of a large grain boundary area, as well as climb-controlled surpassing of obstacles by dislocations.

# 5. IMPROVING THE PRINTABILITY OF THIN WALLS

## 5.1. Background

In the previous chapter we investigated the processability of simple, bulk geometries. However, the inherent design flexibility of laser powder bed fusion (PBF-LB/M) renders it most interesting for the fabrication of geometries not achievable otherwise [138,139]. This is particularly important for the manufacture of thin-wall sections (thickness <1 mm) for cooling channels, heat exchangers, or lattice structures, amongst other applications. Additive manufacturing (AM) of thin sections (compared to bulkier parts) presents some additional challenges associated to heat accumulation, geometrical accuracy, or the presence of residual stresses [51,100,140–145]. Studies on thin-wall structures in the existing literature focus mainly on manufacturability limits in terms of thickness [140,141], on defectology [142,143], on surface quality [51,100], or on mechanical properties [100,144,145]. Further efforts are needed to gain a deep understanding of the relationship between the processing parameters and, more specifically, the scanning strategy, and the resulting microstructure, as this would contribute to enhance thin wall performance.

Obtaining a good surface quality is important for most additively manufactured components, but it is crucial in thin walls, given the difficulty of applying post-processing steps such as surface grinding, polishing, or machining in internal cooling channels or in complex lattice structures [146]. A common method to improve surface quality of bulk parts and thin walls consists of adding one or more contour or border scans following hatching. Several studies have analyzed the effect of border scans on the surface roughness [51], on the residual stress distribution [51,147–149], as well as on the mechanical properties [147–149] of additively manufactured parts. A few works in the literature have compared the effect of printing the border scans before or after the hatch or infill scans (pre- and post-contouring, respectively) during PBF-LB/M of bulk parts. Ren et al. [150] investigated the influence of the contour scan sequence on the surface roughness of a copper alloy, reporting that pre-contouring led to a smaller roughness. Artzt et al. [51] described the effect of the number and order of contour scans on residual stresses and surface roughness in a Ti-6Al-4V (wt.%) alloy, concluding that a pre-contour strategy results in the best compromise between the two properties studied. Finally, Reiber et al. [151] also showed how a pre-contour scan is more suitable to improve surface quality and to reduce subsurface porosity in Scalmalloy. The influence of pre-contouring on the texture, as well as on the grain and melt pool structure of thin walls remains underexplored. To the best of our knowledge, no studies have, in particular, tackled this problem in the Inconel 939 (IN939) Ni-based superalloy.

In this chapter we analyze the effect of pre-contouring on the printability of IN939 thin-wall structures of different thicknesses fabricated by PBF-LB/M. Microstructural features such as the texture, the grain size and shape, and the melt pool depth are discussed. This study provides guidelines for improving the fabrication of thin sections.

## 5.2. Methods

PBF-LB/M was performed using the setup previously described, with a reduced build volume (RBV) platform (Figure 5-1a). Several samples with external dimensions 10x10x10 mm$^3$ and containing thin walls with thicknesses of 500, 700, 900, 1100, 1300, and 1500 μm (Figure 5-1b) were printed using the two different scanning strategies. In the first one (Figure 5-1c), manufacturing of the hatch region was followed by two contour passes. This strategy constitutes the baseline of this study and will be referred to as *post-contouring*. In the second strategy (Figure 5-1d) a border pass is added prior to the manufacturing of the hatch and the two "post-hatch" contours. This strategy will be termed *pre-contouring*. The contour scans were always manufactured using a laser power (P) of 175 W, a scanning speed (v) of 750 mm·s$^{-1}$, a contour distance (distance between adjacent contour passes) of 45 μm (Figure 5-1e), and an offset (overlap between the contour and the hatch) of 30 μm (Figure 5-1e). The hatch was printed using the two parameter sets within the optimum processability window for IN939 bulk samples, $h_d50$ and $h_d70$ (see Chapter 4), in order to analyze the influence of post- and pre-contouring on two hatch microstructures. As a reminder, the two parameter sets were $h_d50$ (P = 250 W, v = 1.167 m·s$^{-1}$, $h_d$ = 50 μm), which gave rise in bulk samples to a columnar microstructure with a <001> fiber texture, and $h_d70$ (P = 250 W, v = 1.167 m·s$^{-1}$, and $h_d$ = 70 μm), which generated in bulk samples a weakly textured polycrystal with irregularly shaped grains. XZ cross-sections of the printed samples (Figure 5-1b) were prepared using standard metallographic techniques and they were characterized by optical microscopy (OM) and by electron backscattered diffraction (EBSD), as specified in Section 3.3.2. The conditions for EBSD mapping were 20 kV, 3.2 nA, and a step size of 1 μm. The dimensions of the melt pools corresponding to different printing conditions were measured through OM of etched samples, considering only the melt pools of the last layer.

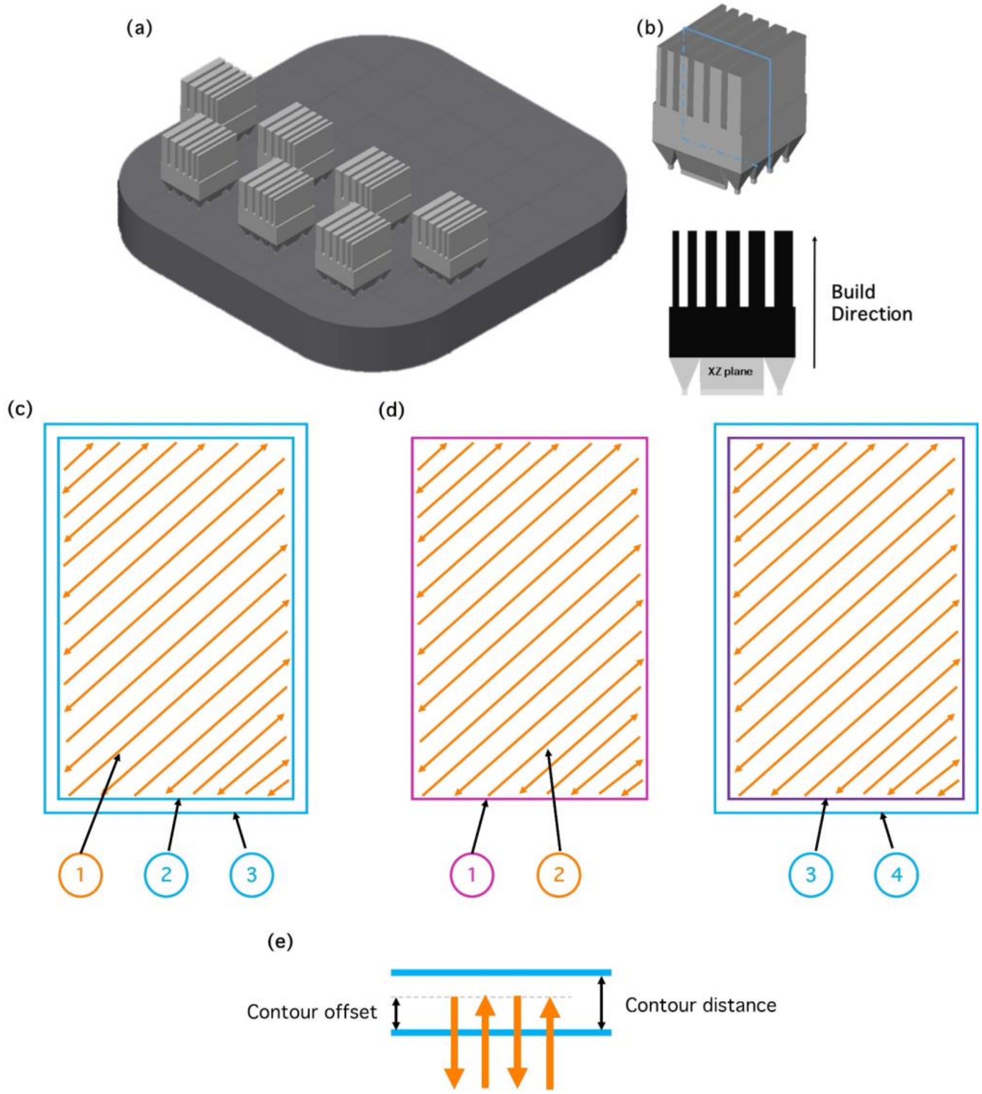

Figure 5-1: (a) Distribution of the samples on the reduced build volume (RBV) substrate; (b) schematic showing the XZ cross-section of printed samples; (c) post-contour, and (d) pre-contour scanning strategies, where the scanning sequence is specified using numbers; (e) illustration of the contour distance and contour offset.

## 5.3. Results and discussion

The addition of a pre-contour had only a moderate influence in the texture, for all section thicknesses investigated. Figure 5-2 shows the EBSD inverse pole figure (IPF) maps in the build direction (BD) for samples of all the investigated thicknesses printed using the following parameter sets and scanning strategies: $h_d50$, post-contour (Figure 5-2a), $h_d50$, pre-contour (Figure 5-2b), $h_d70$, post-contour (Figure 5-2c), and $h_d70$, pre-contour (Figure 5-2d). In all cases the microstructure in the border regions is populated by relatively equiaxed and weakly oriented grains, while the center regions are formed by columnar grains with a <001> fiber texture (<001> crystallographic direction parallel to BD, <001>//BD), in agreement with earlier studies on IN939 thin walls [100]. The remainder of this study will focus on the center regions. The maximum intensity of the IPFs in the center regions (Figure 5-2), which ranges from 8.9 to 19.4 for $h_d50$ samples and from 6.4 to 13.6 for the $h_d70$ specimens, is significantly higher than that reported in Chapter 4 for bulk samples processed using the same scanning parameter sets, which amounted to 7.3 ($h_d50$) and 2.5 ($h_d70$), respectively. The strongly textured and columnar nature of the microstructure in thin sections can be attributed to enhanced epitaxial growth due to heat accumulation and to the directionality of its dissipation [149].

Figure 5-3a illustrates the influence of the section thickness and of the scanning strategy on the volume fraction of grains in the center regions oriented with a <001> crystallographic direction within 15° of the BD. The volume fraction calculation was performed by integrating the corresponding maximum of the orientation distribution function. The graph on the left-hand side illustrates the average values corresponding to all the samples investigated, while the plots on the right-hand side show average data corresponding to $h_d50$ (top) or to $h_d70$ (bottom) samples. The volume fraction of oriented grains in post-contour samples increases with decreasing thickness for the two hatch distances investigated, as reported earlier for Rene 108 [143] and IN939 [100] thin sections. However, this trend is not as clear in the samples manufactured with a pre-contour strategy, where the presence of the first border pass would result in a lower directionality of heat dissipation. In any case, the influence of the addition of a pre-contour pass on the fraction of <001>//BD oriented grains is relatively small.

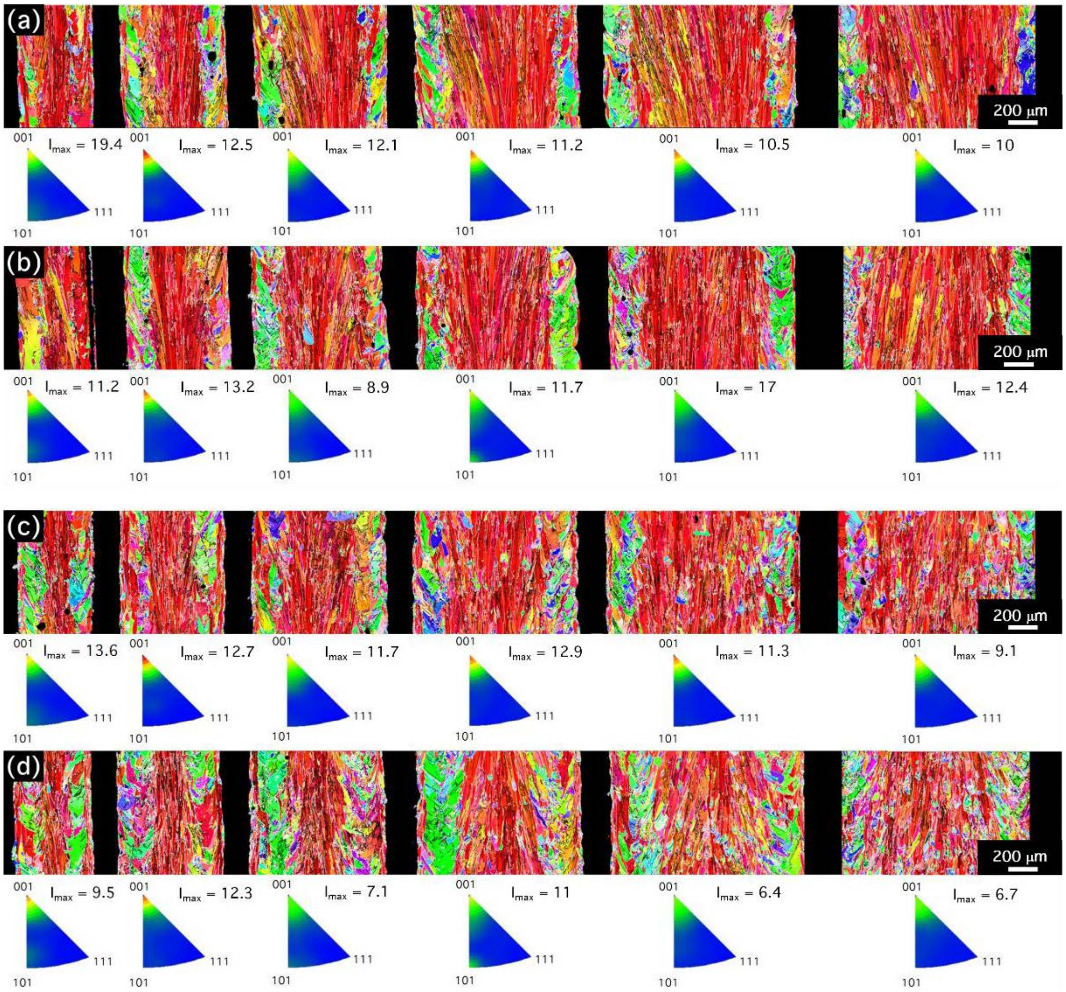

Figure 5-2: IPF EBSD maps in the BD and inverse pole figures corresponding to the center regions of thin sections printed using the following hatch distances and scanning strategies: (a) $h_d50$, post-contour; (b) $h_d50$, pre-contour; (c) $h_d70$, post-contour; (d) $h_d70$, pre-contour.

The effect of pre-contouring on the grain shape and aspect ratio is also modest irrespective of the section thickness. Figure 5-4 illustrates the longitudinal ($LI_l$) and transverse ($LI_t$) average line intercepts, and Figure 5-5 shows the line intercept ratios (LIR) in the center region for all the investigated samples. $h_d50$ specimens consistently present longer and wider grains than $h_d70$ samples. Irrespective of the thickness and contour scanning strategy, the average LIR is always higher than 2. In $h_d50$ samples the LIR increases with increasing thickness, while in $h_d70$ samples LIR does not change significantly with thickness. Bulk samples printed using the same process parameter sets have the following grain sizes and aspect ratios: $h_d50$ ($LI_l$ = 36 μm, $LI_t$ = 16 μm, LIR = 2.25), $h_d70$ ($LI_l$ = 13 μm, $LI_t$ = 9 μm, LIR = 1.4), reported in Section 4.3.2. All thin sections possess more elongated and wider grains than their bulk counterparts, the differences being particularly pronounced for $h_d70$

samples. The addition of a pre-contour scan results in a slight reduction in both grain size and aspect ratio for most section thicknesses and processing conditions ($h_d$*50* or $h_d$*70*).

However, the addition of a pre-contour scan does have a significant effect on the melt pool depth (*d*). Figure 5-6 depicts the influence of the scanning strategy on the melt pool depth for all the wall thicknesses and processing conditions investigated. Irrespective of the hatch distance and of the scanning strategy, a decrease in thickness leads to an increase in *d*, and such dependency can be attributed to the heat accumulation in thinner parts as reported in [142,152]. For all the conditions shown here, the melt pool size is significantly larger than that of IN939 bulk samples, where *d*~138 μm for both $h_d$*50* and $h_d$*70* conditions. The introduction of a pre-contour leads to a clear decrease in *d* irrespective of the thickness and of the processing conditions ($h_d$*50* or $h_d$*70*).

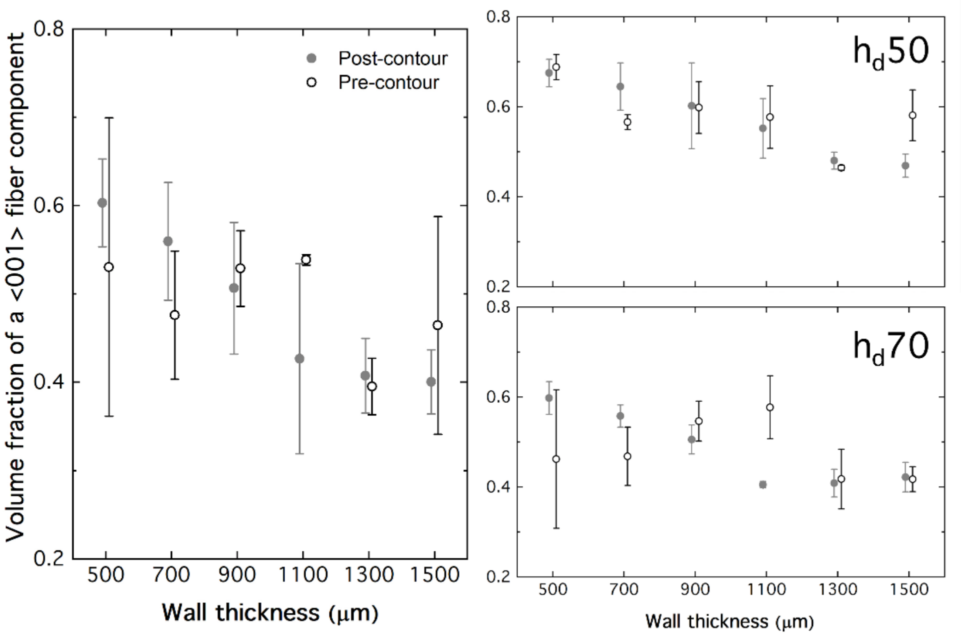

Figure 5-3: Volume fraction of crystallites in the center region that are oriented with BD within 15º of the <001> direction. The large graph on the left-hand side illustrates the average values corresponding to all the samples investigated, while the smaller plots on the right-hand side show separately the average values corresponding to samples manufactured with $h_d$*50* (top) and $h_d$*70* (bottom). Full symbols correspond to samples manufactured with post-contour, and empty symbols correspond to samples manufactured using a pre-contour strategy.

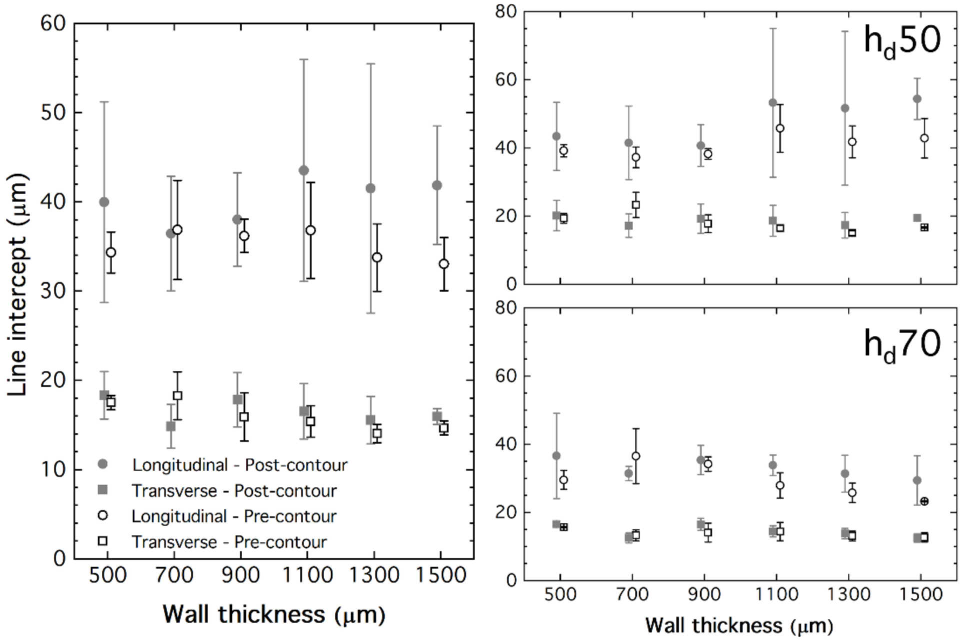

Figure 5-4: Average line intercepts along the longitudinal and transverse directions in the center region. The large graph on the left-hand side illustrates the average values corresponding to all the samples investigated, while the smaller plots on the right-hand side show separately the average values corresponding to samples manufactured with *h*$_d$*50* (top) and *h*$_d$*70* (bottom). Full symbols correspond to samples manufactured with post-contour, and empty symbols correspond to samples manufactured using a pre-contour strategy.

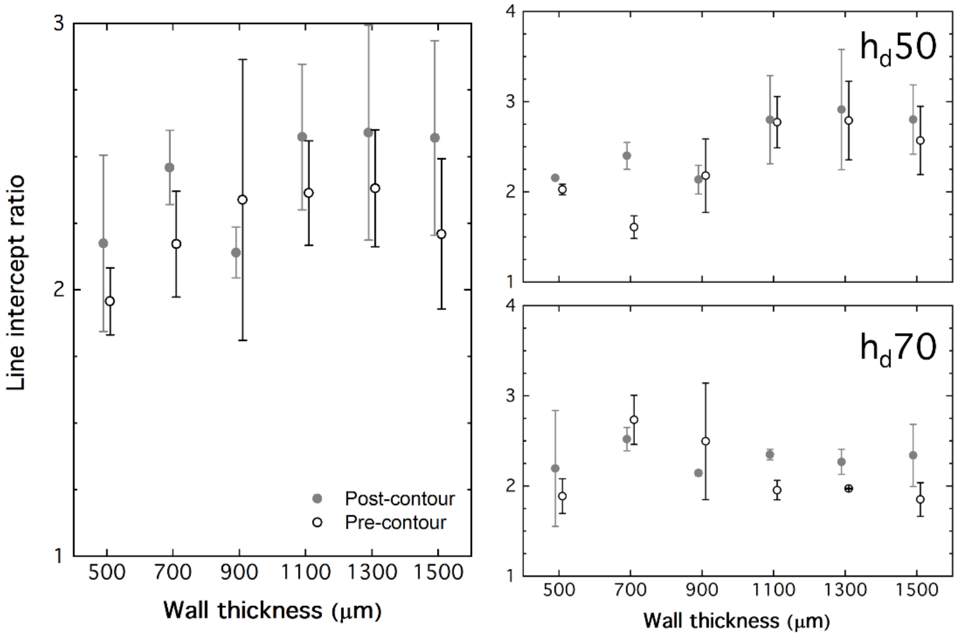

Figure 5-5: Average line intercept ratio in the center region. The large graph on the left-hand side illustrates the average values corresponding to all the samples investigated, while the smaller plots on the right-hand side show separately the average values corresponding to samples manufactured with *h*$_d$*50* (top) and *h*$_d$*70* (bottom). Full symbols correspond to samples manufactured with post-contour, and empty symbols correspond to samples manufactured using a pre-contour strategy.

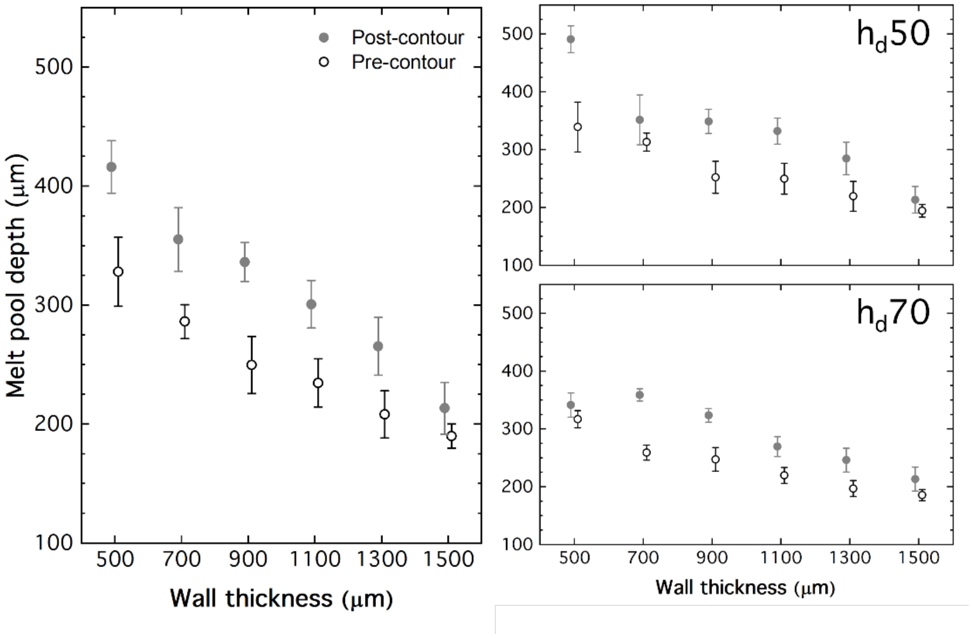

Figure 5-6: Variation of the average melt pool depth with wall thickness. The large graph on the left-hand side illustrates the average values corresponding to all the samples investigated, while the smaller plots on the right-hand side show separately the average values corresponding to samples manufactured with *h<sub>d</sub>50* (top) or *h<sub>d</sub>70* (bottom). Full symbols correspond to samples manufactured with post-contour, and empty symbols correspond to samples manufactured using a pre-contour strategy.

Zagade et al. [62] recently proposed the following expression (Eq. 5.1) to relate the normalized melt pool depth ($d/\omega$, where $\omega$ is the laser beam radius) to the normalized enthalpy ($\Delta H/h_s$, where $h_s$ is the enthalpy of melting) [21,60,61], which gives a measure of the balance between the input and dissipated energies:

$$\frac{d}{\omega} = 0.08\left(\frac{\Delta H}{h_s}\right)^{1.4} = 0.08\left(\frac{AP(\omega/v)}{\pi\omega^2\sqrt{\alpha(\omega/v)}}\cdot\frac{1}{\rho C T_s}\right)^{1.4} \qquad (5.1).$$

Equation 5.1 includes both material properties such as $A$, the absorptivity, $\alpha$, the thermal diffusivity, $\rho$, the density, $C$, the specific heat, and $T_s$, the solidus temperature, as well as processing parameters such as $P$ and $v$. The constants 0.08 and 1.4 were obtained by fitting a large number of experimental data from alloys Ti-6Al-4V (wt.%), AlSi10Mg (wt.%), and SS316 by the least squares method [62]. Here, we utilize equation 5.1 to calculate $\Delta H/h_s$ from the melt pool dimensions corresponding to the investigated thin sections and the results are plotted in Figure 5-7a-d. The IN939 thermal properties were taken from [107]. For reference, the data points corresponding to $h_d50$ and $h_d70$ manufacturing conditions in IN939 bulk samples (in both cases $\Delta H/h_s \approx 29.4$ as for both conditions $d$~138 μm), are represented by star symbols in Figure 5-7a-d. Incidentally, this $\Delta H/h_s$ value is very similar to that corresponding to the threshold for the transition between the conduction and keyhole welding modes in 316L steel ($\Delta H/h_s \approx 30 \pm 4$) [21], red gold ($\Delta H/h_s \approx 28.31$) [61], and bronze ($\Delta H/h_s \approx 27.34$) [61]. This threshold value is, in general, regarded as the optimum processability condition. Thus, we can assume that the threshold between the conduction and keyhole modes in the IN939 alloy investigated here is close to 29.4 (star symbol). As shown in Figure 5-7a and 5-7b, for the thin walls investigated here the $h_d50$ and $h_d70$ processing conditions fall clearly within the keyhole mode regime. Also, irrespective of the processing conditions ($h_d50$ or $h_d70$), reducing the wall thickness results in a shift along the $d/\omega$ vs. $\Delta H/h_s$ curve towards higher $\Delta H/h_s$ values.

On the other hand, as described earlier (Figure 5-6), introducing a pre-contour leads to a reduction in $d/\omega$, and thus to a decrease in $\Delta H/h_s$. That is, the presence of solidified material along the border regions as a consequence of the pre-contour pass enables further avenues for heat dissipation, leading to a shift along the $d/\omega$ vs. $\Delta H/h_s$ curve towards the conduction regime (Figure 5-7c and Figure 5-7d). In agreement with this, as an example, Figure 5-8 compares the transition in melt pool shape in areas close to the border in 700 μm walls printed using the $h_d70$ parameter set and post- (Figure 5-8a) and pre-contouring (Figure 5-8b). In the absence of the pre-contour scan, teardrop-like melt pools, with a tendency to exhibit keyhole porosity, develop. However, pre-contouring results in rounder, pore-free melt pools in the hatch scanning point exposure closest to the surface. Overall porosity is reduced by an average of 0.3 % from post- to pre-contour scans, reaching a relative density of 99.6 ± 0.1 % for pre-contour samples. The same effect has been observed for all the range of wall thicknesses investigated. Figure 5-7e illustrates the magnitude of the reduction in melt pool depth and in $\Delta H/h_s$ due to pre-contouring as a function of wall thickness. The effect becomes, as expected, more pronounced as the wall thickness decreases, as the ratio between the volume of the pre-manufactured border pass and that of the hatch becomes larger. For a given wall thickness $t$ the ratio between the melt pool depth for pre- and post-contour samples, calculated from equation 5.1, can be expressed as the ratio between the thermal diffusivity values shown below:

$$\left(\frac{d_{pre-contour}}{d_{post-contour}}\right)_i = \left(\frac{\alpha_{post-contour}}{\alpha_{pre-contour}}\right)_i^{0.7} \qquad (5.2).$$

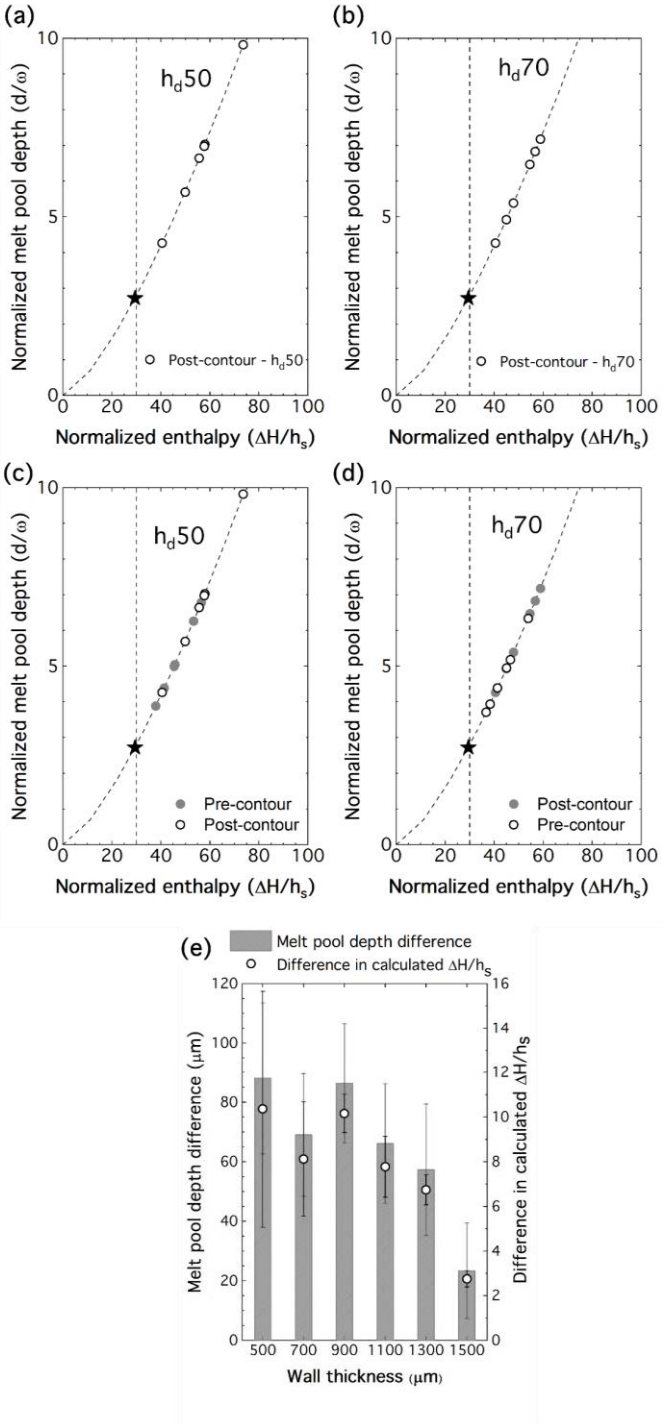

Figure 5-7: Normalized melt pool depth as a function of normalized enthalpy for: (a) $h_d50$, post-contour; (b) $h_d70$, post-contour; (c) $h_d50$, post- and pre-contour; (d) $h_d70$, post- and pre-contour. The star symbol represents the $h_d50$ and $h_d70$ data for bulk IN939 samples (~29.4) [99], which is regarded as the transition between the conduction and the keyhole modes. The labels indicate the wall thicknesses in μm. (e) Effect of pre-contouring on the melt pool depth and on the normalized enthalpy as a function of wall thickness. The differences in normalized enthalpy are calculated from the regression curves (a-d).

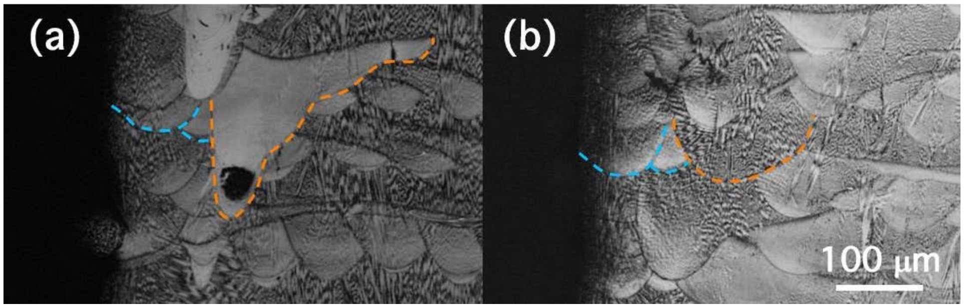

Figure 5-8: Optical micrographs illustrating the melt pool morphology in the area close to the border of 700 µm walls printed using the $h_d70$ parameter set with (a) post-contouring and (b) pre-contouring. Blue dashed lines indicate contour scans, while orange dashed lines indicate hatch (or in-fill) scans.

The mechanism through which the pre-contour scan enhances the overall thermal diffusivity of thin sections has been illustrated in Figure 5-9, where we show how the previously solidified material offers an additional support for heat dissipation (Figure 5-9e).

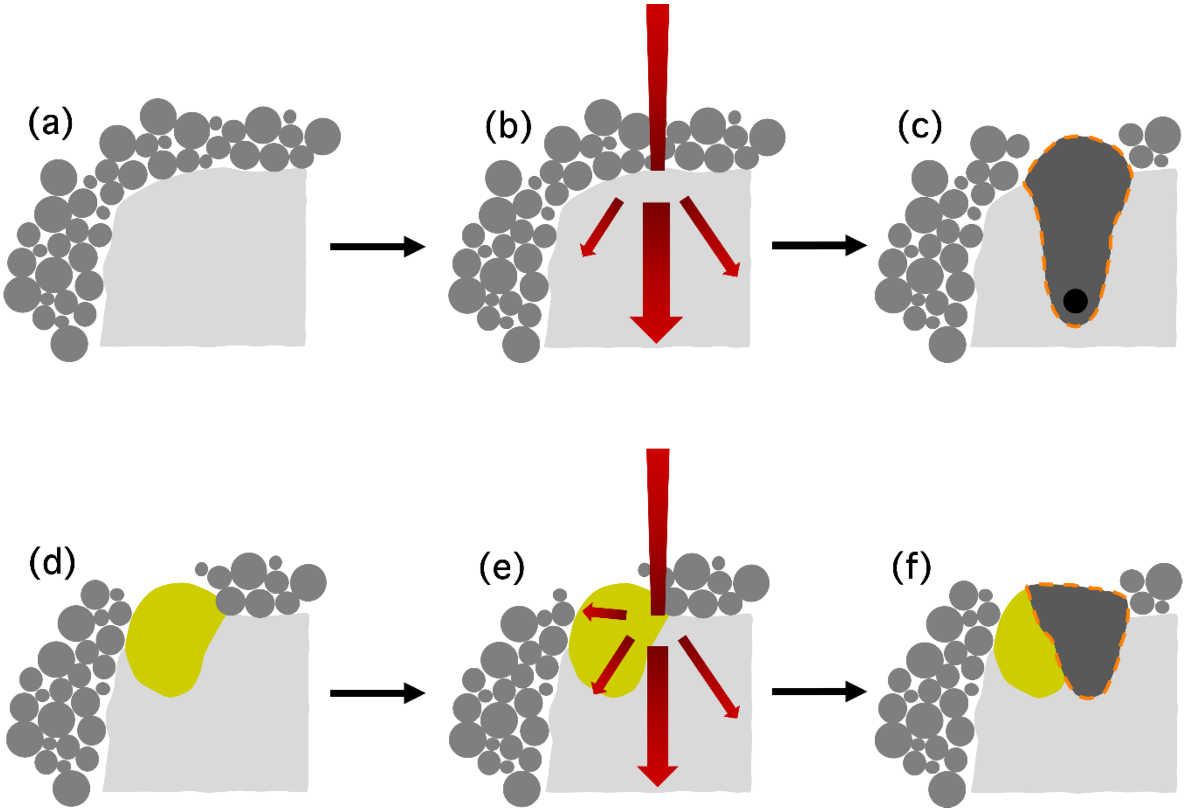

Figure 5-9: Schematics of the melt process for a point exposure in the hatch region close to the surface of the sample. (a), (b), and (c) correspond to the post-contour strategy, and (d), (e), and (f) correspond to the pre-contour strategy. In (d), the yellow shape represents the melt pool of the pre-contour scan. The red arrows in (b), and (e) represent the direction of heat dissipation.

## 5.4. Conclusions

This work investigates the influence of the addition of a border scan prior to hatching (pre-contouring) on the printability of IN939 thin walls with thicknesses ranging from 500 to 1500 μm. In particular, the effect on the texture, the grain shape, and the melt pool structure are investigated for two processing conditions that gave rise to different microstructures and high density values in bulk samples ($h_d50$ and $h_d70$, Section 4.3.2). The following conclusions can be drawn from this chapter:

1. Irrespective of the wall thickness the border regions are populated by relatively equiaxed and weakly oriented grains, while the center regions are formed by columnar grains with a <001>//BD fiber texture, whose intensity is higher than that present in bulk samples manufactured using the same processing conditions.
2. The introduction of a pre-contour scan has only a moderate influence on the texture or on the grain size and shape, for all the wall thicknesses investigated.
3. Pre-contouring leads to a significant decrease of the melt pool depth, an effect that is amplified with decreasing wall thickness. The extra solidified material along the border regions resulting from the pre-contour scan facilitates heat dissipation, partially compensating for the reduced heat dissipation inherent to thin sections, thereby shifting the normalized enthalpy towards lower values for a given set of scanning parameters, not only reducing melt pool depth, but also keyhole porosity.
4. Pre-contouring constitutes a useful tool to improve the processability of IN939 thin-wall structures via PBF-LB/M and it is anticipated that the beneficial effect of this choice of scanning strategy could be extended to improve the PBF-LB/M processability of thin walls in other alloy systems.

# 6. INFLUENCE OF AS-BUILT MICROSTRUCTURE ON RECRYSTALLIZATION

## 6.1. Background

Post-processing thermal treatment of precipitation-strengthened Ni-based superalloys is a crucial step in the production of final components for application in demanding environments. The thermal treatment conditions will determine the nature, volume fraction, size, and morphology of the precipitates, as well as the final grain size [153]. These are of utmost importance to achieve the desired mechanical response at high temperatures, where good creep resistance is a must. After many years of development, the optimum thermal treatment steps for legacy alloys manufactured through traditional routes have been well established [5,90]. However, the unique and metastable nature of PBF-LB/M microstructures calls for a redesigning of the standard thermal treatment schedule in order to achieve satisfactory properties.

According to classic physical metallurgy literature, in order for recrystallization to take place, the material needs to have a certain amount of stored energy, traditionally achieved through plastic deformation [154]. However, additively manufactured parts are intended to be net-shape (or at least near-net-shape), and therefore deformation is not an option to introduce dislocations. Fortunately, the extreme cooling rates and the repeated heating and cooling cycles the material undergoes during fabrication result in a metastable microstructure, with a high density of dislocations in the AB state [155]. This has been proven sufficient to induce recrystallization upon thermal treatment, albeit with certain difficulties [156,157]. One major challenge with PBF-LB/M parts is their slower recrystallization kinetics (i.e. higher recrystallization temperatures), which are generally attributed to solute segregation at the cell boundaries [156–159] or to Zener pinning of precipitates present in the AB state [160–163].

IN939 is no exception to the aforementioned difficulties regarding the onset of recrystallization, and studies on the thermal treatment of PBF-LB/M IN939 parts have been highlighted in Section 2.4.2. PBF-LB/M of IN939. The need of a solution treatment is agreed upon, not only because it will prevent the appearance of detrimental η precipitates in the final parts [102], but also because it can induce recrystallization and grain growth, necessary for good creep performance [117,164]. Many different solution treatments have been suggested, with no clear consensus on what the appropriate schedule is in order to achieve full recrystallization and grain growth [94,102,103,105,113–115]. There is, thus, a clear need to understand the influence of the AB microstructure on the recrystallization kinetics of PBF-LB/M, in a way that will allow the establishment of an appropriate solution treatment.

In this chapter, we show the different evolution of two distinct AB microstructures upon solution treatment, elucidating the driving mechanisms and the key microstructural aspects that induce (or stall) recrystallization and grain growth.

### 6.2. Methods

The samples printed for this part are 10 x 10 x 10 mm$^3$ cubes, with inverted pyramid supports (Figure 6-1a). The cubes were printed in two levels, as shown in Figure 6-1b, to obtain a larger number of samples per print, and to assess possible influences of print height on the microstructure. In order to induce two distinct initial microstructures while keeping near-full density, we used the optimized scanning parameter sets $h_d50$ and $h_d70$ (Section 4.3.2), with a standard meander scanning strategy and 67º rotation between layers. As a reminder, the laser power is set to 250 W, the point distance to 70 μm, and the exposure time to 50 μs ($v = 1.167\ m \cdot s^{-1}$).

The thermal treatments were performed in a Naberthem 3000 vacuum furnace. A total of 9 different solution treatment conditions were performed, 1, 4, and 8 h at 1100ºC, 1150ºC, and 1200ºC. The temperature-time plots for all thermal treatments are shown in Figure 6-1c. The data corresponds to the actual treatments and was acquired with the help of a type S thermocouple (Naberthem) placed inside the vacuum furnace in the vicinity of the samples. Due to certain limitations in the setup, the heating rate was limited to 4.5ºC$\cdot$min$^{-1}$, and the cooling rate to 2.5ºC$\cdot$min$^{-1}$ (from the solution temperature down to ~600ºC, when the cooling rate slows down). This furnace was chosen to perform the treatments given the possibility of working under vacuum conditions to avoid any influence of oxidation, and due to the reliability of the time and temperature control as compared to other available systems. However, it must be mentioned that the cooling rates are insufficient to induce the desired precipitate distributions.

In that sense, once a desirable recrystallization state was identified, 55 x 12 x 12 mm$^3$ blanks were printed using the $h_d70$ scanning parameter set and a stripes scanning strategy, in the same way as in Section 4.2. These tensile blanks were submitted to a solution treatment, followed by a two-step ageing (1000ºC for 6 h, 800ºC for 4 h), performed in a Carbolite CWF 1300 chamber furnace (Carbolite Gero Ltd.). After each of the treatment steps in the muffle furnace, the samples were air cooled, leading to a much faster cooling rate as compared to the vacuum furnace, and to a more convenient precipitate distribution.

The microstructure of both as-built and heat-treated cubes, as well as that of the thermally treated tensile blanks, was thoroughly characterized. Different XZ cross-sections were cut and polished according to the procedures described in Section 3.3.

Large EBSD maps shown in this study were acquired using a step size of 1 μm, a beam current of 3.2 nA, and an acceleration voltage of 20 kV. A minimum of 4 areas (1.1 x 0.7 $mm^2$) were characterized for each condition in order to get representative information. Additional smaller area EBSD maps were acquired in the AB condition for both microstructures, with a reduced step size of 0.1 μm to obtain more accurate data regarding geometrically necessary dislocation (GND) density. To evaluate precipitate size, shape, and distribution using SEM, the surface of the samples was electrochemically etched using the procedure described in Section 3.3.2.1. Additionally, lamellae from both AB cubes and from the thermally treated tensile blanks were prepared following the methodology described in Section 3.3.2.4 for more detailed characterization of precipitate sizes and nature.

The mechanical behavior of the PBF-LB/M IN939 samples after the full thermal treatment (1200ºC/8 h., 1000ºC/6 h., 800ºC/4 h.) was assessed in tension, with cylindrical samples (22 mm gauge length and 4 mm diameter – Figure 3-3) machined out of blanks. Tensile tests were performed at 23ºC, 700ºC, 800ºC, and 950ºC, according to ASTM E8 and E21 standards.

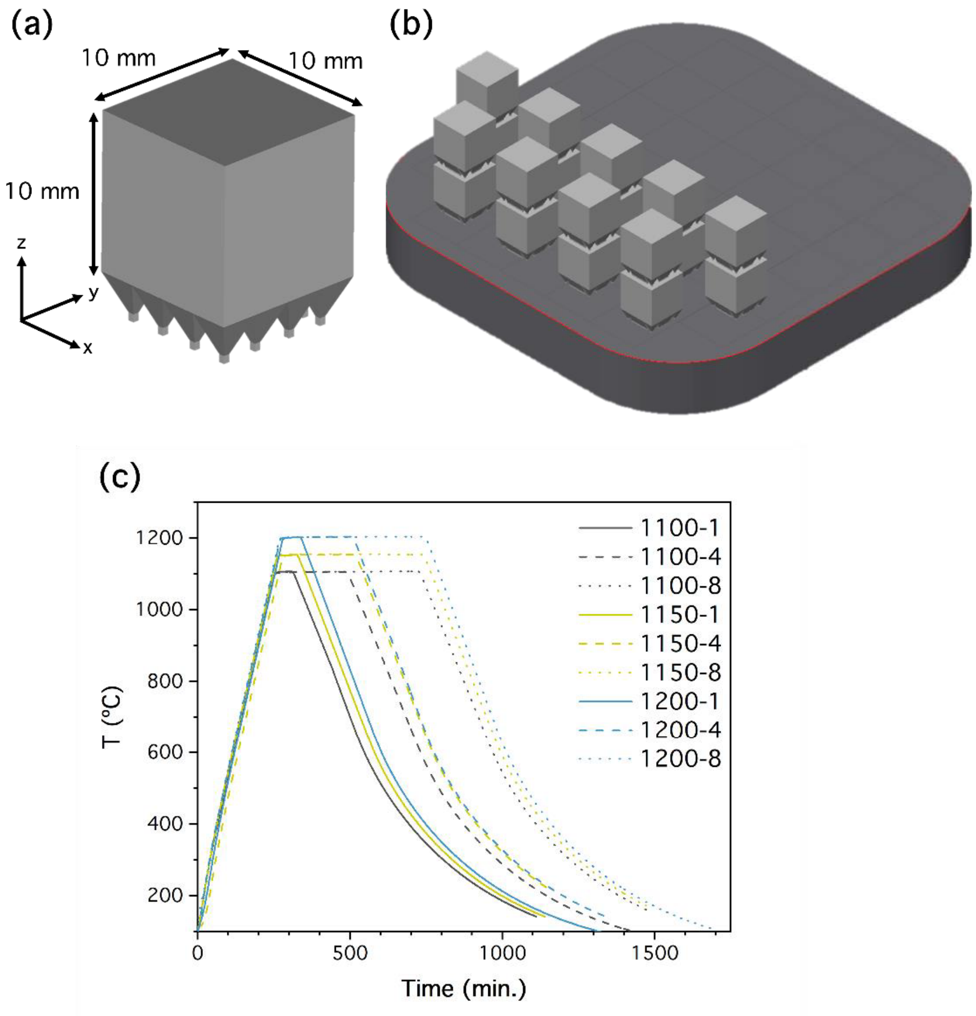

Figure 6-1: (a) Cubes fabricated for this study. (b) Distribution of the cubes on the reduced build volume (RVB); a second layer of cubes is printed on top of the first one to assess the potential effect of part-stacking on defects and microstructure. (c) Temperature profiles for all 9 thermal treatment conditions, acquired with a thermocouple placed next to the treated samples inside the vacuum furnace.

## 6.3. Results

### *6.3.1. As-built microstructure*

Figure 6-2 illustrates the microstructure and the microtexture of $h_d50$ and $h_d70$ samples. Figure 6-2a and 6-2c, in particular, show, respectively, the IPF EBSD maps in the BD, while Figs. 6-2b and 6-2d present the corresponding (100), (110), and (111) pole figures. In agreement with Figure 4-4, $h_d50$ samples show a large fraction of columnar grains oriented with a <001> direction parallel to the BD (<001>//BD). The volume fraction of the <001>//BD component (defined as orientations within 15º of the ideal fiber and calculated from the orientation distribution function (ODF)), is 0.31 ± 0.01. In contrast, the $h_d70$

processing condition yields a polycrystal with more equiaxed and randomly oriented grains. In this case, the <001>//BD volume fraction is reduced to 0.16 ± 0.02, indicating that increasing the hatch distance by 20 µm nearly halves the fiber texture component.

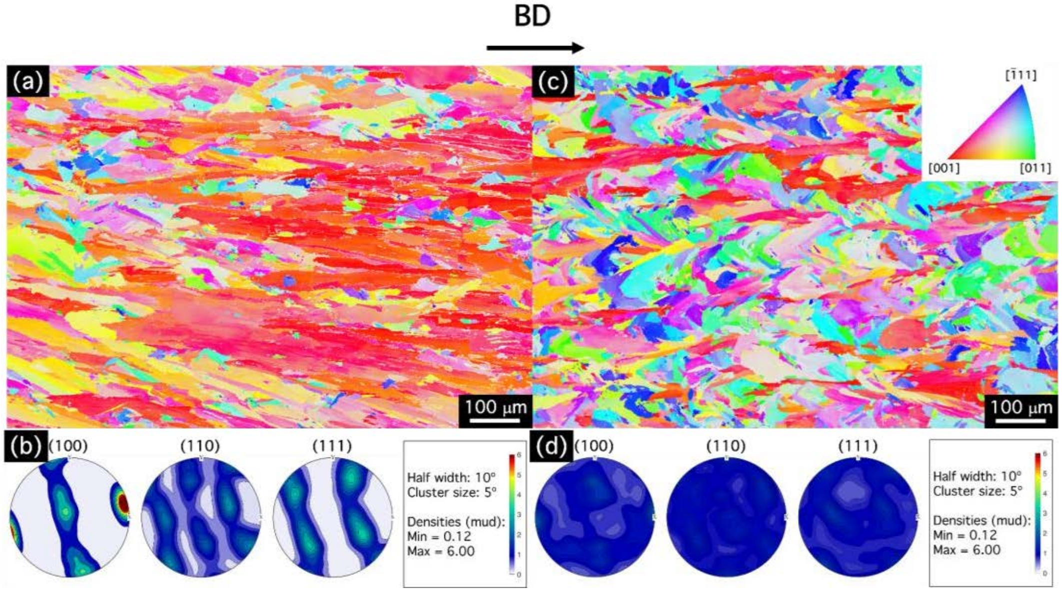

Figure 6-2: (a, c) IPF coloring EBSD maps in the build direction, and (b, d) pole figures for $h_d50$ (a, b), and $h_d70$ (c, d) samples in the as-built state.

The differences in grain shape and size can be more clearly seen in the corresponding grain boundary maps (Figure 6-3a for $h_d50$, Figure 6-3b for $h_d70$). High angle grain boundaries (HAGB, θ>15º) are shown in black, low angle boundaries (LAGB, $\theta \in 2\text{-}15º$) in light blue, and Σ3 twin boundaries (TB) in red. The grains in $h_d50$ are larger in size than those in $h_d70$, with longitudinal line intercepts (LI$_l$) of 22.9 and 13.6 µm, respectively. The columnar nature of $h_d50$ is further supported by its average aspect ratio (AR) of 2.2, compared to 1.5 for $h_d70$. Figure 6-3c presents the misorientation angle distribution for both cases, alongside the Mackenzie distribution (corresponding to a random distribution of cubes). Both conditions show a large fraction of LAGBs, typical of PBF-LB/M microstructures [50]. This fraction is significantly higher in $h_d50$ samples (0.21 ± 0.03) than in $h_d70$ (0.13 ± 0.01). These values were calculated for misorientation angles between 3 and 15º to avoid potential artifacts from surface preparation. In both cases LAGBs are primarily associated with the columnar grains aligned along the BD as shown in light blue in Figure 6-3a,b.

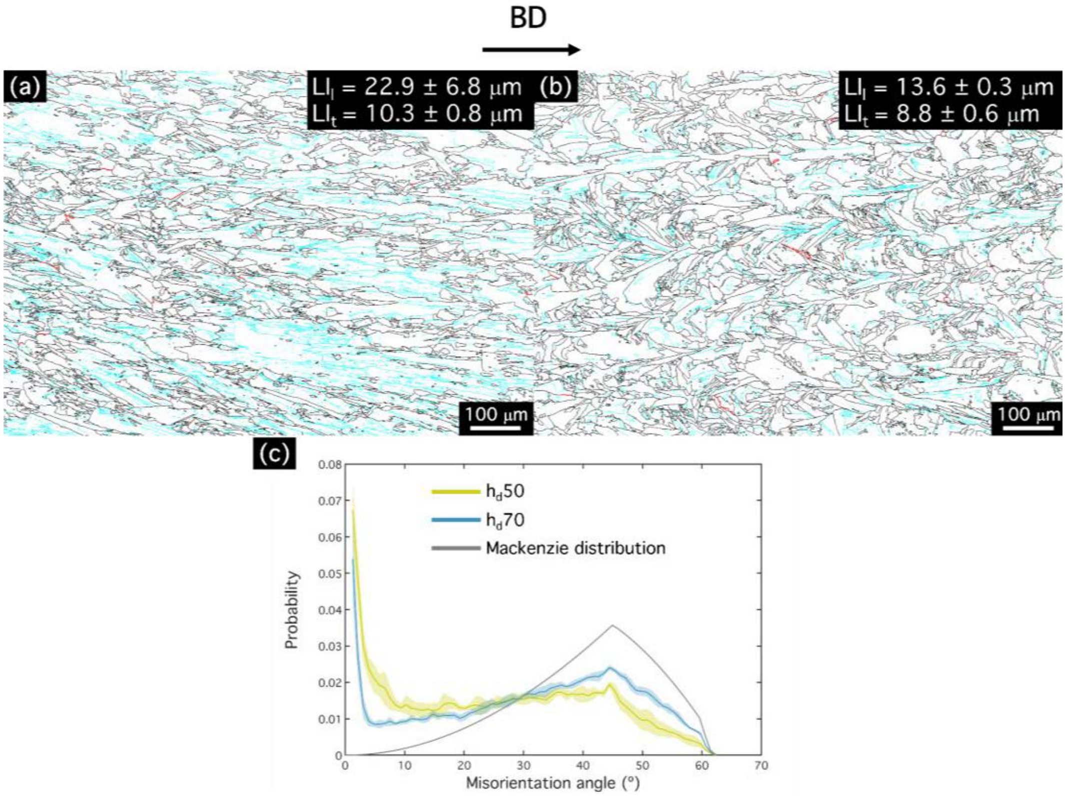

Figure 6-3: Grain boundary maps for (a) $h_d50$, and (b) $h_d70$ samples in the as-built state. Black lines correspond to HAGBs (θ>15º), light blue lines to LAGBs (θ∈2-15º), and red lines correspond to TBs. The inserts at the top right corner of the maps indicate longitudinal (LI$_l$) and transverse (LI$_t$) line intercepts. (c) Comparison of the misorientation angle distribution corresponding to $h_d50$ and $h_d70$ samples with the Mackenzie distribution. The shaded overlays in (c) represent standard deviations, for the histograms were calculated using at least 4 maps for each case.

Geometrically necessary dislocation (GND) densities were also characterized in the as-built state as they are believed to play a significant role in the microstructural evolution at elevated temperatures [156,158]. GND density can be estimated from local misorientations between neighboring points, using data acquired via EBSD [165]. It serves as a useful indicator of the stored energy in the form of thermomechanical strain resulting from the thermal cycling inherent to PBF-LB/M processing [155,157]. Grains subjected to higher amounts of strain exhibit higher GND densities, while strain-free grains (such as a fully recovered or recrystallized ones), display significantly lower values.

Figure 6-4a and 6-4b show the GND density maps for hd50 and hd70, respectively. As expected for PBF-LB/M microstructures [155,157], both conditions exhibit high dislocation densities, predominantly aligned with the BD (Figure 6-4e). The GND distributions reveal slight differences between the two conditions. While the mean GND densities are $1.04\cdot10^{14}$

$m^{-2}$ for $h_d50$ and $1.02 \cdot 10^{14}$ $m^{-2}$ for $h_d70$, the $h_d50$ condition shows a broader distribution, with a slightly higher area fraction of GND densities exceeding $1.5 \cdot 10^{14}$ $m^{-2}$.

These larger maps were used for comparing microstructures and assessing the effects of thermal treatments (see Section 6.3.2). However, as they were acquired using a 1 µm step size, their quantitative accuracy is limited [166]. To mitigate this limitation, additional smaller-area maps were acquired with a reduced step size of 0.1 µm (Figure 6-4c, d). The mean GND densities derived from these high-resolution maps are $5.2 \cdot 10^{14}$ for $h_d50$ and $5.4 \cdot 10^{14}$ $m^{-2}$ for $h_d70$, values that are significantly higher and in line with previously reported data for PBF-LB/M alloys [167]. The GND density distribution for these higher resolution maps (Figure 6-4f) shows a very similar shape to the one in Figure 6-4e, but shifted towards density values roughly five times higher. Due to the greater spatial coverage provided by the larger maps, they are used in the following sections for comparative purposes, while the more accurate values from the smaller maps are employed in calculations in Section 6.4.1.

Figure 6-5 illustrates the precipitate distribution in the AB state. Similar to the findings reported in Section 4.3.2 (Figure 4-6), no γ' precipitates were observed in neither $h_d50$ nor $h_d70$ samples. Only (Ti,Nb,Ta)C carbides were found. The SEM micrographs in Figure 6-5a,b and the TEM bright field micrograph in Figure 6-5c confirm preferential precipitation of these carbides in cell and grain boundaries. Their composition, rich in Ti, Nb, and Ta, was determined by means of TEM EDX (Figure 6-5d). In terms of size, both SEM and TEM micrographs were utilized, revealing very similar size distributions for the $h_d50$ and the $h_d70$ conditions (Figure 6-5e). The average size of the MC carbides is 71 nm for $h_d50$ and 66 nm for $h_d70$, and their area fractions were practically equal, at approximately 0.008.

Overall, the AB microstructure of the 10 x 10 x 10 $mm^3$ cubes shows the same characteristics as the microstructure of the cuboids presented in Chapter 4 and printed with the same scanning parameter combinations. The change in geometry does not result in any appreciable change in the outcome of the print. Furthermore, no significant differences were observed between the two different layers of cubes printed for this study (Figure 6-1b).

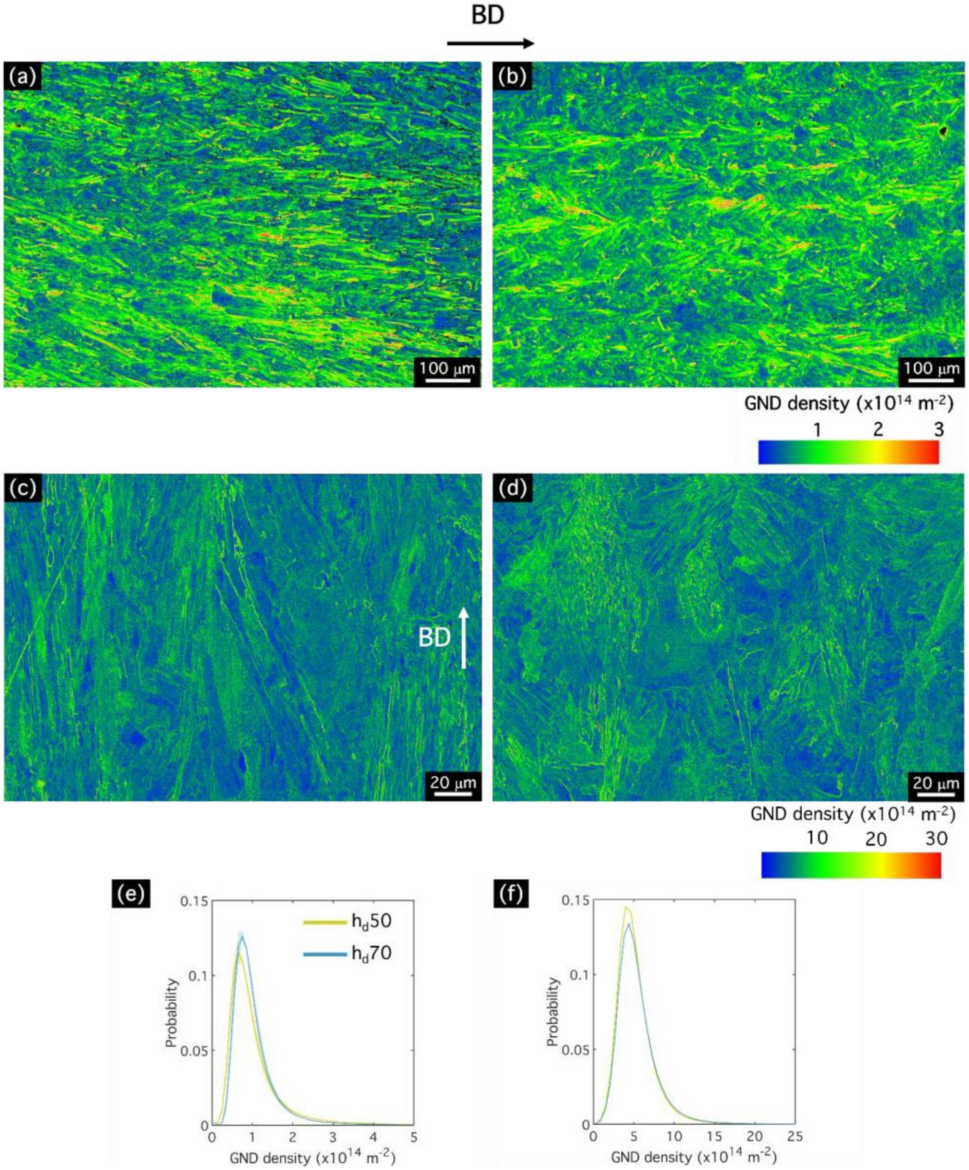

Figure 6-4: Geometrically necessary dislocation (GND) density maps for (a,c) *$h_d$50*, and (b,d) *$h_d$70* samples in the as-built state. Maps (a,b) were obtained with a 1 µm step size, and (c,d) using 0.1 µm. GND density distribution corresponding to the maps (e) in (a, b), and (f) in (c,d). The shaded overlay in (e) represents standard deviations, for the histograms were calculated using at least 4 maps for each case.

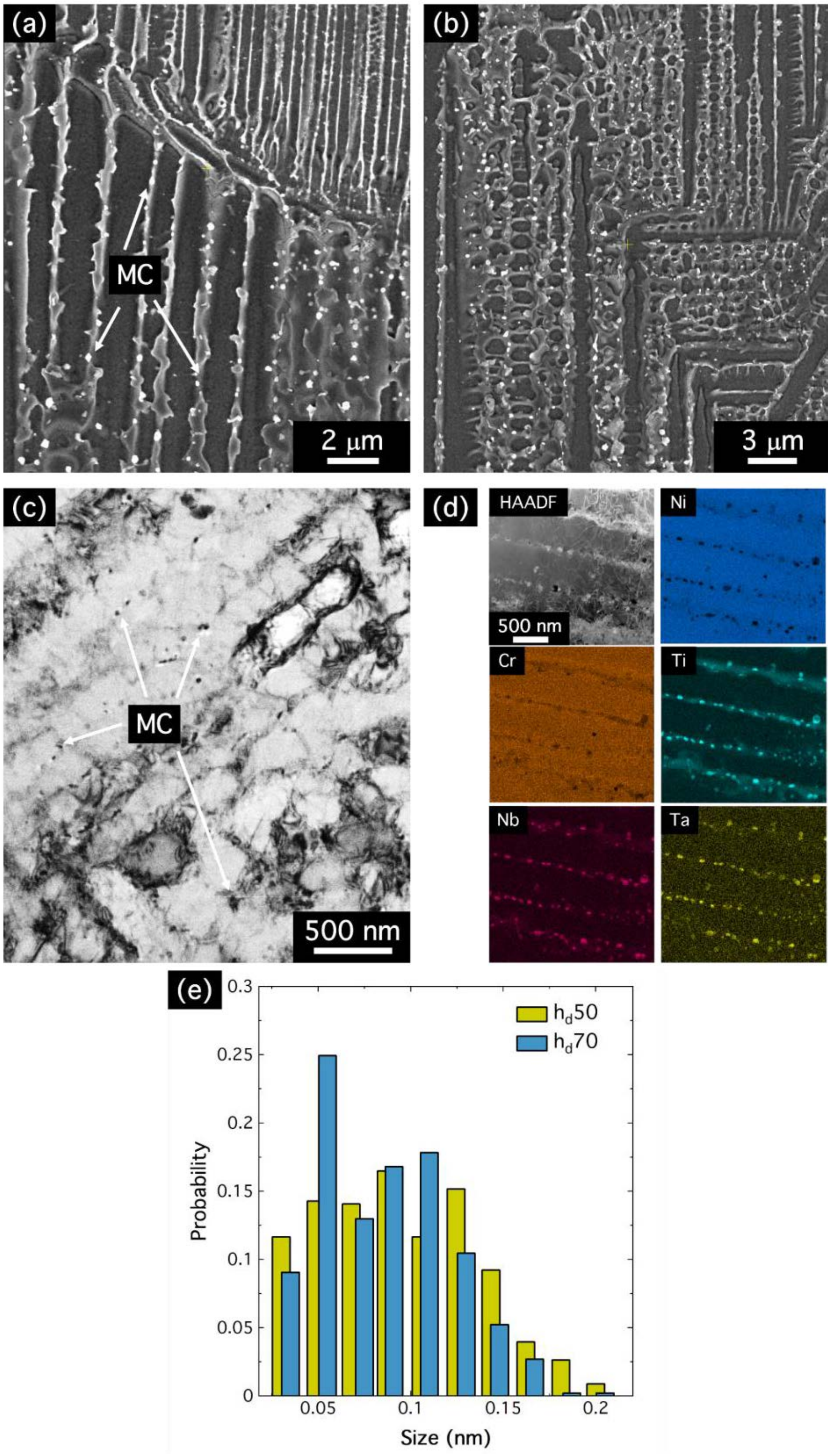

Figure 6-5: MC carbide distribution in the AB state: (a,b) SEM micrographs corresponding to (a) $h_d50$ and (b) $h_d70$ samples; (c) TEM HAADF micrograph of a $h_d70$ sample; (d) TEM EDX analysis of (Ti,Nb,Ta)C carbides in a $h_d50$ sample; (e) size distribution in $h_d50$ and $h_d70$ samples.

### *6.3.2. Microstructural evolution upon thermal treatment*

The microstructure of the samples produced under the two different printing conditions was examined after each of the nine solution treatments (1, 4, and 8 hours at 1100ºC, 1150ºC, and 1200ºC) to assess the influence of the initial microstructure, treatment temperature, and duration. Figure 6-6 shows the IPF EBSD maps in the BD for $h_d50$ samples as a function of time and temperature. Columnar grains exhibiting a strong <001>//BD fiber texture are retained across all thermal treatments, except for the 1200ºC/8 h condition (Figure 6-6j), where significantly larger grains with varying crystallographic orientations are observed. The corresponding (100), (110), and (111) direct pole figures (Figure 6-7) confirm the persistence of the fiber texture after thermal treatment, with some variation in intensity. For the $h_d70$ samples, the more equiaxed and randomly oriented grain structure observed in the as-built state is also maintained across thermal treatments, as shown in the IPB EBSD maps in the BD of Figure 6-8. Similar to $h_d50$, no significant differences are observed between treatments until the 1200 °C/8 h condition, where grain growth becomes evident. All $h_d70$ samples exhibit a weak crystallographic texture, as reflected in the (100), (110), and (111) direct pole figures of Figure 6-9.

To compare the crystallographic texture evolution in $h_d50$ and $h_d70$ samples, the volume fraction of the <001>//BD component was quantified for the as-built condition and all thermal treatments. The results confirm two clearly different populations: the highest <001>//BD volume fraction in $h_d70$ is 0.16 ± 0.02 (in the as-built state) while the lowest value for $h_d50$ is 0.21 ± 0.06 (1200ºC/8 h.). Thus, the crystallographic texture is largely preserved under thermal exposure, and remains strongly dependent on the orientation of the as-built microstructure, even at high levels of recrystallized area fraction.

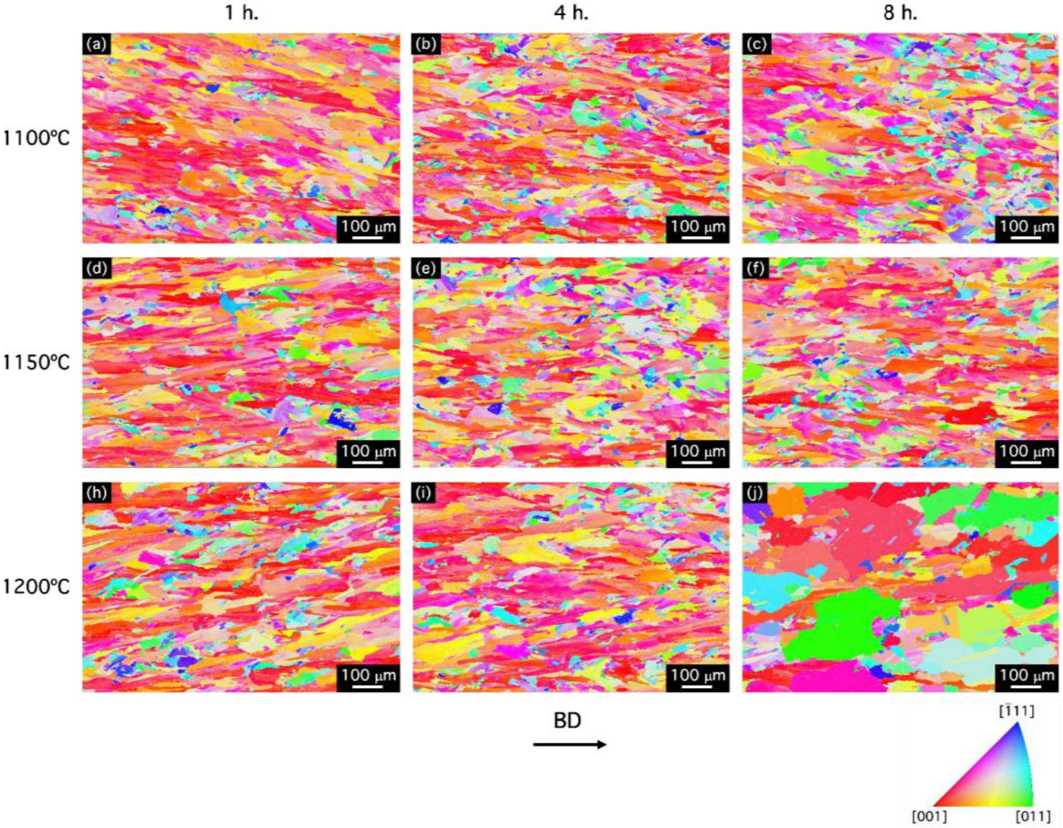

Figure 6-6: IPF coloring EBSD maps in the build direction for $h_d50$ samples after the 9 different thermal treatments.

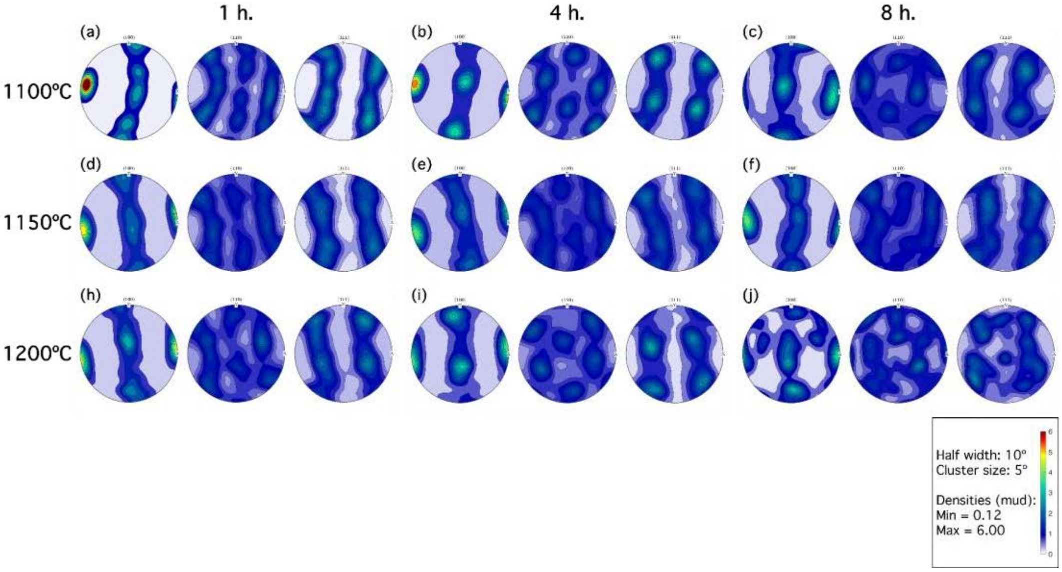

Figure 6-7: Pole figures obtained from EBSD data for $h_d50$ samples after the 9 different thermal treatments.

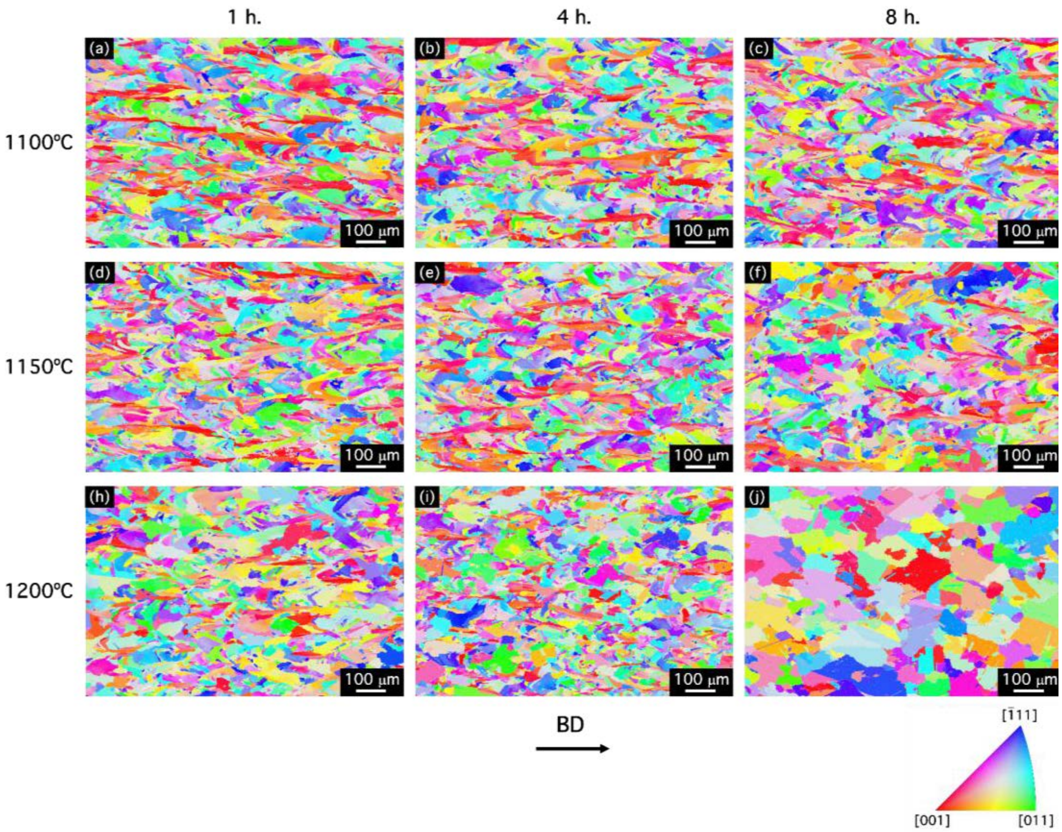

Figure 6-8: IPF coloring EBSD maps in the build direction for $h_d70$ samples after the 9 different thermal treatments.

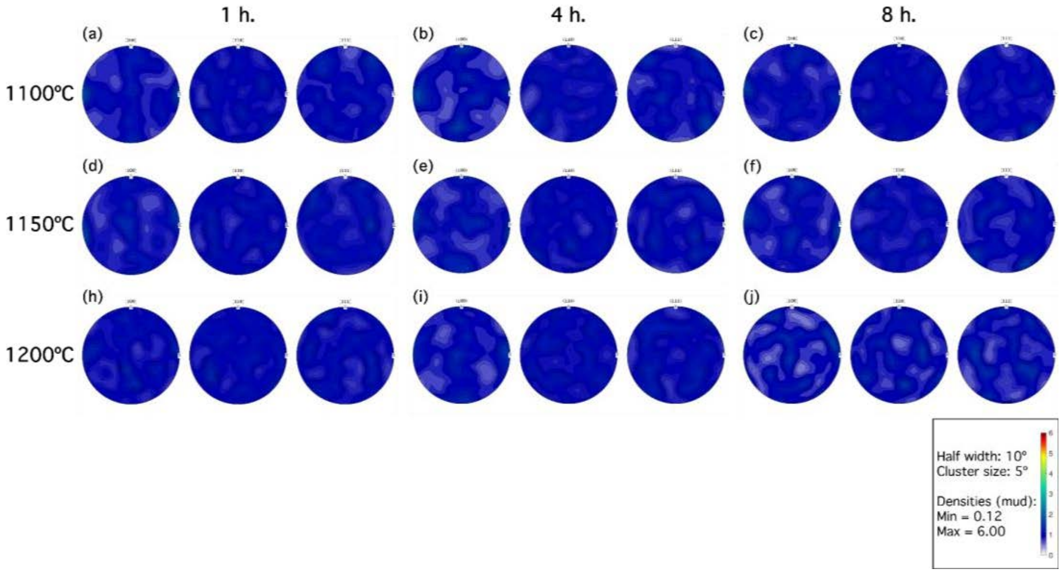

Figure 6-9: Pole figures obtained from EBSD data for $h_d70$ samples after the 9 different thermal treatments.

Figure 6-10 presents the GND density maps for *hd50* samples after thermal treatment. Areas with lower GND densities (blue), correspond to virtually strain-free grains, i.e. fully recovered or recrystallized grains. For most treatments (Figure 6-10a-i), there are no significant differences compared to the AB state (Figure 6-4a), with a fairly homogeneous distribution of GND densities. Only after 8 h at 1200ºC (Figure 6-10j) is a clear evolution observed: a large area fraction of strain-free grains emerges, while the remaining grains retain GND densities comparable to those in other thermal treatment conditions or in the as-built state.

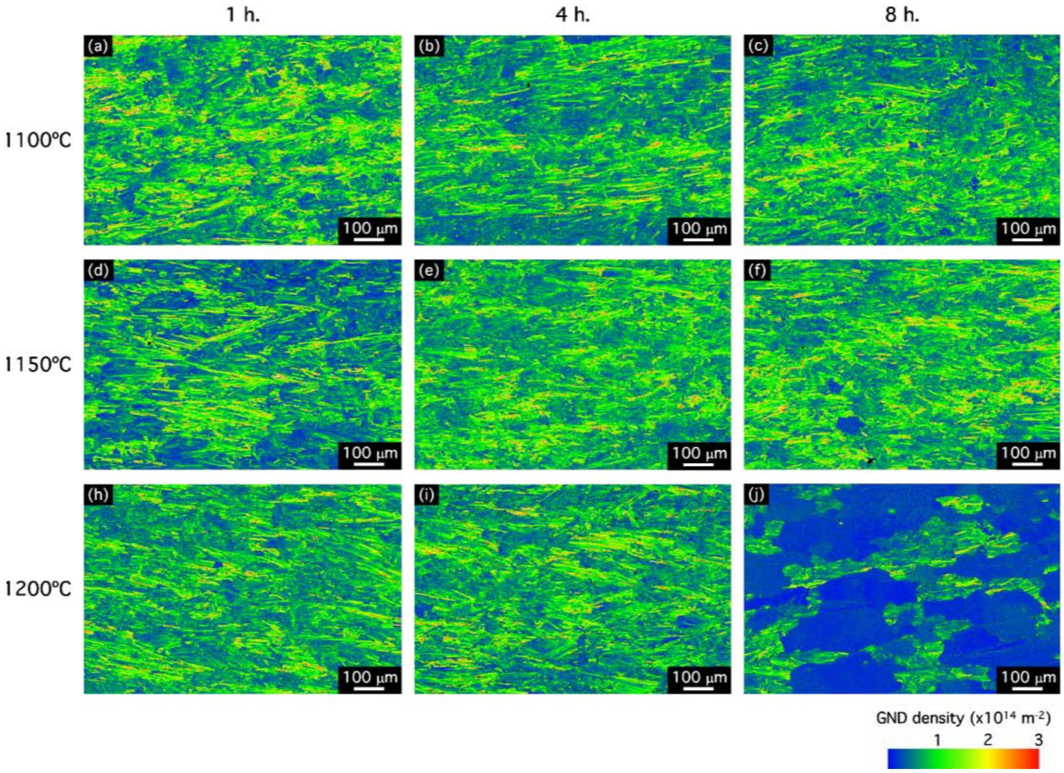

Figure 6-10: GND density for $h_d50$ samples after the 9 different thermal treatment conditions.

For $h_d70$, the evolution upon thermal treatment seems to be more gradual (Figure 6-11). Evidence of recrystallization begins to emerge after 8h at 1100ºC (Figure 6-11c), or after 4h at 1150ºC (Figure 6-11e), where some small scattered strain-free grains (blue) can be observed. These strain-free regions expand significantly after 8h at 1150ºC (Figure 6-11f), 1h at 1200ºC (Figure 6-11h), and 4h at 1200ºC (Figure 6-11i). Finally, after 8h at 1200ºC (Figure 6-11j) the microstructure appears to be fully recrystallized, with only very small regions still exhibiting large GND densities.

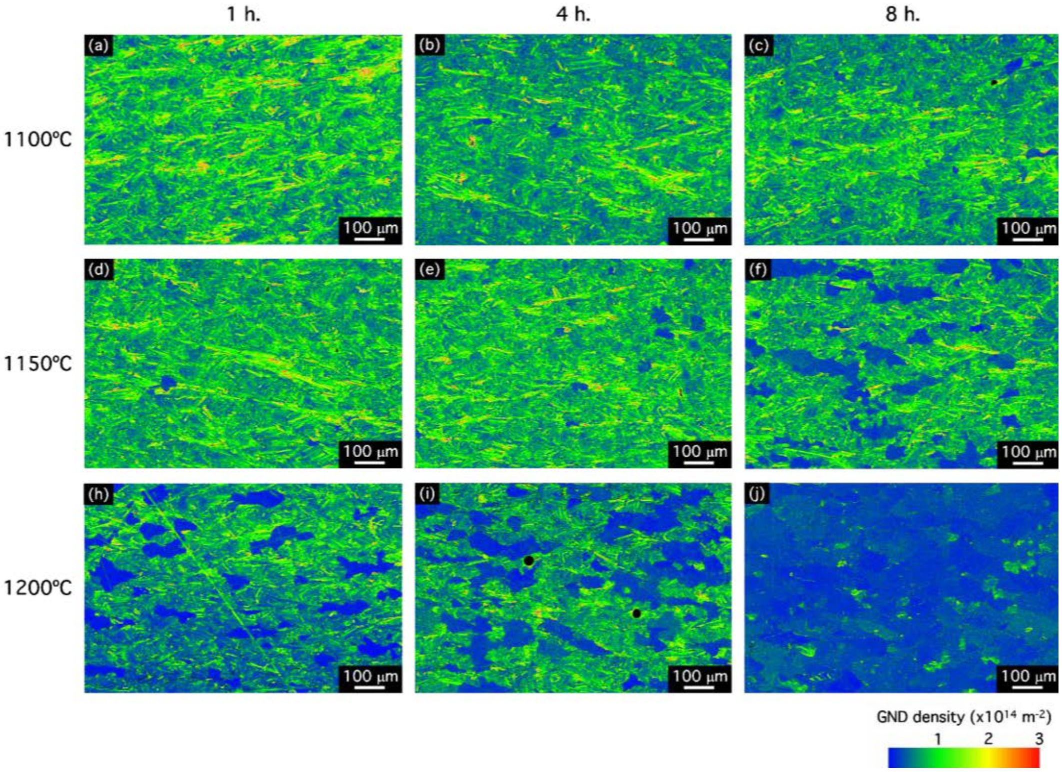

Figure 6-11: GND density for $h_d70$ samples after the 9 different thermal treatment conditions.

Figure 6-12 and Figure 6-13 illustrate the grain boundary maps corresponding to $h_d50$ and $h_d70$ samples treated using the nine solution treatments investigated. In the case of $h_d50$ specimens (Figure 6-12), the columnar structure is mostly preserved, with most grains elongated along the BD, except after 8h at 1200ºC (Figure 6-12j). At this condition, where a reduction in GND density and a slight weakening of the texture were previously observed, the grains exhibit substantial growth and a notable increase in the fraction of Σ3 twin boundaries (colored in red). These features are characteristic of a recrystallized state, with the Σ3 boundaries representing annealing twins [154,158]. In the case of $h_d70$ samples (Figure 6-13), the small equiaxed grains found in the AB state (Figure 6-3b) are still present after most thermal treatments. As with $h_d50$, the evolution of GB character and the appearance of annealing twins follow a trend consistent with the previously observed GND density evolution. A significant fraction of TBs appear after 8 h at 1150ºC (Figure 6-13f) and 4h at 1200ºC (Figure 6-13i), and a very large TB fraction develops after 8h at 1200ºC (Figure 6-13j), indicating a very advanced recrystallized state.

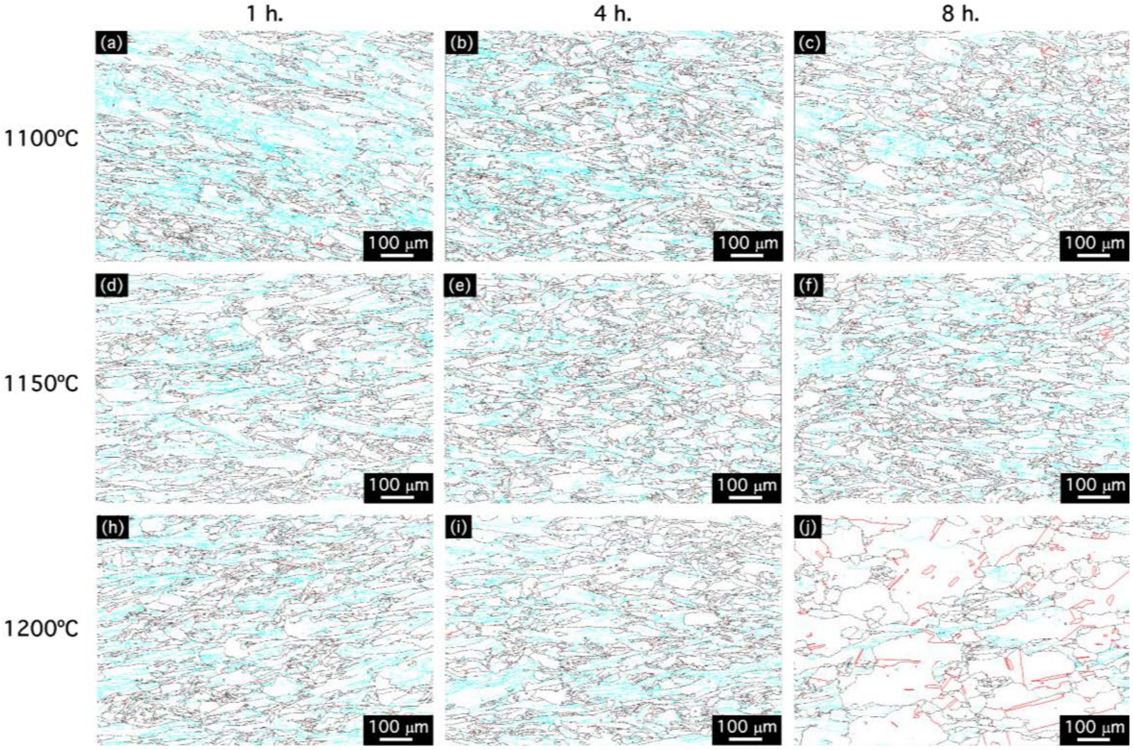

Figure 6-12: Grain boundary maps for *$h_d$50* samples after the 9 different thermal treatments. HAGBs are plotted in black, LAGBs in blue, and TBs are plotted in red.

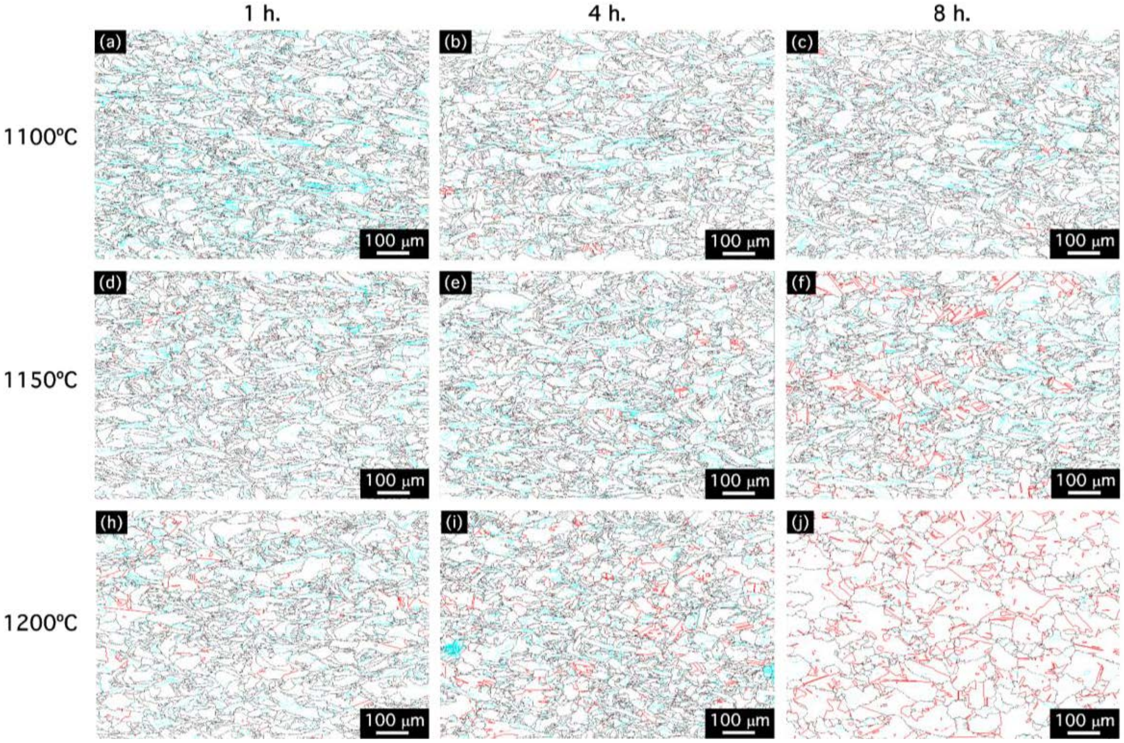

Figure 6-13: Grain boundary maps for *$h_d$70* samples after the 9 different thermal treatments. HAGBs are plotted in black, LAGBs in blue, and TBs are plotted in red.

To assess the recrystallization kinetics of the two different microstructures, we used the GND density maps (Figure 6-10 and Figure 6-11). Although there is no universal consensus on how to measure recrystallization using EBSD data [168], we adopt the commonly used criterion that recrystallized grains are characterized by their very low intragranular misorientations [154]. These misorientations can be quantified via the kernel average misorientation (KAM), from which we calculate the GND density [122]. While thresholds of KAM < 1° or < 0.5° are frequently reported, depending on the acquisition conditions and angular resolution of the system, we selected a threshold based on a KAM of 0.5°[169,170]. Considering the Burgers vector of a Ni-based superalloy and the step size used in the acquisition of the large EBSD maps, this corresponds to a GND density of $6.88 \cdot 10^{13}$ $m^{-2}$. This is the cutoff value we have considered to identify recrystallized grains and calculate the recrystallized area fractions reported in Figure 6-14 as a function of the dwell time for the three solution temperatures investigated.

Figure 6-14 illustrates, first, that the recrystallization temperature of PBF-LB/M IN939 is considerably higher than that of cast IN939, which becomes fully recrystallized after 4 h at 1160ºC [91]. Additionally, clear differences in the onset of recrystallization between the two starting microstructures are observed, with $h_d70$ exhibiting recrystallization at lower temperatures and shorter dwell times than $h_d50$ (Figure 6-14). At 1100ºC no signs of recrystallization are observed for any of the AB microstructures. At 1150ºC, $h_d70$ exhibits a significant RX area fraction, close to 0.4, after 8 h. In contrast, $h_d50$ shows no measurable evolution, even after prolonged exposure. Substantial recrystallization occurs for both conditions only at 1200ºC. In the case of *hd70*, a noticeable RX fraction (0.18) appears after just 4 h, increasing to 0.96 after 8 h, indicating near-complete recrystallization. For *hd50*, recrystallization proceeds more slowly, with no significant changes until 8 h, after which an RX area fraction of 0.82 is observed.

Figure 6-14: Recrystallized area fraction as a function of dwell time for solution treatments at 1100ºC, 1150ºC, and 1200ºC for $h_{d}50$ and $h_{d}70$ microstructures.

Figure 6-15 illustrates the evolution of several microstructural parameters as a function of the RX fraction. Figure 6-15a shows the evolution of the volume fraction of the <001>//BD component with the RX fraction. For $h_{d}70$, the volume fraction remains practically unchanged as the recrystallization advances. In the case of $h_{d}50$, there is a relatively large scatter in the volume fractions of samples having undergone no (or very little) recrystallization. Although the $h_{d}50$ sample with the highest RX fraction (0.82) shows the lowest texture intensity (0.21), the absence of intermediate data points and the variability among the non-recrystallized samples prevent any definitive conclusions regarding the texture evolution of strongly textured conditions. Nevertheless, when comparing the two initial microstructures, it is evident that the AB crystallographic texture has a lasting influence on the texture after solution treatment, regardless of the treatment conditions and the recrystallization state.

Figure 6-15b illustrates the evolution of the GND density with the RX fraction. A good correlation can be established, despite a relatively large scatter in the non-recrystallized samples. This is expected, given that the recrystallization was indirectly assessed using GND density maps. In the recrystallized state, the grains are generally free of GNDs, therefore a larger fraction of recrystallized grains naturally leads to a reduction in the GND density. As previously mentioned, the values were obtained from the large area maps and are thus qualitative rather than quantitatively precise. In the AB state, $h_d50$ and $h_d70$ exhibit nearly identical mean GND densities ($1.04 \cdot 10^{14}$ and $1.02 \cdot 10^{14}$ $m^{-2}$, respectively). While treatments at 1100 °C appear to slightly increase the mean GND density, all non-recrystallized conditions fall within a range of $0.94 \times 10^{14}$ to $1.24 \times 10^{14}$ $m^{-2}$. For $h_d70$, a gradual decrease in mean GND density is observed with increasing treatment time at 1150 °C and 1200 °C, reflecting progressive recrystallization, reaching a minimum of $0.45 \times 10^{14}$ $m^{-2}$ after 8 h at 1200 °C. In contrast, $h_d50$ does not exhibit this progressive decline due to the limited recrystallization observed, except for the 1200 °C/8 h condition, where a significant drop in GND density is noted.

The correlation between the RX area fraction and the TBs, illustrated in Figure 6-15c, is even more pronounced than that observed for GND density. A clear linear correlation is evident, independent of $h_d$, ranging from approximately 0.1 in the non-recrystallized state to around 0.45 in the fully recrystallized condition. This strongly supports the interpretation that these are annealing twins, typically found in FCC metals with low stacking fault energy after recrystallization [154,158].

Finally, Figure 6-15d presents the evolution of the LAGB fraction as a function of the recrystallized area fraction. In $h_d70$ samples, which begin with a significantly lower initial LAGB fraction than $h_d50$ specimens (0.13 and 0.21, respectively), a nearly linear correlation is observed: the LAGB fraction decreases progressively as RX advances. This is consistent with the expectation that non-recrystallized grains, which retain internal strain, contain a higher fraction of LAGBs, whereas recrystallized grains exhibit low internal misorientations and, consequently, negligible LAGB content. In contrast, $h_d50$ samples show a decrease in LAGB fraction even before the onset of recrystallization. Once recrystallization begins, the subsequent decrease in LAGBs is comparatively minor. This behavior suggests that some recovery processes may precede or partially decouple from full recrystallization in the more textured $h_d50$ microstructure.

Figure 6-15: (a) Volume fraction of the <001>//BD component, (b) mean GND density, (c) TB fraction, and (d) LAGB fraction as a function of recrystallized area fraction. For (a) and (d), regressions are shown for each printing condition separately, for they are two independent data populations. For (b) and (c), the regression is calculated with all data points.

### *6.3.3. Mechanical properties after thermal treatment*

The microstructure of thermally treated tensile blanks, subjected to a 1200ºC/8 h solution treatment followed by a two-step ageing treatment (1000ºC/6 h. + 800ºC/4 h) shows practically full recrystallization and substantial grain growth (Figure 6-16a), with a very fine and homogenous bimodal distribution of γ' precipitates, together with inter- and intragranular carbides (Figure 6-16b,c,d). The carbides (black particles in Figure 6-16b) measure roughly

0.8 µm. Primary γ’ is 125 ± 25 nm in size, whilst secondary γ’ is 12 ± 3 nm. This homogeneous precipitate distribution is considerably different to that found in the samples presented in Section 4.3.3 (Figure 4-9), where the limitations in cooling rates resulted in coarser γ’ precipitates with flower-like morphologies.

Figure 6-17 shows the results of tensile tests conducted at 23ºC, 700ºC, 800ºC, and 950ºC for PBF-LB/M IN939 samples subjected to the aforementioned 1200ºC/8 h solution treatment followed by two-step ageing. These samples are hereafter referred to as *PBF-LB/M-1200/8*. The results are compared with those of *PBF-LB/M-1160/4* and *Cast-1160/4*, which correspond to PBF-LB/M and cast IN939, respectively, both treated with a 1160 °C/4 h solution step followed by the same two-step ageing, the standard thermal treatment for IN939 [90,91]. The PBF-LB/M-1160/4 data correspond to the samples from Section 4.3.3, and Cast-1160/4 data are sourced from [91–93].

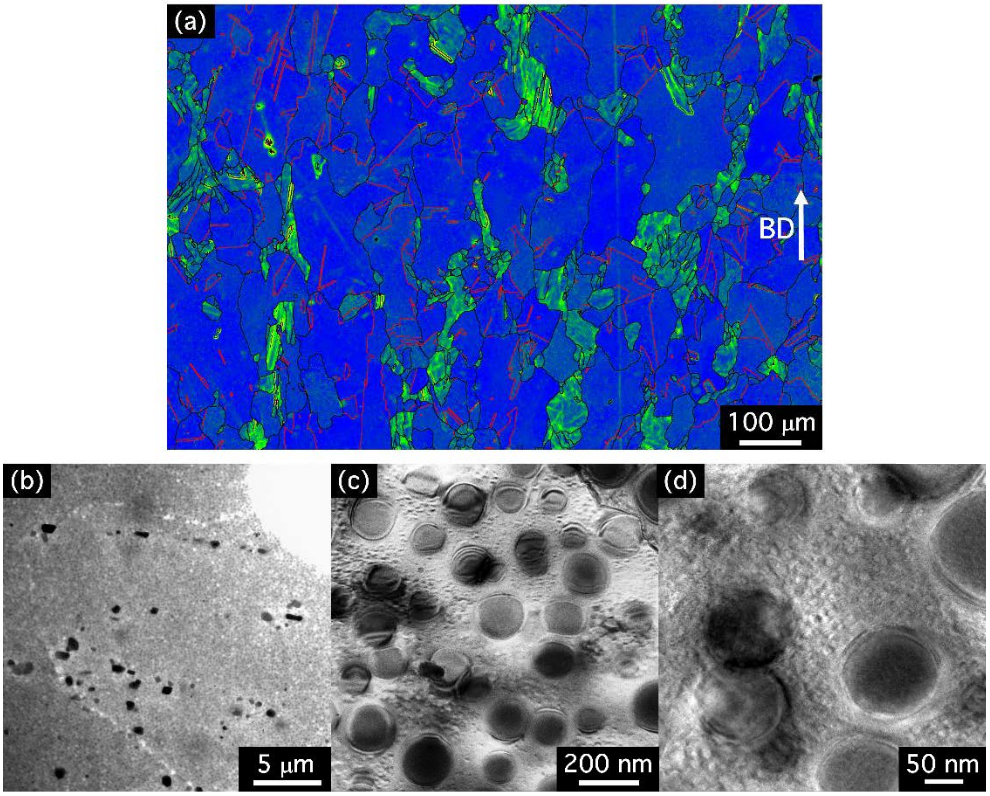

Figure 6-16: Microstructure of a $h_d$*70* sample subjected to a 1200ºC/8 h solution treatment followed by a two-step ageing treatment (1000ºC/6 h + 800ºC/4 h). (a) Overlapped EBSD GND and grain boundary maps; (b-d) bright field TEM micrographs at different magnifications illustrating the γ’ precipitate distribution.

The *PBF-LB/M-1200/8* sample, which is fully recrystallized, exhibits higher yield strength (YS) and ultimate tensile strength (UTS) values from RT to 950ºC (Figure 6-17a,b).

The modification of the thermal treatment results not only in higher strengths, but also in a more gradual decay of the mechanical properties at high temperatures for the PBF-LB/M material, seen most clearly in the smaller change in YS from 700ºC to 800ºC (Figure 6-17a). For 1200ºC/8 h., YS goes from 870 to 765 MPa, whereas in 1160ºC/4 h. samples, it goes from 773 to 437 MPa. In terms of elongation at break (Figure 6-17c), the change in thermal treatment yields a slightly less ductile material throughout the full temperature range, especially at 950ºC.

Overall, the increase in the first thermal treatment step improves the mechanical properties of PBF-LB/M IN939 through mechanisms that will be discussed in Section 6.4.3.

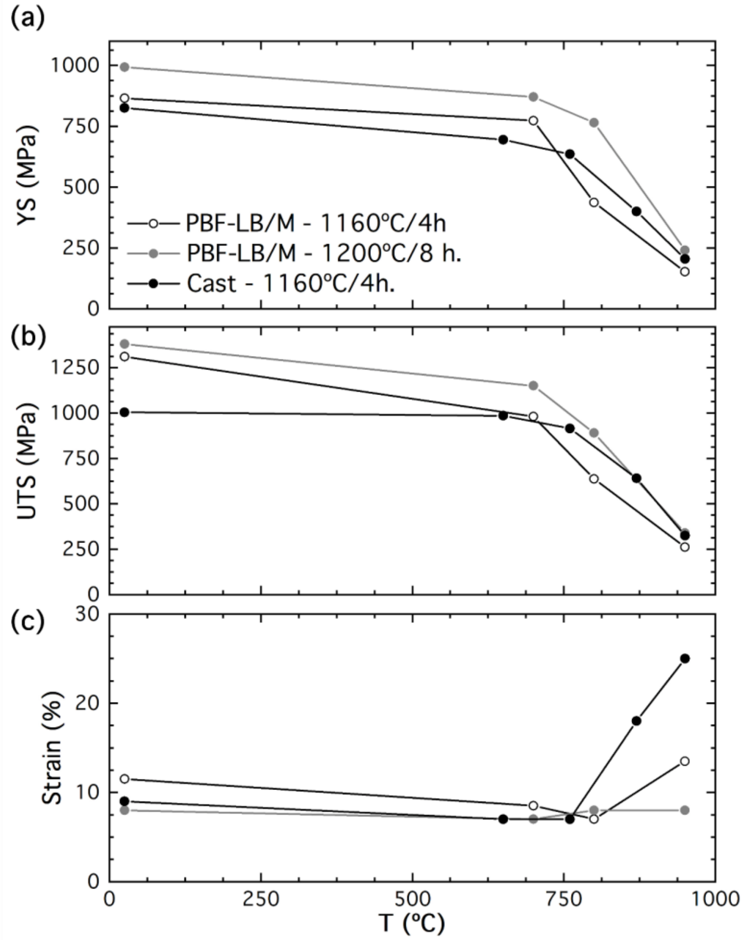

Figure 6-17: (a) Yield strength (MPa), (b) ultimate tensile strength (MPa), and (c) elongation at break for PBF-LB/M samples after the standard thermal treatment [99], PBF-LB/M samples after the modified thermal treatment, and for cast samples after standard thermal treatment.

## 6.4. Discussion

### *6.4.1. Recrystallization in PBF-LB/M and cast IN939 specimens: an energy balance perspective*

The recrystallization temperature of PBF-LB/M IN939 is significantly higher than that of cast IN939 (1200ºC compared to 1160ºC), regardless of the AB microstructure, and overall recrystallization kinetics seem more sluggish in the former, in agreement with earlier studies in IN939 and other alloys [103,116,158,164]. In the following the driving and dragging forces affecting the recrystallization kinetics in PBF-LB/M IN939 are assessed.

The main driving force for recrystallization is the stored energy in the form of dislocations ($P_D$) [154]:

$$P_D = \alpha \rho G b^2 \qquad (6.1),$$

where $\alpha$ is a constant of value 0.5, $\rho$ is the dislocation density, $G$ is the shear modulus, and $b$ is the Burgers vector [154]. In a PBF-LB/M part, these dislocations arise from the rapid solidification process and the repeated thermal cycles during fabrication [155,157]. This driving force is counteracted by the pressure arising from the high angle grain boundary curvature ($P_C$):

$$P_c = \frac{2\gamma_b}{R} \qquad (6.2),$$

where $R$ is the radius of a newly nucleated grain and $\gamma_b$ is the grain boundary energy [154]. In the presence of second phase particles, there is an additional dragging force, due to the pinning effect that they have on the grain boundaries (Smith-Zener drag) ($P_{SZ}$):

$$P_{SZ} = \frac{3F_V\gamma_b}{d} \qquad (6.3),$$

where $F_V$ is the volume fraction of the pinning particles, and $d$ is their size [154]. The resulting net pressure on a newly created nucleus is:

$$P = P_D - P_C - P_{SZ} \qquad (6.4).$$

For recrystallization to occur, the overall net pressure must be positive. The mean GND density in the AB state measured from higher resolution EBSD maps is of the same order or magnitude for $h_d50$ and for $h_d70$ specimens ($5.2 \cdot 10^{14}$ and $5.4 \cdot 10^{14}$ $m^{-2}$, respectively). Assuming a shear modulus of 80 GPa and a Burgers vector of 0.253 nm, the corresponding driving pressure for recrystallization ($P_D$) is calculated to be 1.34 MPa for $h_d50$ and 1.39 MPa for $h_d70$. The volume fraction of MC carbides in the AB state is roughly 0.008 for both microstructures. These particles range in size from 10 to 200 nm, with an average size of approximately 71 and 66 nm for $h_d50$ and for $h_d70$ respectively. The mean $\gamma_b$ was calculated considering a simplification of the Read-Shockley equation for LAGB [154]:

$$\gamma_b(\theta) = \gamma_m \left(\frac{\theta}{\theta_m}\right)\left(1 - \ln\left(\frac{\theta}{\theta_m}\right)\right) \quad (6.5),$$

were $\gamma_m$ is the energy of a HAGB (1 J·m$^{-2}$) [154,171], and $\theta_m$ is the critical angle (15º). For LAGBs ($\theta < 15$º), the $\gamma_b$ follows the relation in (6.5), and for HAGBs ($\theta < 15$º), we consider $\gamma_b$ = 1 J·m$^{-2}$. The resulting mean $\gamma_b$ values are 0.90 for $h_d50$ and 0.91 J·m$^{-2}$ for $h_d70$. The dragging pressure from the secondary particles ($P_{SZ}$) amounts, then, to $3 \cdot 10^5$ Pa for $h_d50$ and $3.3 \cdot 10^5$ Pa for $h_d70$. From the calculated $P_D$ and $P_{SZ}$ values, the critical radius (R) required for a newly nucleated grain to grow can be estimated. This radius is approximately 1.75 µm, implying that grains smaller than this will have their growth inhibited. Although these estimates are approximate, the calculated critical grain size is relatively large considering the typical values for cast specimens, usually closer to 0.5 µm (although not unreasonably large) [154,158,172,173]. The stored energy in the form of GNDs, while non-negligible, appears insufficient to drive recrystallization under conditions where it occurs readily in cast specimens, likely due to the strong pinning effect of MC carbides at grain boundaries.. At sub-solvus temperatures no recrystallization is observed in any of the samples, most likely due to the dragging force of the aforementioned carbides. As the temperature increases beyond the solvus, MC carbides coarsen, thereby reducing their pinning force (as described in eq. 6.3) and facilitating the nucleation and growth of new grains. The pinning effect of MC carbides has been pinpointed as the primary factor behind the high recrystallization temperatures observed in PBF-LB/M Ni-based superalloys. Their coarsening has been identified as a prerequisite for recrystallization to proceed [160–163], in agreement with our findings.

### *6.4.2. Influence of the initial microstructure on the recrystallization kinetics*

The reason behind the different recrystallization kinetics observed in $h_d50$ and $h_d70$ specimens is unclear. The microstructural features that govern the magnitude of the principal driving and dragging forces are not significantly different between $h_d50$ and $h_d70$: both exhibit similar mean GND densities ($5.2 \cdot 10^{14}$ and $5.4 \cdot 10^{14}$ m$^{-2}$), comparable average grain boundary energies (0.90 and 0.91 $J{\cdot}m^{-2}$), and practically indistinguishable carbide distributions.

One clear difference in the as-built (AB) microstructure, previously unaccounted for in the calculations, is the density of HAGBs. Due to their smaller grain sizes, $h_{d}70$ samples exhibit a HAGB density of $0.85 \pm 0.01\ mm^{-1}$, more than twice that of $h_{d}50$ ($0.41 \pm 0.04\ mm^{-1}$). A higher HAGBs density suggests a greater number of potential nucleation sites [154]. Additionally, the weaker texture in the AB $h_{d}70$ condition is associated with higher misorientation between adjacent grains, which are thus energetically more favorable for nucleation and growth [154]. A larger number of favorable nucleation sites would be expected to promote concurrent nucleation events, ultimately resulting in a finer recrystallized grain structure [158]. This hypothesis is supported by the area-weighted major axis length of fitted ellipses (excluding Σ3 twin boundaries), which is 381 ± 33 µm for $h_{d}50$ and 208 ± 50 µm for $h_{d}70$, indicating a finer recrystallized microstructure in the latter.

The GB maps in Figure 6-18 clearly illustrate the differences in grain size and morphology after a 1200ºC/8 h treatment. In the $h_{d}50$ microstructure (Figure 6-18a-c) there is a lower number of recrystallized grains (characterized by the absence of LAGBs and the presence of TBs), surrounded by columnar grains with high densities of LAGBs. In contrast, $h_{d}70$ (Figure 6-18d-f) exhibits a greater number of smaller recrystallized grains, many of which contain a high density of TBs. Figure 6-18c and 6-18f highlight representative recrystallized grains in $h_{d}50$ and $h_{d}70$ respectively, underscoring the significant size differences between them.

Thus, despite $h_{d}50$ and $h_{d}70$ having nearly identical dislocation densities (i.e., stored energy), similar distributions of secondary phases, and practically identical average grain boundary energies, the $h_{d}70$ condition exhibits faster recrystallization. This is attributed to its higher density of favorable nucleation sites, driven by its finer initial grain structure and weaker crystallographic texture.

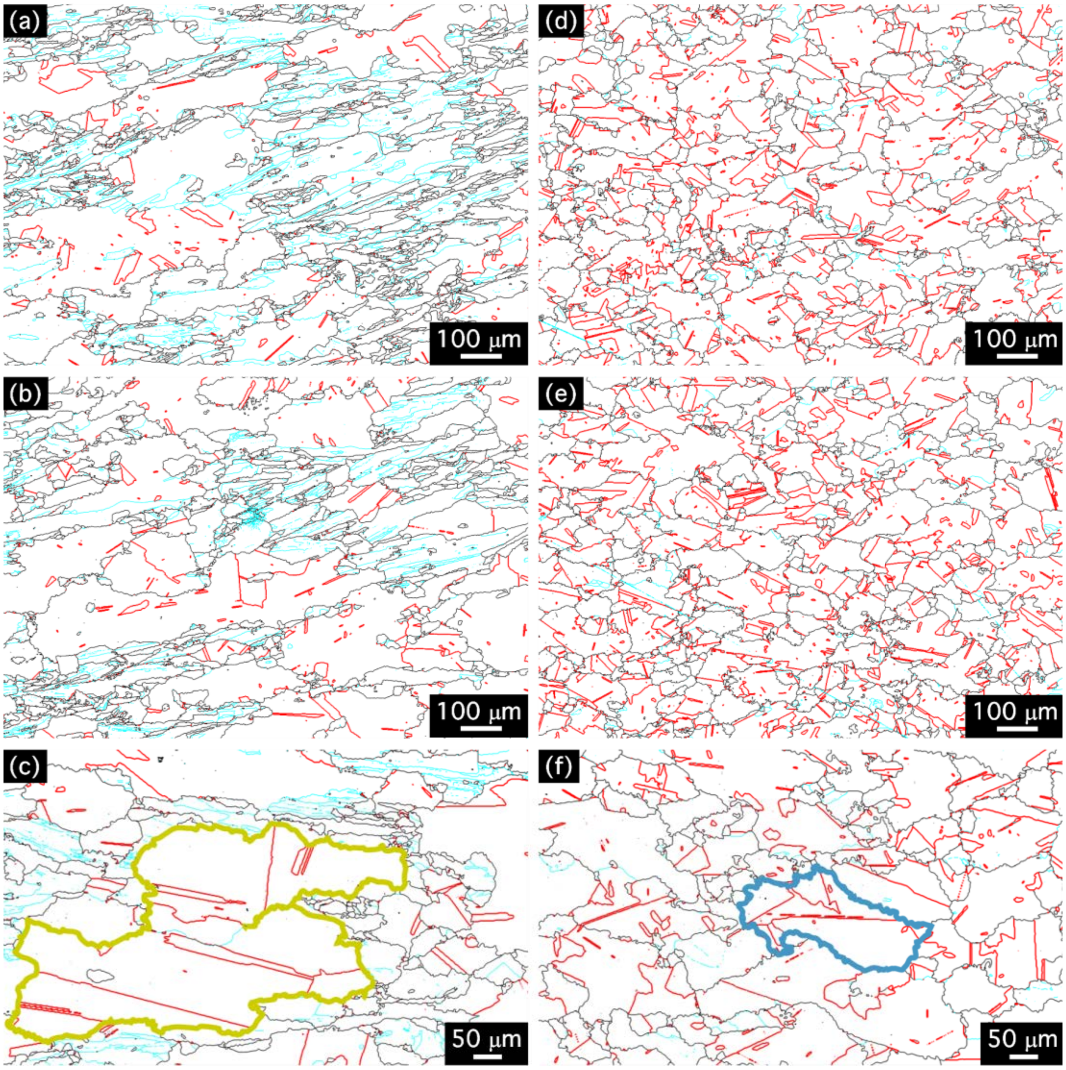

Figure 6-18: GB maps illustrating the microstructure of the PBF-LB/M IN939 alloy after 8h at 1200ºC for (a,b) $h_d50$ and (d,e) $h_d70$ conditions. (c,f) Higher magnification maps with highlighted recrystallized grains in (c) $h_d50$ and (d) $h_d70$ samples.

### 6.4.3. *Influence of recrystallization on the mechanical properties*

The results in section 6.3.3 show a clear improvement in mechanical properties throughout the full temperature range after a 1200ºC/8 h. + 1000ºC/6 h. + 800ºC/4 h. treatment compared to both the cast and the PBF-LB/M samples with standard thermal treatments (Figure 6-17). The good performance of PBF-LB/M-1160 IN939 at low temperatures after standard thermal treatment was attributed to the Hall-Petch effect, while the rapid softening at T > 700ºC was mostly blamed on a combination of grain boundary sliding (GBS), promoted by the small grain sizes, and a suboptimal precipitate distribution (due to an inappropriate cooling rate after ageing) (see Section 4.4.2). In turn, the combination of a larger grain size, obtained by applying higher temperatures during the solution treatment, and a more adequate precipitate distribution results in an enhanced mechanical response of the PBF-LB/M material. At low temperatures, the improved precipitate distribution compensates for the reduced Hall-Petch strengthening (which scales with $d^{-1/2}$, where $d$ is the average grain size). At elevated temperatures, the combined effect of precipitate strengthening and the coarser grain structure results in yield strengths exceeding those typically found in cast IN939 samples.

The strain rate sensitivity (*m*) provides further insight into the deformation mechanisms at play (Figure 6-19). For the PBF-LB/M-1160ºC/4 h condition, the rapid increase in *m* at T > 700ºC highlights the growing influence of diffusion-related deformation processes (GBS being the most likely contributor). In contrast, PBF-LB/M-1200ºC/8 h exhibits the lowest *m* value across the entire temperature range (from room temperature to 950ºC), remaining below 0.1 even at the highest temperatures. This suggests that GBS-related deformation mechanisms are not active in this condition [136], supporting the hypothesis that a beneficial synergy between grain boundary precipitates (specifically $M_{23}C_6$ carbides) and an increased grain size effectively suppresses GBS.

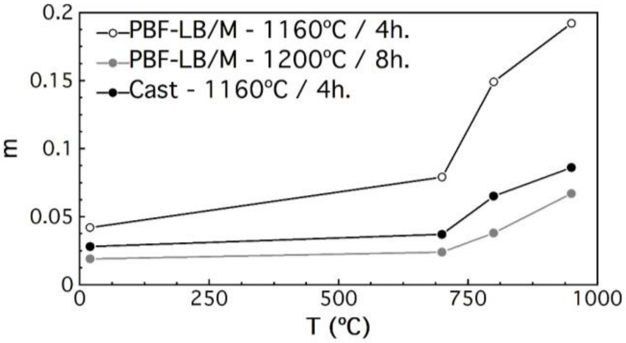

Figure 6-19: Comparison of the temperature-dependent evolution of strain rate sensitivity (m) for PBF-LB/M IN939 samples subjected to the standard thermal treatment [32], PBF-LB/M samples treated with the modified thermal cycle, and cast IN939 samples after standard heat treatment.

A low strain rate sensitivity is usually associated with improved creep resistance, a key requirement for IN939 components. Our findings align with previous studies reporting clear enhanced creep resistance and increased high temperature yield strength following recrystallization, highlighting the importance of increasing solution treatment temperatures [108,117]. While PBF-LB/M IN939 often outperforms the cast material in yield strength at room and high temperatures, it still tends to fall short of the creep resistance required for demanding applications [94,105,108,109,113,117]. A similar limitation in creep performance may be expected in our case, despite the encouraging tensile results and low strain rate sensitivities observed at high temperatures. Dedicated creep testing should be performed in future studies to better understand the deformation mechanisms at high temperatures. Nonetheless, our results confirm that increasing the solution treatment temperature, combined with controlled cooling rates that promote grain growth and favorable precipitate distributions, is essential for improving the high temperature mechanical response of PBF-LM/M IN939.

## 6.5. Conclusion

In this chapter we have tested the influence of different solution thermal treatments on the recrystallization kinetics for two different AB microstructures of PBF-LB/M IN939. The main findings of this part are:

1. The recrystallization temperature for PBF-LB/M IN939 is higher than for cast material. Therefore, the standard heat treatment schedule is not sufficient to induce recrystallization in additively manufactured parts.
2. The AB microstructure influences the recrystallization kinetics of PBF-LB/M IN939. A smaller AB grain size, together with a weaker texture, results in a higher number of favorable nucleation sites, leading to faster nucleation and to a smaller recrystallized grain size.
3. Smith-Zener pinning of MC carbides existing in the AB state is the main dragging force behind the sluggish recrystallization of PBF-LB/M IN939. As temperature increases and the carbides coarsen, the pinning effect becomes weaker, thus triggering recrystallization.
4. The modification of the solution treatment to 1200ºC for 8 h promotes sufficient recrystallization and grain growth, improving the mechanical properties at high temperatures due to a decrease in diffusion-related deformation mechanisms.

# 7. MELT POOL OVERLAP AS A TOOL FOR MICROSTRUCTURE DESIGN

## 7.1. Background

Perhaps the biggest advantage of most AM techniques is the flexibility they offer in terms of design, enabling the production of geometries not achievable otherwise. The design freedom inherent to PBF-LB/M is not only limited to the production of near-net shapes, but it also applies to the microstructure of the printed parts. Fully exploiting this capability requires, however, the development of predictive approaches that enable the site-specific control of microstructure during AM.

Several factors affect the microstructure of as-built (AB) PBF-LB/M parts. The solidification or growth rate (*R*) and the temperature gradient (*G*) determine the morphology (planar, cellular, columnar dendritic, equiaxed dendritic), as well as the size of the solidification structure (see Section 2.2.4.1. Solidification and crystal growth) [64]. While there are examples of microstructural design based on the control of the columnar to equiaxed transition (CET) in PBF-EB/M [174,175], the typical ranges of *R* and *G* inherent to laser powder bed fusion result frequently in columnar microstructures as a consequence of epitaxial growth (in the absence of inoculants) [50].

The crystallographic texture, in turn, is mostly controlled by heat dissipation. After nucleation, the growth of grains in which the preferred growth direction (<001> in the case of cubic systems) is closely aligned with the direction of heat dissipation is favored [64]. There is an implicit dependence between the thermal gradient and the melt pool geometry, and it is commonly accepted that after nucleation, grains grow in a direction normal to the melt pool boundaries. In the absence of scan rotation, and for semicircular melt pools, AB parts tend to exhibit a <011> fiber texture, where <011> directions align preferentially with the build direction (BD) (<011>//BD), although regions with columnar grains oriented with <001> directions parallel to BD (<001>//BD) are also present in the vicinity of the melt pool centerlines. When a rotation is applied between layers (typically 90 or 67º), the intensity of the <011>//BD component decreases, and in turn the <001>//BD texture becomes dominant [70–72]. Thus, the microstructure of most PBF-LB/M Ni-based alloys, manufactured using standard procedures, which usually include such interlayer rotations, is formed by columnar grains with a strong <001>//BD texture [50].

Achieving excellent local control of the AB microstructure is of paramount importance, for it has implications in terms of post-processing, mechanical properties, and corrosion resistance [50]. Part- or location-specific microstructure design during PBF-LB/M is, however, a complex task. Earlier studies have reported several tools to achieve this goal: alteration of the laser scanning parameters (e.g. laser power ($P$), scanning speed ($v$), hatch distance ($h_d$)) [70,176] and/or the scanning strategies (e.g. stripes, chessboard, meander) [177–181], post-processing heat treatments [156,182,183], addition of inoculants [184,185], or utilization of beam shaping strategies [29,30,186]. For example, Sofinowski et al. [177,180] achieved a high level of microstructural control during PBF-LB/M of 316L stainless steel through modifications of the scan direction. Using relatively low scanning speeds ($0.6\ \mathrm{m \cdot s^{-1}}$), they present a methodology to locally control the growth direction of the grains, and thus the crystallographic texture of the AB parts. Sofras et al. [181] applied the same concept (control of scanning direction) to design the crystallographic texture of a 316L steel in order to either suppress or favor twinning induced plasticity (TWIP) effects upon mechanical testing. Montero-Sistiaga et al. [30,186] utilized different beam shapes to modify the microstructure of AB 316L steel and Hastelloy X parts. A laser with a Gaussian power profile led to relatively small grains with weak textures, while using a top-hat power profile resulted in a coarser microstructure with strongly textured columnar grains. A similar strategy was employed by Hadibeik et al. [29] to tune the amorphous fraction and the mechanical properties in a bulk metallic glass (BMG). Fardan et al. [178] recently showed how the stripe size and the stripe overlap could be effectively utilized to control the grain size and the texture intensity during PBF-LB/M of Ni-based superalloy CM247LC. It was shown that the combination of small stripe sizes and sufficient stripe overlap led to substantial remelting and to the dominance of a strong <001> fiber texture, whilst larger stripe sizes and lower degrees of remelting gave rise to more weakly oriented and equiaxed grains. However, in order to induce the formation of columnar grains with a strong fiber texture, the authors rely on a large degree of remelting, which hinders productivity and is not necessarily desirable in larger parts. Significant work is still needed to achieve the degree of microstructural control during

PBF-LB/M that would be desirable to optimize AB part properties for advanced applications in many AM alloys in a fast, inexpensive, and productive manner.

In this chapter, we present a simple approach for site-specific microstructure design during PBF-LB/M of Inconel 939 (IN939), building upon the findings of the previous chapters, providing guidelines for effectively tailoring microstructure during PBF-LB/M of IN939 complex geometry parts.

## 7.2. Methods

### *7.2.1. Sample fabrication*

Two types of specimens were manufactured for this study. Figure 7-1 illustrates the first set of samples, which are 8 x 8 x 8 $mm^3$ cubes. The four specimens shown in Figure 7-1 were produced with the goal of investigating the effect of the "domain" size (or, in other words, the scan track length (*l*)) and/or the domain orientation with respect to BD on microstructure development. Within each cube, the two shades of gray indicate domains that were manufactured using the $h_d50$ (P = 250 W, v = 1.167 $m \cdot s^{-1}$, $h_d$ = 50 µm, dark gray) and $h_d70$ (P = 250 W, v = 1.167 $m \cdot s^{-1}$, $h_d$ = 70 µm, light gray) scanning parameter sets, the optimum scanning parameter combinations identified in Chapter 4. As a reminder, in bulk samples $h_d50$ parameters yield samples with strongly textured <001>//BD columnar grains, while $h_d70$ conditions result in randomly oriented equiaxed microstructures. The first cube (Figure 7-1a) consists of two stacked 8 x 8 x 4 $mm^3$ domains, the second (Figure 7-1b) consists of two 4 x 8 x 8 $mm^3$ domains, and the third (Figure 7-1c) and fourth (Figure 7-1d) specimens are formed by alternating 4 x 4 x 4 $mm^3$ and 2 x 2 x 2 $mm^3$ domains, respectively. For simplicity, these four PBF-LB/M manufactured cubes will be named hereafter "8x8", "4x8", "4x4", and "2x2". Each domain corresponds to a different STL file. The scan direction corresponding to the last layer of all the manufactured cubes (SD) was oriented parallel to either the X or the Y axis (Figure 7-1) to facilitate the post-processing characterization of the melt-pool morphology.

On the other hand, in order to understand the combined effect of *l* and of $h_d$ on the actual energy input, laser scans consisting of 5 adjacent bidirectional passes (*multitracks*) were melted using different values of these two variables on top of 8 x 8 x 5 $mm^3$ PBF-LB/M-manufactured IN939 substrates (Figure 7-2a,b). The number of tracks per multitrack was set to 5 in order to approach stable printing conditions. The multitracks were produced by combining the *P* and *v* values that are common to both *$h_d$50* and *$h_d$70* conditions (250 W, 1.167 $m \cdot s^{-1}$), with 7 hatch distances ($h_d$ = 40, 50, 60, 70, 80, 90, 100 μm), and four scan track lengths (l = 1, 2, 3, and 4 mm). A total of 28 different manufacturing conditions were thus explored.

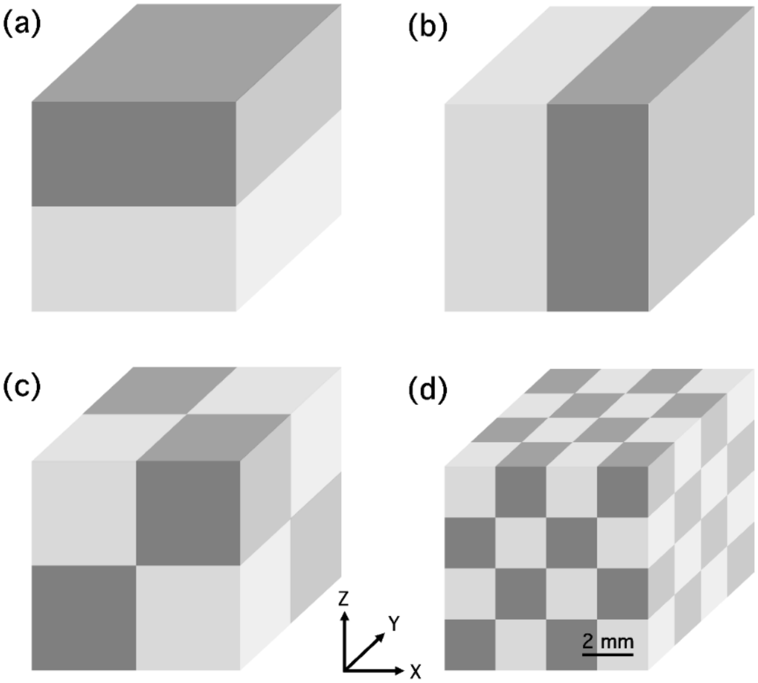

Figure 7-1: 8 x 8 x 8 $mm^3$ cubic samples manufactured by PBF-LB/M. (a) 8 x 8, (b) 4 x 8, (c) 4 x 4, and (d) 2 x 2. The different shades of gray indicate the *$h_d$50* (dark) and *$h_d$70* (light) sets of scanning parameters.

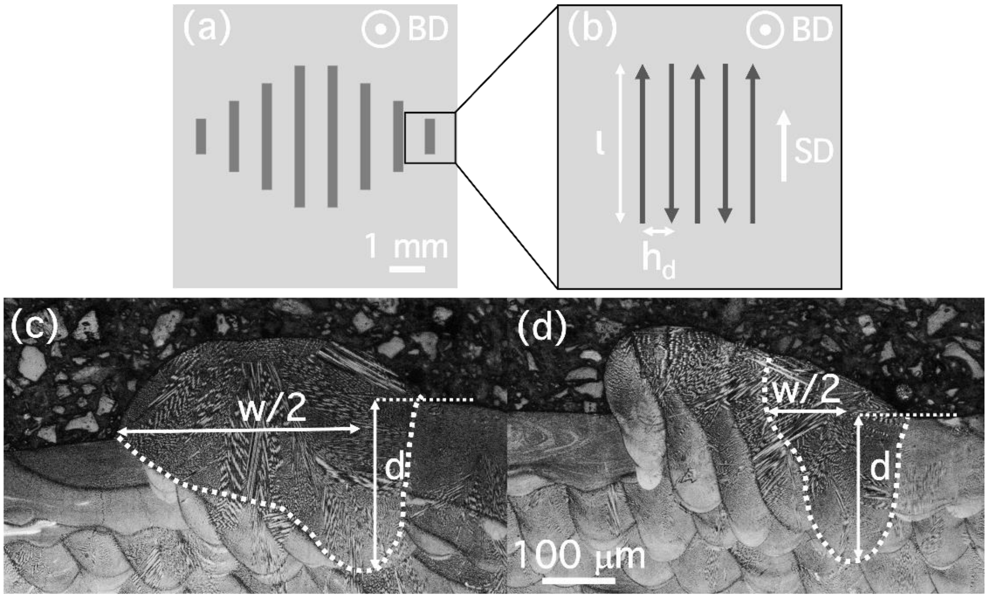

Figure 7-2: (a) Schematic illustrating several *multitracks* with scan track lengths ranging from 1 to 4 mm. (b) A magnified view of one *multitrack*, where the scan track length (*l*), and the hatch distance ($h_d$) are indicated. (c, d) Optical micrographs illustrating cross sections of the melt pools corresponding to multi-tracks with scan track lengths of (c) 1 mm and (d) 4 mm. The outline of the melt pool corresponding to the last track of each multitrack has been highlighted using a white dotted line, and the two melt pool characteristics that have been measured (width (*w*), depth (*d*)) are also indicated.

### *7.2.2. Sample characterization*

After fabrication, the cubic samples were removed from the build plate and prepared for characterization with OM and SEM following the procedures described in Section 3.3. Optical micrographs (OM) of the last layer of the samples were obtained using an Olympus BX51 light optical microscope, at a magnification of 100X. The melt pool depth (*d*) and width (*w*) were obtained by averaging the values corresponding to (at least) three different cross-sections, which were measured using the Image J software. Figure 7-3a and 7-3b are optical micrographs depicting, as an example, the melt pool stacking within the last layer of an 8x8 sample manufactured with $h_d50$ (Figure 7-3a) and $h_d70$ conditions (Figure 7-3b). Due to the significant overlap between adjacent melt pools (Figure 7-3c and 7-3d), only the melt pool half-width can be measured, and for the calculation of the full width we will assume that melt pools are symmetrical. In the multitrack specimens, only the last melt pool out of the five that integrate each group (outlined in Figure 7-2c, 7-2d, white dotted line) was considered. Note the asymmetry in width in the melt pools in Figure 7-2c, Figure 7-2d, which is due both to the overlap with the previously solidified material, which has enhanced thermal conductivity in comparison with the powder, as well as to the heat accumulation in previous tracks. Again, for the calculation of the full width in the multitrack samples, we have measured the half-width (*w/2*) highlighted in Figure 7-2c and Figure 7-2d, and considered the full width as double that value (as if the melt pools were indeed symmetrical).

The microstructure of the manufactured samples was examined by electron backscattered diffraction (EBSD). All EBSD maps were obtained using an accelerating voltage of 20 kV and a beam current of 6.4 nA. For large area EBSD maps, the step size was set at 2 µm, and for smaller maps it was set at 1 µm. EBSD data processing and analysis was performed using the HKL Channel5 software (Oxford Instruments) and the MTEX toolbox (5.10.2) [121] in MATLAB. Inverse pole figure (IPF) maps illustrating the orientation of the BD are shown for all manufactured cubes. Pole figures (PFs) were plotted using de la Vallée Poussin kernel, a band width of 10º, and a cluster size of 5º. Texture intensity quantification was carried out considering both the multiples of uniform distributions (MUD) from the pole figures, as well as by calculating the volume fractions ($V_f$) associated to different components by integration of the orientation distribution function (ODF), with a spread of 15º. Average grain sizes were estimated from the line intercepts (LI) measured along directions parallel and perpendicular to the BD, which will be referred to as longitudinal ($LI_l$) and transverse ($LI_t$) LI, respectively.

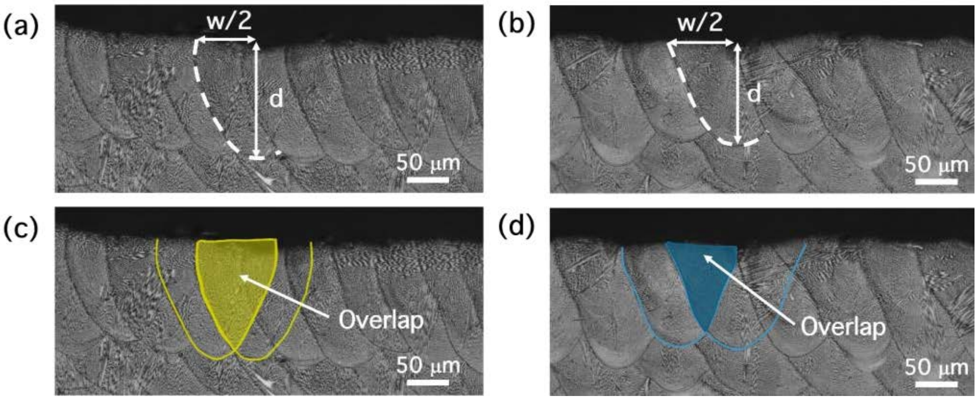

Figure 7-3: (a, b) Optical micrographs illustrating the melt pool stacking within the last layer of 8x8 samples manufactured with (a) $h_d50$, and (b) $h_d70$ conditions. (c, d) Schematic highlighting the overlapping area between adjacent melt pools in a direction perpendicular to the scan direction.

## 7.3. Results

### *7.3.1. Influence of the domain size on the microstructure*

Figure 7-4 compares large-area EBSD IPF maps in the BD corresponding to the cubic 8x8, 4x8, 4x4, and 2x2 samples. In the first three specimens (Figure 7-4a, 7-4b, 7-4c), which are formed by larger domains, clear differences between the texture in regions processed with $h_d50$ and $h_d70$ conditions can be appreciated. In particular, it is possible to qualitatively distinguish between areas where the dominant texture component is the <001>//BD fiber ($h_d50$, dark gray domains in Figure 7-1), and areas with more randomly oriented grains ($h_d70$, light gray domains in Figure 7-1). These two textures are similar to those reported for bulk IN939 samples using the same manufacturing conditions [99]. In the 2x2 specimen (Figure 7-4d), however, $h_d50$ and $h_d70$ manufacturing conditions give rise to undistinguishable microstructures, which contain a very large area fraction of columnar grains with a <001>//BD fiber texture. In the four cubic samples shown in Figure 7-4 the interfaces between $h_d50$ and $h_d70$ domains that are perpendicular to the BD are smooth, while those parallel to the BD retain the more randomly oriented microstructure as a result of the lack of sufficient overlap between the different STLs corresponding to each domain. Although useful to distinguish between different regions within the manufactured samples, these regions are not a result of local scanning parameter modifications and will thus not be discussed any further.

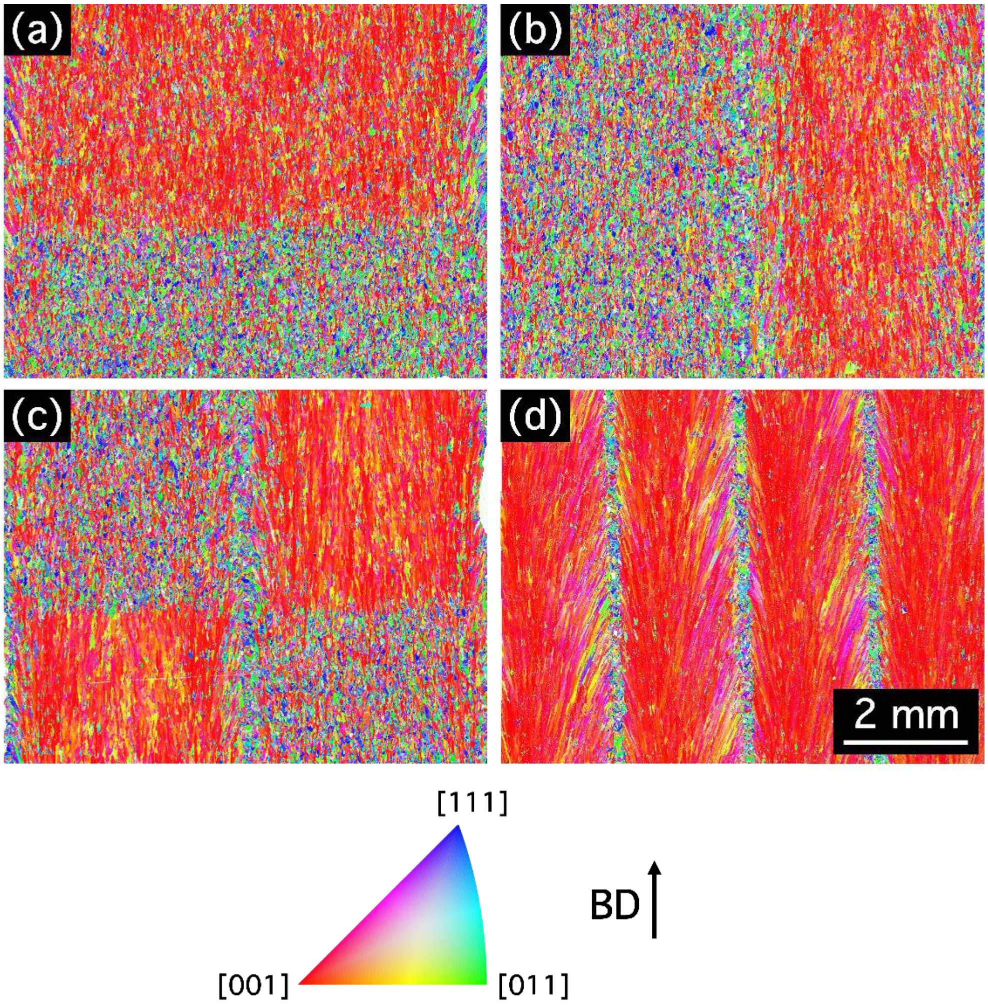

Figure 7-4: Large field of view EBSD IPF maps in the BD for (a) 8x8, (b) 4x8, (c) 4x4, and (d) 2x2 samples manufactured with $h_d50$ and $h_d70$ domains as shown in Figure 7-1.

The microstructure within $h_d50$ and $h_d70$ domains in samples 8x8, 4x8, 4x4, and 2x2 is described in more detail in Figure 7-5-8. In Figure 7-5 the microstructure corresponding to the 8x8 sample is shown by means of EBSD IPF maps in the BD (Figure 7-5a,b), by the grain boundary maps (GB) (Figure 7-5c,d), and by the (100), (110), and (111) direct PFs (Figure 7-5e,f) for $h_d50$, and $h_d70$ domains, respectively. The $h_d50$ domains (Figure 7-5a,c) are characterized predominantly by grains elongated along BD and a dominant <001>//BD fiber texture. The average line intercepts are $LI_l = 29$ µm and $LI_t = 11$ µm, which is equivalent to a line intercept ratio (LIR, $LI_l$/ $LI_t$) of 2.6. The $h_d70$ domain (Figure 7-5b,d) is formed by more equiaxed, weakly oriented grains, with $LI_l = 13$ µm and $LI_t = 8$ µm, and with LIR = 1.6. The maximum texture intensities, in MUD, are 7.5 and 1.8 for the $h_d50$ and $h_d70$ domains, respectively. The microstructure of $h_d50$ and $h_d70$ domains in the 4x8 samples (Figure 7-6) is very similar to that depicted in Figure 7-5 for the corresponding domains in 8x8 specimens. In the $h_{d}50$ domain, $LI_l$ = 30 µm, $LI_t$ = 9 µm, and LIR = 3.3; in the $h_{d}70$ domain, $LI_l$ = 14 µm, $LI_t$ = 7 µm, and LIR = 2. The maximum texture intensities amount to 10.3 and 2.1 MUD, respectively. Similarly, as illustrated in Figure 7-7, the microstructures of $h_{d}50$ and $h_{d}70$ domains in the 4x4 specimens resemble those found in 4x8 and 8x8 samples. In the $h_{d}50$ domain, $LI_l$ = 33 µm, $LI_t$ = 10 µm, and LIR = 3.3; in the $h_{d}70$ domain $LI_l$ = 13 µm, $LI_t$ = 8 µm, and LIR = 1.6. The maximum texture intensities increase slightly to 12.8 and 2.9 MUD for the $h_{d}50$ and $h_{d}70$ domains, respectively, and an incipient, weak <001>//BD fiber texture becomes apparent in the $h_{d}70$ domain. The microstructures described above for $h_{d}50$ and $h_{d}70$ domains in the 8x8, 4x8, and 4x4 samples are comparable to those reported earlier for bulk IN939 samples printed with the same scanning parameter sets [99]. However, when the domain size is further reduced, such as in the 2x2 sample (Figure 7-8), both $h_{d}50$ and $h_{d}70$ regions exhibit columnar grains with strong <001>//BD fiber textures, and with notably higher maximum texture intensities (19.4 and 11.3 MUD, respectively). The grain size also increases significantly: in $h_{d}50$ domains $LI_l$ = 104 µm, $LI_t$ = 18 µm, and LIR = 5.8; in $h_{d}70$ domains $LI_l$ = 93 µm, $LI_t$ = 24 µm, and LIR = 3.9.

In summary, our results show a strong influence of the domain size on the microstructure. Given the fact that the same two sets of processing parameters were utilized to manufacture the $h_{d}50$ and $h_{d}70$ domains in all cubic samples, the drastic change in grain size, shape and orientation observed in the smallest domains (2x2 specimen, Figure 7-4d and Figure 7-8) proves that microstructural development is highly dependent on the scan track length. In the following we will attempt to rationalize this dependence.

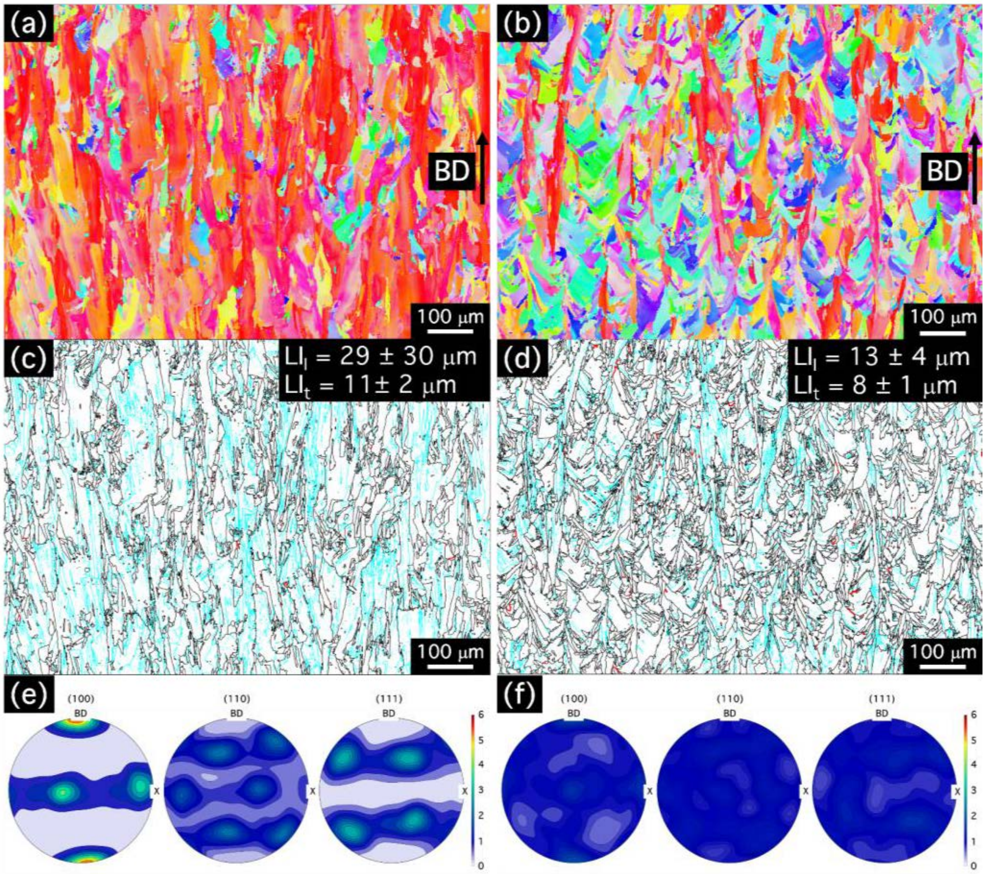

Figure 7-5: Microstructure within $h_d50$ (a,c,e) and $h_d70$ (b,d,f) domains of the 8x8 sample. (a,b) EBSD IPF maps in the BD; (c,d) GB maps (HAGBS are plotted in black, LAGBs are plotted in blue, and twin boundaries are plotted in red), and (e,f) direct (100), (110), and (111) pole figures.

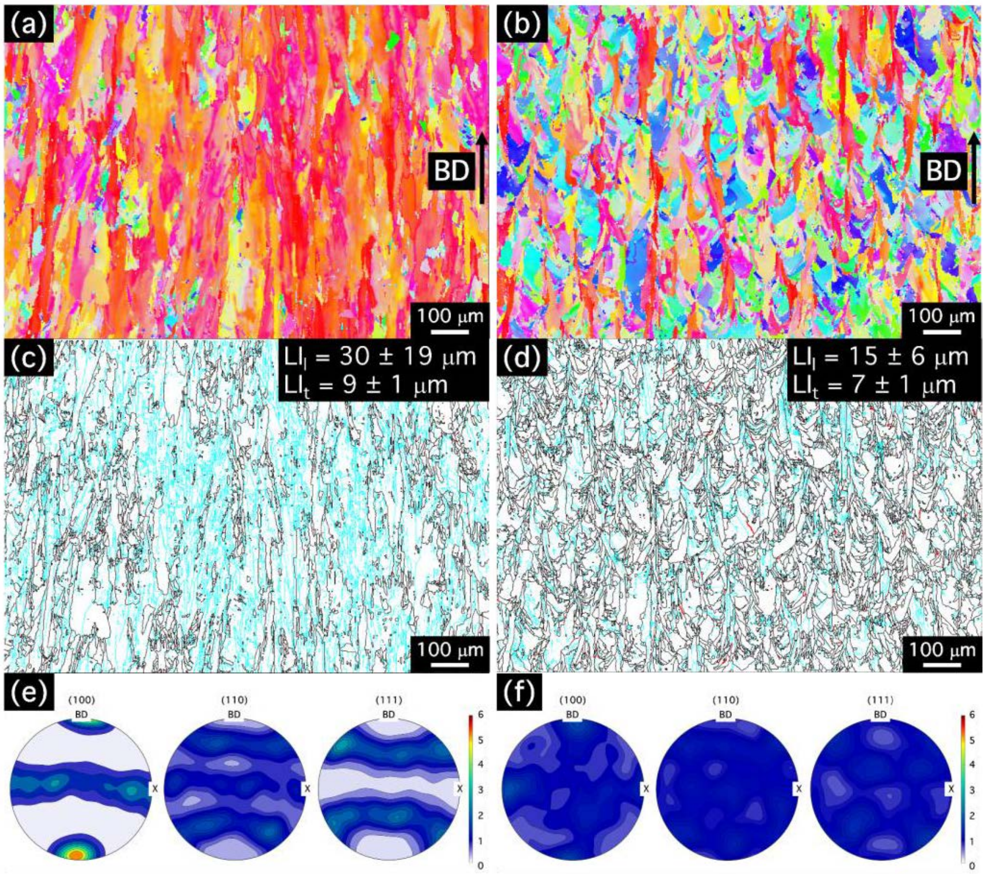

Figure 7-6: Microstructure within *h<sub>d</sub>50* (a,c,e) and *h<sub>d</sub>70* (b,d,f) domains of the 4x8 sample. (a,b) EBSD IPF maps in the BD; (c,d) GB maps (HAGBS are plotted in black, LAGBs are plotted in blue, and twin boundaries are plotted in red), and (e,f) direct (100), (110), and (111) pole figures.

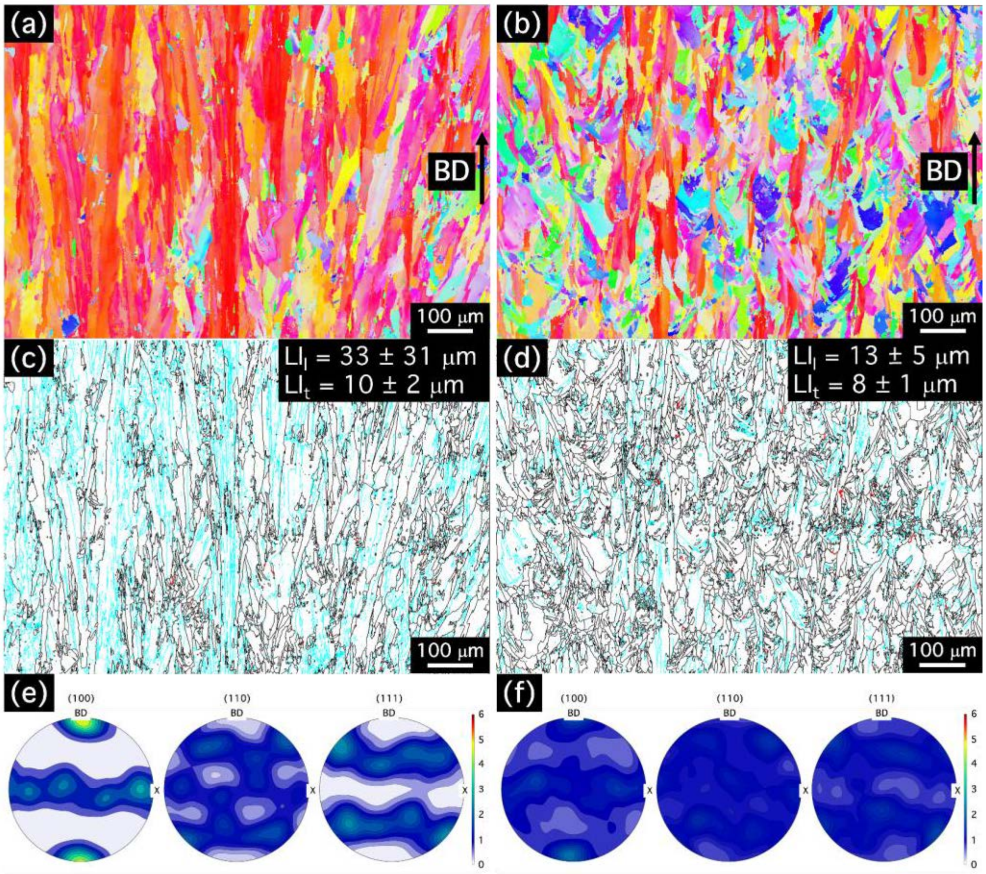

Figure 7-7: Microstructure within $h_d50$ (a,c,e) and $h_d70$ (b,d,f) domains of the 4x4 sample. (a,b) EBSD IPF maps in the BD; (c,d) GB maps (HAGBS are plotted in black, LAGBs are plotted in blue, and twin boundaries are plotted in red), and (e,f) direct (100), (110), and (111) pole figures.

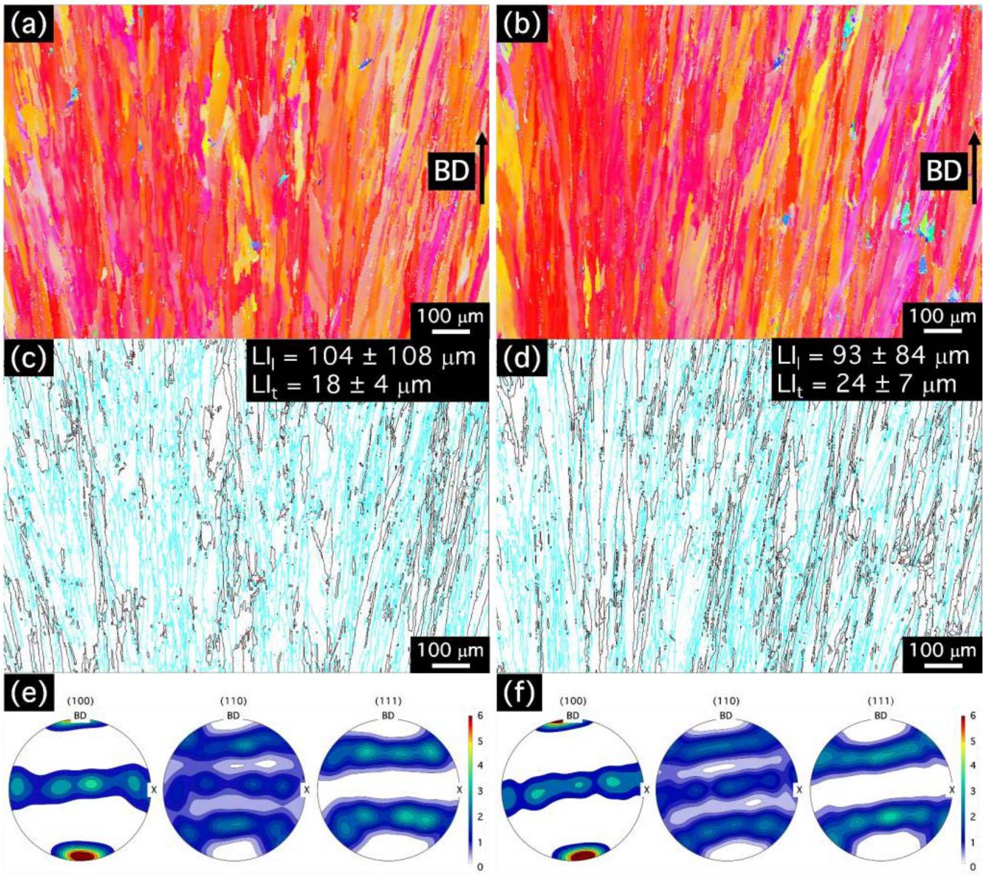

Figure 7-8: Microstructure within $h_d50$ (a,c,e) and $h_d70$ (b,d,f) domains of the 2x2 sample. (a,b) EBSD IPF maps in the BD; (c,d) GB maps (HAGBS are plotted in black, LAGBs are plotted in blue, and twin boundaries are plotted in red), and (e,f) direct (100), (110), and (111) pole figures.

### 7.3.2. Influence of the scan track length on the melt pool geometry

It is known that the laser scanning parameters determine the shape of the melt pool. As a simplistic rule of thumb, increasing $P$ deepens the melt pool, and decreasing $v$ widens it [21,43]. In order to investigate the origin of the drastic change in microstructure observed in the 2x2 specimens (Figure 7-4d and Figure 7-8), we will first analyze whether this change can be associated to variations of the melt pool geometry with the domain size (or, equivalently, with the scan track length ($l$)). Figure 7-9 compares the variation of the melt pool width ($w$) (Figure 7-9a), melt pool depth ($d$) (Figure 7-9b), and width to depth ratio $w/d$ (Figure 7-9c) in $h_d50$ and $h_d70$ domains within the 8x8, 4x8, 4x4, and 2x2 specimens. Measurements of $w$ and $d$ were performed on the last manufactured layer as described in Figure 7-3. Care was taken to ensure that the scan direction in that last layer was parallel to one of the domain sides, in such a way that $l = 8$ mm for 8x8 samples, $l = 4$ mm for 4x8 and 4x4 samples, and $l = 2$ mm for 2x2 samples. It can be seen in Figure 7-9 that, when $l \geq 4$

mm, the melt pool size remains moderately stable, and relatively similar for $h_d50$ and $h_d70$ conditions, and the $w/d$ ratio is close to unity. However, when $l = 2$ mm, as in 2x2 samples, the melt pools become significantly larger. Most notably, $w$ (Figure 7-9a) increases from ~150 µm to 490 µm and to 384 µm for $h_d50$ and $h_d70$ conditions, respectively. The increase in $d$ (Figure 7-9b) with decreasing $l$ is less drastic, although also clearly noticeable. More specifically, $d$ increases from ~140 µm to 218 µm and to 186 µm for $h_d50$ and $h_d70$ conditions, respectively. Figure 7-9c illustrates a significant increase of the melt pool $w/d$ ratio to a value larger than 2 when $l = 2$ mm for both $h_d50$ and $h_d70$ conditions.

The increase in $w/d$ ratio when $l = 2$ mm could explain the development of stronger <001>//BD fiber textures in the 2x2 sample (Figure 7-8), as the growth of grains with <001> directions parallel to BD will be favored in wide and shallow melt pools [69]. However, the similarity between $w$ and $d$ in $h_d50$ and $h_d70$ domains when $l \geq 4$ mm (Figure 7-9) suggests that melt pool shape *alone* does not determine microstructural development as these domains have very different microstructures (Figure 7-5-8. Thus, it is necessary to find an alternative parameter that can be effectively used to explain and control microstructure development during PBF-LB/M of the investigated IN939 alloy.

Figure 7-9: (a) Melt pool width, (b) melt pool depth, and (c) width to depth ratio, as a function of scan track length.

### 7.3.3. *Melt pool overlap as a microstructure design parameter*

In the following we will test whether the melt pool overlap can be a good microstructure predictor. We will focus in particular on the melt pool overlap fraction in the direction perpendicular to the scan direction (SD) and to BD ($O_h$), which can be calculated as $(w - h_d)/w$. Figure 7-10 plots the variation of the volume fraction of material with a <001>

direction oriented within 15º of BD ($V_{f<001>//BD}$) (Figure 7-10a), calculated by integration of the corresponding ODF, and LIR (Figure 7-10b) with respect to the $O_h$ for $h_d50$ and $h_d70$ domains in 8x8, 4x8, 4x4, and 2x2 samples (a total of 8 domains, two in each sample). There is a clear linear correlation between both $V_{f<001>//BD}$ and LIR with $O_h$. In particular, when $O_h < 0.6$, $V_{f<001>//BD} < 0.2$, and LIR < 2. Also, both $V_{f<001>//BD}$ and LIR increase linearly with $O_h$. Thus, it seems reasonable to select a threshold $O_h$ value of 0.6 as a microstructure selection parameter, below which PBF-LB/Med IN939 alloy will show an equiaxed, weakly oriented microstructure, and above which columnar grains with a strong <001>//BD fiber texture will develop.

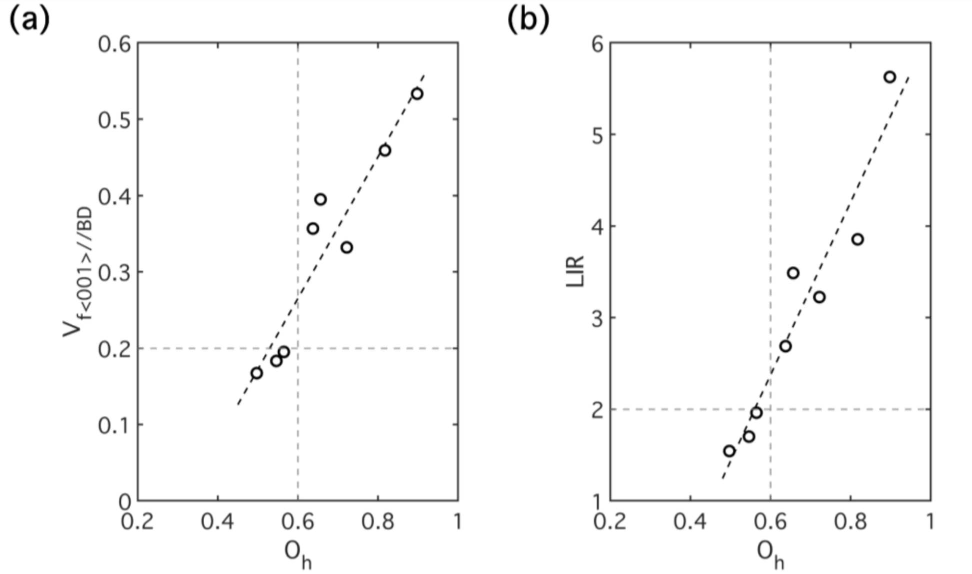

Figure 7-10: Effect of the melt pool overlap in (a) the volume fraction of the <001>//BD component, and (b) the line intercept ratio, for $h_d50$ and $h_d70$ domains in 8x8, 4x8, 4x4, and 2x2 samples. The horizontal and vertical dashed lines indicate the selected thresholds for (a) the volume fraction of the <001>//BD component (=0.2) and (b) the line intercept ratio (=2).

In order to determine the relationship between the overlap and processing parameters such as $l$ and $h_d$, 28 multitracks were printed with the same $P$ and $v$ values as those utilized to manufacture the cubic samples, and with combinations of 7 $h_d$ (40, 50, 60, 70, 80, 90, 100 µm), and four scan track lengths ($l$ =1, 2, 3, and 4 mm). Figure 7-11 illustrates the variation of $w$ (Figure 7-11a) and $d$ (Figure 7-11b), and of the corresponding $O_h$ (Figure 7-11c), with $h_d$ and $l$ for the 28 multitrack printing conditions investigated. For a fixed $h_d$, $w$ and $d$ increase with decreasing $l$. The increase in $w$ and $d$ is more pronounced for small $h_d$. Conversely, for a fixed $l$, $w$ and $d$ increase with decreasing $h_d$, and the increase is most notable for $l < 2$ mm.

The melt pool overlap fraction increases as $l$ and $h_d$ decrease but is more sensitive to changes in the latter (for $h_d$ affects melt pool width and $O_h$ simultaneously).

The dashed line in Figure 7-11c indicates the 0.6 threshold overlap value previously selected from Figure 7-10. For $l$ = 1.62 mm (i.e, the average $l$ in a 2x2 sample with 67º interlayer rotation), the two $h_d$ values used in the present study (50 and 70 µm, solid yellow dots in Figure *7-11*c) give rise to an $O_h$ that is larger than 0.6 and, in agreement with the discussion above, to a strong <001>//BD fiber texture, as shown in Figure 7-8. Figure 7-11c suggests that, if the selection of 0.6 as a threshold overlap is accurate, in order to manufacture 2x2 domains with weak textures using a meander strategy with a 67º interlayer rotation, we should increase $h_d$ (see arrow in Figure 7-11c) beyond 82 µm. In order to check the validity of this prediction, a new 2x2 cubic sample was manufactured with domains printed with the same $P$ and $v$ conditions but alternating $h_d$ values of 50 ($h_d50$) and 100 µm ($h_d100$) (see blue dot in Figure 7-11c). Figure 7-11d shows a wide field of view EBSD IPF map in the BD of the new 2x2 sample. Indeed, as predicted, the microstructure is now formed by alternating regions with strong and weak textures. As depicted in more detail in Figure 7-12, in the $h_d50$ domains, $LI_l$ = 83 µm, $LI_t$ = 23 µm, and LIR = 3.6. Conversely, in the $h_d100$ domains $LI_l$ = 15 µm, $LI_t$ = 10 µm, and LIR = 1.5. The maximum texture intensities are 12.7 and 2.5 MUD for the $h_d50$ and $h_d100$ domains, respectively. A note must be made here regarding the need to ensure that the selected scanning parameters will not result in lack of fusion due to insufficient overlap. We have used the full melting criterion presented by Tang et al. [37].

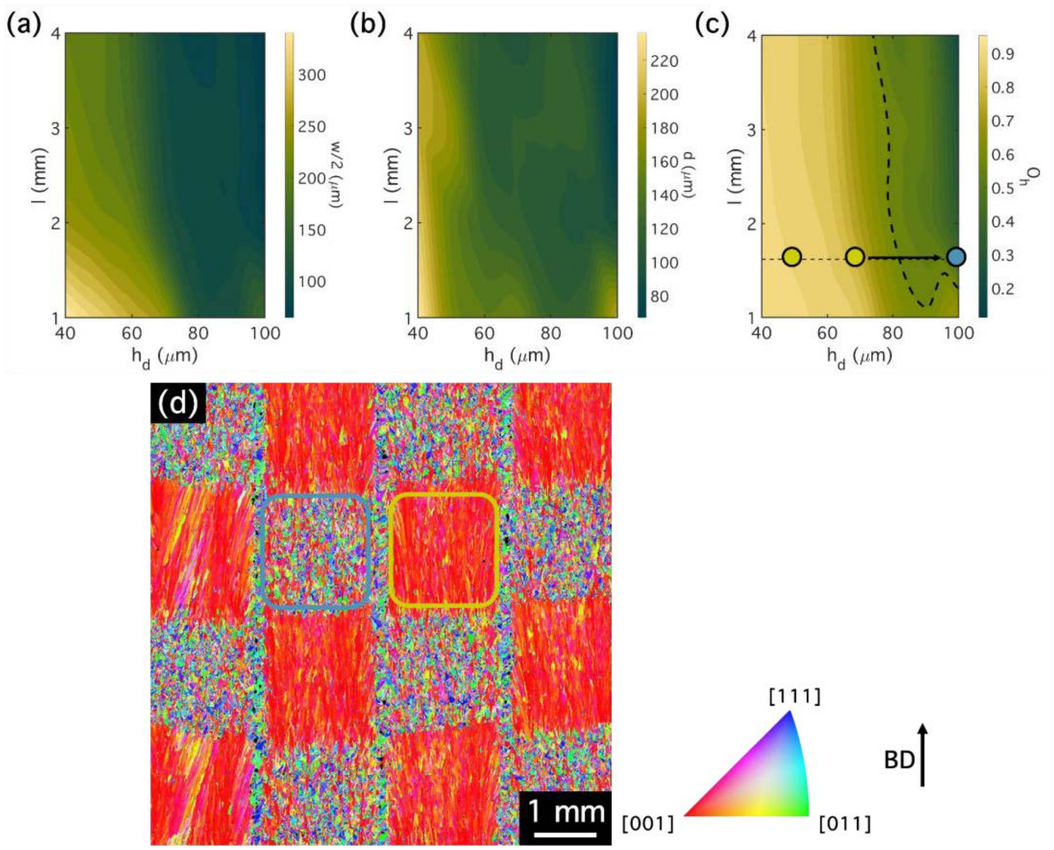

Figure 7-11: Variation of (a) $w/2$, (b) $d$, and (c) $O_h$ as a function of $l$ and $h_d$ in the multitrack samples. In (c) the black dashed line indicates the 0.6 $O_h$ threshold; the yellow dots indicate $h_d50$ and $h_d70$ conditions in the 2x2 sample, and the blue dot indicates the $h_d100$ conditions selected for the manufacturing of the new 2x2 sample shown in (d). (d) Large field of view EBSD IPF map in the BD for a 2x2 sample manufactured with $h_d50$ (yellow outline) and $h_d100$ (blue outline) domains.

In summary, our results show that $O_h$ can be used as an accurate and simple predictor of microstructure development during laser powder bed fusion of the IN939 alloy, at least for the $P$ and $v$ conditions investigated (250 W and 1.167 $m \cdot s^{-1}$). Furthermore, this work also emphasizes the possibility to use multitracks as a high throughput method to gather extensive experimental data with very limited resources and, in particular, to build $O_h$ maps that are the basis for successful microstructure prediction in bulk samples.

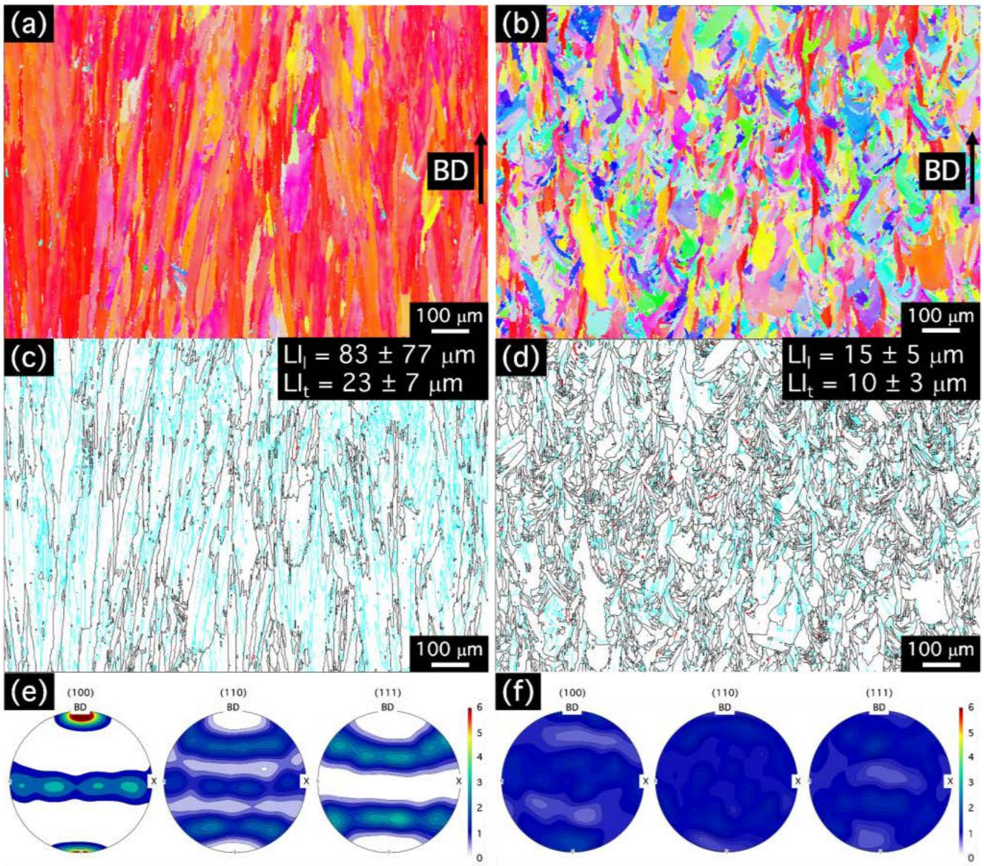

Figure 7-12: EBSD (a),(b) IPF-BD coloring maps, (c),(d) GB maps, and (e),(f) pole figures for 2x2 mm$^2$ domains printed using (a),(c),(e) $h_d$ = 50 µm, and (b),(d),(f) $h_d$ = 100 µm. For all cases P = 250 W, and v = 1.167 m·s$^{-1}$.

## 7.4. Discussion

### *7.4.1. Rationalizing the role of the melt pool overlap as a microstructure design parameter*

In the following we attempt to understand the origin of the suitability of $O_h$ as a simple and accurate predictor of microstructural development during PBF-LB/M of IN939, at least for the $P$ and $v$ conditions investigated here (P = 250 W, v = 1.167 m·s$^{-1}$). Earlier studies have reported a strong influence of the number of remelting cycles undergone by the processed material on texture and microstructure development [178,187]. Manufacturing each scan track involves melting powder as well as remelting a fraction of solid material from adjacent layers and scan tracks. Remelting favors the growth of already existing grains oriented in a preferred growth direction (<001>//BD for IN939), preventing newly nucleated grains from growing. The more melting cycles the material undergoes, the more chances the grains oriented in a <001>//BD direction will have to outgrow other grains.

It seems obvious that the overlap will have a strong effect on remelting. As a first approximation, in the following we estimate the influence of $O_h$ on the number of melting cycles during fabrication of a single layer in 8x8 samples processed using $h_d50$ and $h_d70$ conditions, for which $O_h = 0.64$ and 0.5, respectively. Figure 7-13a and 7-13b are two optical micrographs where 5 adjacent melt pools belonging to the last layer of these two samples are highlighted, respectively. For the calculation of the remelting cycles we will assume that melt pools are semi-ellipses, that $w/2$ and $d$ are the semi-major axes, and that $h_d$ is their offset in a direction normal to both the SD and BD. Figure 7-13c and Figure *7-13*d illustrate the schematic representation of a layer of idealized semi-elliptical melt pools with the dimensions measured from the samples depicted in Figure 7-13a and Figure *7-13*b, respectively. Increasingly darker shades of gray in Figure 7-13a-d indicate a higher number of local melting cycles within one melt pool during fabrication of the single layer. Figure 7-13e shows the area fraction of a single melt pool that has gone through 1, 2, and 3 melting cycles during fabrication of a layer as a function of $O_h$. In $h_d50$ melt pools the area fractions undergoing 1,2, and 3 cycles are, respectively, 0.07, 0.43, and 0.50, while in $h_d70$ melt pools the corresponding fractions are 0.22, 0.78, and 0. As expected, increasing $h_d$ decreases remelting. In particular, a 22% decrease in overlap increases the fraction of material that is only melted once by as much as 214%. The high sensitivity of $O_h$ to changes in the fraction of material that is melted only once explains its potential as a significant microstructure predictor.

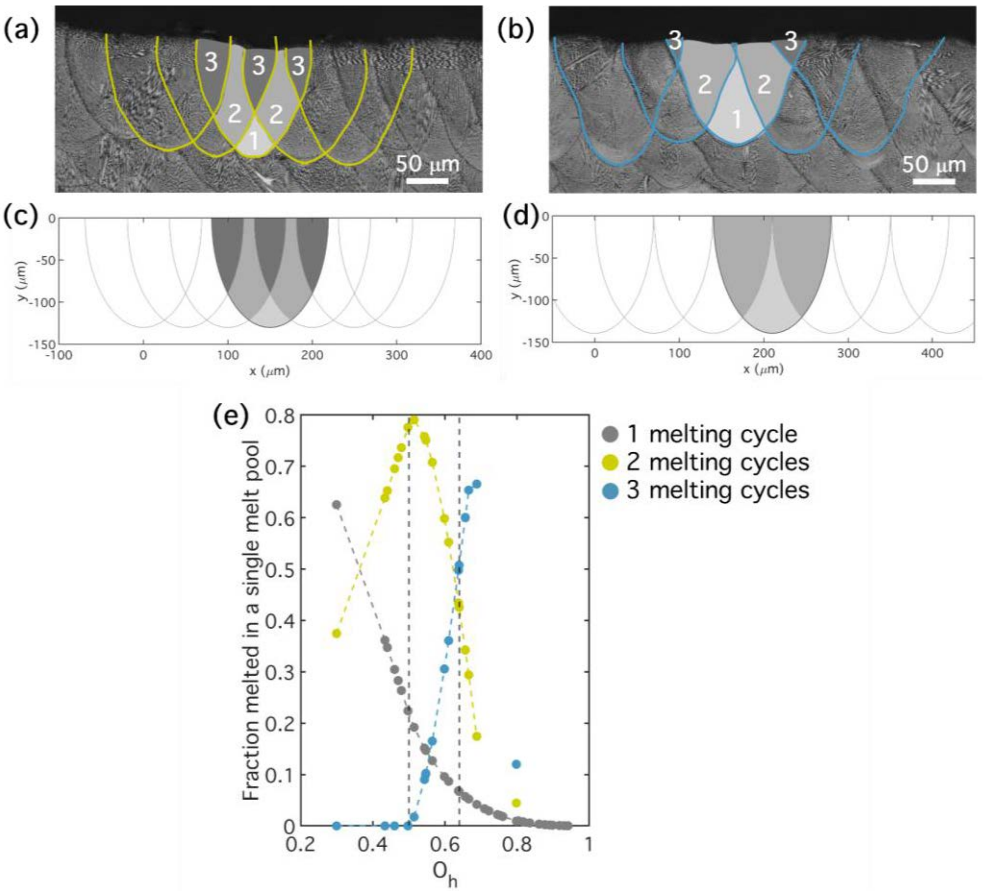

Figure 7-13: (a, b) Optical micrographs where 5 adjacent melt pools within the last layer of an 8x8 sample manufactured using (a) $h_d50$, and (b) $h_d70$ conditions are highlighted. The numbers refer to the number of melting cycles during fabrication of one layer. (c, d) Representation of the melt pools for (c) $h_d50$, and (d) $h_d70$ as ideal semi-ellipses with the minor axis equal to *w* and the major axis equal to 2*d*. Increasingly darker shades of gray indicate regions that underwent a higher number of melting cycles during fabrication of a single layer. (e) Area fraction of a melt pool undergoing 1,2, and 3 melting cycles during fabrication of a single layer as a function of $O_h$. The vertical dashed lines indicate the melt pool overlap for $h_d70$ (0.5), and for $h_d50$ (0.64).

The suitability of $O_h$ as a simple and accurate predictor of microstructural development during PBF-LB/M of IN939 has been tested in the current study only for one set of *P* and *v* conditions (P = 250 W, v = 1.167 m·s$^{-1}$). In the following we explore whether the use of the overlap can be extended to other *P* and *v* conditions. Figure 7-14 compares the variation of $V_{f<001>//BD}$ (Figure 7-14a) and LIR (Figure 7-14b) with respect to $O_h$ for the 8 different domains from this study ($h_d50$ and $h_d70$ domains in 8x8, 4x8, 4x4, and 2x2 samples, data plotted in Figure 7-10) as well as for samples from two previous studies [99,101], in which the IN939 alloy was processed using the same machine and different *P*, *v*, $h_d$, and *l* conditions (P ∈ (250-300) W, *v* ∈ (0.875-1.4) m·s$^{-1}$, $h_d$ ∈ (50-90) μm, *l* ∈ (0.74-6.64) mm). Figure 7-14 reveals that when $O_h$ > 0.6 there is a large scatter, and no clear correlation can be established.

For example, in samples produced with very low scanning speeds (dark blue symbols in Figure 7-14) equiaxed, weakly oriented grains are produced even when $O_h > 0.9$. The reasons behind the observed scatter are unclear. However, $O_h$ values below 0.6 yield *always* weak textures ($V_{f<001>//BD} < 0.2$) and equiaxed grains (LIR < 2), regardless of the processing conditions.

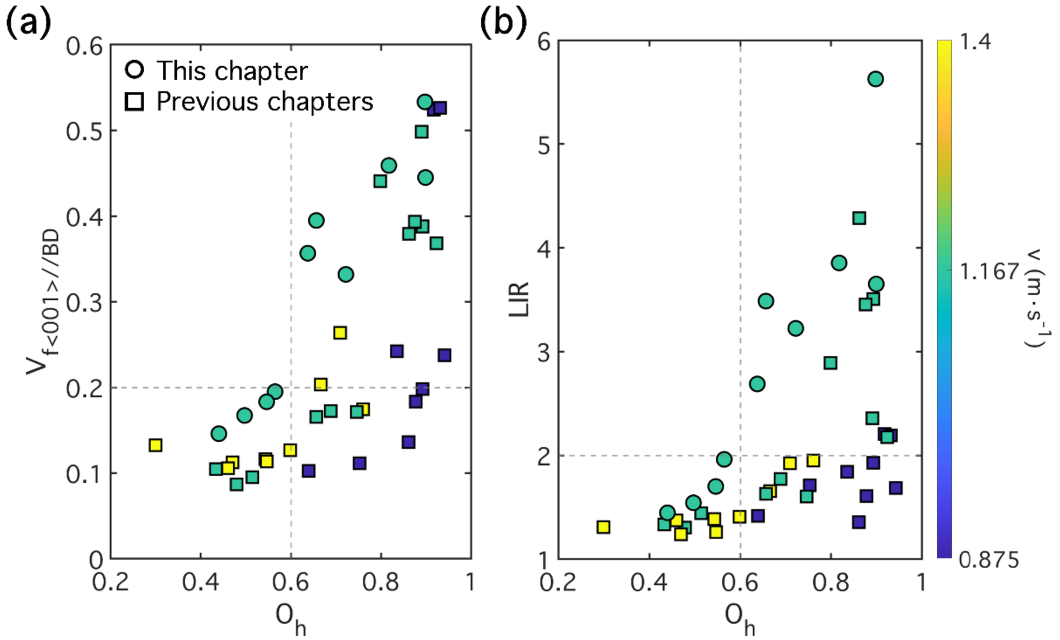

Figure 7-14: (a) Volume fraction of the <001>//BD component, and (b) line intercept ratio, as a function of $O_h$. Data correspond to for the 8 different domains from this study ($h_d50$ and $h_d70$ domains in 8x8, 4x8, 4x4, and 2x2 samples, data plotted in Figure 7-10) as well as to samples from two previous studies [99,101]. The color coding reflects the scanning speed. The horizontal dashed lines indicate the thresholds for (a) the volume fraction of the <001>//BD component (=0.2) and (b) the line intercept ratio (=2).

### *7.4.2. An analytical approach for microstructural design based on the melt pool overlap*

The Rosenthal equation (1) was first developed to describe the temperature evolution during welding, and its wide use stems from its simplicity and its ability to predict the spatial and temporal evolutions of $T$. It has the following expression:

$$T = T_0 + \frac{AP}{2\pi\kappa r} exp - v\left[\frac{r-x}{2\alpha}\right] \quad (7.1),$$

where $T_0$ is the substrate temperature, $A$ is the surface absorptivity, $\kappa$ is the thermal conductivity, $r$ is the radial distance from the heat source ($r = \sqrt{x^2 + y^2 + z^2}$), with $x$ as the distance in the direction in which the laser is moving, and $\alpha$ is the thermal diffusivity.

The Rosenthal equation has been successfully applied to model PBF-LB/M processes in the conduction mode. For example, it was used by Tang et al. [37] to obtain estimates of the melt pool dimensions in order to predict lack-of-fusion occurrences, and by Promoppatum et al. [188] to predict melt pool dimensions, temperature gradient, cooling rate, and solidification rate, that were in good agreement with more complex numerical predictions and with experimental results. While the Rosenthal equation provides relatively good estimates of $T$ at the melt pool boundaries, this does not necessarily apply to the interior of melt pools [67]. Furthermore, this equation assumes that heat transfer is governed only by conduction, neglecting both radiation and convection, and thus its validity within the keyhole regime is questionable, as convection plays an increasingly significant role in heat transfer as we enter said regime.

Our results have shown that $h_d$ and $l$ have a notable influence on $O_h$ and, in turn, on the resulting microstructure. Recently, Phan et al. [189] introduced a modification of the Rosenthal equation which accounts for these two variables:

$$T_0 = T_{preheat} + \frac{AP}{2\pi\kappa((vt_r)^2+h_d^2)^{1/2}} \cdot exp - v\left[\frac{((vt_r)^2+h_d^2)^{1/2}-vt_r)}{2\alpha}\right] \qquad (7.2),$$

where $T_{preheat}$ is the powder bed preheat temperature (RT in this study) and $t_r$ is the rescan time. For a sample with an average scan track length $l$, and fabricated using a constant scanning speed $v$, Phan et al. assumed that $t_r = (l/2)/v$ [189], i.e., they defined $t_r$ as the time it takes the laser to travel from the edge of the sample to the point of reference and, as shown in Figure 7-15b, this leads to inconsistencies for small $l$ values (for the range of scanning parameters tested in this study, and assuming A = 0.3). Thus, here we will define $t_r$ as the time it takes the laser to return to a location directly adjacent to a point of reference, separated only by $h_d$ ($t_r = l/v$). Figure 7-15a shows the evolution of $T_0$ as a function of $l$ and of $h_d$ predicted by equation 2 for the conditions used to manufacture the multitracks (P = 250 W and v = 1.167 m·s$^{-1}$, $h_d$ between 40 and 100 μm, and $l$ comprised between 1 and 4 mm). While the $T_0$ curves for all $h_d$ values tend to the same baseline value at larger $l$, the differences for $l$ < 3 mm are noticeable. In particular, for a constant $h_d$, $T_0$ increases with decreasing $l$, while for a constant $l$, $T_0$ increases with decreasing $h_d$. The evolution of $T_0$ with $h_d$ and with $l$ shown in Figure 7-15a is consistent with our observations of the evolution of the melt pool size as a function of these two variables shown in Figure 7-9.

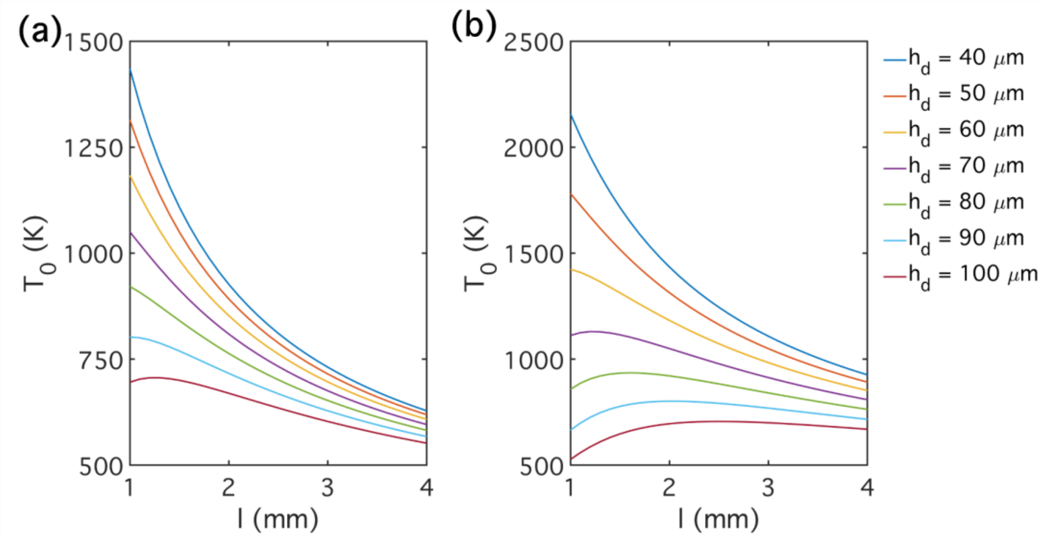

Figure 7-15: Evolution of $T_0$ as a function of l and $h_d$ for P = 250 W and v = 1.167 m·s$^{-1}$.

A change in $T_0$ has a direct impact on the effective energy input. In PBF-LB/M, when discussing energy input, most studies use the volumetric energy density ($E_v$), as it encompasses four of the main laser scanning parameters in a simple expression [55]:

$$E_v = \frac{P}{v \cdot h_d \cdot t} \tag{7.3}$$

For a given setup and material, $E_v$ illustrates rather well the optimum energy input regime. However, it does not necessarily relate well to melt pool dimensions, and it does not include any material-dependent properties, which hinders the comparison between alloying systems [57,190]. The normalized (or dimensionless) enthalpy ($\Delta H/h_s$) is another variable used in the welding and PBF-LB/M communities to express energy input as a combination of different processing parameters [60,61]:

$$\frac{\Delta H}{h_s} = \frac{AP}{\rho(C_p(T_s - T_0) + L_m)\sqrt{\pi\omega^3 v\alpha}} \quad (7.4),$$

where $\rho$ is the density, $C_p$ is the specific heat capacity, $T_s$ is the melting temperature, $L_m$ is the latent heat of fusion, $\omega$ is the laser beam radius. A reported advantage of the normalized enthalpy is the possibility of directly relating energy input to melt pool depth and of comparing between different materials and systems [61,62]. A third option is to consider a normalized volumetric energy density ($E_v^*$) [58,59]:

$$E_v^* = \frac{P^*}{v^* h_d^* t^*} = \frac{AP}{(2vh_d t)(\rho C_p(T_s - T_0))} \quad (7.5),$$

which includes similar material-related parameters as the normalized enthalpy. None of these three variables include the effect of $l$, and $\Delta H/h_s$ does not include $h_d$ either.

Figure 7-16a and 7-16b show the variation of $O_h$ with $\Delta H/h_s$ and $E_v^*$, respectively, for the PBF-LB/M-manufactured IN939 $h_d50$ and $h_d70$ domains of the cubic samples from the current study, and for those of our two previous studies [99,101], using $T_0$ = RT. A large scatter of the data is observed, and no clear correlations can be derived. In particular, in Figure 7-16a, all samples with the same combination of $P$ and $v$ are wrongly considered to have the same energy input, and the same applies in Figure 7-16b to all samples printed using the same $P$, $v$, and $h_d$. Figure 7-16c and 7-16d show the variation of $O_h$ with $\Delta H/h_s$ and $E_v^*$, respectively, calculated using the $T_0$ derived from the modified Rosenthal equation (7.2). The $\Delta H/h_s$ and $E_v^*$ thus calculated, which will be named hereafter *modified* $\Delta H/h_s$ and *modified* $E_v^*$, account for the effect of $l$ and $h_d$ on the heat accumulation during PBF-LB/M processing. With this modification, the correlation between $O_h$ and the *modified* $\Delta H/h_s$ (Figure 7-16c) is considerably better than that of $\Delta H/h_s$. This effect is even more clear in Figure 7-16d, which shows the high correlation between $O_h$ and the *modified* $E_v^*$ over the whole range of studied scanning parameters ($R^2$=0.86). The regression curve corresponding to the data in Figure 7-16d is given by:

$$O_h = 0.45 \ln(Modified\ E_v^*) + 0.28 \qquad (7.6).$$

Figure 7-17 compares the $O_h$ values predicted by equation (7.6) with the $O_h$ measured experimentally in the $h_d50$ and $h_d70$ domains of 8x8, 4x8, 4x4, and 2x2 samples (Figure 7-4), as well as in other bulk IN939 samples of our previous studies [99,101]. The agreement between the predicted and measured values is good, with a 93 % accuracy at determining whether $O_h$ will be below or above the 0.6 threshold.

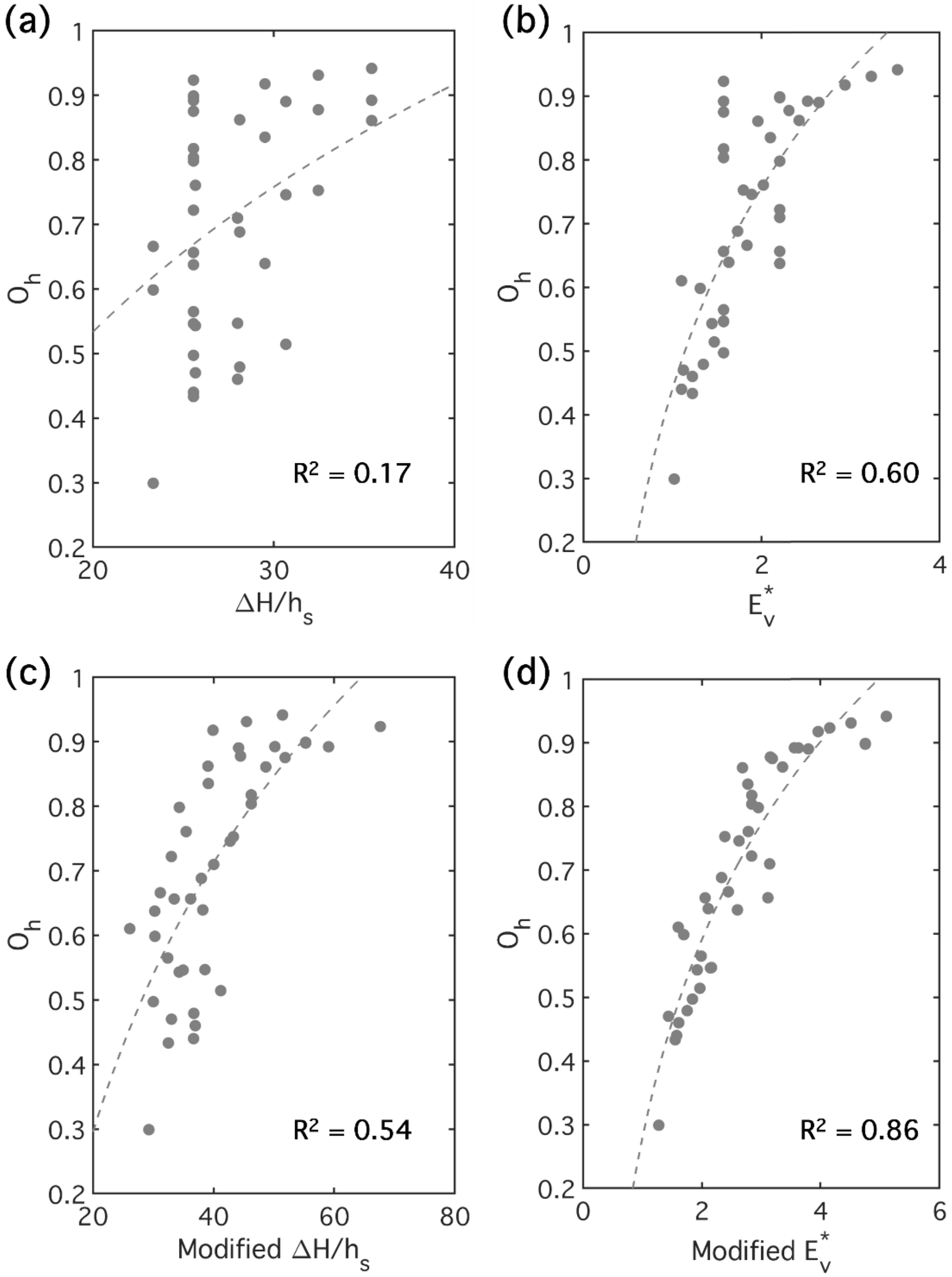

Figure 7-16: Melt pool overlap ($O_h$) as a function of (a) normalized enthalpy, (b) normalized volumetric energy density, (c) modified normalized enthalpy, and (d) modified normalized volumetric energy density.

Given the high correlation of the data in Figure 7-16d, we will now examine whether we can utilize the relationship of $O_h$ with the *modified* $E_v^*$ as an analytical approach for microstructural design in the 2x2 sample. As mentioned earlier, in this cubic sample the average $l$ is equal to 1.62 mm. We can then fix two more scanning parameters (for example, $h_d = 70$ μm and $v = 1.167$ m·s$^{-1}$) and use equation (7.6) to calculate the value of $P$ for which $O_h = 0.6$ (threshold value determined in section 7.3.3). The result is 180 W. Thus, any value of *P* lower than 180 W should yield $O_h < 0.6$, and thus a domain with weak texture and equiaxed grains. To test the validity of this analytical approach for microstructure design, we manufactured a 2x2 sample by alternating the $h_d70$ domains of Figure 7-4d with domains printed using the same $h_d$ and *v*, but with P = 175 W ($h_d70$-$175$) instead of P = 250 W. The microstructure and the texture corresponding to each domain is shown in Figure 7-18. Representative $h_d70$ and $h_d70$-$175$ domains are highlighted with yellow and blue squares, respectively. When the *P* is reduced to 175 W, the $V_{f\,<001>//BD} = 0.2$, and the grains are relatively equiaxed (LIR = 1.5). Both characteristics comply with the aforementioned criteria for an "equiaxed, weakly textured" domain.

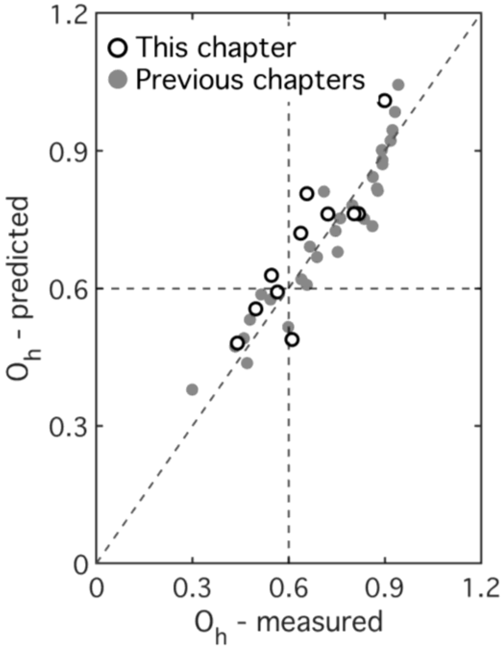

Figure 7-17: Comparison between the $O_h$ values predicted from the logarithmic fit given by eq. (6) (Figure 7-16d), and the experimentally measured $O_h$. Full symbols correspond to data from previous studies [99,101], and empty symbols correspond to data from this study.

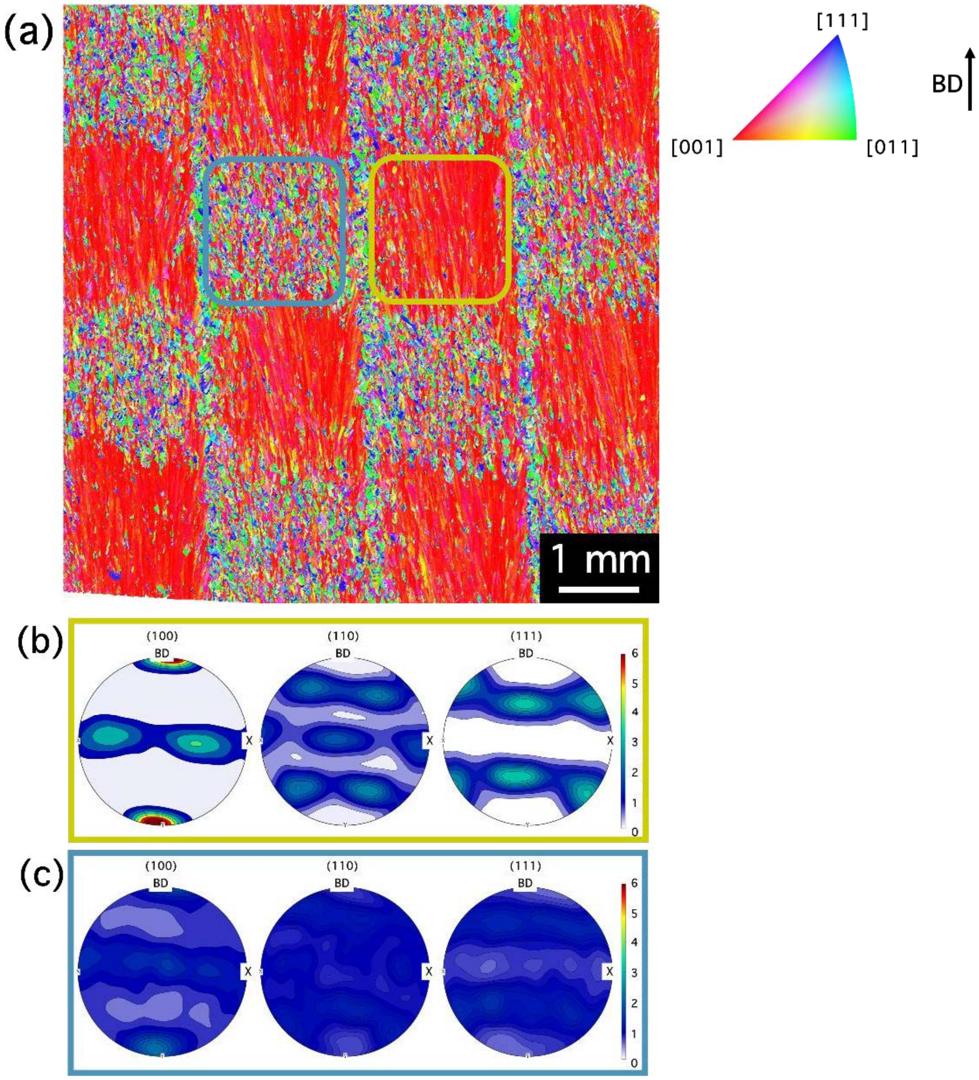

Figure 7-18: (a) EBSD IPF coloring map in the BD corresponding to a 2x2 sample formed by $h_d$ *70* (yellow square) and $h_d$ *70-175* (blue square) domains, as well as (b, c) the corresponding pole figures.

### *7.4.3. Outlook*

In this work we present empirical and analytical approaches for microstructural control during PBF/M-LB of the IN939 alloy over a relatively wide range of processing conditions. It must be emphasized that we have utilized a layer thickness of 60 μm, and fast scanning speed, which are common practice in industry for enhanced productivity, as well as a standard 67º layer rotation. Advanced tools for microstructural design are in great need for the manufacture of complex geometry specimens, where processing conditions must be adapted for sections with different thicknesses, a daunting task that is usually undertaken in industry by time-consuming trial and error methods, and it is often too complex to be accomplished successfully. In Figure 7-19, the methods for microstructure control presented here have been used to design the logo of our Sustainable Metallurgy group at IMDEA Materials, reversing the areas with strongly/weakly textured microstructures, as 2D proxy of their applicability to complex geometries. We envision that these approaches could be easily extended to other Ni-based superalloys, and eventually to other metallic materials.

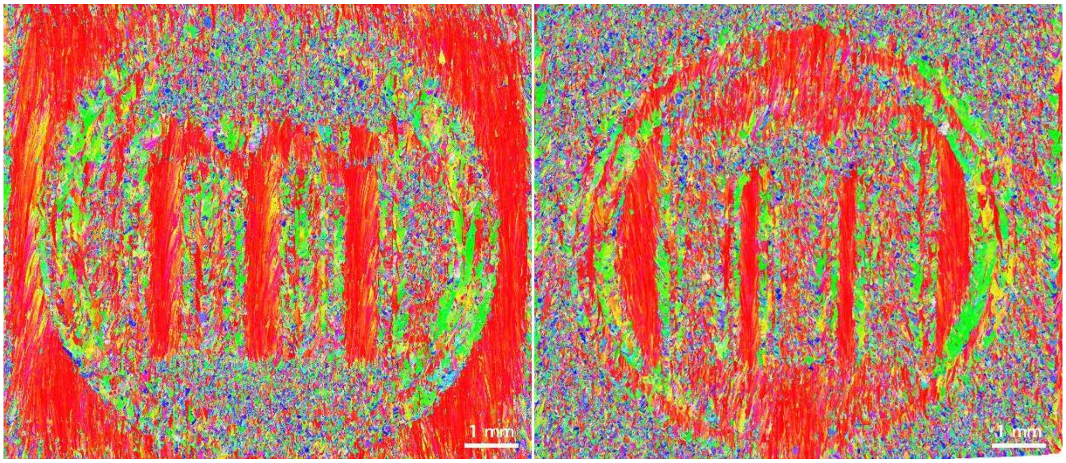

Figure 7-19: Large EBSD IPF maps showing examples of 2D microstructure design. The depicted design is the Sustainable metallurgy group logo. The areas of strongly and weakly textured microstructures are reversed. The scanning parameters for each region were selected using the logarithmic fit from eq. (6) to ensure the desired $O_h$ was achieved.

## 7.5. Conclusions

This work aims to develop a simple and effective methodology to control and design microstructures within IN939 parts with complex geometries by PBF-LB/M, using industrially scalable scanning strategies. Both empirical and analytical approaches are presented to select the processing parameters leading to the development of either columnar grains with <001>//BD fiber textures or equiaxed, weakly oriented grains, at a local scale. The following conclusions can be drawn from this study:

1. The scan track length and the hatch distance have a strong influence in microstructure development during PBF-LB/M of the IN939 Ni-based superalloy. Columnar microstructures with strong <001>//BD fiber textures become dominant as $l$ decreases, for a fixed $h_d$, and as $h_d$ decreases, for a fixed $l$.
2. The melt pool overlap perpendicular to SD and BD is an effective design tool that allows to accurately predict microstructure during PBF-LB/M of IN939. Processing conditions leading to overlaps below a threshold of 0.6 avoid excessive epitaxial

growth and thus result in equiaxed, weakly oriented microstructures for a relatively wide range of $P$, $v$, and $h_d$ PBF-LB/M conditions.

3. The scan track length affects the actual energy input during fabrication, and it needs to be accounted for when selecting the scanning parameters. The combination of a modified Rosenthal equation and a reformulated version of the normalized volumetric energy density, incorporating the scan geometry and the material properties, are shown to constitute an effective analytical microstructure prediction framework. In particular, we demonstrate that a simple logarithmic regression from this modified $E_v^*$ with respect to the melt pool overlap can be used to predict the scanning parameters (beyond the realm of those tested empirically) that are suitable to manufacture the microstructures of choice.
4. Multitracks are a fast, simple, and high-throughput experimental solution to build melt-pool overlap contour plots for multiple combinations of $P$, $v$, $l$, and $h_d$. It has been shown that they constitute a very valuable tool for the empirical selection of adequate scanning parameters to obtain the desired microstructures.

# 8. CONCLUSIONS

PBF-LB/M processing on Ni-based superalloys is a subject of indisputable interest, offering promising advancements in fields such as aeronautics and the energy industry. Many efforts have been made to produce good quality parts, and extensive work has been done expanding the understanding of the process and its effects.

This study addresses various aspects related to PBF-LB/M processing of IN939. The first focus is processability, with the objective of mitigating defect formation, in a variety of geometries. It then deals with the influence of the AB microstructure on the recrystallization kinetics. The mechanical properties of PBF-LB/M IN939 are assessed after different thermal treatments and compared to those of cast parts. Finally, the possibility of locally tuning the microstructure by using the melt pool overlap as a key tool. Based on the main results reported in this thesis, the following conclusions can be extracted:

- IN939 can be successfully processed using PW PBF-LB/M, achieving relative densities consistently exceeding 99.5 % and crack densities of $0.25 \times 10^{-2}$ $mm \cdot mm^{-2}$. Two different sets of scanning parameters were identified as optimum, namely $P = 250$ W, $v = 1.167$ $m \cdot s^{-1}$, $h_d = 70$ μm, $E_v = 51$ $J \cdot mm^{-3}$ ($h_d70$), and $P = 250$ W, $v = 1.167$ $m \cdot s^{-1}$, $h_d = 50$ μm, $E_v = 71$ $J \cdot mm^{-3}$ ($h_d50$).
- The two selected optimum scanning parameter combinations lead to distinct microstructures. Processing conditions with lower energy densities ($h_d70$) lead to weakly textured, relatively fine grained polycrystals, with irregularly shaped grains, while higher energy inputs ($h_d50$) yield columnar structures with strong <001> fiber textures parallel to the BD (<001>//BD). In both cases the AB microstructures are formed by a cellular substructure, with MC carbides rich in Ti, Ta, and Nb. No evidence of other precipitates was found.
- When printing thin sections, incorporating a pre-contour scan improves the processability of IN939. This modified scanning strategy enhances heat dissipation, resulting in shallower melt pools and an increase in relative density of 0.3 % associated to the reduction of subsurface keyhole porosity.
- The recrystallization temperature of PBF-LB/M IN939 is higher than that of cast IN939, primarily due to the Smith-Zener pinning effect exerted by MC carbides

present in the AB state. Increasing the temperature causes a carbide coarsening, which in turn facilitates recrystallization.

- The AB microstructure has a strong influence on the recrystallization kinetics. A smaller grain size, together with a weaker <001>//BD texture, as in $h_d70$, provides a higher number of favorable nucleation sites, lowering the recrystallization temperature and resulting in smaller recrystallized grains.
- A modified solution treatment (1200ºC/8 h), compared to the standard treatment (1160ºC/4 h), enhances mechanical properties across the temperature range from room temperature to 950ºC. Larger grain sizes reduce diffusion-related deformation mechanisms such as grain boundary sliding (GBS), while a well-distributed precipitate population offsets the potential reduction in Hall-Petch strengthening at lower temperatures.
- The melt pool overlap in a direction perpendicular to the BD and to the SD ($O_h$) has been identified as a valuable parameter for predicting and designing microstructures in PBF-LB/M IN939. An $O_h$ below 0.6 restricts epitaxial grain growth, yielding weakly textured microstructures with equiaxed grains.
- The scan track length and the hatch distance have a significant impact on the energy input. Both empirical (multitrack prints) and semi-analytical (modified normalized volumetric energy density) tools were employed to capture the coupled influence of $h_d$ and $l$ on microstructure evolution. These tools were successfully applied to achieve site-specific microstructure control.

# 9. FUTURE WORK

The work presented here introduces novel findings that pave the way for further investigations into the PBF-LB/M processing of IN939 and other alloys. To build upon this foundation, the following suggestions are proposed for future research.

**Assessment of the creep properties of PBF-LB/M:**

This study has focused exclusively on the tensile properties of PBF-LB/M IN939. However, creep resistance is a paramount concern in high-temperature alloys like IN939, and it should be thoroughly characterized. Future studies should examine the influence of the AB microstructure, the recrystallized area fraction and comparisons with cast material. Furthermore, fatigue properties – often a known limitation of additively manufactured components – should also be assessed under various conditions.

**Development of an improved analytical solution to the energy input:**

Building upon existing solutions like the Rosenthal equation or the Eagar-Tsai model, a new physics-based analytical models that not only accounts for the effect of laser power and scanning speed, but that also incorporates additional factors such as the hatch distance and the geometry. In the presented results we parametrized the geometry using the scan track length, but other formulas should be explored. One potential approach could involve incorporating the specific surface area (or surface-to-volume ratio), which might better reflect the effect of geometrical features on the thermal diffusivity.

An accurate yet simple analytical model could enable the definition of isenthalpic volumes or surfaces, facilitating the selection of optimal scanning parameters tailored to specific geometries. Such models, being computationally efficient, could also be used in real-time monitoring systems and support the implementation of closed-loop control strategies in the printing process.

**Application of the microstructural design concepts to heterostructured materials:**

Heterostructured materials are composed of different phases of domains with distinct physical or chemical properties [191]. Based on the results presented in Chapter 7 regarding the site-specific control of the microstructure, new heterostructured components could be produced, with potentially superior mechanical performance. Combining strongly oriented columnar microstructures with weakly textured finer ones may offer valuable insights into the mechanical behavior of such systems. Special attention should be given to the nature and quality of the interfaces. Furthermore, as suggested by the findings in Chapter 6, controlled, localized recrystallization could be intentionally induced at selected locations within printed parts to enhance performance or tailor properties.

# REFERENCES

[1] About ITP Aero, (n.d.). https://www.itpaero.com/en/about-itp-aero/ (accessed June 9, 2025).

[2] ITP Aero, ITP Aero becomes first aeroengine company to obtain EASA certification for an additive manufactured structural component, (n.d.). https://www.itpaero.com/en/the-spanish-air-and-space-force-awards-itp-aero-the-framework-agreement-for-the-inorganic-maintenance-of-its-aircraft-engines/ (accessed June 9, 2025).

[3] S. Singamneni, Y. LV, A. Hewitt, R. Chalk, W. Thomas, D. Jordison, Additive Manufacturing for the Aircraft Industry: A Review, J. Aeronaut. Aerosp. Eng. 08 (2019).

[4] G. Rasiya, A. Shukla, K. Saran, Additive Manufacturing-A Review, Mater. Today Proc. 47 (2021) 6896–6901.

[5] R.C. Reed, The Superalloys fundamentals and applications, Cambridge University Press, Cambridge, 2006.

[6] ISO/ASTM 52900, Standard Terminology for Additive Manufacturing General Principles Part 1: Terminology, Am. Soc. Test. Mater. (2015).

[7] T. Wohlers, T. Gornet, J. Mostow, A. Ghany, R. Kircher, N. Zealand, W. Associates, S. Africa, History of additive manufacturing, Wohlers Rep. 2016-2022 (2022). https://dx.doi.org/10.2139/ssrn.4474824.

[8] Wohlers TW, Wohlers Report 2024, 2024.

[9] W.J. Sames, F.A. List, S. Pannala, R.R. Dehoff, S.S. Babu, The metallurgy and processing science of metal additive manufacturing, Int. Mater. Rev. 61 (2016) 315–360.

[10] A.J. Pinkerton, Lasers in additive manufacturing, Opt. Laser Technol. 78 (2016) 25–32.

[11] M. Laleh, E. Sadeghi, R.I. Revilla, Q. Chao, N. Haghdadi, A.E. Hughes, W. Xu, I. De Graeve, M. Qian, I. Gibson, M.Y. Tan, Heat treatment for metal additive manufacturing, Prog. Mater. Sci. 133 (2023) 101051.

[12] T. DebRoy, H.L. Wei, J.S. Zuback, T. Mukherjee, J.W. Elmer, J.O. Milewski, A.M.

Beese, A. Wilson-Heid, A. De, W. Zhang, Additive manufacturing of metallic components – Process, structure and properties, Prog. Mater. Sci. 92 (2018) 112–224.

[13] A. Mostafaei, A.M. Elliott, J.E. Barnes, F. Li, W. Tan, C.L. Cramer, P. Nandwana, M. Chmielus, Binder jet 3D printing—Process parameters, materials, properties, modeling, and challenges, Prog. Mater. Sci. 119 (2021) 100707.

[14] B. Brandau, A. Da Silva, C. Wilsnack, F. Brueckner, A.F.H. Kaplan, Absorbance study of powder conditions for laser additive manufacturing, Mater. Des. 216 (2022) 110591.

[15] Y.A. Mayi, M. Dal, P. Peyre, M. Bellet, R. Fabbro, Physical mechanisms of conduction-to-keyhole transition in laser welding and additive manufacturing processes, Opt. Laser Technol. 158 (2023) 108811.

[16] J. Yang, L.M. Schlenger, M.H. Nasab, S. Van Petegem, F. Marone, R.E. Logé, C. Leinenbach, Experimental quantification of inward Marangoni convection and its impact on keyhole threshold in laser powder bed fusion of stainless steel, Addit. Manuf. 84 (2024).

[17] S. Patel, M. Vlasea, Melting modes in laser powder bed fusion, Materialia 9 (2020) 100591.

[18] B. Li, C. Li, H. Chunlei, Predicting temperature field in keyhole-mode selective laser melting with combined heat sources: a rapid model, Phys. Scr. 98 (2023).

[19] R. Cunningham, C. Zhao, N. Parab, C. Kantzos, J. Pauza, K. Fezzaa, T. Sun, A.D. Rollett, Keyhole threshold and morphology in laser melting revealed by ultrahigh-speed x-ray imaging, Science (80-. ). 363 (2019).

[20] V. Gunenthiram, P. Peyre, M. Schneider, M. Dal, F. Coste, I. Koutiri, R. Fabbro, Experimental analysis of spatter generation and melt-pool behavior during the powder bed laser beam melting process, J. Mater. Process. Technol. 251 (2018) 376–386.

[21] W.E. King, H.D. Barth, V.M. Castillo, G.F. Gallegos, J.W. Gibbs, D.E. Hahn, C. Kamath, A.M. Rubenchik, Observation of keyhole-mode laser melting in laser powder-bed fusion additive manufacturing, J. Mater. Process. Technol. 214 (2014) 2915–2925.

[22] D. Grange, A. Queva, G. Guillemot, M. Bellet, J.D. Bartout, C. Colin, Effect of processing parameters during the laser beam melting of Inconel 738: Comparison

between simulated and experimental melt pool shape, J. Mater. Process. Technol. 289 (2021) 116897.

[23] I. Yadroitsev, Selective laser melting: Direct manufacturing of 3D-objects by selective laser melting of metal powders, 2009.

[24] P. Urquhart, Review of rare earth doped fibre lasers and amplifiers, IEE Proc. J Optoelectron. 135 (1988) 385.

[25] G. Nordet, C. Gorny, Y. Mayi, J. Daligault, M. Dal, A. Effernelli, E. Blanchet, F. Coste, P. Peyre, Absorptivity measurements during laser powder bed fusion of pure copper with a 1 kW cw green laser, Opt. Laser Technol. 147 (2022) 107612.

[26] G.E. Bean, D.B. Witkin, T.D. McLouth, D.N. Patel, R.J. Zaldivar, Effect of laser focus shift on surface quality and density of Inconel 718 parts produced via selective laser melting, Addit. Manuf. 22 (2018) 207–215.

[27] R. Moore, G. Orlandi, T. Rodgers, D. Moser, H. Murdoch, F. Abdeljawad, Microstructure-Based Modeling of Laser Beam Shaping During Additive Manufacturing, Jom 76 (2024) 1726–1736.

[28] J. Singh, J.P. Oliveira, H. Taylor, J. Mireles, R. Wicker, A holistic approach for evaluation of Gaussian versus ring beam processing on structure and properties in laser powder bed fusion, J. Mater. Process. Technol. 325 (2024) 118293.

[29] S. Hadibeik, H. Ghasemi-Tabasi, A. Burn, S. Lani, F. Spieckermann, J. Eckert, Controlling the Glassy State toward Structural and Mechanical Enhancement: Additive Manufacturing of Bulk Metallic Glass Using Advanced Laser Beam Shaping Technology, Adv. Funct. Mater. 34 (2024) 1–16.

[30] M.L. Montero-Sistiaga, M. Godino-Martinez, K. Boschmans, J.P. Kruth, J. Van Humbeeck, K. Vanmeensel, Microstructure evolution of 316L produced by HP-SLM (high power selective laser melting), Addit. Manuf. 23 (2018) 402–410.

[31] L. Caprio, A.G. Demir, B. Previtali, Comparative study between CW and PW emissions in selective laser melting, J. Laser Appl. 30 (2018).

[32] L. Caprio, A.G. Demir, B. Previtali, Influence of pulsed and continuous wave emission on melting efficiency in selective laser melting, J. Mater. Process. Technol. 266 (2019) 429–441.

[33] S. Li, H. Xiao, K. Liu, W. Xiao, Y. Li, X. Han, J. Mazumder, L. Song, Melt-pool

motion, temperature variation and dendritic morphology of Inconel 718 during pulsed- and continuous-wave laser additive manufacturing: A comparative study, Mater. Des. 119 (2017).

[34] Y. Tian, J.A. Muñiz-Lerma, M. Brochu, Nickel-based superalloy microstructure obtained by pulsed laser powder bed fusion, Mater. Charact. 131 (2017) 306–315.

[35] C.Y. Yap, C.K. Chua, Z.L. Dong, Z.H. Liu, D.Q. Zhang, L.E. Loh, S.L. Sing, Review of selective laser melting: Materials and applications, Appl. Phys. Rev. 2 (2015).

[36] K.G. Weldeanenia, S.K. Kassegne, P.J. Ramulu, Governing of Melt Pool Solidification Parameters and Microstructure Evolution Indicator During SLM - Ti6Al4V Alloy Through Parametric Sweep Optimization, Eng. Reports 7 (2025) 1–13.

[37] M. Tang, P.C. Pistorius, J.L. Beuth, Prediction of lack-of-fusion porosity for powder bed fusion, Addit. Manuf. 14 (2017) 39–48.

[38] M.A. Obeidi, Metal additive manufacturing by laser-powder bed fusion:Guidelines for process optimisation, Results Eng. 15 (2022) 100473.

[39] C. Schwerz, F. Schulz, E. Natesan, L. Nyborg, Increasing productivity of laser powder bed fusion manufactured Hastelloy X through modification of process parameters, J. Manuf. Process. 78 (2022) 231–241.

[40] A. Mostafaei, C. Zhao, Y. He, S. Reza Ghiaasiaan, B. Shi, S. Shao, N. Shamsaei, Z. Wu, N. Kouraytem, T. Sun, J. Pauza, J. V. Gordon, B. Webler, N.D. Parab, M. Asherloo, Q. Guo, L. Chen, A.D. Rollett, Defects and anomalies in powder bed fusion metal additive manufacturing, Curr. Opin. Solid State Mater. Sci. 26 (2022) 100974.

[41] I.H. Ahn, Determination of a process window with consideration of effective layer thickness in SLM process, Int. J. Adv. Manuf. Technol. 105 (2019) 4181–4191.

[42] D. Jansen, T. Hanemann, M. Radek, A. Rota, J. Schröpfer, M. Heilmaier, Development of actual powder layer height depending on nominal layer thicknesses and selection of laser parameters, J. Mater. Process. Technol. 298 (2021) 117305.

[43] E. Correa-Gómez, V.M. Moock, A. Caballero-Ruiz, L. Ruiz-Huerta, Improving melt pool depth estimation in laser powder bed fusion with metallic alloys using the thermal dose concept, Int. J. Adv. Manuf. Technol. (2024) 3463–3471.

[44] W. Zhang, M. Tong, N.M. Harrison, Scanning strategies e ff ect on temperature ,

residual stress and deformation by multi-laser beam powder bed fusion manufacturing, Addit. Manuf. 36 (2020) 101507.

[45] T. Fritsch, V. Luzin, B. Ferrari, J. Sim, J. Schr, A. Evans, G. Bruno, Materials & Design Impact of scan strategy on principal stresses in laser powder bed fusion, 244 (2024).

[46] H. Jia, H. Sun, H. Wang, Y. Wu, H. Wang, Scanning strategy in selective laser melting (SLM): a review, Int. J. Adv. Manuf. Technol. 113 (2021) 2413–2435.

[47] M. Krasniqi, F. Löffler, R. Tutsch, Influence of scanning strategies on dimensional accuracy in laser powder bed fusion, Meas. Sensors (2025) 101840.

[48] S. Catchpole-Smith, N. Aboulkhair, L. Parry, C. Tuck, I.A. Ashcroft, A. Clare, Fractal scan strategies for selective laser melting of 'unweldable' nickel superalloys, Addit. Manuf. 15 (2017) 113–122.

[49] M.N. Doğu, S. Ozer, M.A. Yalçın, K. Davut, M.A. Obeidi, C. Simsir, H. Gu, C. Teng, D. Brabazon, A comprehensive study of the effect of scanning strategy on IN939 fabricated by powder bed fusion-laser beam, J. Mater. Res. Technol. 33 (2024) 5457–5481.

[50] T. Mukherjee, J.W. Elmer, H.L. Wei, T.J. Lienert, W. Zhang, S. Kou, T. DebRoy, Control of grain structure, phases, and defects in additive manufacturing of high-performance metallic components, Prog. Mater. Sci. 138 (2023) 101153.

[51] K. Artzt, T. Mishurova, P.P. Bauer, J. Gussone, P. Barriobero-Vila, S. Evsevleev, G. Bruno, G. Requena, J. Haubrich, Pandora's box-influence of contour parameters on roughness and subsurface residual stresses in laser powder bed fusion of Ti-6Al-4V, Materials (Basel). 13 (2020) 1–24.

[52] T.N. Le, S. Rauniyar, V.H. Nismath, K. Chou, An investigation into the effects of contouring process parameters on the up-skin surface characteristics in laser powder-bed fusion process, Manuf. Lett. 35 (2023) 707–716.

[53] B. Farhang, B.B. Ravichander, J. Ma, A. Amerinatanzi, N. Shayesteh Moghaddam, The evolution of microstructure and composition homogeneity induced by borders in laser powder bed fused Inconel 718 parts, J. Alloys Compd. 898 (2022) 162787.

[54] I. Yadroitsev, A. Gusarov, I. Yadroitsava, I. Smurov, Single track formation in selective laser melting of metal powders, J. Mater. Process. Technol. 210 (2010) 1624–

1631.

[55] D. Gu, Y. Shen, Effects of processing parameters on consolidation and microstructure of W-Cu components by DMLS, J. Alloys Compd. 473 (2009) 107–115.

[56] M.A. Buhairi, F.M. Foudzi, F.I. Jamhari, A.B. Sulong, N.A.M. Radzuan, N. Muhamad, I.F. Mohamed, A.H. Azman, W.S.W. Harun, M.S.H. Al-Furjan, Review on volumetric energy density: influence on morphology and mechanical properties of Ti6Al4V manufactured via laser powder bed fusion, Prog. Addit. Manuf. 8 (2023) 265–283.

[57] U. Scipioni Bertoli, A.J. Wolfer, M.J. Matthews, J.P.R. Delplanque, J.M. Schoenung, On the limitations of Volumetric Energy Density as a design parameter for Selective Laser Melting, Mater. Des. 113 (2017) 331–340.

[58] J.C. Ion, H.R. Shercliff, M.F. Ashby, Diagrams for laser materials processing, Acta Metall. Mater. 40 (1992) 1539–1551.

[59] M. Thomas, G.J. Baxter, I. Todd, Normalised model-based processing diagrams for additive layer manufacture of engineering alloys, Acta Mater. 108 (2016) 26–35.

[60] D.B. Hann, J. Iammi, J. Folkes, A simple methodology for predicting laser-weld properties from material and laser parameters, J. Phys. D. Appl. Phys. 44 (2011).

[61] H. Ghasemi-Tabasi, J. Jhabvala, E. Boillat, T. Ivas, R. Drissi-Daoudi, R.E. Logé, An effective rule for translating optimal selective laser melting processing parameters from one material to another, Addit. Manuf. 36 (2020).

[62] P. Zagade, B.P. Gautham, A. De, T. DebRoy, Analytical estimation of fusion zone dimensions and cooling rates in part scale laser powder bed fusion, Addit. Manuf. 46 (2021).

[63] D.A. Porter, K.E. Easterling, M.Y. Sherif, Phase Transformations in Metals and Alloys, CRC Press, Boca Raton, 2021.

[64] W. Kurz, D.J. Fisher, Fundamentals of Solidification, 4th ed., Trans Tech Publications Ltd., Zurich, 1998.

[65] R.R. Dehoff, M. Kirka, W.J. Sames, H. Bilheux, A.S. Tremsin, L.E. Lowe, S.S. Babu, Site specific control of crystallographic grain orientation through electron beam additive manufacturing, Mater. Sci. Technol. (United Kingdom) 31 (2015) 931–938.

[66] V.P. Narayana Samy, M. Schäfle, F. Brasche, U. Krupp, C. Haase, Understanding the

mechanism of columnar–to-equiaxed transition and grain refinement in additively manufactured steel during laser powder bed fusion, Addit. Manuf. 73 (2023) 103702.

[67] P. Promoppatum, S.C. Yao, P.C. Pistorius, A.D. Rollett, A Comprehensive Comparison of the Analytical and Numerical Prediction of the Thermal History and Solidification Microstructure of Inconel 718 Products Made by Laser Powder-Bed Fusion, Engineering 3 (2017) 685–694.

[68] S.M. Elahi, R. Tavakoli, I. Romero, D. Tourret, Grain growth competition during melt pool solidification — Comparing phase-field and cellular automaton models, Comput. Mater. Sci. 216 (2023) 111882.

[69] R. Tavakoli, D. Tourret, Phase-field study of polycrystalline growth and texture selection during melt pool solidification, IOP Conf. Ser. Mater. Sci. Eng. 1281 (2023) 012011.

[70] J. Pauza, A. Rollett, Simulation Study of Hatch Spacing and Layer Thickness Effects on Microstructure in Laser Powder Bed Fusion Additive Manufacturing using a Texture-Aware Solidification Potts Model, J. Mater. Eng. Perform. 30 (2021) 7007–7018.

[71] A. Keshavarzkermani, R. Esmaeilizadeh, U. Ali, P.D. Enrique, Y. Mahmoodkhani, N.Y. Zhou, A. Bonakdar, E. Toyserkani, Controlling mechanical properties of additively manufactured hastelloy X by altering solidification pattern during laser powder-bed fusion, Mater. Sci. Eng. A 762 (2019) 138081.

[72] F. Geiger, K. Kunze, T. Etter, Tailoring the texture of IN738LC processed by selective laser melting (SLM) by specific scanning strategies, Mater. Sci. Eng. A 661 (2016) 240–246.

[73] T. Mukherjee, J.S. Zuback, A. De, T. DebRoy, Printability of alloys for additive manufacturing, Sci. Rep. 6 (2016) 19717.

[74] A.A. Martin, N.P. Calta, S.A. Khairallah, J. Wang, P.J. Depond, A.Y. Fong, V. Thampy, G.M. Guss, A.M. Kiss, K.H. Stone, C.J. Tassone, J. Nelson Weker, M.F. Toney, T. van Buuren, M.J. Matthews, Dynamics of pore formation during laser powder bed fusion additive manufacturing, Nat. Commun. 10 (2019) 1–10.

[75] R. Snell, S. Tammas-Williams, L. Chechik, A. Lyle, E. Hernández-Nava, C. Boig, G. Panoutsos, I. Todd, Methods for Rapid Pore Classification in Metal Additive

Manufacturing, JOM 72 (2020) 101–109.

[76] Y.T. Tang, C. Panwisawas, J.N. Ghoussoub, Y. Gong, J.W.G. Clark, A.A.N. Németh, D.G. McCartney, R.C. Reed, Alloys-by-design: Application to new superalloys for additive manufacturing, Acta Mater. 202 (2021) 417–436.

[77] D. Dye, O. Hunziker, R.C. Reed, Numerical analysis of the weldability of superalloys, Acta Mater. 49 (2001) 683–697.

[78] D.N. Luu, W. Zhou, S.M.L. Nai, Mitigation of liquation cracking in selective laser melted Inconel 718 through optimization of layer thickness and laser energy density, J. Mater. Process. Technol. 299 (2022).

[79] X. Zhang, H. Chen, L. Xu, J. Xu, X. Ren, X. Chen, Cracking mechanism and susceptibility of laser melting deposited Inconel 738 superalloy, Mater. Des. 183 (2019) 108105.

[80] W. Wang, R. Zhang, A.A. Shirzadi, D.S. Balint, L. Aucott, J. Jiang, Thermal cracking: Clarifying the effects of phases, voids and grains through characterisation and crystal plasticity modelling, J. Mech. Phys. Solids 186 (2024) 105600.

[81] N. Nothomb, I. Rodriguez-Barber, M.T. Pérez-Prado, N.J. Mena, G. Pyka, A. Simar, Understanding the effect of pre-sintering scanning strategy on the relative density of Zr-modified Al7075 processed by laser powder bed fusion, Addit. Manuf. Lett. 11 (2024) 100253.

[82] N. Zhou, A.D. Dicus, S.A.J. Forsik, T. Wang, G.A. Colombo, M.E. Epler, Development of a New Alumina-Forming Crack-Resistant High-γ′ Fraction Ni-Base Superalloy for Additive Manufacturing, Springer International Publishing, 2020.

[83] D. Schimbäck, P. Mair, M. Bärtl, F. Palm, G. Leichtfried, S. Mayer, P.J. Uggowitzer, S. Pogatscher, Alloy design strategy for microstructural-tailored scandium-modified aluminium alloys for additive manufacturing, Scr. Mater. 207 (2022) 19–21.

[84] A. Mostafaei, R. Ghiaasiaan, I.T. Ho, S. Strayer, K.C. Chang, N. Shamsaei, S. Shao, S. Paul, A.C. Yeh, S. Tin, A.C. To, Additive manufacturing of nickel-based superalloys: A state-of-the-art review on process-structure-defect-property relationship, Prog. Mater. Sci. 136 (2023) 101108.

[85] A.T. Clare, R.S. Mishra, M. Merklein, H. Tan, I. Todd, L. Chechik, J. Li, M. Bambach, Alloy design and adaptation for additive manufacture, J. Mater. Process. Technol. 299

(2022).

[86] M.M. Attallah, R. Jennings, X. Wang, L.N. Carter, Additive manufacturing of Ni-based superalloys: The outstanding issues, MRS Bull. 41 (2016) 758–764.

[87] T.M. Pollock, A.J. Clarke, S.S. Babu, Design and Tailoring of Alloys for Additive Manufacturing, Metall. Mater. Trans. A Phys. Metall. Mater. Sci. 51 (2020) 6000–6019.

[88] B. Kaplan, A comprehensive model for quantitatively predicting the comparative Strain-Age Cracking risk in welded or additively manufactured Ni-base superalloys, Mater. Today Commun. 40 (2024) 109408.

[89] S. Sanchez, P. Smith, Z. Xu, G. Gaspard, C.J. Hyde, W.W. Wits, I.A. Ashcroft, H. Chen, A.T. Clare, Powder Bed Fusion of nickel-based superalloys: A review, Int. J. Mach. Tools Manuf. 165 (2021).

[90] S.W.K. Shaw, Response of IN-939 to Process Variations, in: Superalloys 1980 (Fourth Int. Symp., TMS, 1980: pp. 275–284.

[91] K.M. Delargy, S.W.K. Shaw, G.D.W. Smith, Effects of heat treatment on mechanical properties of high-chromium nickel-base superalloy IN 939, Mater. Sci. Technol. 2 (1986) 1031–1037.

[92] M.R. Jahangiri, M. Abedini, Effect of long time service exposure on microstructure and mechanical properties of gas turbine vanes made of IN939 alloy, Mater. Des. 64 (2014) 588–600.

[93] M.R. Jahangiri, H. Arabi, S.M.A. Boutorabi, Development of wrought precipitation strengthened IN939 superalloy, Mater. Sci. Technol. (United Kingdom) 28 (2012) 1470–1478.

[94] P. Kanagarajah, F. Brenne, T. Niendorf, H.J. Maier, Inconel 939 processed by selective laser melting: Effect of microstructure and temperature on the mechanical properties under static and cyclic loading, Mater. Sci. Eng. A 588 (2013) 188–195.

[95] W. Philpott, M.A.E. Jepson, R.C. Thomson, Comparison of the effects of a conventional heat treatment between cast and selective laser melted IN939 alloy, Adv. Mater. Technol. Foss. Power Plants - Proc. from 8th Int. Conf. (2016) 735–746.

[96] G. Marchese, S. Parizia, A. Saboori, D. Manfredi, M. Lombardi, P. Fino, D. Ugues, S. Biamino, The influence of the process parameters on the densification and

microstructure development of laser powder bed fused inconel 939, Metals (Basel). 10 (2020) 1–19.

[97] S. Banoth, C.W. Li, Y. Hiratsuka, K. Kakehi, The effect of recrystallization on creep properties of alloy in939 fabricated by selective laser melting process, Metals (Basel). 10 (2020) 1–16.

[98] T. Wimmer, Y. Mick, B. Weigand, Experimental investigation into capabilities of laser powder bed fusion to produce wavy macro-channels from IN939, Addit. Manuf. 35 (2020) 101345.

[99] I. Rodríguez-Barber, A.M. Fernández-Blanco, I. Unanue-Arruti, I. Madariaga-Rodríguez, S. Milenkovic, M.T. Pérez-Prado, Laser powder bed fusion of the Ni superalloy Inconel 939 using pulsed wave emission, Mater. Sci. Eng. A 870 (2023) 144864.

[100] A. Fardan, U. Klement, H. Brodin, E. Hryha, Effect of Part Thickness and Build Angle on the Microstructure, Surface Roughness, and Mechanical Properties of Additively Manufactured IN-939, Metall. Mater. Trans. A (2022).

[101] I. Rodríguez-Barber, A.M. Fernández-Blanco, I. Unanue-Arruti, I. Madariaga-Rodríguez, S. Milenkovic, M.T. Pérez-Prado, Precontouring as a Tool to Improve the Laser Powder Bed Fusion Printability of Inconel939 Thin Walls, Adv. Eng. Mater. 2401929 (2024) 1–8.

[102] A.S. Shaikh, M. Rashidi, K. Minet-Lallemand, E. Hryha, On as-built microstructure and necessity of solution treatment in additively manufactured Inconel 939, Powder Metall. (2022) 1–9.

[103] M.N. Doğu, S. Ozer, M.A. Yalçın, K. Davut, G.M. Bilgin, M.A. Obeidi, H. Brodin, H. Gu, D. Brabazon, Effect of solution heat treatment on the microstructure and crystallographic texture of IN939 fabricated by powder bed fusion-laser beam, J. Mater. Res. Technol. 24 (2023) 8909–8923.

[104] S. Ozer, M.N. Doğu, C. Ozdemirel, G.M. Bilgin, M. Gunes, K. Davut, H. Gu, D. Brabazon, Effect of aging treatment on the microstructure, cracking type and crystallographic texture of IN939 fabricated by powder bed fusion-laser beam, J. Mater. Res. Technol. 33 (2024) 574–588.

[105] I. Šulák, T. Babinský, A. Chlupová, A. Milovanović, L. Náhlík, Effect of building

direction and heat treatment on mechanical properties of Inconel 939 prepared by additive manufacturing, J. Mech. Sci. Technol. 37 (2023) 1071–1076.

[106] C. Zeng, H. Ding, U. Bhandari, S.M. Guo, Design of crack-free laser additive manufactured Inconel 939 alloy driven by computational thermodynamics method, MRS Commun. (2022).

[107] H. Ding, S. Emanet, Y. Chen, S. Guo, The potential benefit of pseudo high thermal conductivity for laser powder bed fusion additive manufacturing, Mater. Res. Lett. 11 (2023) 797–805.

[108] S. Banoth, C.W. Li, Y. Hiratsuka, K. Kakehi, The effect of recrystallization on creep properties of alloy in939 fabricated by selective laser melting process, Metals (Basel). 10 (2020) 1–16.

[109] S. Li, S. Gao, W. Zhang, G. Lu, L. Cui, L. Li, Y. Ma, S. Wang, Study of the Crack and Porosity Regulation of a Non-weldable Ni-Based Superalloy Fabricated by Laser Powder Bed Fusion, J. Mater. Eng. Perform. (2024).

[110] P. Hu, Z. Liu, H. Zhang, Y. Li, Q. Zhou, J. Xie, Effect of remelting on cracking of Inconel 939 fabricated via laser powder bed fusion, Mater. Charact. 214 (2024) 114087.

[111] A. Visibile, K.O. Gunduz, M. Sattari, I. Fedorova, M. Halvarsson, J. Froitzheim, High temperature oxidation of inconel 939 produced by additive manufacturing, Corros. Sci. 233 (2024) 112067.

[112] M.N. Doğu, M.A. Obeidi, H. Gu, C. Teng, D. Brabazon, Powder Bed Fusion–Laser Beam of IN939: The Effect of Process Parameters on the Relative Density, Defect Formation, Surface Roughness and Microstructure, Materials (Basel). 17 (2024) 3324.

[113] C. Kumar, S. Reddy, N.K. Eswaramoorthy, P. Ravanappa, V. Chintapenta, D. Srinivasan, P. Kumar, Microstructure optimization for improving creep resistance of additively manufactured Ni-based superalloy IN939 through heat treatment, J. Mater. Sci. 60 (2025) 1545–1560.

[114] I. Kuběna, T. Babinský, L. Náhlík, I. Šulák, Cyclic stress–strain behavior of additively manufactured gamma prime strengthened superalloy at elevated temperatures, Theor. Appl. Fract. Mech. 133 (2024) 104623.

[115] M. Nahmany, D. Moreno, Y. Nahmana, M. Zakai, A.Y. Cohen, M. Shapira, R.

Shneck, Portevin-Le Chatelier Effect in Additively Manufactured and As-Cast Inconel 939 Nickel-Based Superalloy, J. Miner. Mater. Charact. Eng. 12 (2024) 299–315.

[116] P. Piwowarski, D. Moszczyńska, K. Paradowski, M. Wieczorek-Czarnocka, J. Mizera, Influence of Solution Treatment Temperatures on LPBF-Produced Inconel 939 Alloy on Mechanical Performance, Appl. Sci. 14 (2024) 9625.

[117] J. Sedlak, J. Zouhar, Z. Pokorny, J. Robl, S. Kolomy, M. Pagac, K. Kouril, Effect of heat treatment and hot isostatic pressing on the structure and mechanical properties of Inconel 939 manufactured via casting and LPBF, J. Manuf. Process. 145 (2025) 556–570.

[118] W. Betteridge, S.W.K. Shaw, Development of superalloys, Mater. Sci. Technol. (United Kingdom) 3 (1987) 682–694.

[119] J. Schindelin, I. Arganda-Carreras, E. Frise, V. Kaynig, M. Longair, T. Pietzsch, S. Preibisch, C. Rueden, S. Saalfeld, B. Schmid, J.Y. Tinevez, D.J. White, V. Hartenstein, K. Eliceiri, P. Tomancak, A. Cardona, Fiji: An open-source platform for biological-image analysis, Nat. Methods 9 (2012).

[120] I.H. Witten, E. Frank, J. Geller, Data Mining: Practical Machine Learning Tools and Techniques with Java Implementations, SIGMOD Rec. 31 (2002).

[121] F. Bachmann, R. Hielscher, H. Schaeben, Texture analysis with MTEX- Free and open source software toolbox, in: Solid State Phenom., 2010.

[122] M. Calcagnotto, D. Ponge, E. Demir, D. Raabe, Orientation gradients and geometrically necessary dislocations in ultrafine grained dual-phase steels studied by 2D and 3D EBSD, Mater. Sci. Eng. A 527 (2010) 2738–2746.

[123] P. Köhnen, M. Létang, M. Voshage, J.H. Schleifenbaum, C. Haase, Understanding the process-microstructure correlations for tailoring the mechanical properties of L-PBF produced austenitic advanced high strength steel, Addit. Manuf. 30 (2019) 100914.

[124] J. Kundin, A.L.I. Ramazani, U. Prahl, C. Haase, Microstructure Evolution of Binary and Multicomponent Manganese Steels During Selective Laser Melting : Phase-Field Modeling and Experimental Validation, Metall. Mater. Trans. A (2019).

[125] M.R. Jahangiri, H. Arabi, S.M.A. Boutorabi, Comparison of microstructural stability of IN939 superalloy with two different manufacturing routes during long-time aging, Trans. Nonferrous Met. Soc. China (English Ed. 24 (2014) 1717–1729.

[126] A.G. Demir, L. Mazzoleni, L. Caprio, M. Pacher, B. Previtali, Complementary use of pulsed and continuous wave emission modes to stabilize melt pool geometry in laser powder bed fusion, Opt. Laser Technol. 113 (2019).

[127] J. Kim, S. Ji, Y.-S. Yun, J.-S. Yeo, A Review: Melt Pool Analysis for Selective Laser Melting with Continuous Wave and Pulse Width Modulated Lasers, Appl. Sci. Converg. Technol. 27 (2018).

[128] M. Hofele, J. Schanz, A. Roth, D.K. Harrison, A.K.M. De Silva, H. Riegel, Process parameter dependencies of continuous and pulsed laser modes on surface polishing of additive manufactured aluminium AlSi10Mg parts, Materwiss. Werksttech. 52 (2021).

[129] C.A. Biffi, J. Fiocchi, P. Bassani, A. Tuissi, Continuous wave vs pulsed wave laser emission in selective laser melting of AlSi10Mg parts with industrial optimized process parameters: Microstructure and mechanical behaviour, Addit. Manuf. 24 (2018) 639–646.

[130] K. Karami, A. Blok, L. Weber, S.M. Ahmadi, R. Petrov, K. Nikolic, E. V. Borisov, S. Leeflang, C. Ayas, A.A. Zadpoor, M. Mehdipour, E. Reinton, V.A. Popovich, Continuous and pulsed selective laser melting of Ti6Al4V lattice structures: Effect of post-processing on microstructural anisotropy and fatigue behaviour, Addit. Manuf. 36 (2020).

[131] A.B. Kaligar, H.A. Kumar, A. Ali, W. Abuzaid, M. Egilmez, M. Alkhader, F. Abed, A.S. Alnaser, Femtosecond Laser-Based Additive Manufacturing: Current Status and Perspectives, Quantum Beam Sci. 6 (2022).

[132] C.M. Cepeda-Jiménez, F. Potenza, E. Magalini, V. Luchin, A. Molinari, M.T. Pérez-Prado, Effect of energy density on the microstructure and texture evolution of Ti-6Al-4V manufactured by laser powder bed fusion, Mater. Charact. 163 (2020) 110238.

[133] O. Fergani, V. Brotan, M. Bambach, M.T. Pérez-Prado, Texture evolution in stainless steel processed by selective laser melting and annealing, Mater. Sci. Technol. (United Kingdom) 34 (2018) 2223–2230.

[134] Z.C. Cordero, B.E. Knight, C.A. Schuh, Six decades of the Hall–Petch effect – a survey of grain-size strengthening studies on pure metals, Int. Mater. Rev. 61 (2016) 495–512.

[135] S.A.U. Industria de Turbopropulseros, Private communication, n.d.

[136] M.E. Kassner, M.T. Pérez-Prado, Fundamentals of Creep in Metals and Alloys, Elsevier, 2004.

[137] O.A. Kajbyshev, N.G. Zaripov, Superplasticity in metals and ceramics, Cambridge University Press, 2001.

[138] A. Mostafaei, R. Ghiaasiaan, I. Ho, S. Strayer, K. Chang, N. Shamsaei, S. Shao, S. Paul, A. Yeh, Additive manufacturing of nickel-based superalloys : A state-of-the-art review on process-structure-defect-property relationship, Prog. Mater. Sci. 136 (2023) 101108.

[139] D. Herzog, V. Seyda, E. Wycisk, C. Emmelmann, Additive manufacturing of metals, Acta Mater. 117 (2016) 371–392.

[140] Z. Wu, S.P. Narra, A. Rollett, Exploring the fabrication limits of thin-wall structures in a laser powder bed fusion process, Int. J. Adv. Manuf. Technol. 110 (2020) 191–207.

[141] F. Calignano, G. Cattano, D. Manfredi, Manufacturing of thin wall structures in AlSi10Mg alloy by laser powder bed fusion through process parameters, J. Mater. Process. Technol. 255 (2018) 773–783.

[142] Y. Sun, H. Zhao, R. Huang, L. Liu, C. Tan, D. Lin, B. Chen, X. Song, R. Ma, The effect of thickness on the defects and anisotropy of thin-wall Hastelloy X fabricated via laser powder-bed fusion, J. Mater. Res. Technol. 27 (2023) 703–717.

[143] A. Chakraborty, R. Tangestani, W. Muhammad, T. Sabiston, J.-P. Masse, R. Batmaz, A. Wessman, É. Martin, Micro-cracking mechanism of RENÉ 108 thin-wall components built by laser powder bed fusion additive manufacturing, Mater. Today Commun. 30 (2022) 103139.

[144] A. Leicht, C. Pauzon, M. Rashidi, U. Klement, L. Nyborg, E. Hryha, Effect of part thickness on the microstructure and tensile properties of 316L parts produced by laser powder bed fusion, Adv. Ind. Manuf. Eng. 2 (2021) 100037.

[145] G. Meng, Y. Gong, J. Zhang, Z. Jiang, Q. Ren, J. Zhao, Microstructure and mechanical properties of Inconel 718 thin walls prepared by laser direct energy deposition and selective laser melting, Thin-Walled Struct. 193 (2023) 111284.

[146] L. Chen, S. Liang, Y. Liu, L. Zhang, Additive manufacturing of metallic lattice structures : Unconstrained design , accurate fabrication , fascinated performances , and

challenges, Mater. Sci. Eng. R 146 (2021) 100648.

[147] J. Musekamp, T. Reiber, H.C. Hoche, M. Oechsner, M. Weigold, E. Abele, Influence of LPBF-Surface Characteristics on Fatigue Properties of Scalmalloy ®, (2021) 1–19.

[148] H. Karimialavijeh, M. Ghasri-Khouzani, A. Das, M. Pröebstle, Martin, Effect of laser contour scan parameters on fatigue performance of A20X fabricated by laser powder bed fusion, Int. J. Fatigue 175 (2023).

[149] K. Yin, B. Cao, J. Todt, F. Gutmann, H.F. Tunçay, A. Roth, F. Fischer, N. Grübel, A. Pfaff, G.C. Ganzenmüller, J. Keckes, S. Hiermaier, C. Eberl, Manufacturing size effect on the structural and mechanical properties of additively manufactured Ti-6Al-4V microbeams, J. Mater. Sci. Technol. 149 (2023) 18–30.

[150] Z. Ren, D. Wei, S. Wang, D.Z. Zhang, S. Mao, On the role of pre- and post-contour scanning in laser powder bed fusion: Thermal-fluid dynamics and laser reflections, Int. J. Mech. Sci. 226 (2022) 107389.

[151] T. Reiber, J. Rüdesheim, M. Weigold, E. Abele, J. Musekamp, M. Oechsner, Influence of contour scans on surface roughness and pore formation using Scalmalloy® manufactured by laser powder bed fusion (PBF-LB), Materwiss. Werksttech. 52 (2021) 468–481.

[152] S.I. Shahabad, U. Ali, Z. Zhang, A. Keshavarzkermani, R. Esmaeilizadeh, A. Bonakdar, E. Toyserkani, On the effect of thin-wall thickness on melt pool dimensions in laser powder-bed fusion of Hastelloy X: Numerical modeling and experimental validation, J. Manuf. Process. 75 (2022) 435–449.

[153] S.K. Sahu, D.K. Mishra, A. Behera, R.P. Dalai, An overview on the effect of heat-treatment and cooling rates on Ni-based superalloys, Mater. Today Proc. 47 (2021) 3309–3312.

[154] A. Rollett, F. Humphreys, G.S. Rohrer, M. Hatherly, Recrystallization and Related Annealing Phenomena: Second Edition, 2004.

[155] G. Wang, H. Ouyang, C. Fan, Q. Guo, Z. Li, W. Yan, Z. Li, The origin of high-density dislocations in additively manufactured metals, Mater. Res. Lett. 8 (2020) 283–290.

[156] S. Gao, Z. Hu, M. Duchamp, P.S.S.R. Krishnan, S. Tekumalla, X. Song, M. Seita, Recrystallization-based grain boundary engineering of 316L stainless steel produced via selective laser melting, Acta Mater. 200 (2020) 366–377.

[157] S. Gao, Z. Li, S. Van Petegem, J. Ge, S. Goel, J.V. Vas, V. Luzin, Z. Hu, H.L. Seet, D.F. Sanchez, H. Van Swygenhoven, H. Gao, M. Seita, Additive manufacturing of alloys with programmable microstructure and properties, Nat. Commun. 14 (2023).

[158] Y.T. Tang, A. Hoang Pham, S. Utada, J.S. Zhang, Y. Zhuge, S. Morito, K. Arakawa, D.G. McCartney, R.C. Reed, A Correlative In Situ and Ex Situ Analysis of Static Recrystallisation in a New Superalloy for 3D-Printing, Miner. Met. Mater. Ser. (2024) 836–848.

[159] T. Voisin, J.-B. Forien, A. Perron, S. Aubry, N. Bertin, A. Samanta, A. Baker, Y.M. Wang, New insights on cellular structures strengthening mechanisms and thermal stability of an austenitic stainless steel fabricated by laser powder-bed-fusion, Acta Mater. 203 (2021) 116476.

[160] J. Xu, H. Brodin, R.L. Peng, V. Luzin, J. Moverare, Effect of heat treatment temperature on the microstructural evolution of CM247LC superalloy by laser powder bed fusion, Mater. Charact. 185 (2022) 111742.

[161] S. Sun, Q. Teng, Y. Xie, T. Liu, R. Ma, J. Bai, C. Cai, Q. Wei, Two-step heat treatment for laser powder bed fusion of a nickel-based superalloy with simultaneously enhanced tensile strength and ductility, Addit. Manuf. 46 (2021) 102168.

[162] O.M.D.M. Messé, R. Muñoz-Moreno, T. Illston, S. Baker, H.J. Stone, Metastable carbides and their impact on recrystallisation in IN738LC processed by selective laser melting, Addit. Manuf. 22 (2018) 394–404.

[163] Y.T. Tang, C. Panwisawas, B.M. Jenkins, J. Liu, Z. Shen, E. Salvati, Y. Gong, J.N. Ghoussoub, S. Michalik, B. Roebuck, P.A.J. Bagot, S. Lozano-Perez, C.R.M. Grovenor, M.P. Moody, A.M. Korsunsky, D.M. Collins, R.C. Reed, Multi-length-scale study on the heat treatment response to supersaturated nickel-based superalloys: Precipitation reactions and incipient recrystallisation, Addit. Manuf. 62 (2023) 103389.

[164] S. Banoth, C.W. Li, Y. Hiratsuka, K. Kakehi, The effect of recrystallization on creep properties of alloy in939 fabricated by selective laser melting process, Metals (Basel). 10 (2020) 1–16.

[165] W. Pantleon, Resolving the geometrically necessary dislocation content by conventional electron backscattering diffraction, Scr. Mater. 58 (2008) 994–997.

[166] S.I. Wright, D.P. Field, M.M. Nowell, Post processing effects on GND calculations from EBSD-based orientation measurements, IOP Conf. Ser. Mater. Sci. Eng. 89 (2015) 012049.

[167] K. Prasad, M. Obana, A. Ito, S. Torizuka, Synchrotron diffraction characterization of dislocation density in additively manufactured IN 718 superalloy, Mater. Charact. 179 (2021) 111379.

[168] A. Ayad, M. Ramoul, A.D. Rollett, F. Wagner, Quantifying primary recrystallization from EBSD maps of partially recrystallized states of an IF steel, Mater. Charact. 171 (2021) 110773.

[169] T. Ogawa, H. Dannoshita, Y. Adachi, K. Ushioda, Effect of initial microstructures prior to cold-rolling and intercritical annealing on ferrite recrystallization and ferrite-to-austenite phase transformation in Nb bearing low-carbon steels, J. Phys. Conf. Ser. 1270 (2019) 012016.

[170] M. Sanjari, M. Mehdi, Y. He, E.J. Hilinski, S. Yue, L.A.I. Kestens, A. Edrisy, Tracking the Evolution of Annealing Textures from Individual Deformed Grains in a Cross-Rolled Non-oriented Electrical Steel, Metall. Mater. Trans. A 48 (2017) 6013–6026.

[171] M.D. Sangid, H. Sehitoglu, H.J. Maier, T. Niendorf, Grain boundary characterization and energetics of superalloys, Mater. Sci. Eng. A 527 (2010) 7115–7125.

[172] S. Ukai, K. Taya, K. Nakamura, M.S. Aghamiri, N. Oono, S. Hayashi, T. Okuda, Directional recrystallization by zone annealing in a Ni-based ODS superalloy, J. Alloys Compd. 744 (2018) 204–210.

[173] L.H. Rettberg, T.M. Pollock, Localized recrystallization during creep in nickel-based superalloys GTD444 and René N5, Acta Mater. 73 (2014) 287–297.

[174] A. Plotkowski, J. Ferguson, B. Stump, W. Halsey, V. Paquit, C. Joslin, S.S. Babu, A. Marquez Rossy, M.M. Kirka, R.R. Dehoff, A stochastic scan strategy for grain structure control in complex geometries using electron beam powder bed fusion, Addit. Manuf. 46 (2021) 102092.

[175] X. Ding, Y. Koizumi, K. Aoyagi, T. Kii, N. Sasaki, Y. Hayasaka, K. Yamanaka, A. Chiba, Microstructural control of alloy 718 fabricated by electron beam melting with expanded processing window by adaptive offset method, Mater. Sci. Eng. A 764

(2019) 138058.

[176] S.D. Jadhav, S. Dadbakhsh, L. Goossens, J.P. Kruth, J. Van Humbeeck, K. Vanmeensel, Influence of selective laser melting process parameters on texture evolution in pure copper, J. Mater. Process. Technol. 270 (2019) 47–58.

[177] K.A. Sofinowski, S. Raman, X. Wang, B. Gaskey, M. Seita, Layer-wise engineering of grain orientation (LEGO) in laser powder bed fusion of stainless steel 316L, Addit. Manuf. 38 (2021).

[178] A. Fardan, A. Fazi, J. Schröder, T. Mishurova, T. Deckers, G. Bruno, M. Thuvander, A. Markström, H. Brodin, E. Hryha, Microstructure tailoring for crack mitigation in CM247LC manufactured by powder bed fusion – Laser beam, Addit. Manuf. 99 (2025).

[179] B. Attard, S. Cruchley, C. Beetz, M. Megahed, Y.L. Chiu, M.M. Attallah, Microstructural control during laser powder fusion to create graded microstructure Ni-superalloy components, Addit. Manuf. 36 (2020) 101432.

[180] K. Sofinowski, M. Wittwer, M. Seita, Encoding data into metal alloys using laser powder bed fusion, Addit. Manuf. 52 (2022).

[181] C. Sofras, J. Čapek, X. Li, C.C. Roth, C. Leinenbach, R.E. Logé, M. Strobl, E. Polatidis, Site-specifically tailored microstructures with enhanced strength and hardening through laser powder bed fusion, Mater. Des. 237 (2024).

[182] D.D.R. Peachey, C.P. Carter, A. Garcia-Jimenez, A. Mukundan, D.N. Leonard, M.A. Charpagne, Z.C. Cordero, Directional recrystallization of an additively manufactured Ni-base superalloy, Addit. Manuf. 60 (2022) 103198.

[183] E. Hernández-Nava, P. Mahoney, C.J. Smith, J. Donoghue, I. Todd, S. Tammas-Williams, Additive manufacturing titanium components with isotropic or graded properties by hybrid electron beam melting/hot isostatic pressing powder processing, Sci. Rep. 9 (2019) 1–11.

[184] M.B. Wilms, S.-K. Rittinghaus, M. Goßling, B. Gökce, Additive manufacturing of oxide-dispersion strengthened alloys: Materials, synthesis and manufacturing, Prog. Mater. Sci. 133 (2023) 101049.

[185] M.Z. Ghodsi, S. Khademzadeh, E. Marzbanrad, M.H. Razmpoosh, N. De Marchi, E. Toyserkani, Development of Yttria-stabilized zirconia reinforced Inconel 625 metal

matrix composite by laser powder bed fusion, Mater. Sci. Eng. A 827 (2021) 142037.

[186] M.L. Montero-Sistiaga, S. Pourbabak, J. Van Humbeeck, D. Schryvers, K. Vanmeensel, Microstructure and mechanical properties of Hastelloy X produced by HP-SLM (high power selective laser melting), Mater. Des. 165 (2019) 107598.

[187] T. Lyu, Y. Zou, Remelting-based microstructure engineering in laser powder bed fusion: A case study in 316L stainless steel, Scr. Mater. 257 (2025) 116469.

[188] P. Promoppatum, S.C. Yao, P.C. Pistorius, A.D. Rollett, P.J. Coutts, F. Lia, R. Martukanitz, Numerical modeling and experimental validation of thermal history and microstructure for additive manufacturing of an Inconel 718 product, Prog. Addit. Manuf. 3 (2018) 15–32.

[189] M.A.L. Phan, O. Dew, I. Todd, Predictive process diagram for parameters selection in laser powder bed fusion to achieve high-density and low-cracking built parts, Addit. Manuf. 85 (2024) 104145.

[190] Q. Luo, N. Huang, T. Fu, J. Wang, D.L. Bartles, T.W. Simpson, A.M. Beese, New insight into the multivariate relationships among process, structure, and properties in laser powder bed fusion AlSi10Mg, Addit. Manuf. Submitted (2023) 103804.

[191] Y. Zhu, X. Wu, Heterostructured materials, Prog. Mater. Sci. 131 (2023) 101019.